The Correlation between Astrocytic Calcium and fMRI Signals is Related to the Thalamic Regulation of Cortical States

Dissertation

zur Erlangung des Grades eines
Doktors der Naturwissenschaften

der Mathematisch-Naturwissenschaftlichen Fakultät
und
der Medizinischen Fakultät
der Eberhard-Karls-Universität Tübingen

vorgelegt
von

Maosen Wang
aus Gansu, China

February - 2018

Tag der mündlichen Prüfung: .....

Dekan der Math.-Nat. Fakultät: Prof. Dr. W. Rosenstiel

Dekan der Medizinischen Fakultät: Prof. Dr. I. B. Autenrieth

1. Berichterstatter: Dr. Xin Yu

2. Berichterstatter: Prof. Dr. / PD Dr. / Dr. Cornelius Schwarz

Prüfungskommission: Dr. Xin Yu

Prof. Dr. Cornelius Schwarz

Prof. Dr. Sandra Beer-Hammer

Prof. Dr. Andreas Bartels

Erklärung / Declaration:

Ich erkläre, dass ich die zur Promotion eingereichte Arbeit mit dem Titel:

„Correlation between astrocytic calcium and fMRI signals relate to thalamic regulation of cortical states “

selbständig verfasst, nur die angegebenen Quellen und Hilfsmittel benutzt und wörtlich oder inhaltlich übernommene Stellen als solche gekennzeichnet habe. Ich versichere an Eides statt, dass diese Angaben wahr sind und dass ich nichts verschwiegen habe. Mir ist bekannt, dass die falsche Abgabe einer Versicherung an Eides statt mit Freiheitsstrafe bis zu drei Jahren oder mit Geldstrafe bestraft wird.

I hereby declare that I have produced the work entitled “The correlation between astrocytic calcium and fMRI signals is related to the thalamic regulation of cortical states”, submitted for the award of a doctorate, on my own (without external help), have used only the sources and aids indicated and have marked passages included from other works, whether verbatim or in content, as such. I swear upon oath that these statements are true and that I have not concealed anything. I am aware that making a false declaration under oath is punishable by a term of imprisonment of up to three years or by a fine.

Tübingen, den ....

Datum / Date Unterschrift /Signature

Acknowledgements

First of all, I would like to thank my supervisor, Dr. Xin Yu, for giving me the opportunity to join his lab, for his time and efforts on my doctoral project. With Dr. Xin's support, I tackled all aspects of my doctoral project, both technical and intellectual, with determination and success .

Secondly, I would like to thank Prof. Dr. Cornelius Schwarz and Prof. Dr. Sandra Beer-Hammer for being my doctoral advisory board members, for their invaluable instructions, comments, and time on my work.

I would like to thank our collaborator, Prof. Dr. Terrence Sejnowski, from UCSD for the instructions and help to this project.

I thank Dr. Rolf Pohmann and Prof. Dr. Klaus for their excellent technical guidance and support on MRI.

I thank Dr. Heule Rahel and Dr. Deshmane Anagha for helpful suggestions and comments for the thesis.

I would like to thank all my colleagues who provide the technical and animal maintenance support, thanks for their time and efforts.

And for the rats, I appreciate their sacrifice for the project; I cannot do anything for them but treat them with respect and care.

I am grateful to my dear friends and colleagues, for the wonderful times that we have spent together especially for Yi He and Hao Mei. I have learned so much from them. Yi He helps me a lot in the research and daily life.

Thanks to everyone in my life, as being parts of my life and help me to grow.

Special thanks to my family. My parents encourage me to follow my heart to pursue my dream.

Contents

Abbreviations 1
Abstract 2
1 3
Introduction 3
2 5
Development of a fiber optic recording system for cell-type specific calcium recordings in the rat brain . 5
2.1 Motivation 5
2.2 Methods 6
2.3 Results and discussion 6
2.4 Conclusion 7
3 8
The correlation between neuronal/astrocytic calcium and simultaneously acquired fMRI signal 8
3.1 Motivation 8
3.2 Methods 8
3.3 Results and discussion 9
3.4 Conclusion 9
4 11
Intrinsic astrocytic calcium spikes correlated with the brain states transition 11
4.1 Can intrinsic and evoked astrocytic calcium occur concurrently? 11
4.2 Propagation speed of the intrinsic astrocytic calcium signal 12
4.3 Identifying the subcortical nuclei involved in the intrinsic astrocytic calcium spikes 13
4.4 Intrinsic astrocytic calcium spikes are preserved in free moving rats 15
5 16
Neuronal calcium and the resting-state BOLD signal 16
6 18
Optogenetically driven single-vessel fMRI 18
Discussion and Outlook 19

Reference 22
List of papers and statement of contributions 27
Appendix 28
A.1 Brain-state dependent astrocytic Ca^{2+} signals are coupled to both positive and negative BOLD-fMRI signals 28
Main text 29
Supporting Information 39
Movie legends 71
A.2 Ultra-slow single-vessel BOLD and CBV-based fMRI spatiotemporal dynamics and their correlation with neuronal Intracellular calcium signals 72
Main text 73
STAR Method 90
Movie legend 91
A.3 Sensory and optogenetically driven single-vessel fMRI 92
Main text 93
Supporting Information 100
A.4 Directly mapping the single-vessel hemodynamic signal with Multi-echo Line-scanning fMRI (MELS-fMRI) 119
Main text 120
Supporting Information 142

Abbreviations

BOLD – Blood oxygen level dependent

MRI – Magnetic resonance imaging

fMRI – Functional magnetic resonance imaging

LFP – Local Field Potential

MUA – Multi-unit activity

GECIs – Genetic encoded calcium indicators

GFAP – Glial fibrillary acidic protein

FP – Forepaw

FP-S1 – Forepaw somatosensory cortex

SEP – Sensory evoked potential

RCaMP – Red-shifted variant, genetically encoded calcium indicators

BC – Barrel cortex

AC – alpha-chloralose

Miniscope – The miniature fluorescence microscope

Abstract

BOLD fMRI has been wildly used for mapping brain activity, but the cellular contribution of BOLD signals is still controversial. In this study, we investigated the correlation between neuronal/astrocytic calcium and the BOLD signal using simultaneous GCaMP-mediated calcium and BOLD signal recording, in the event-related state and in resting state, in anesthetized and in free-moving rats. To our knowledge, the results provide the first demonstration that evoked and intrinsic astrocytic calcium signals could occur concurrently accompanied by opposite BOLD signals which are associated with vasodilation and vasoconstriction. We show that the intrinsic astrocytic calcium is involved in brain state changes and is related to the activation of central thalamus. First, by simultaneous LFP and fiber optic calcium recording, the results show that the coupling between LFP and calcium indicates that neuronal activity is the basis of the calcium signal in both neurons and astrocytes. Second, we found that evoked neuronal and astrocytic calcium signals are always positively correlated with BOLD responses. However, intrinsic astrocytic calcium signals are accompanied by the activation of the central thalamus followed by a striking negative BOLD signal in cortex, which suggests that central thalamus may be involved in the initiation of the intrinsic astrocytic calcium signal. Third, we confirmed that the intrinsic astrocytic calcium signal is preserved in free moving rats. Moreover, the occurrences of intrinsic astrocytic calcium spikes are coincident with the transition between different sleep stages, which suggests intrinsic astrocytic calcium spikes reflect brain state transitions. These results demonstrate that the correlation between astrocytic calcium and fMRI signals is related to the thalamic regulation of cortical states. On the other hand, by studying the relationship between vessel–specific BOLD signals and spontaneous calcium activity from adjacent neurons, we show that low frequency spontaneous neuronal activity is the cellular mechanism of the BOLD signal during resting state.

1

Introduction

Blood oxygen level dependent (BOLD) contrast in the functional magnetic resonance imaging (fMRI) signal reflects the dynamic ratio of the oxyhemoglobin and deoxyhemoglobin in the vessel. The changes in hemodynamic signals follow the altered metabolic demand or blood flow (Ogawa et al., 1990). The main topic of more than 2,000 papers published in the last decade is "BOLD fMRI," according to PubMed. However, it remains controversial to use the BOLD signal as a surrogate for brain activity since the BOLD signal reflects the brain activity indirectly. The understanding of origins and the cellular contributions of BOLD signal are crucial for interpreting and manipulating the BOLD signal in the healthy and pathological brain.

Previously, simultaneous electrophysiology and BOLD fMRI recording has shown that the local field potential (LFP) is better than multi-unit activity (MUA) for estimating the BOLD response (Logothetis et al., 2001), indicating that neuronal input and intracortical processing cause the BOLD signal rather than neuronal output (Buzsáki et al., 2012; Logothetis et al., 2001; Logothetis and Wandell, 2004). However, it is technically demanding to compensate for the electromagnetic interference produced during BOLD signal acquisition. Furthermore, glial cells are not electrically excitable (Perea and Araque, 2005), which make it difficult to address the linkage between glial cells and the BOLD signal. Alternatively, calcium concentration is a potential indicator for cellular activity in neuronal and glial cells in the MRI scanner (Clapham, 1995). Schulz et. al developed a platform to monitor the neuronal and glial calcium activity and the BOLD signal simultaneously (Schulz et al., 2012b). Despite its success in studying the correlation between cell-type specific activity and the BOLD signal, questions have been raised about the cell-type specificity (Hoogland et al., 2011; Nimmerjahn et al., 2004; Schulz et al., 2012b) and bioeffects (Kang et al., 2010; Rasmussen et al., 2016) of the calcium sensitive dyes, which were used in this study. The development of genetically encoded calcium indicators (GECIs, e.g., GCaMP) makes it possible to further study the cellular contribution to the BOLD signal from neurons and astrocytes directly.

The term "neurovascular coupling" is used to refer to the temporal and the spatial coupling between the neural activities and cerebral blood signals (changes in blood flow, blood volume, or hemodynamic signal) (Cauli and Hamel, 2010). Logothesis et al. reported that the increased

neuronal activity evoked by sensory stimuli drives the positive BOLD signal in anesthetized (Logothetis et al., 2001) and awake (Goense and Logothetis, 2008) monkeys. Additionally, it has been shown that the decreases in neuronal activity correlate with negative BOLD signal beyond the stimulated regions of the cortex in the monkey (Shmuel et al., 2006), and that it is relative to spontaneous neuronal activity and arteriolar vasoconstriction (Devor et al., 2007). The astrocyte is well suited to relay the signal from neurons to vessels because of its processes surrounding the synaptic cleft and because its endfeet cover more than 99% of the arterial surface (Anderson and Nedergaard, 2003; Harder et al., 1998; Iadecola and Nedergaard, 2007; Takano et al., 2006). In the past two decades, a number of research groups have reported that astrocytes serve as a mediator in neurovascular coupling, although several studies have shown controversial results (Hillman, 2014). In summary, the signaling of neuron-glia-vascular network underlies the fMRI signals, which primarily reflect the blood flow and hemodynamic vascular signal.

Interestingly, previously studies have shown that the elevated astrocytic calcium signal coupled with both vasodilation (Takano et al., 2006; Zonta et al., 2003) and vasoconstriction (Attwell et al., 2010; Mulligan and MacVicar, 2004) in varied conditions (Gordon et al., 2007; MacVicar and Newman, 2015). Evoked dilations are mediated by the formation of prostaglandin E2 (PGE2) and epoxyeicosatrienoic acids (EETs), while constrictions are mediated by the 20-hydroxyeicosatetraenoic acid (20-HETE) (Attwell et al., 2010; Mishra et al., 2011). However, there is no direct study to clarify how the astrocytic calcium could be involved in the bidirectional regulation of the fMRI signal. This thesis elucidates the correlation between the BOLD and calcium signals in neurons or astrocytes, and then highlights the contribution of astrocytic calcium to the BOLD signal through simultaneous BOLD and calcium recordings. It is organized as follows. Chapter 2 introduces the experimental setup we developed for fiber optic calcium recording, and demonstrates the electrophysiological basis of calcium in neurons or astrocytes. Chapter 3 examines the correlation between the BOLD signal and calcium either in neurons or astrocytes. Chapter 4 describes the spatiotemporal features of intrinsic astrocytic calcium. Chapter 5 studies the relationship between the spontaneous neuronal calcium and resting state BOLD signal. The sixth and final section is the discussion and outlook for this study.

2

Development of a fiber optic recording system for cell-type specific calcium recordings in the rat brain

2.1 Motivation

The first aim of this project is to specify the cellular contribution to BOLD fMRI signals through studying the correlation between cell-type specific activity and BOLD signals. Therefore, ideally, BOLD signals and cell-type specific activity should be monitored simultaneously. However, electromagnetic interference compensation is technically demanding with simultaneous electrophysiology and BOLD recordings. Furthermore, it is not suitable to monitor the astrocytic activity by electrophysiology because of the passive current characteristics of astrocytes (Filippov et al., 2003). Therefore, an MRI-compatible method to read out the neuronal and astrocytic activity needs to be developed (This chapter describes the platform which was used in Apendix 1 and 2).

Intracellular ionized calcium as a second messenger (Clapham, 1995) is an ideal surrogate for neuronal (Baker et al., 1971; Kerr et al., 2000; Sabatini et al., 2002) or astrocytic activity (Scemes and Giaume, 2006; Sofroniew and Vinters, 2010). Several studies have shown that astrocytic calcium increases in processes preceding the onset of functional hyperemia. This suggests that astrocytes are a potential regulator of neurovascular coupling (Lind et al., 2013; Otsu et al., 2015; Winship et al., 2007). Genetically encoded calcium sensors (GCaMP) composed of GFP, calmodulin and M13 make it possible to probe the neuronal and astrocytic activity by the cell-type specific promoters. Here, we decided to develop a fiber optic recording system for cell-type specific calcium recordings. The calcium activity recorded by the optical fiber is the integrated fluorescence signal in the vicinity of the fiber tip. Notably, the range of the signal source are comparable with the LFP and the BOLD signal (voxel size = 400x400 μm) located underneath the fiber tip. By this means, it is reasonable to investigate the correlation between electrophysiology (LFP) and calcium signals as well as the correlation between calcium and BOLD signals in this study.

2.2 Methods

Viral transfection (transduction) was used to express GCaMP6f in either neurons or astrocytes by cell-type specific promoters (Syn promoter for neurons (Hioki et al., 2007); GFAP promoter for astrocytes (Nolte et al., 2001)). Immunostaining was used to verify the cellular specificity. Additionally, to show the GCaMP expression in the forepaw somatosensory cortex (FP-S1) of the whole brain slice, a wide-field fluorescent image was acquired.

Simultaneous electrophysiology and calcium signals were recorded to study the correlation between electrophysiology and calcium signals in neurons or astrocytes. The electrode and fiber optic probe were attached together with close contact between the fiber optic tip and electrode tip, and then inserted into the FP-S1. To elicit FP-S1 responses we used forepaw (FP) electrical stimuli (3Hz, 4s at different stimulation intensities; or 3Hz, 1.0mA at different stimulation durations).

2.3 Results and discussion

GCaMP was expressed in either neurons or astrocytes by cell-type specific promoters in FP-S1 of the rat brain. A striking difference in the GCaMP expression patterns was observed in cortical neurons and astrocytes, which exhibited the morphology properties of neurons and astrocytes (Shigetomi et al., 2013a). The immunostaining shows that GCaMP was mainly observed in NeuN positive cells by transduction with the NeuN promoter, which is the neuron-specific marker.

The electrode and fiber optic probes were attached with the tips close together, and then inserted into the FP-S1. Upon the electrical stimulation, we observed the sensory evoked potential (SEP) and the calcium signal in the traces. In the enlarged view, we could see the individual SEP and calcium signal for each stimulation pulse. Response latency of neuronal calcium is about 15 ms with a full width at half maximum (FWHM) of 150~200 ms. The amplitude of the SEP and calcium response are positively correlated as shown in the scatter plot figure (See in Fig.S1, appendix 1). It is worth noting that intrinsic neuronal calcium spikes coupled with the peaks of the spontaneous LFPs, which is the basis to study the correlation between neuronal activity and resting state BOLD signals in the fifth section.

On the other hand, we also expressed GCaMP in astrocytes by the viral vector with the Glial fibrillary acidic protein (GFAP) promoter, which is the specific marker for astrocytes (Nolte et al., 2001). In contrast, the sensory evoked astrocytic calcium signal was a unitary event after a 4 s train of stimulation pulses, and the FWHM was proportional to the duration of stimulation. In

addition, the individual trace showed that there is roughly 1~1.7 s response latency, which is slightly shorter than previously reported calcium signal onsets (Nizar et al., 2013; Petzold et al., 2008; Schummers et al., 2008; Wang et al., 2006), but fall into the early onset range in a few recent studies (Lind et al., 2013; Otsu et al., 2015; Winship et al., 2007). Recently, Yo Otsu et al. reported that astrocyte processes reliably respond to sensory stimulation with a rapid onset that is comparable with that of surrounding neurons. However, the astrocyte soma shows a relatively slow response onset (Otsu et al., 2015). This may account for the early onset astrocytic calcium signal in this study. Since the astrocytic calcium signal that we recorded is the integrated fluorescence signal underneath the tip of the fiber, fiber optic recording cannot distinguish the calcium in the astrocyte processes from somata calcium.

2.4 Conclusion

Both the GCaMP express patterns and the colocalization of the GCaMP and cell-type specific markers shows that the GCaMP expression in neurons and astrocytes is well separated in our results by cell-type specific promoters.

Simultaneous electrophysiology and calcium recording show a highly positive correlation between neuronal activity and calcium signal in neurons or astrocytes. Furthermore, neuronal and astrocytic calcium show different response profiles to sensory stimulation in rats. These results indicate that calcium is an ideal surrogate for cellular activity. Furthermore, they demonstrate the technical potential to monitor the cellular specific activity by fiber optic calcium recording.

All of these conclusions suggest that it is feasible to monitor the cell-type specific activity in the MRI scanner by GCaMP mediated fiber optic calcium recording, which is the basis to study the cellular contribution to the BOLD signal.

3

The correlation between neuronal/astrocytic calcium and simultaneously acquired fMRI signal

3.1 Motivation

Real-time activity monitoring from neurons and astrocytes with simultaneous BOLD signal recording is essential for studying the cellular contribution to BOLD signals because the neuron-glia-vascular coupling is dependent on the brain's physiological condition. The BOLD signal and activity of two populations of cells (i.e., neurons and astrocytes) should ideally be detected simultaneously in the same brain region. The combination of GCaMP and RCaMP (red-shifted variant, genetically encoded calcium indicators) yields a new method for multi-color cell-type specific activity imaging (Akerboom et al., 2013). Nevertheless, the co-expression of GCaMP (in astrocytes) and RCaMP (in neurons) is problematic as revealed by our preliminary results. On the other hand, because the calcium affinity, binding kinetics, and expression efficiency are different between GCaMP and RCaMP, it is not appropriate to compare the neuronal and astrocytic calcium signals detected by different indicators (Akerboom et al., 2013).

Fiber optic calcium recording makes it feasible to monitor the GCaMP mediated calcium signal from astrocytes or neurons in deep cortical layers (or nuclei) in rats, even using the multiple channels to simultaneously monitor the calcium activity at multiple sites at large brain scales, e.g., monitoring the calcium in the bilateral hemisphere or the circuit dynamics across the brain (Kim et al., 2016a). In this study, we develop a two-channel fiber optic calcium recording system to monitor the BOLD and calcium signals from neurons or astrocytes in bilateral FP-S1, respectively.

3.2 Methods

GCaMP was expressed in neurons from left FP-S1, and in astrocytes from right FP-S1. Upon bilateral FP electric stimulation at different intensities, the evoked BOLD signals, as well as the neuronal and astrocytic calcium signals from bilateral hemispheres, were recorded simultaneously.

3.3 Results and discussion

The amplitude of the evoked neuronal and astrocytic calcium signals is proportional to the stimulation intensities, matching the corresponding BOLD signals. The scatter plots of the amplitude of BOLD versus the calcium responses show a strong positive correlation between BOLD and neuronal/astrocytic calcium signals (See in Fig.1F, appendix 1).

However, there is an outlier shown in the scatter plot of the astrocytic calcium versus the BOLD responses (See in Fig.1F, appendix 1). Consequently, we checked the raw traces of the BOLD and the calcium signal with the outlier event, which shows a relatively higher astrocytic calcium spike paired with lower BOLD signal response compared with the other responses (See in Fig.1G, appendix 1). This unexpected outlier event suggests that the increased astrocytic calcium signal may correlate with the varied BOLD signal and may play different roles in neuroglial and gliolvascular regulation. In some cases, it may even be independent of sensory stimulation.

Then we record the spontaneous astrocytic calcium signal with LFP. Interestingly, we also observed strong intrinsic astrocytic calcium spikes, which coincide with a reduced LFP signal shown in the traces and the spectrogram. After aligning all of the LFP and the corresponding astrocytic calcium spikes based on calcium peaks, we detected a robust reduction of LFP spectral power. Certainly, when we performed the astrocytic calcium recording with resting-state fMRI simultaneously, we also observed the intrinsic calcium spikes. Then we used the spike timing and amplitude signal as a regressor to correlate with the resting-state fMRI signal. A strong negative correlation was shown in the whole cortex of the brain. The time course of the fMRI signal from the whole cortex shows that the intrinsic astrocytic calcium spikes were coincident with the decreased BOLD signal. Therefore, the intrinsic astrocytic calcium signal is correlated to both negative neuronal and BOLD signal. Further study shows that the intrinsic astrocytic calcium negatively correlated with the neuronal calcium signal during resting state by simultaneous bilateral calcium recording (neuronal calcium, left FP-S1; astrocytic calcium, right FP-S1).

3.4 Conclusion

The evoked neuronal calcium signals are positively correlated with neuronal activity and the BOLD signal. In contrast, we found two distinct astrocytic calcium correlated neurovascular coupling events: the evoked astrocytic calcium signals were positively correlated to the neuronal activity (LFP and calcium) and BOLD signals; however, the intrinsic astrocytic calcium signals

were correlated to negative neuronal and BOLD signals. As a result, we revealed two different neurovascular coupling events in the brain.

4

Intrinsic astrocytic calcium spikes correlated with the brain states transition

4.1 Can intrinsic and evoked astrocytic calcium occur concurrently?

Given the previous outlier observation, the first question that we would like to answer is whether the intrinsic and evoked astrocytic calcium signals could occur concurrently, and how this phenomenon regulates the BOLD fMRI signal.

To answer this question, we first need to distinguish the intrinsic astrocytic calcium signals from the evoked ones. The results in section 3 show that the duration of the intrinsic astrocytic calcium signal is about 8 s (See in Fig.2B and 2E, appendix 1), and that the evoked astrocytic calcium signal is proportional to the period of the stimulation (See in Fig.S3, appendix 1). This means that we may separate the intrinsic from the evoked astrocytic signal by further extending the stimulation duration. Here, we applied 30 s FP stimulation with 90 s off period in the block design experiment. Interestingly, besides the typical plateau-like evoked astrocytic calcium responses, the astrocytic calcium spikes were occasionally superimposed in the early phase of the 30 s stimulation periods. Whenever the astrocytic calcium spikes occurred, the corresponding BOLD signal is relatively reduced in the FP-S1 and cortex (See in Fig.3D-3F, appendix 1). The intrinsic astrocytic calcium spikes were also detected in the middle or end of the 30 s stimulation period, and even during the stimulation-off period (See in S8, appendix 1). Furthermore, the intrinsic astrocytic calcium spikes are independent of the arterial blood pressure and respiration (See in Fig.S18 and S19, appendix 1).

We grouped the astrocytic calcium responses into two distinct categories, the Evoked Only and Concurrent events (evoked + intrinsic) based on the occurrence of astrocytic calcium spikes, and then we averaged the calcium and BOLD traces, respectively. The average of BOLD responses showed evident reduction upon the Concurrent events in comparison to the Evoked Only events (See in Fig.3E and 3F, appendix 1).

The time-lapse function maps from MRI demonstrate the overall BOLD signal change in the brain and show a typical evoked fMRI signal in the FP-S1 for Evoked Only events. However, for

Concurrent events, we observed a clearly reduced fMRI response in the FP region, accompanied by a broad negative BOLD signal through the whole cortex during the early phase of the 30 s stimulation (See in Fig.3F, appendix 1).

We also performed another experiment where two optic probes were inserted into FP-S1 and into barrel cortex (BC). The evoked astrocytic calcium showed a local response in FP-S1 upon the forepaw electrical stimulation (4 s, 3 Hz, 330us pulse duration), whereas the intrinsic astrocytic calcium signals were detectable in both brain regions. Accordingly, we use the astrocytic calcium spikes in BC as the indicator for the occurrence of intrinsic astrocytic calcium. The results show that the intrinsic astrocytic calcium signal could occur during the stimulation, and correlates with the negative BOLD signal in the cortex (See in Fig.3A-3C, appendix 1).

These results demonstrate that the evoked and intrinsic astrocytic calcium could occur concurrently and correlate with the opposite (positive or negative) fMRI signal with unique spatial localization in the brain. Previous studies have reported that elevated astrocytic calcium was correlated with vasoconstriction and vasodilation in different conditions (Attwell et al., 2010; MacVicar and Newman, 2015; Mulligan and MacVicar, 2004; Takano et al., 2006; Tran and Gordon, 2015; Zonta et al., 2003). As far as we are aware, this is the first study to demonstrate that astrocytic calcium related vasoconstriction could coexist with vasodilation through neurovascular coupling from a whole-brain perspective.

4.2 Propagation speed of the intrinsic astrocytic calcium signal

The next step is to investigate the spatiotemporal features of the intrinsic astrocytic calcium signal. The previous results have shown that the intrinsic astrocytic calcium signal is coupled with the negative BOLD signal in the whole cortex. Now, we would like to ask whether the intrinsic astrocytic calcium signal exhibits the similar spatial features as the whole-cortex negative BOLD signals. For the temporal features, it has been reported that the astrocytic calcium signal could propagate in the brain with a relatively slow speed as waves (Cornell-Bell et al., 1990), so-called calcium waves, which are induced by neuronal activity (Dani et al., 1992) and mediated by glutamate (Cornell-Bell et al., 1990) as well as ATP (Guthrie et al., 1999) release. The reported speed of propagation from either pathological or normal conditions varied from 4 to 60 μm/s (Chuquet et al., 2007; Haas et al., 2005; Kuchibhotla et al., 2009; Kuga et al., 2011; Miyazaki et al., 1986; Parri and Crunelli, 2001).

These studies motivated us to explore the spatial and propagation features of the intrinsic astrocytic calcium signal detected in this work. Here, we expressed GCaMP in astrocytes

bilaterally in the FP-S1 with two-channel fiber optic recordings upon the activation of left FP-S1. We also observed distinct Evoked Only and Concurrent events using simultaneous fMRI and astrocytic calcium recording as described in previous results. Interestingly, the intrinsic astrocytic calcium spikes elicited by forepaw stimulation are detectable in both hemispheres. However, the evoked astrocytic calcium signals can only be detected in a local area (See in Fig.4A, appendix 1). This result indicates that the intrinsic astrocytic calcium could travel through the cortex.

By subtracting the Evoked Only events from the Concurrent events, we could determine the intrinsic calcium signal in the activated FP-S1. Then, we superimpose the intrinsic calcium signal detected in the two hemispheres. The enlarged figure showed little difference in the latencies between the two hemispheres (See in Fig.4B, appendix 1). The scatter plot illustrates the estimated latencies of the intrinsic calcium spikes simultaneously recorded from two channels (See in Fig.4C, appendix 1). We observed that the latencies varied from 2 to 4 s. This may be caused by the fact that we cannot control the occurrence of the intrinsic astrocytic spikes after the forepaw stimulation. However, there is no significant difference in the latencies of the intrinsic calcium spikes from two hemispheres.

Our original assumption was that the intrinsic calcium signal is initiated from the activated FP-S1 and then propagates to the other regions. This would mean that we could calculate the speed of propagation for intrinsic calcium spikes by the latency difference and the distance between two recording sites. However, the results reject this original assumption, and instead demonstrate that the intrinsic astrocytic calcium signal occurs globally and instantaneously in the cortex, which indicates that subcortical nuclei projecting to the cortex may be involved in the initiation of the intrinsic astrocytic calcium signal.

4.3 Identifying the subcortical nuclei involved in the intrinsic astrocytic calcium spikes

The results shown in section 4.2 drove us to identify the potential subcortical regions which are relevant to the intrinsic astrocytic calcium spikes. Since we could perform fMRI with simultaneous astrocytic calcium recording, we could investigate the two distinct Evoked Only and Concurrent events using on/off block design trials. By mapping the event-related whole brain function, we can search for the brain activity specific to the Concurrent events, compare with Evoked Only events, and then specify the region which may relate to intrinsic astrocytic calcium signal. Upon stimulation, we observed typical activation of FP-S1 during the Evoked

Only events. However, for the Concurrent events, there is an apparent activation in the central and mediodorsal thalamus, which is even extended to the midbrain reticular formation in the early phase of the Concurrent events. Immediately following the central thalamus activation, there is a global negative BOLD signal with reduced positive BOLD response in FP-S1 (See in Fig.5B and 5C, appendix 1). By co-registering the activation map with the brain atlas, we could identify the activated thalamic and midbrain regions(See in Fig.5D, appendix 1), which are the major components of the ascending arousal system (Steriade et al., 1993). The group analysis of the BOLD signal changes from FP-S1 and cortex shows a reduced BOLD signal during Concurrent events, but in the central thalamus, there is an increase of the BOLD signal during the early phase of stimulation (See in Fig.5E, appendix 1).

These studies suggest that the activity in the subcortical arousal pathway may contribute to the astrocytic calcium related fMRI signal changes through thalamic regulation. Furthermore, to verify the central thalamic activity coinciding with Concurrent events, we recorded the LFP in the central thalamus simultaneously with cortical astrocytic calcium and LFP recordings (See in Fig.6A, appendix 1). The position of the electrode tip was confirmed by MRI after the recording (See in Fig.S11, appendix 1). We observed an accumulated increase in LFP power before the Concurrent events in FP-S1 and the central thalamus. By calculating the average of the LFP spectrogram, we could observe a strong LFP power increase in both the thalamus and the cortex before stimulation during Concurrent events, followed by reduced power. Moreover, there is a definite increase in the beta band detected in the central thalamus during Concurrent events in the early phase of the stimulation, which may directly contribute to the increased BOLD signal detected only during Concurrent events (See in Fig.6, appendix 1).

The results showed that central thalamus activities are related to the intrinsic astrocytic calcium, which coupled with the negative BOLD signal in the cortex. Now, we would like to know how the central thalamus activities regulate the cortical activity. Experiments on optogenetic stimulation of neurons in the central thalamus conducted by Jia Liu et al. (Liu et al., 2015) have shown that the central thalamus could frequency-selectively control the cortical activity in rats. In addition, electrical stimulation of the central thalamus could improve the level of consciousness after seizure (Gummadavelli et al., 2015).

In summary, these results demonstrated that the central thalamus is involved in the astrocytic calcium related fMRI signal changes, which may be associated with transition between brain states.

4.4 Intrinsic astrocytic calcium spikes are preserved in free moving rats

Until now, all the results were acquired from anesthetized rats with alpha-chloralose (AC), which is known to enhance GABAergic inhibition throughout the brain and central nervous system. As it works similarly to other GABAergic anesthetics, AC enhances the inhibitory effect of interneurons. It is crucial to determine how much of the observation of the negative relationship between the intrinsic calcium signal and the negative BOLD signal is related to the anesthetic drug. Urethane has been used extensively for electrophysiological recordings in animals. In this study, we also repeated simultaneous fMRI and astrocytic calcium recordings in the urethane-anesthetized rat. We observed similar correlation patterns to rats anesthetized with alpha-chloralose. This result demonstrates that the negative correlation of intrinsic astrocytic calcium signal with the BOLD signal is not caused by the alpha-chloralose specific anesthetic effect. However, the negative coupling pattern of the BOLD signal with intrinsic astrocytic calcium spikes may vary across different animals due to the various anesthetic effects of urethane. On the other hand, it is not feasible to reproduce our finding in rats with all kinds of anesthetics to exclude that the finding is drug dependent.

All of these factors drove us to reproduce the finding in free moving rats. Astrocytic calcium signal and LFP were recorded simultaneously in free-moving rats, and the result shows that intrinsic astrocytic calcium spikes are preserved in free moving rats. Furthermore, the intrinsic astrocytic calcium spikes correlate with the transition between different sleep stages (See in Fig.S15, appendix 1). The features of LFP were used to identify and characterize the sleep stages. These results further highlight the involvement of the intrinsic astrocytic calcium signal in the mediation of brain state changes, similar to what has been reported in urethane-anesthetized rats (Poskanzer and Yuste, 2011).

5

Neuronal calcium and the resting-state BOLD signal

Resting state fMRI was used to map widespread functional connectivity by BOLD signal coherence in the brain during rest (Lee et al., 2013). Simultaneous electrophysiology and BOLD recording suggested that neuronal activity is coupled with the global BOLD signal fluctuations under resting state conditions (Schölvinck et al., 2010). In most of the previous reports, the functional connectivity was calculated based on the resting-state BOLD signal, which is acquired from large voxels (0.4x0.4x0.4 mm^3 in rats; 3.0x3.0x3.0 mm^3 in human). Using neuronal activity to specify the basis of the conventional resting-state BOLD signal may be questionable due to the significant gap in spatial sensitivity between neuronal activity recordings and the BOLD signal in each voxel. Our previous work has demonstrated the possibility to map vessel-specific BOLD signal (single-vessel BOLD) from distinct vessel-dominated versus parenchyma-dominated voxels in rat brains (See in Fig.1, appendix 3) (Yu et al., 2016a). In the present study, our results have shown that the evoked neuronal calcium signals are positively correlated with both LFP and BOLD signals On the other hand, the spontaneous neuronal calcium peaks were coupled with the activity of spontaneous LFP (See in Fig.S1, appendix 1), which shows that the neuronal calcium signal is an ideal indicator of neuronal activity in resting state.

In this study, to specify the neuronal basis of the resting-state BOLD signal, we monitored the single-vessel BOLD signal with an in-plane resolution of 100 x 100 μm^2; the temporal resolution was 1 s, with simultaneously calcium signal recording from the adjacent neurons. We observe a clear positive correlation between neuronal calcium in the 0.01 to 0.1 Hz range and vessel-specific BOLD signal (See in Fig.4 and 5, appendix 2). At the same time, spontaneous neuronal calcium signal shows an LFP coupled oscillation (See in Fig.6, appendix 2), and power spectrogram shows higher power in 1-10 Hz than the GFP control group. The average calcium signal spectral power in the 1-10 Hz band was correlated to the vessel-specific BOLD signal as well. These results indicate that neural activity is the origin of the vessel-specific BOLD signal fluctuations in resting state brain. Further study was performed in awake humans, and spatially smoothing the functional signal from 1 mm to 5 mm (FWHM) indicates that vessel connectivity is the basis of the large voxel-based signal in resting state correlation maps (See in Fig.7,

appendix 2). Therefore, these results reveal that the spontaneous low frequency neuronal activity is the cellular mechanism of the resting-state BOLD signal by studying the correlation between vessel-specific BOLD signal and spontaneous calcium activity from adjacent neurons.

6

Optogenetically driven single-vessel fMRI

In the previous chapters, we demonstrated that the evoked BOLD signal is positively correlated with the increased calcium signal in either neurons or astrocytes; The intrinsic astrocytic calcium spikes involved in the brain state transition through the thalamocortical pathway; The low frequency spontaneous neuronal calcium activity is highly correlated with the fluctuation of the resting-state BOLD signal in adjacent vessel. But the causality between cellular activity and the BOLD signal is still elusive.

Optogenetics is the technology to control the cellular activity (excitation or inhibition) with high-temporal and high cell-type specificity by delivering the optic stimulus. Optogenetics is an ideal technique to study the causality between cellular activity and BOLD signal directly. In present study, we establish a platform to investigate the causal association between the neuronal activity and BOLD signal by combining the BOLD recording with optogenetics. To increase the spatial and temporal resolution of the BOLD signal, we used the line-scanning-based FLASH fMRI method to monitor both arteriole and venule signal at 50 × 50 μm in-plane resolution and 100-ms temporal resolution (See in Fig. S2, appendix 3). We also compared the BOLD responses driven by FP stimulus and optogenetic stimulus. The results demonstrate that BOLD signal evoked by sensory or optogenetic stimulus shows similar vascular response pattern (See in Fig. 2E and 2F, appendix 3). This means that optogenetics is an alternative way to study the cellular source of the BOLD signal.

On the other hand, the fMRI signal can be acquired at different echo-times (TE, 3~30 ms) with a 100 ms sampling rate (See in Figs. 1B-1C and S1, appendix 4). This method detects the TE-dependent fMRI signal, which extends the single-vessel dynamic mapping and assists the optimization of quantitative fMRI modeling.

Discussion and Outlook

The objective of this project is to illuminate cellular contributions to the BOLD signal. We focused on how astrocytic calcium is associated with BOLD fMRI signals, and how the astrocytic calcium is involved in brain state transitions. Using simultaneous GCaMP-mediated calcium and BOLD signal recording, we observed that evoked and intrinsic astrocytic calcium signal could occur concurrently with opposite BOLD signals which are related to vasodilation and vasoconstriction. We show that the intrinsic astrocytic calcium related brain state changes are mediated by the central thalamus.

In this study, we first developed a simultaneous LFP and fiber optic calcium recording platform. We verified that the coupling between LFP and calcium signals in neurons or astrocytes, indicating that the calcium signal is an ideal surrogate for neuronal activity. Secondly, we identified two distinct astrocytic calcium signals, evoked and intrinsic, which are related to opposite BOLD signal. Event-related fMRI mapping reveals that the central thalamus may be involved in the initiation of the intrinsic astrocytic calcium signal. Thirdly, the intrinsic astrocytic calcium signal is detectable in free moving rats, which excludes the possibility of an anesthetic effect. Moreover, the occurrences of the intrinsic astrocytic calcium spikes are coincident with the transition between different sleep stages, which suggests that intrinsic astrocytic calcium spikes are involved in the brain states transition. Finally, we also studied the relationship between the vessel–specific BOLD signal and spontaneous calcium activity from adjacent neurons. In summary, this study demonstrates that: 1) intrinsic astrocytic calcium mediates brain state transition through thalamic regulation; 2) spontaneous neuronal activity at low frequency is the cellular mechanism of the BOLD signal during resting state.

The suppression of fast potential changes (observed as the depression of LFP) is an index of spreading depolarization/depression, which can cause vasoconstriction and ischemia, and also exhibits a decreased BOLD signal in the brain (Ayata and Lauritzen, 2015). In the clinic, spreading depression is considered as the mechanism and therapeutic target of the pathophysiology of numerous diseases, such as migraine (Ayata et al., 2006; Lauritzen, 2001), ischemic stroke and brain injury. However, it also can be induced by an overabundance of noxious conditions, such as the mechanical lesion, potassium, vigorous electrical stimulus,

hyperthermia, neurotransmitters, etc. (Ayata and Lauritzen, 2015). These reports drove us to verify whether the intrinsic astrocytic calcium spikes we found in this study are related to spreading depolarization/ depression. In fact, in this study, fiber optic implantation was seen to induce a focal lesion. In some cases, we observed the vigorous stimulation-induced spreading depression related calcium elevations (See in Fig.S9, appendix 1), which show distinct spatiotemporal features from intrinsic astrocytic calcium. First, the amplitude of the spreading depression related astrocytic calcium signal is much greater than the intrinsic/evoked calcium signal. However, unlike the intrinsic astrocytic calcium signals, the spreading depression related astrocytic calcium signals are not bihemispherically detectable. Second, intrinsic astrocytic calcium signals occurred instantaneously in the two hemispheres accompanied by the activation of the central thalamus and midbrain reticular formation. Nevertheless, during spreading depression, the astrocytic calcium signal is initiated in a local brain region and then propagates slowly to other regions (Chuquet et al., 2007). Third, intrinsic and sensory evoked astrocytic calcium signals could occur concurrently and regulate the BOLD signal in opposite directions. Spreading depression is accompanied by dramatic disruption of brain ion homeostasis, causing the electrical silence and the silencing of neuronal responses (Kunkler and Kraig, 2003).

The occurrence of intrinsic astrocytic calcium signals is associated with the activation of the central thalamus and midbrain reticular formation, which is related to the regulation of brain state. Although most of the results were acquired from rats anesthetized with alpha-chloralose or Urethane, it is still possible that the brain state changes occasionally under normal physiological conditions. Interestingly, simultaneous astrocytic calcium and LFP recordings in free-moving rat exhibit intrinsic astrocytic calcium spikes, and are coincident with the transition between sleep stages. Sleep stage was classified using the features of LFP. This result excludes the possibility that intrinsic astrocytic calcium is anesthetic dependent and indicates that intrinsic astrocytic calcium is involved in brain state transition. Simultaneous calcium and fMRI recording in the awake animal offers further prospects for studying the correlation between cellular activity and brain state changes.

In this study, although there is considerable consistency among the results showing the correlation between the LFP and calcium signals as well as between the calcium and BOLD signals, the causal association between intrinsic astrocytic calcium signal and the negative BOLD signal needs to be further clarified. The astrocytic calcium signal is assumed to relay signals from neurons to vessels. A recent study shows neuronal activity-associated vasodilation perseveres in IP3 type-2 receptor (R2) knock-out mice ($IP3R2^{-/-}$), in which the primary pathway

for astrocytic calcium release from the stores in blocked, implying a parallel astrocytic calcium-independent neurovascular coupling pathway (Nizar et al., 2013). More recent evidence reveals that astrocytic calcium is elevated not via release from calcium stores but via entry through ATP-gated channels in the membrane (Mishra et al., 2016). Also, it suggests that astrocytes mediate neurovascular coupling via capillary pericytes. One prospective direction to study the causality between the astrocytic calcium and BOLD signal is by using transgenic mice with inhibited the astrocytic calcium pathways or modified function of capillary pericytes.

In this study, immunostaining and the profiles of calcium responses demonstrate the high cell-type specificity of genetically encoded calcium indicators. Fiber-optic recordings monitored the integrated signal of distinct cell populations underneath the tip of the fiber. The development of the miniature fluorescence microscope (Miniscope) offers the possibility to study cellular mechanisms of hemodynamic responses by monitoring individual cell or sub-cell units activity in the MRI scanner (Cai et al., 2016; Ghosh et al., 2011). This is crucial, especially for astrocytes because of the distinct calcium spatiotemporal features in the somata and processes (Otsu et al., 2015). Moreover, fiber optics can access most of the brain area in theory, and it is feasible to study the brain circuit dynamics from a whole-brain perspective by combining optogenetic and multi-channel fiber optic recording (Kim et al., 2016a)

Reference

Adelsberger, H., Garaschuk, O., and Konnerth, A. (2005). Cortical calcium waves in resting newborn mice. Nature neuroscience *8*, 988-990.

Akerboom, J., Carreras Calderon, N., Tian, L., Wabnig, S., Prigge, M., Tolo, J., Gordus, A., Orger, M.B., Severi, K.E., Macklin, J.J.*, et al.* (2013). Genetically encoded calcium indicators for multi-color neural activity imaging and combination with optogenetics. Front Mol Neurosci *6*, 2.

Anderson, C.M., and Nedergaard, M. (2003). Astrocyte-mediated control of cerebral microcirculation. Trends in neurosciences *26*, 340-344.

Attwell, D., Buchan, A.M., Charpak, S., Lauritzen, M., Macvicar, B.A., and Newman, E.A. (2010). Glial and neuronal control of brain blood flow. Nature *468*, 232-243.

Ayata, C., Jin, H., Kudo, C., Dalkara, T., and Moskowitz, M.A. (2006). Suppression of cortical spreading depression in migraine prophylaxis. Annals of neurology *59*, 652-661.

Ayata, C., and Lauritzen, M. (2015). Spreading depression, spreading depolarizations, and the cerebral vasculature. Physiological reviews *95*, 953-993.

Baker, P.F., Hodgkin, A.L., and Ridgway, E.B. (1971). Depolarization and calcium entry in squid giant axons. The Journal of physiology *218*, 709-755.

Buzsáki, G., Anastassiou, C.A., and Koch, C. (2012). The origin of extracellular fields and currents—EEG, ECoG, LFP and spikes. Nature reviews neuroscience *13*, 407-420.

Cai, D.J., Aharoni, D., Shuman, T., Shobe, J., Biane, J., Song, W., Wei, B., Veshkini, M., La-Vu, M., and Lou, J. (2016). A shared neural ensemble links distinct contextual memories encoded close in time. Nature *534*, 115.

Cauli, B., and Hamel, E. (2010). Revisiting the role of neurons in neurovascular coupling. Frontiers in neuroenergetics *2*.

Chuquet, J., Hollender, L., and Nimchinsky, E.A. (2007). High-resolution in vivo imaging of the neurovascular unit during spreading depression. Journal of Neuroscience *27*, 4036-4044.

Clapham, D.E. (1995). Calcium signaling. Cell *80*, 259-268.

Cohen, L.B., Keynes, R.D., and Hille, B. (1968). Light scattering and birefringence changes during nerve activity. Nature *218*, 438-441.

Cornell-Bell, A.H., Finkbeiner, S.M., Cooper, M.S., and Smith, S.J. (1990). Glutamate induces calcium waves in cultured astrocytes: long-range glial signaling. Science *247*, 470-473.

Cox, R.W. (1996). AFNI: software for analysis and visualization of functional magnetic resonance neuroimages. Computers and biomedical research, an international journal *29*, 162-173.

Dani, J.W., Chernjavsky, A., and Smith, S.J. (1992). Neuronal activity triggers calcium waves in hippocampal astrocyte networks. Neuron *8*, 429-440.

Devor, A., Tian, P., Nishimura, N., Teng, I.C., Hillman, E.M., Narayanan, S.N., Ulbert, I., Boas, D.A., Kleinfeld, D., and Dale, A.M. (2007). Suppressed neuronal activity and concurrent arteriolar vasoconstriction may explain negative blood oxygenation level-dependent signal. The Journal of neuroscience : the official journal of the Society for Neuroscience *27*, 4452-4459.

Filippov, V., Kronenberg, G., Pivneva, T., Reuter, K., Steiner, B., Wang, L.-P., Yamaguchi, M., Kettenmann, H., and Kempermann, G. (2003). Subpopulation of nestin-expressing progenitor cells in the adult murine hippocampus shows electrophysiological and morphological characteristics of astrocytes. Molecular and Cellular Neuroscience *23*, 373-382.

Ghosh, K.K., Burns, L.D., Cocker, E.D., Nimmerjahn, A., Ziv, Y., Gamal, A.E., and Schnitzer, M.J. (2011). Miniaturized integration of a fluorescence microscope. Nature methods *8*, 871-878.

Goense, J.B., and Logothetis, N.K. (2008). Neurophysiology of the BOLD fMRI signal in awake monkeys. Curr Biol *18*, 631-640.

Gordon, G.R., Mulligan, S.J., and MacVicar, B.A. (2007). Astrocyte control of the cerebrovasculature. Glia *55*, 1214-1221.
Grinvald, A., Lieke, E., Frostig, R.D., Gilbert, C.D., and Wiesel, T.N. (1986). Functional architecture of cortex revealed by optical imaging of intrinsic signals. Nature *324*, 361-364.
Gummadavelli, A., Motelow, J.E., Smith, N., Zhan, Q., Schiff, N.D., and Blumenfeld, H. (2015). Thalamic stimulation to improve level of consciousness after seizures: evaluation of electrophysiology and behavior. Epilepsia *56*, 114-124.
Guthrie, P.B., Knappenberger, J., Segal, M., Bennett, M.V., Charles, A.C., and Kater, S.B. (1999). ATP released from astrocytes mediates glial calcium waves. Journal of Neuroscience *19*, 520-528.
Haas, B., Schipke, C.G., Peters, O., Söhl, G., Willecke, K., and Kettenmann, H. (2005). Activity-dependent ATP-waves in the mouse neocortex are independent from astrocytic calcium waves. Cerebral cortex *16*, 237-246.
Harder, D.R., Alkayed, N.J., Lange, A.R., Gebremedhin, D., and Roman, R.J. (1998). Functional hyperemia in the brain. Stroke *29*, 229-234.
Hillman, E.M. (2014). Coupling mechanism and significance of the BOLD signal: a status report. Annual review of neuroscience *37*, 161-181.
Hioki, H., Kameda, H., Nakamura, H., Okunomiya, T., Ohira, K., Nakamura, K., Kuroda, M., Furuta, T., and Kaneko, T. (2007). Efficient gene transduction of neurons by lentivirus with enhanced neuron-specific promoters. Gene therapy *14*, 872-882.
Hoogland, T.M., Kuhn, B., and Wang, S.S. (2011). Preferential loading of bergmann glia with synthetic acetoxymethyl calcium dyes. Cold Spring Harb Protoc *2011*, 1228-1231.
Huttunen, J.K., Grohn, O., and Penttonen, M. (2008). Coupling between simultaneously recorded BOLD response and neuronal activity in the rat somatosensory cortex. NeuroImage *39*, 775-785.
Iadecola, C., and Nedergaard, M. (2007). Glial regulation of the cerebral microvasculature. Nature neuroscience *10*, 1369-1376.
Kang, J., Kang, N., Yu, Y., Zhang, J., Petersen, N., Tian, G.-F., and Nedergaard, M. (2010). Sulforhodamine 101 induces long-term potentiation of intrinsic excitability and synaptic efficacy in hippocampal CA1 pyramidal neurons. Neuroscience *169*, 1601-1609.
Kerr, R., Lev-Ram, V., Baird, G., Vincent, P., Tsien, R.Y., and Schafer, W.R. (2000). Optical imaging of calcium transients in neurons and pharyngeal muscle of C. elegans. Neuron *26*, 583-594.
Kim, C.K., Yang, S.J., Pichamoorthy, N., Young, N.P., Kauvar, I., Jennings, J.H., Lerner, T.N., Berndt, A., Lee, S.Y., and Ramakrishnan, C. (2016a). Simultaneous fast measurement of circuit dynamics at multiple sites across the mammalian brain. Nature methods *13*, 325-328.
Kim, C.K., Yang, S.J., Pichamoorthy, N., Young, N.P., Kauvar, I., Jennings, J.H., Lerner, T.N., Berndt, A., Lee, S.Y., Ramakrishnan, C*., et al.* (2016b). Simultaneous fast measurement of circuit dynamics at multiple sites across the mammalian brain. Nature methods *13*, 325-328.
Kuchibhotla, K.V., Lattarulo, C.R., Hyman, B.T., and Bacskai, B.J. (2009). Synchronous hyperactivity and intercellular calcium waves in astrocytes in Alzheimer mice. Science *323*, 1211-1215.
Kuga, N., Sasaki, T., Takahara, Y., Matsuki, N., and Ikegaya, Y. (2011). Large-scale calcium waves traveling through astrocytic networks in vivo. Journal of Neuroscience *31*, 2607-2614.
Kunkler, P.E., and Kraig, R.P. (2003). Hippocampal spreading depression bilaterally activates the caudal trigeminal nucleus in rodents. Hippocampus *13*, 835-844.
Lauritzen, M. (2001). Cortical spreading depression in migraine. Cephalalgia *21*, 757-760.
Lee, M.H., Smyser, C.D., and Shimony, J.S. (2013). Resting-state fMRI: a review of methods and clinical applications. American Journal of Neuroradiology *34*, 1866-1872.

Lind, B.L., Brazhe, A.R., Jessen, S.B., Tan, F.C., and Lauritzen, M.J. (2013). Rapid stimulus-evoked astrocyte Ca2+ elevations and hemodynamic responses in mouse somatosensory cortex in vivo. Proceedings of the National Academy of Sciences *110*, E4678-E4687.
Liu, J., Lee, H.J., Weitz, A.J., Fang, Z., Lin, P., Choy, M., Fisher, R., Pinskiy, V., Tolpygo, A., and Mitra, P. (2015). Frequency-selective control of cortical and subcortical networks by central thalamus. Elife *4*.
Logothetis, N.K., Pauls, J., Augath, M., Trinath, T., and Oeltermann, A. (2001). Neurophysiological investigation of the basis of the fMRI signal. Nature *412*, 150-157.
Logothetis, N.K., and Wandell, B.A. (2004). Interpreting the BOLD signal. Annu Rev Physiol *66*, 735-769.
MacVicar, B.A., and Newman, E.A. (2015). Astrocyte Regulation of Blood Flow in the Brain. Cold Spring Harbor perspectives in biology *7*, a020388.
Madesen, M. (1992). A simplified formulation of the gamma variate function. Phys Med Bid *37*, 1597-1600.
Mishra, A., Hamid, A., and Newman, E.A. (2011). Oxygen modulation of neurovascular coupling in the retina. Proceedings of the National Academy of Sciences *108*, 17827-17831.
Mishra, A., Reynolds, J.P., Chen, Y., Gourine, A.V., Rusakov, D.A., and Attwell, D. (2016). Astrocytes mediate neurovascular signaling to capillary pericytes but not to arterioles. Nature neuroscience *19*, 1619.
Miyazaki, S.-I., Hashimoto, N., Yoshimoto, Y., Kishimoto, T., Igusa, Y., and Hiramoto, Y. (1986). Temporal and spatial dynamics of the periodic increase in intracellular free calcium at fertilization of golden hamster eggs. Developmental biology *118*, 259-267.
Mulligan, S.J., and MacVicar, B.A. (2004). Calcium transients in astrocyte endfeet cause cerebrovascular constrictions. Nature *431*, 195-199.
Nimmerjahn, A., Kirchhoff, F., Kerr, J.N., and Helmchen, F. (2004). Sulforhodamine 101 as a specific marker of astroglia in the neocortex in vivo. Nature methods *1*, 31-37.
Nizar, K., Uhlirova, H., Tian, P., Saisan, P.A., Cheng, Q., Reznichenko, L., Weldy, K.L., Steed, T.C., Sridhar, V.B., MacDonald, C.L.*, et al.* (2013). In vivo stimulus-induced vasodilation occurs without IP3 receptor activation and may precede astrocytic calcium increase. The Journal of neuroscience : the official journal of the Society for Neuroscience *33*, 8411-8422.
Nolte, C., Matyash, M., Pivneva, T., Schipke, C.G., Ohlemeyer, C., Hanisch, U.K., Kirchhoff, F., and Kettenmann, H. (2001). GFAP promoter‐controlled EGFP‐expressing transgenic mice: A tool to visualize astrocytes and astrogliosis in living brain tissue. Glia *33*, 72-86.
Ogawa, S., Lee, T.-M., Kay, A.R., and Tank, D.W. (1990). Brain magnetic resonance imaging with contrast dependent on blood oxygenation. Proceedings of the National Academy of Sciences *87*, 9868-9872.
Otsu, Y., Couchman, K., Lyons, D.G., Collot, M., Agarwal, A., Mallet, J.-M., Pfrieger, F.W., Bergles, D.E., and Charpak, S. (2015). Calcium dynamics in astrocyte processes during neurovascular coupling. Nature neuroscience *18*, 210-218.
Parri, H.R., and Crunelli, V. (2001). Pacemaker calcium oscillations in thalamic astrocytes in situ. Neuroreport *12*, 3897-3900.
Perea, G., and Araque, A. (2005). Glial calcium signaling and neuron–glia communication. Cell calcium *38*, 375-382.
Petzold, G.C., Albeanu, D.F., Sato, T.F., and Murthy, V.N. (2008). Coupling of neural activity to blood flow in olfactory glomeruli is mediated by astrocytic pathways. Neuron *58*, 897-910.
Poskanzer, K.E., and Yuste, R. (2011). Astrocytic regulation of cortical UP states. Proceedings of the National Academy of Sciences *108*, 18453-18458.
Ramos-Cabrer, P., Weber, R., Wiedermann, D., and Hoehn, M. (2005). Continuous noninvasive monitoring of transcutaneous blood gases for a stable and persistent BOLD contrast in fMRI studies in the rat. NMR in biomedicine *18*, 440-446.

Rasmussen, R., Nedergaard, M., and Petersen, N.C. (2016). Sulforhodamine 101, a widely used astrocyte marker, can induce cortical seizure-like activity at concentrations commonly used. Sci Rep *6*, 30433.
Sabatini, B.L., Oertner, T.G., and Svoboda, K. (2002). The life cycle of Ca(2+) ions in dendritic spines. Neuron *33*, 439-452.
Scemes, E., and Giaume, C. (2006). Astrocyte calcium waves: what they are and what they do. Glia *54*, 716-725.
Schölvinck, M.L., Maier, A., Frank, Q.Y., Duyn, J.H., and Leopold, D.A. (2010). Neural basis of global resting-state fMRI activity. Proceedings of the National Academy of Sciences *107*, 10238-10243.
Schulz, K., Sydekum, E., Krueppel, R., Engelbrecht, C.J., Schlegel, F., Schroter, A., Rudin, M., and Helmchen, F. (2012a). Simultaneous BOLD fMRI and fiber-optic calcium recording in rat neocortex. Nature methods *9*, 597-602.
Schulz, K., Sydekum, E., Krueppel, R., Engelbrecht, C.J., Schlegel, F., Schröter, A., Rudin, M., and Helmchen, F. (2012b). Simultaneous BOLD fMRI and fiber-optic calcium recording in rat neocortex. Nature methods *9*, 597-602.
Schummers, J., Yu, H., and Sur, M. (2008). Tuned responses of astrocytes and their influence on hemodynamic signals in the visual cortex. Science *320*, 1638-1643.
Shigetomi, E., Bushong, E.A., Haustein, M.D., Tong, X., Jackson-Weaver, O., Kracun, S., Xu, J., Sofroniew, M.V., Ellisman, M.H., and Khakh, B.S. (2013a). Imaging calcium microdomains within entire astrocyte territories and endfeet with GCaMPs expressed using adeno-associated viruses. The Journal of general physiology *141*, 633-647.
Shigetomi, E., Bushong, E.A., Haustein, M.D., Tong, X., Jackson-Weaver, O., Kracun, S., Xu, J., Sofroniew, M.V., Ellisman, M.H., and Khakh, B.S. (2013b). Imaging calcium microdomains within entire astrocyte territories and endfeet with GCaMPs expressed using adeno-associated viruses. The Journal of general physiology *141*, 633-647.
Shmuel, A., Augath, M., Oeltermann, A., and Logothetis, N.K. (2006). Negative functional MRI response correlates with decreases in neuronal activity in monkey visual area V1. Nature neuroscience *9*, 569-577.
Sofroniew, M.V., and Vinters, H.V. (2010). Astrocytes: biology and pathology. Acta neuropathologica *119*, 7-35.
Steriade, M., McCormick, D.A., and Sejnowski, T.J. (1993). Thalamocortical oscillations in the sleeping and aroused brain. Science *262*, 679-685.
Takano, T., Tian, G.F., Peng, W., Lou, N., Libionka, W., Han, X., and Nedergaard, M. (2006). Astrocyte-mediated control of cerebral blood flow. Nature neuroscience *9*, 260-267.
Thomason, M.E., Burrows, B.E., Gabrieli, J.D., and Glover, G.H. (2005). Breath holding reveals differences in fMRI BOLD signal in children and adults. NeuroImage *25*, 824-837.
Tian, P., Teng, I.C., May, L.D., Kurz, R., Lu, K., Scadeng, M., Hillman, E.M., De Crespigny, A.J., D'Arceuil, H.E., Mandeville, J.B*., et al.* (2010). Cortical depth-specific microvascular dilation underlies laminar differences in blood oxygenation level-dependent functional MRI signal. Proceedings of the National Academy of Sciences of the United States of America *107*, 15246-15251.
Tran, C.H.T., and Gordon, G.R. (2015). Astrocyte and Microvascular Imaging in Awake Animals Using Two‐Photon Microscopy. Microcirculation *22*, 219-227.
Wang, X., Lou, N., Xu, Q., Tian, G.F., Peng, W.G., Han, X., Kang, J., Takano, T., and Nedergaard, M. (2006). Astrocytic Ca2+ signaling evoked by sensory stimulation in vivo. Nature neuroscience *9*, 816-823.
Winship, I.R., Plaa, N., and Murphy, T.H. (2007). Rapid astrocyte calcium signals correlate with neuronal activity and onset of the hemodynamic response in vivo. The Journal of neuroscience *27*, 6268-6272.
Yu, X., He, Y., Wang, M., Merkle, H., Dodd, S.J., Silva, A.C., and Koretsky, A.P. (2016a). Sensory and optogenetically driven single-vessel fMRI. Nature methods *13*, 337.

Yu, X., He, Y., Wang, M., Merkle, H., Dodd, S.J., Silva, A.C., and Koretsky, A.P. (2016b). Sensory and optogenetically driven single-vessel fMRI. Nature methods *13*, 337-340.
Yu, X., Qian, C., Chen, D.Y., Dodd, S.J., and Koretsky, A.P. (2014). Deciphering laminar-specific neural inputs with line-scanning fMRI. Nature methods *11*, 55-58.
Zonta, M., Angulo, M.C., Gobbo, S., Rosengarten, B., Hossmann, K.-A., Pozzan, T., and Carmignoto, G. (2003). Neuron-to-astrocyte signaling is central to the dynamic control of brain microcirculation. Nature neuroscience *6*, 43-50.

List of papers and statement of contributions

A.1

Wang, M., He, Y., Sejnowski, T., Yu, X.

Positive and negative BOLD fMRI signals are regulated by Ca^{2+} - mediated gliovascular interactions.

Proc Natl Acad Sci USA, 2018

X.Y. and T.S. designed the research. X.Y. and **M.W.** performed research; **M.W.** and Y.H. analyzed data; X.Y., T.S., **M.W.** wrote the paper.

A.2

He, Y., **Wang, M.**, Chen, X., Pohmann, R., Polimeni, J., Scheffler, K., Rosen, B., Kleinfeld, D. and Yu, X.

Ultra-slow single vessel BOLD and CBV–based fMRI spatiotemporal dynamics and their correlation with neuronal intracellular calcium signals.

Neuron, 2018

X.Y., D.K., and B.R. designed the research, Y.H., X.Y., **M.W.** and X.C. performed animal experiments, Y.H., X.Y. and R.P. acquired data, Y.H. analyzed data, K.S., R.P., J.R. and **M.W.** provided key technical support, and X.Y., D.K. and Y.H. wrote the manuscript.

A.3

Yu, X., He, Y., **Wang, M.**, Merkle, H., Dodd, S.J., Silva, A.C., and Koretsky, A.P.

Sensory and optogenetically driven single-vessel fMRI.

Nat Methods, 2016, 13, 337-340, doi:10.1038/nmeth.3765.

X.Y. and A.P.K. initiated the work, developed the method and wrote the paper. Y.H. and **M.W.** helped with 14-T MRI data acquisition and analysis. X.Y. performed MRI experiments at 11.7 T and 14 T.A.C.S. and S.J.D. helped setup the k-space reconstruction. H.M. and S.J.D. designed the radio frequency coil.

A.4

He, Y., **Wang, M.**, Yu, X.

Directly mapping the single - vessel hemodynamic signal with Multi-echo Line - scanning fMRI (MELS - fMRI).

Journal of Cerebral Blood Flow and Metabolism, 2017, under revision.

X.Y.designed the research. Y.H., **M.W.** performed animal experiments; Y.H., X.Y. acquired and analyzed data; X.Y., Y.H. wrote the paper.

Appendix

A.1 Brain-state dependent astrocytic Ca^{2+} signals are coupled to both positive and negative BOLD-fMRI signals

Brain-state dependent astrocytic Ca^{2+} signals are coupled to both positive and negative BOLD-fMRI signals

Brain-state dependent astrocytic Ca^{2+} signals are coupled to both positive and negative BOLD-fMRI signals

Maosen Wang[a,b], Yi He[a,b], Terrence J. Sejnowski[c,d,1], and Xin Yu[a,1]

[a]Translational Neuroimaging and Neural Control Group, High Field Magnetic Resonance Department, Max Planck Institute for Biological Cybernetics, 72076 Tuebingen, Germany; [b]Graduate Training Centre of Neuroscience, International Max Planck Research School, University of Tuebingen, 72074 Tuebingen, Germany; [c]Howard Hughes Medical Institute, Computational Neurobiology Laboratory, Salk Institute for Biological Studies, La Jolla, CA 92037; and [d]Division of Biological Sciences, University of California, San Diego, La Jolla, CA 92093

Contributed by Terrence J. Sejnowski, January 5, 2018 (sent for review June 30, 2017; reviewed by Emery N. Brown and Eric A. Newman)

Astrocytic Ca^{2+}-mediated gliovascular interactions regulate the neurovascular network in situ and in vivo. However, it is difficult to measure directly both the astrocytic activity and fMRI to relate the various forms of blood-oxygen-level-dependent (BOLD) signaling to brain states under normal and pathological conditions. In this study, fMRI and GCaMP-mediated Ca^{2+} optical fiber recordings revealed distinct evoked astrocytic Ca^{2+} signals that were coupled with positive BOLD signals and intrinsic astrocytic Ca^{2+} signals that were coupled with negative BOLD signals. Both evoked and intrinsic astrocytic calcium signal could occur concurrently or respectively during stimulation. The intrinsic astrocytic calcium signal can be detected globally in multiple cortical sites in contrast to the evoked astrocytic calcium signal only detected at the activated cortical region. Unlike propagating Ca^{2+} waves in spreading depolarization/depression, the intrinsic Ca^{2+} spikes occurred simultaneously in both hemispheres and were initiated upon the activation of the central thalamus and midbrain reticular formation. The occurrence of the intrinsic astrocytic calcium signal is strongly coincident with an increased EEG power level of the brain resting-state fluctuation. These results demonstrate highly correlated astrocytic Ca^{2+} spikes with bidirectional fMRI signals based on the thalamic regulation of cortical states, depicting a brain-state dependency of both astrocytic Ca^{2+} and BOLD fMRI signals.

BOLD-fMRI | astrocyte | calcium | brain states | glia-vascular coupling

The blood-oxygen-level-dependent (BOLD) signal is used in many fMRI studies as a surrogate for brain activity, but the link between the two signals is indirect, which makes the interpretation of BOLD signals problematic. The neurovascular coupling that underpins functional MRI (fMRI) brain mapping (1) has been characterized by simultaneous intracortical recordings and fMRI (2). Among the neurovascular signaling events, it remains ambiguous how gliovascular interactions, especially that mediated by the astrocytic Ca^{2+} signal, are involved in the neurovascular network (3–6). Astrocytic Ca^{2+} signals in both in situ and in vivo environments can occur in coordination with, or independently of, each other, suggesting specific and variable coupling mechanisms (5, 7–13). It is difficult to directly measure astrocytic activity, which may vary according to different normal brain states and pathological conditions (14–17), while simultaneously utilizing fMRI.

It is possible to use genetically encoded Ca^{2+} indictors (GECIs, e.g., GCaMP) to acquire cell type-specific Ca^{2+} signals via optical fiber, which can be measured during fMRI imaging without radiofrequency and magnetic gradient-switch induced interference (2, 18–21). In particular, GCaMP6f shows fast Ca^{2+} binding kinetics and high sensitivity comparable to the Ca^{2+}-sensitive dyes, such as Oregon Green BAPTA-1 (OGB-1) (18, 20). Besides two-photon microscopy (22) or wide-field calcium imaging (23), the Ca^{2+}-sensitive dye and GCaMP-mediated Ca^{2+} signal can be directly recorded using optical fiber implanted into animal brains (19, 24, 25). The fMRI signal may be simultaneously acquired with the Ca^{2+} signal from neurons or astrocytes specifically loaded with Ca^{2+}-sensitive dyes (19). These studies show that it is feasible to monitor the many possible ways that astrocytes mediate BOLD signals through specific neurovascular coupling events.

We have observed the expected positive correlation between the evoked neuronal/astrocytic Ca^{2+} signals and BOLD fMRI signal in activated cortical areas; however, an unexpected intrinsic astrocytic Ca^{2+} signal showing negative correlation with both neuronal and fMRI signals can occur concurrently with the evoked neurovascular coupling events. In contrast to the spreading depolarization/depression-based traveling Ca^{2+} waves in the brain (26, 27), this intrinsic astrocytic Ca^{2+} signal represents distinct spatiotemporal features that occur simultaneously in both hemispheres without propagation delays (28–32). The instantaneously altered brain activity that is associated with the intrinsic astrocytic Ca^{2+} signal is a unique astrocyte-mediated change in brain state (9, 33, 34).

We provide evidence that subcortical nuclei projecting to the entire cortex are responsible for regulating the astrocytic calcium-coupled bidirectional fMRI signal. By using astrocytic Ca^{2+} signal-based event-related fMRI analysis, positive BOLD signals were

Significance

The role of astrocytes on brain function is controversial in many aspects. It remains challenging to specify the in vivo functional impact of astrocytic calcium signal when mediating vasodilation/constriction at varied physiological or pathophysiological conditions. Here, we applied simultaneous fMRI and GCaMP-mediated Ca^{2+} optical fiber recording to detect distinct astrocytic Ca^{2+} signals (evoked vs. intrinsic) coupled to positive and negative blood-oxygen-level-dependent signals, respectively and concurrently, with unique spatial and temporal patterns. Not only did we demonstrate the distinct neurovascular coupling events coupled to the evoked and intrinsic astrocytic calcium signals, but also revealed the thalamic regulation mechanism underlying the astrocytic calcium-mediated brain state switch. This astrocytic-relevant regulatory mechanism could underlie numerous brain disorder and injury models relevant to gliovascular disruption.

Author contributions: T.J.S. and X.Y. designed research; M.W., Y.H., and X.Y. performed research; M.W., Y.H., and X.Y. analyzed data; and M.W., T.J.S., and X.Y. wrote the paper.

Reviewers: E.N.B., Massachusetts General Hospital; E.A.N., University of Minnesota.

The authors declare no conflict of interest.

[1]To whom correspondence may be addressed. Email: terry@salk.edu or xin.yu@tuebingen.mpg.de.

This article contains supporting information online at www.pnas.org/lookup/suppl/doi:10.1073/pnas.1711692115/-/DCSupplemental.

detected at the central and mediodorsal thalamic nuclei extending to the midbrain reticular formation, which is associated with the intrinsic astrocytic Ca^{2+} signal followed by the negative BOLD signals in the cortex. This result is consistent with a resting-state fMRI study of unanesthetized macaques, showing increased thalamic fMRI signals with widespread signal decreases in the neocortex during elevated arousal states (15). This work demonstrates that astrocytes might be involved in mediating the bidirectional fMRI signal arising from the thalamic regulation of brain states, demonstrating a way to bridge the study of brain function among the cellular, network, and systems levels.

Results

Identifying the Neurovascular Coupling Events with Simultaneous fMRI and Neuronal/Astrocytic Ca^{2+} Recordings. We recorded the cell type-specific Ca^{2+} signal simultaneously with the local field potential (LFP). GCaMP6f was expressed by viral injection into the forepaw somatosensory cortex (FP-S1) of the rat brain, specifically into neurons or astrocytes (Fig. 1*A*). The sensory-evoked Ca^{2+} signal from neurons matched well with the evoked LFP for each electrical stimulus, and the amplitude of the Ca^{2+} signal was positively correlated with that of the LFP, as shown in Fig. 1*B* and *SI Appendix*, Fig. S1. Spontaneous Ca^{2+} spikes were also detected from neurons whose amplitudes were positively correlated with those of the spontaneous LFPs (*SI Appendix*, Fig. S1 *D* and *F*). The latency of the neuronal Ca^{2+} signal reported by GCaMP6f was ~15 ms with a full width of half maximum (FWHM) of 150–200 ms (*SI Appendix*, Fig. S2*A*), similar to the kinetics of GCaMP6f-mediated Ca^{2+} signals reported previously (20, 24).

In contrast to the neuronal Ca^{2+} signal, the sensory-evoked astrocytic Ca^{2+} signal was a unitary event following a train of electrical stimuli to the forepaw (Fig. 1*B*). The latency of the astrocytic Ca^{2+} signal was 1.0–1.7 s, and the FWHM was proportional to the stimulus duration, matching the simultaneously acquired BOLD signal (*SI Appendix*, Figs. S2 *B* and C and S3). The latency detected by optical fiber could reflect fast astrocytic Ca^{2+} signals within astrocyte processes (11, 35). The spread function of the astrocytic Ca^{2+} signal is derived from the sum of individual astrocytes exposed under the tip of optical fiber, which have varied response kinetics as observed in vivo with two-photon microscopy (5, 10). These results clearly demonstrated that the GCaMP6f-mediated Ca^{2+} signal from either neurons or astrocytes is specifically detectable in vivo via optical fiber, showing distinct temporal features to sensory stimulation. It is noteworthy that the evoked fluorescent Ca^{2+} signal is independent of the hemoglobin-based intrinsic optical signal, similar to the previous fiber optic Ca^{2+} studies (details in *Materials and Methods*) (21, 25).

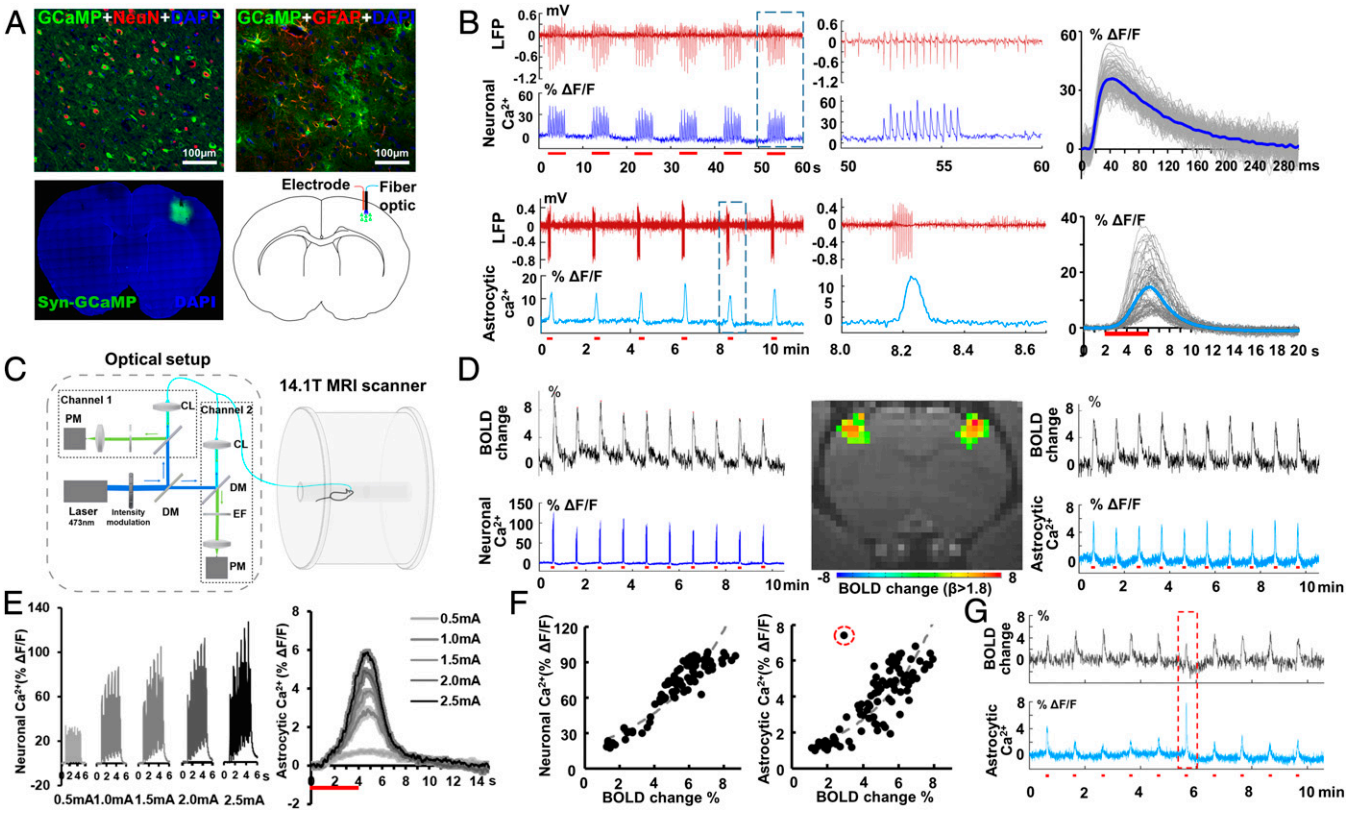

Fig. 1. Sensory-evoked neuronal/astrocytic Ca^{2+} recordings with simultaneous LFP or BOLD fMRI. (*A*) The colocalized GCaMP (green) with neurons (NeuN, red), or with astrocytes (GFAP, red). (*Lower*) Immunostaining image (*Left*) and a schematic drawing (*Right*) for simultaneous LFP and fiber-optic Ca^{2+} recording. (*B*) Simultaneous LFP (red) and Ca^{2+} signal traces (blue) from neurons or astrocytes in FP-S1 with forepaw electrical stimulation (3 Hz, 4 s, 1 mA). (*Center*) Enlarged figures of the dashed box in *Left*. (*Right*) The averaged trace of evoked Ca^{2+} signal (gray lines are individual traces from six rats). (*C*) The schematic drawing of the two-channel fiber-optic recording system with fMRI (CL, coupling lens; DM, dichroic mirror; EF, emission filter; PM, photomultiplier). (*D*) The time courses of evoked fMRI signal from bilateral FP-S1 and simultaneous neuronal (*Left*)/astrocytic (*Right*) Ca^{2+} signal (*Inset*, a representative color-coded BOLD-fMRI map at 2.0 mA). (*E*) The stimulation intensity-dependent Ca^{2+} signal from neurons or astrocytes. (*F*) The scatter plot of the evoked Ca^{2+} signal amplitude vs. simultaneous fMRI peak amplitude at different stimulation intensities (red dashed circle, outlier). (*G*) The traces of BOLD-fMRI and astrocytic Ca^{2+} signals show the outlier event (red dashed box) with increased astrocytic Ca^{2+} signal, but reduced BOLD-fMRI signal (*SI Appendix*, Table S1 shows the occurrence rate of the unexpected astrocytic event).

A two-channel fluorescent signal recording system was developed to simultaneously detect the BOLD signal and the Ca^{2+} signal from neurons and astrocytes from the forepaw somatosensory cortex of both hemispheres, respectively (Fig. 1 *C* and *D*). The neuronal and astrocytic Ca^{2+} signals were correlated with the BOLD-fMRI evoked signal across electrical stimulation intensities (Fig. 1 *E* and *F* and *SI Appendix*, Fig. S4). However, a novel event was detected in which a high-amplitude astrocytic Ca^{2+} signal was coupled with a reduced amplitude BOLD fMRI signal in a single trial-on/off block design paradigm. This outlier indicates that astrocytic Ca^{2+} signaling might play another role in neuroglial and gliovascular interaction.

We investigated the properties of the intrinsic astrocyte Ca^{2+} spikes and its relationship to the simultaneously acquired fMRI signal. In rats anesthetized with α-chloralose, intrinsic astrocytic Ca^{2+} spikes occurred simultaneously with a transient frequency shift in hypersynchronized LFP bursts (Fig. 2*A*), previously described as intermittent or continuous hypersynchrony during different EEG stages (36). During the spontaneous LFP frequency shifts, there was a transient suppression of the power spectral density [Fig. 2 *B* and *C*, nonoverlapping confidence intervals (CIs); *SI Appendix*, Table S2], as well as a decrease in the fMRI signal throughout the cortex (Fig. 2 *D* and *E*). There was a negative correlation between the resting state fMRI signal and the intrinsic astrocytic Ca^{2+} spikes (Fig. 2*D* and *SI Appendix*, Fig. S5). The astrocytic Ca^{2+} spike-triggered average of the simultaneously acquired LFP power spectral profile and fMRI signal were computed. The negative BOLD signal was much delayed (−2.64 ± 0.25 s) (Fig. 2*F*) compared with the mean onset of the astrocyte Ca^{2+} spike (−4.29 ± 1.04 s) (Fig. 2*F* and *SI Appendix*, Fig. S6, the negative value is set from the zero time at the peak of astrocytic Ca^{2+} spikes, nonoverlapping Cis; *SI Appendix*, Table S2). The mean estimated onset of LFP frequency shift (−4.77 ± 1.44 s) preceded the estimated onset of the astrocyte Ca^{2+} spike, although the difference was not statistically significant. In addition, previous studies showed that the high frequency LFP power reduction occurred earlier than the astrocytic Ca^{2+} spikes in both the cortex and hippocampus of mice anesthetized with urethane (9, 30). Thus, the intrinsic astrocytic Ca^{2+} signal elevation is possibly involved in mediating this particular neurovascular event. It is noteworthy that two-channel bilateral Ca^{2+} recording (left hemisphere, neurons; right hemisphere, astrocytes) during the resting state also shows the negative correlation of the intrinsic astrocytic Ca^{2+} spike to the neuronal Ca^{2+} transients. Power spectral analysis of the neuronal Ca^{2+} transients shows similar frequency suppression shift to that of the spontaneous LFP signal (*SI Appendix*, Fig. S7).

Elevated astrocytic Ca^{2+} signals can affect vasoconstriction or vasodilation, depending on conditions (7, 8, 12, 37), but these seldom coexist during neurovascular coupling events. Interestingly, intrinsic astrocytic Ca^{2+} spikes can occur in the FP-S1 and barrel cortex concurrently with the astrocytic Ca^{2+} signal evoked by forepaw electrical stimulation (Fig. 3 *A* and *B*). As with the spontaneous astrocytic Ca^{2+} recording during the resting state, the intrinsic astrocytic Ca^{2+} spikes during stimulation were correlated with the negative BOLD signal throughout the cortex,

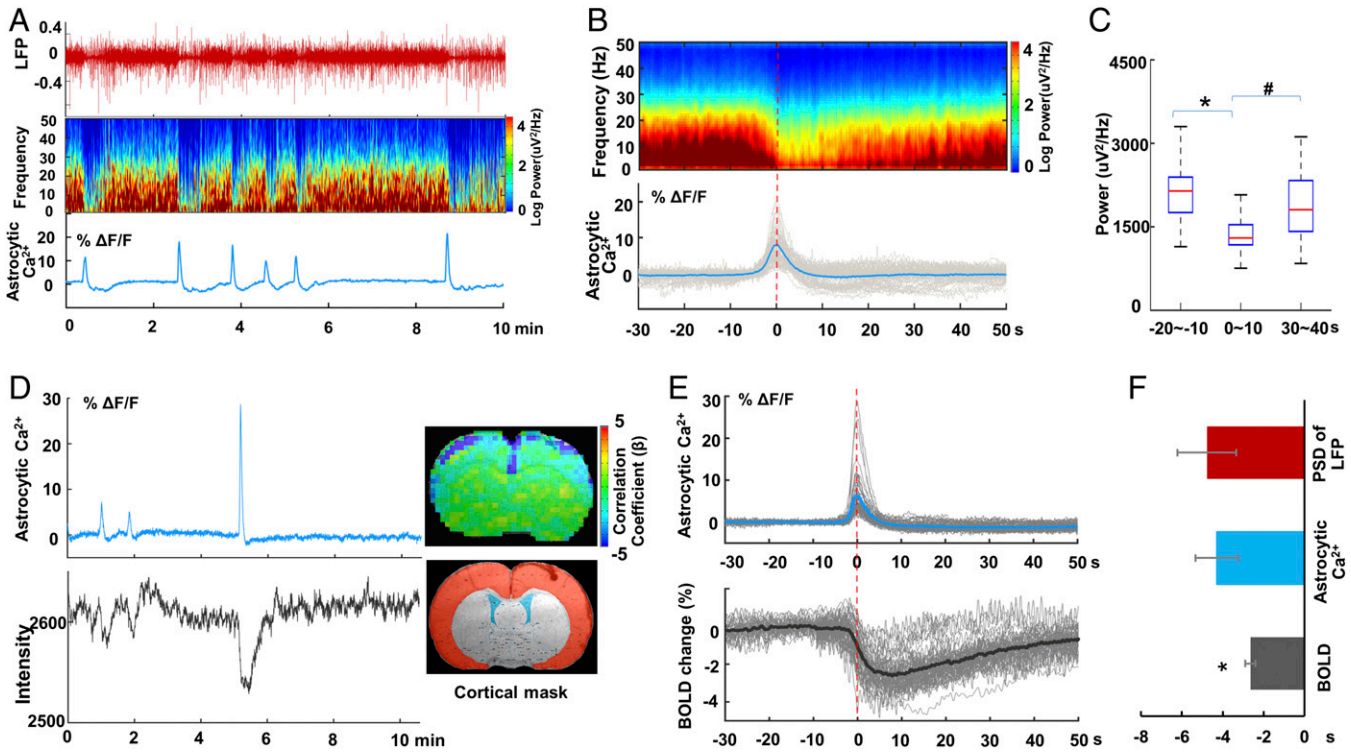

Fig. 2. Intrinsic astrocytic Ca^{2+} spikes negatively correlate with neuronal and BOLD signals. (*A*) The representative traces of the LFP (*Top*), the power spectra of LFP (*Middle*), and the intrinsic astrocytic Ca^{2+} signal (*Bottom*) in FP-S1 (1-s sliding window with 0.1-s steps, 9 tapers). (*B*) The average spectrogram of the LFP is aligned based on the simultaneously acquired peak time of the intrinsic astrocytic Ca^{2+} spikes (red dashed line as time 0). (*C*) The integrated LFP power spectral density (2 ~ 50 Hz) at different phases according to the intrinsic astrocytic Ca^{2+} spikes (*P = 9.5e-22; #P = 3.6e-11, paired t test; 54 traces of 6 rats). (*D*) The representative traces of the intrinsic astrocytic Ca^{2+} spikes and simultaneous fMRI signal acquired from the entire cortex (*Upper Inset*: color-coded negative correlation map; *Lower Inset*: ROI in red contour; details in *SI Appendix*, Fig. S5). (*E*) The averaged time course of the fMRI signal is aligned based on the simultaneous acquired peak time of the intrinsic astrocytic Ca^{2+} spikes (red dashed line as time 0, 52 traces of 6 rats). (*F*) Estimated onset times of the intrinsic astrocytic Ca^{2+} spikes, the LFP spectral power shift, and the fMRI signal reduction (time 0 at the peak time of the astrocytic Ca^{2+} spikes; one-way ANOVA followed by Tukey's multiple comparison test F = 31.94; *P = 5.1e-12, n_{LFP_Ca} = 6; n_{fMRI_Ca} = 6 rats).

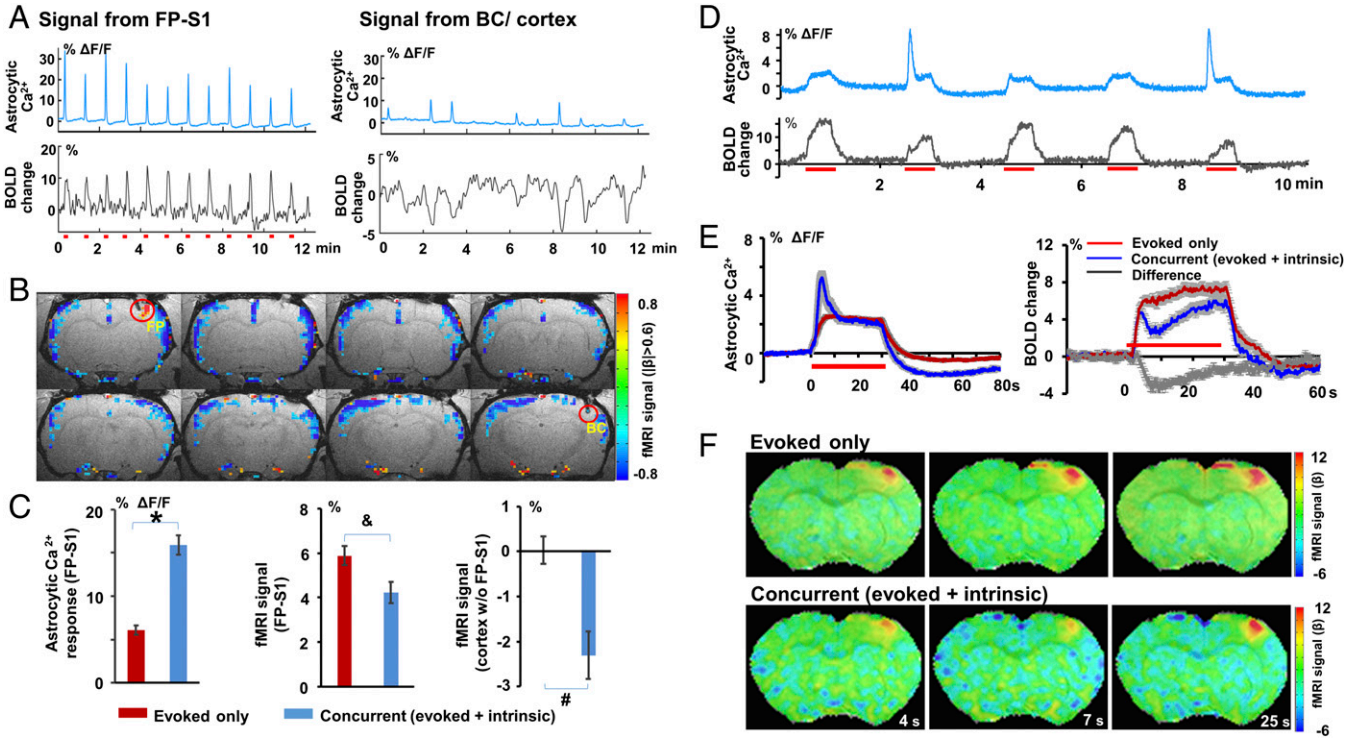

Fig. 3. Two-channel recording of the evoked and intrinsic astrocytic Ca^{2+} signal in FP-S1 and barrel cortex (BC). (*A*) The time courses of the evoked astrocytic Ca^{2+} signal and the fMRI signal from FP-S1 (*Left*) upon forepaw stimulation (3 Hz, 4 s, 1.5 mA), and the concurrent intrinsic astrocytic Ca^{2+} signal from BC and the fMRI signal from the entire cortex except FP-S1 (*Right*). (*B*) The correlation map of the fMRI signal with the intrinsic astrocytic Ca^{2+} spikes detected in BC shows negative correlation across the entire cortex except FP-S1. (*C*) The amplitude of the astrocytic Ca^{2+} signal (evoked-only) is significantly lower than that of the concurrent events in FP-S1 (*Left*, $*P = 2.0e\text{-}15$), but the fMRI signal change is significant lower in the concurrent events (*Center*, $\&P = 0.026$). The fMRI signal in the entire cortex except FP-S1 shows negative amplitude of the concurrent events, which is significantly lower than the evoked-only events (*Right*, $\#P = 2.8e\text{-}07$; evoked-only, trial # = 81; concurrent, trial # = 50, rats, $n = 7$). (*D*) The representative traces of astrocytic Ca^{2+} and corresponding fMRI signals with 30-s forepaw stimulation (evoked-only vs. concurrent: epoch 2, 5 vs. 1, 3, 4). (*E*) The mean astrocytic Ca^{2+} traces of the two events (*Left*) and the simultaneously acquired fMRI time course (*Right*; gray line, difference; evoked-only, trial # = 84 vs. concurrent, trial # = 23, mean ± SEM, rats, $n = 5$). (*F*) The representative time-lapsed BOLD-fMRI map shows FP-S1 activation during the 30-s stimulation of evoked-only and concurrent events.

with the exception of FP-S1 (Fig. 3 *B* and *C*, nonoverlapping CIs; *SI Appendix*, Table S2), where the FP-S1 BOLD signal with the concurrent (intrinsic and evoked) astrocytic Ca^{2+} signals was also lower than that with the evoked-only astrocytic Ca^{2+}signal ($P = 0.026$, Student t test two-tailed), although it was not showing nonoverlapping CIs (*SI Appendix*, Table S2). In contrast, the amplitude of the intrinsic astrocytic Ca^{2+} spike was significantly higher than the normally evoked astrocytic Ca^{2+} spike (Fig. 3*C*, nonoverlapping CIs; *SI Appendix*, Table S2). The concurrent astrocytic Ca^{2+} spiking events were better characterized in the 30-s forepaw stimulation block design experiment, which showed the intrinsic astrocytic Ca^{2+} spike superimposed on the early phase of the evoked astrocytic Ca^{2+} signal (Fig. 3*D*). The averaged time courses and time-lapsed functional maps revealed the reduced fMRI signal in the FP-S1 and the negative fMRI signal from the whole cortex upon the intrinsic astrocytic Ca^{2+} spiking events (Fig. 3 *E* and *F*). Furthermore, the intrinsic astrocytic Ca^{2+} spikes were also detected at different phases of the 30-s stimulation and the stimulation-off period (*SI Appendix*, Fig. S8 *A* and *B*). These results clearly demonstrated that two independent astrocytic Ca^{2+} signals (evoked vs. intrinsic) could concurrently occur with a unique combination of coexisting positive and negative BOLD signals in the brain.

Specifying the Spatiotemporal Features of the Intrinsic Astrocytic Ca^{2+} Spikes. Given that brain trauma may accompany the surgical procedure, we examined the possibility that the astrocytic Ca^{2+} signal is associated with spreading depolarization/depression (27). Astrocytic Ca^{2+} signals from two hemispheres in the 30-s stimulation block design were measured to determine whether the intrinsic astrocytic Ca^{2+} spike elicited by the stimulation traveled through the cortex. If the astrocytic Ca^{2+} spike was triggered from the activated FP-S1 due to the stimulation-induced spreading depolarization/depression, it should appear as a signal propagating through the cortex following stimulation (26, 28, 31). Fig. 4*A* shows that the intrinsic astrocytic Ca^{2+} spikes not only occurred in the activated FP-S1, but also were detected in FP-S1 of the opposite hemisphere despite the fact that no evoked astrocytic and fMRI signals were detected together with the negative BOLD signal through the cortex. The onset of the intrinsic astrocytic Ca^{2+} spike in activated FP-S1 during stimulation was measured by subtracting the normally evoked astrocytic Ca^{2+} spike to clearly display the overlapping onsets of the intrinsic astrocytic Ca^{2+} spikes detected from both hemispheres (Fig. 4*B*). The latencies of the intrinsic astrocytic Ca^{2+} spiking events in the two hemispheres varied from 2 to 4 s after the stimulus, but with little difference between them (Fig. 4*C*, *Left*, 2.29 ± 0.31 s vs. *Right*, 2.42 ± 0.12 s, paired t test, $P = 0.26$; CI values in *SI Appendix*, Table S2). Periodically, the intrinsic astrocytic Ca^{2+} spike appeared at a later phase of the 30-s stimulation period and was detected in the other hemisphere with the same onset time (*SI Appendix*, Fig. S8 *C* and *D*).

This simultaneous appearance of the intrinsic astrocytic Ca^{2+} spikes in both hemispheres is inconsistent with previously reported astrocytic Ca^{2+} waves of spreading depression with propagation speed at ∼20–40 μm/s (31, 32, 38), as well as the astrocytic Ca^{2+}

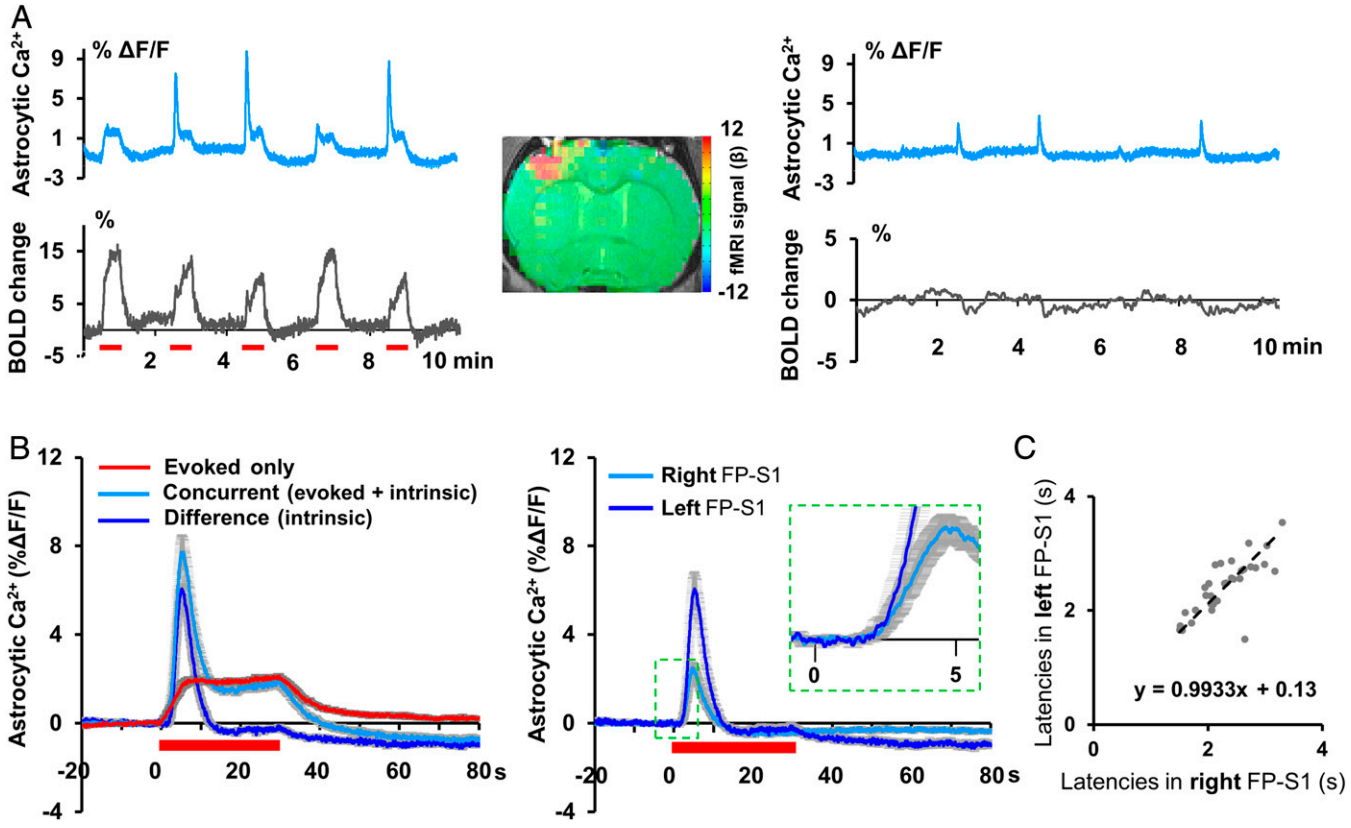

Fig. 4. Bilateral astrocytic Ca^{2+} recordings with simultaneous fMRI. (*A*) The representative traces of astrocytic Ca^{2+} and simultaneous BOLD signal in FP-S1 of both hemispheres with 30-s right forepaw stimulation (*Inset*: BOLD-fMRI map with left FP-S1 activation; concurrent events: epoch 2, 3, 5). (*B*) The mean time course of the astrocytic Ca^{2+} signal from evoked-only events vs. the concurrent (evoked + intrinsic) events (*Left*). The intrinsic astrocytic Ca^{2+} spike in the activated FP-S1 can be represented by subtracting the two events, which shows similar onset time to the intrinsic astrocytic Ca^{2+} spike detected in the opposite hemisphere (*Right*; mean ± SEM, rats, $n = 6$). *Inset* is a magnified figure of the dashed box. (*C*) The scatter plot of the latency estimated from the intrinsic astrocytic Ca^{2+} spikes of two hemispheres (Trial # = 32; rats, $n = 6$).

wave propagation detected in the hippocampus (60 μm/s) (30). The spreading depression events elicited Ca^{2+} signals at a higher intensity of electrical stimulation. Despite the high Ca^{2+} signal detected in both neurons and astrocytes upon the occurrence of spreading depression in the stimulated hemisphere, no Ca^{2+} signal was detected in the other hemisphere (*SI Appendix*, Fig. S9), consistent with a previous study showing that spreading depression is confined to the ipsilateral hemisphere with focal ischemia (29). This shows that the intrinsic astrocytic Ca^{2+} signal that mediates global neurovascular coupling in the cortex is independent of spreading depolarization/depression induced by brain lesions.

Using fMRI to Identify the Subcortical Functional Nuclei Correlated with the Intrinsic Astrocytic Ca^{2+} Signal. Subcortical nuclei that project throughout the entire neocortex could be responsible for the intrinsic astrocytic Ca^{2+}-mediated neurovascular coupling events. Based on the on/off stimulation block design, the neurovascular coupling events were separated into two groups: those in which only the evoked astrocytic Ca^{2+} signal was present in the activated cortex, i.e., evoked-only events, and those with concurrent evoked and intrinsic astrocytic Ca^{2+} signals, i.e., concurrent (evoked + intrinsic) bilateral events (Fig. 5*A*). The amplitudes of the astrocytic Ca^{2+} spike of the concurrent events were significantly higher than those of the evoked-only events (Fig. 3*C*) and were therefore also used to specify the two categories (Fig. 5*B*). The event-related fMRI analysis showed focal FP-S1 activation for the evoked events, but for the concurrent events, the amplitude of the BOLD signal in the FP-S1 was significantly reduced and a prolonged negative BOLD signal was detected throughout the cortex as well as in the subcortical regions (Fig. 5*C* and Movie S1). Interestingly, a positive BOLD signal was also detected in the central and mediodorsal thalamic nuclei at an early phase of the stimulation for concurrent events (Fig. 5 *B* and *C*). In addition, the subcortical activity pattern extended beyond the thalamus; particularly, from the central lateral and mediodorsal lateral thalamus to the midbrain reticular formation (Fig. 5*D*, brain atlas overlapped; *SI Appendix*, Fig. S10, multislice functional map; Movie S2, 3D rendering video). Simultaneous recording of fMRI and Ca^{2+} signals can therefore be used to locate specific functional nuclei underlying unique neurovascular coupling on a whole-brain scale.

To confirm the thalamic BOLD activation during concurrent events, the LFP in the central thalamic region was recorded simultaneously with the astrocytic Ca^{2+} recording in the cortex. The central lateral (CL) thalamic regions were specifically targeted based on the BOLD functional map with the concurrent events, showing bilateral activation pattern covering a region of the brain atlas 400–500 μm in extant (Fig. 5*D*). For precise localization, the position of the electrode tip for each experiment was imaged by MRI (*SI Appendix*, Fig. S11). Fig. 6*A* shows the power spectral density of the LFP signal recorded from both the central thalamic region and the FP-S1, as well as the astrocytic Ca^{2+} signal detected in the FP-S1 in response to electrical stimulation of the forepaw. Interestingly, an elevated spectral power level was detected in both the thalamus and cortex before the induction of the intrinsic astrocytic Ca^{2+} spike from the on/off stimulation trial, followed by reduced power levels. A similar phenomenon was shown by the two-channel bilateral Ca^{2+} recording

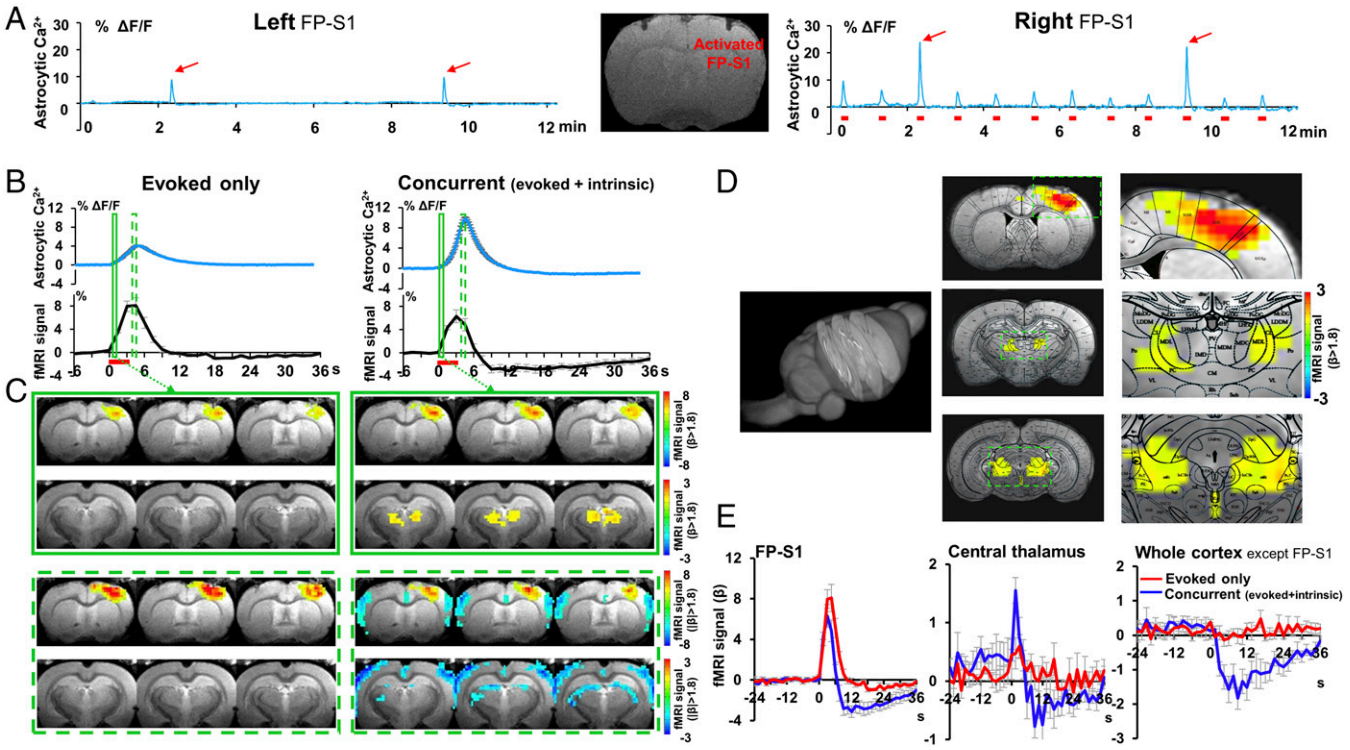

Fig. 5. Subcortical fMRI activation patterns underlying the intrinsic astrocytic Ca^{2+} spikes. (*A*) The representative traces of the FP-S1 astrocytic Ca^{2+} signals in both hemispheres (Right FP-S1 activation, 12 epochs, 3 Hz, 4 s, 1.5 mA; *Inset*, fiber traces in the anatomical MRI image; concurrent events, epoch 3 and 10, red arrows). (*B*) The averaged astrocytic Ca^{2+} and simultaneous fMRI signal of the evoked-only and concurrent events. (*C*) The time-lapsed function maps at 1.5 s (solid green box) and 4.5 s (dashed green box) after onset of stimulation (*Left*: evoked-only FP-S1 activation; *Right*: concurrent events, thalamic activation at 1.5 s, followed by the negative fMRI signal in the cortex and ventricle areas at 4.5 s). (*D*) The concurrent event functional maps at 1.5 s were overlapped on three anatomic slices characterized from a 3D whole brain and the corresponding brain atlas (*Right*: the enlarged images with activity patterns on the FP-S1, central thalamus, and the midbrain reticular formation region). (*E*) The time course of the BOLD fMRI signal from FP-S1, central thalamic region, and the whole cortex except FP-S1 (trial # = 72; rats: n = 6, mean ± SEM).

setup (left FP-S1, neuronal Ca^{2+} vs. right FP-S1, astrocytic Ca^{2+}). An increased EEG-like power level of neuronal Ca^{2+} transients was detected before the intrinsic astrocytic Ca^{2+} events upon electrical stimulation, followed by reduced power levels as well (*SI Appendix*, Fig. S12). These results indicate that the intrinsic astrocytic Ca^{2+} events may rely on the brain state fluctuation.

The event-related analysis scheme used previously was applied to acquire the mean power spectral density of the LFP signal based on the evoked-only events and concurrent events of the simultaneously recorded astrocytic Ca^{2+} signal (Fig. 6 *B* and *C*). The power levels in different EEG frequency bands before and after the stimulation in the evoked-only events indicated no difference between recordings from the thalamus and cortex (Fig. 6 *B* and *C*). In contrast, for the concurrent events, a higher EEG power level occurred before the onset of stimulation and a short transient in the EEG power spectrum was detected at frequencies up to 40 Hz upon stimulation (Fig. 6*B*). Quantitative analysis of the different EEG frequency bands in both the thalamus and cortex showed no detectable difference between both events in the delta band (1–4 Hz). For concurrent events, both the theta (4–8 Hz) and alpha band (8–13 Hz) power levels were significantly higher before stimulation than in evoked-only events (Fig. 6*C*, nonoverlapping CIs; *SI Appendix*, Table S2). Similar patterns were also shown in the EEG-like power spectral analysis for the simultaneously acquired neuronal Ca^{2+} signal (*SI Appendix*, Fig. S12). Also noteworthy is that the beta band (13–30 Hz) power level increased upon stimulation and was significantly higher than during the evoked events, which could contribute to the positive BOLD signal detected only in the concurrent events (Fig. 6*B*). The increased power in the beta frequency band in the thalamus may be attributable to a desynchronized arousal fluctuation that may shift the cortex to more alert brain states and underlie the intrinsic astrocytic Ca^{2+}-mediated neurovascular coupling events.

Discussion

Simultaneously recorded fMRI and GCaMP-mediated Ca^{2+} signals were used to characterize the cell-specific neurovascular coupling events underlying two types of fMRI signals in anesthetized rats. In addition to the conventionally evoked BOLD fMRI signal positively correlated to the neuronal and astrocytic Ca^{2+} signal, an intrinsic astrocytic Ca^{2+} spike was observed that showed unique spatiotemporal features in the cortex and was accompanied by reduced power levels in the EEG across a broad range of frequencies and a negative BOLD signal throughout the cortex. Periodically, the intrinsic and evoked astrocytic Ca^{2+} signals occurred concurrently with neurovascular coupling events at opposite signs, demonstrating that two distinct gliovascular effects on vessel constriction and dilation can occur in vivo under the same conditions. Furthermore, both fMRI brain mapping and LFP recording revealed that increased activity in the thalamic nuclei preceded the intrinsic astrocytic Ca^{2+} signal followed by the negative BOLD signal throughout the cortex. This suggests that the astrocyte-coupled bidirectional fMRI signal originates from thalamic regulation of brain state changes, which may be related to the anticorrelated thalamic and cortical fMRI signals observed during fluctuations in the state of arousal (15).

Previous studies of simultaneous fMRI and electrophysiology have demonstrated that the positive BOLD signal is correlated with increased neuronal activity, and that the negative BOLD

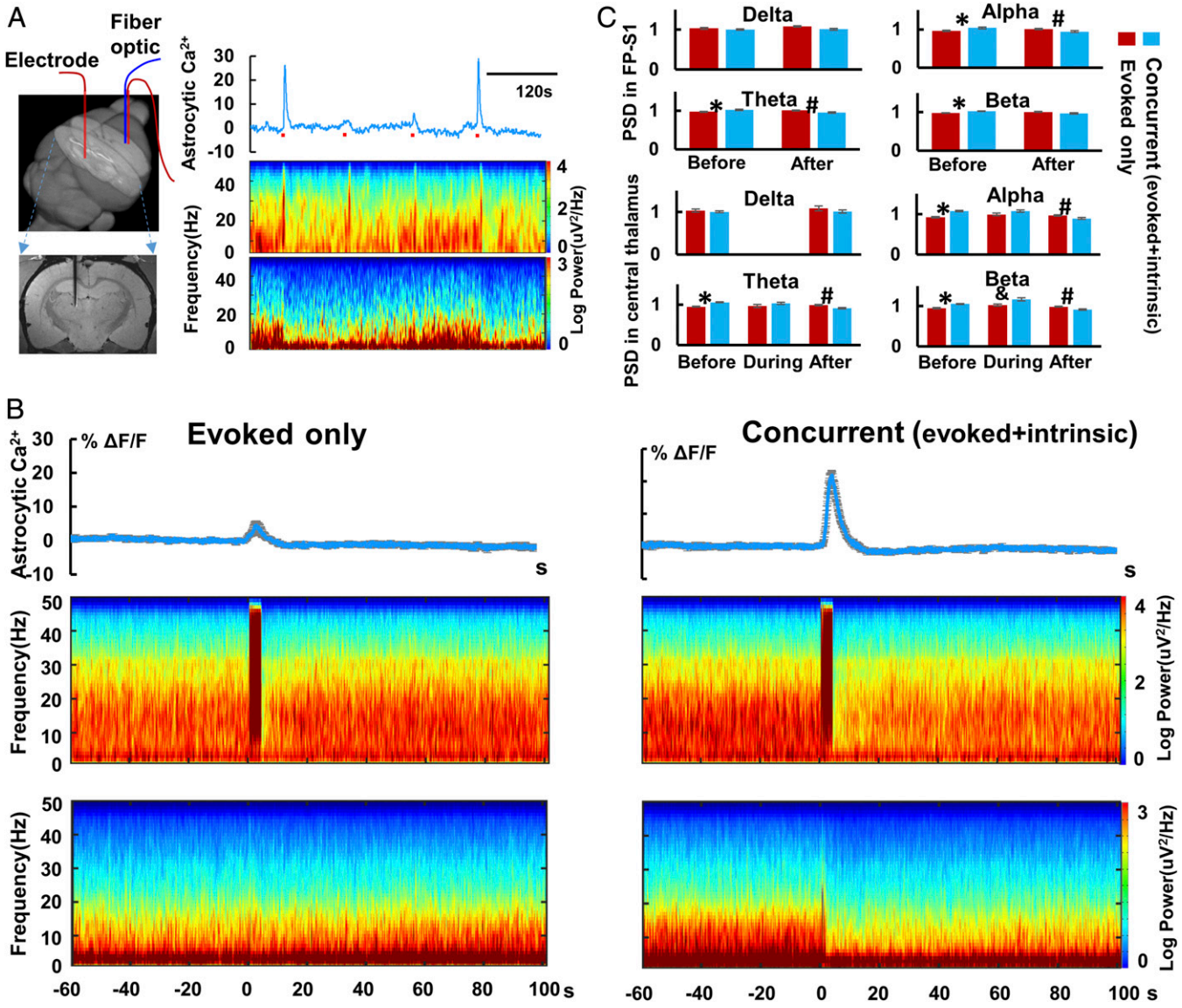

Fig. 6. Simultaneous astrocytic Ca^{2+} recording and the LFP recordings in both central thalamus and FP-S1. (*A*) The representative trace of the FP-S1 astrocytic Ca^{2+} signal (*Top Right*), the LFP power spectrogram in FP-S1 (*Middle Right*) and the contralateral central thalamus (*Bottom Right*) with forepaw electrical stimulation (3 Hz, 4 s, 1.5 mA; *Inset*, 2D slices with electrode insertion in the central thalamic region). (*B*) Evoked-only and concurrent events were separated to show the averaged astrocytic Ca^{2+} signal and LFP power spectrogram (1-s sliding window with 0.1-s steps, 9 tapers). (*C*) The normalized mean spectral power of different EEG bands (evoked-only, red, trial # = 98; concurrent, blue, trial # = 57, rats, $n = 4$) at different phases of the stimulation on/off trials (before: −40 to −20 s; during: 0–1.5 s; and after: 60–80 s; FP-S1: theta, $*P = 1.5e\text{-}05$, $\#P = 0.012$; alpha, $*P = 1.3e\text{-}07$, $\#P = 0.019$; beta, $*P = 1.6e\text{-}07$; central thalamic region: theta, $*P = 0.00018$, #, $P = 0.0025$; alpha, $*P = 3.3e\text{-}05$, #, $P = 0.0068$; beta, $*P = 0.00010$, $\&P = 0.0022$, $\#P = 0.0025$; mean ± SEM; delta power was calculated from 4-s windows in 0.1-s steps).

signal from the surrounding cortical area is associated with decreased neuronal activity (2, 39). It has also been established that the BOLD fMRI signal is directly linked to the hemodynamic signal coupled to the blood flow changes mediated by vascular activity, but the detailed neurovascular coupling events contributing to the bidirectional fMRI signal changes remain unclear (1). Earlier studies have shown that the astrocytic Ca^{2+} signal plays a crucial role in controlling blood flow through gliovascular interaction (3, 4) and especially vasoconstriction and vasodilation under a variety of conditions (7, 8, 12, 40). Upon sensory stimulation, increased neuronal activity (both LFP and neuronal Ca^{2+} signals) is correlated with the evoked astrocytic Ca^{2+} in vivo signal as well as the BOLD fMRI signal, enabling the direct measurement of the fMRI signal with the underlying neuron–glia–vascular interaction (Fig. 1). Optical fiber was used to record the Ca^{2+} signal from astrocytes in deep cortical layers, in contrast to the previous in vivo optical measurement from superficial layers of the cortex (5, 10, 19, 41), enabling the detection of the Ca^{2+} signal from a population of astrocytes located in layer 5 of the cortex. The optical fiber integrated the Ca^{2+} signal from both astrocytic soma and processes directly coupled to pyramidal neurons located at layer 5, which could account for the 1- to 1.7-s latency of the evoked astrocytic Ca^{2+} signal, which is shorter than reported in previous studies (5, 10). Several other optical imaging studies have also reported the rapid onset of evoked Ca^{2+} signal in astrocytes in vivo (11, 35), as well as fast miniature Ca^{2+} transients in the hippocampal slice (42), indicating that the evoked astrocytic signal may be involved in neurovascular coupled vessel dilation underlying the positive BOLD fMRI signal. It is noteworthy that the activity-coupled

vasodilation persists in mice with IP3-2 receptor knock-out ($IP3R2^{-/-}$) to inhibit the astrocytic Ca^{2+} intracellular release, therefore indicating that there may be a parallel pathway to mediate the astrocytic Ca^{2+}-independent vasodilation (5, 43). Interestingly, a recent study reported the astrocytic calcium fluctuation in $IP3R2^{-/-}$ mice upon startle responses (44). In contrast, the capillary dilation could be controlled by glial Ca^{2+} signal (43). In $IP3R2^{-/-}$ mice, the capillary dilation is abolished where the glial Ca^{2+} signal is reduced (6). This study suggests that the astrocytic Ca^{2+} signal may mediate the neurovascular coupling through capillary control. In addition, the causal relationship of the astrocytic Ca^{2+} signal with BOLD fMRI can be further specified in transgenic mice with inhibited astrocytic Ca^{2+} intracellular release and pericyte-deficient mice (5, 45).

Astrocytic Ca^{2+}-mediated vessel constriction has been observed in vivo under spreading suppression (31). Similarly, the death of pericytes in the ischemic brain also causes capillary constriction in vivo (46). It remains to be determined whether the elevated astrocytic Ca^{2+} causes negative BOLD signal changes through vasoconstriction during normal functioning. Here, we showed that the intrinsic astrocytic Ca^{2+} spike was the crucial linkage of neurovascular coupling to mediate the negative BOLD signal in the whole cortex. The data show that the intrinsic astrocytic Ca^{2+} spike is accompanied by decreased high frequency (3–40 Hz) power of the spontaneous LFP signal with a slight lag, consistent with two-photon imaging studies in mice anesthetized with urethane (9). The absence of slow-frequency oscillations in the present study could be due to anesthetics and differences with α-chloralose (36, 47). Interestingly, in the hippocampus of mice anesthetized with urethane, astrocytic Ca^{2+} waves have been reported to correlate with the decreased power level in both infraslow and high-frequency ranges, as well as with reduced blood flow (30). Besides the spontaneous neuronal oscillation, the astrocytic Ca^{2+} transients have also been reported to be coupled with carbachol-induced oscillations in the hippocampal brain slices (34). Therefore, the intrinsic astrocytic Ca^{2+}-coupled negative BOLD signal may represent one of the multiple ways that astrocytes affect neurovascular coupling and modulate brain states (7).

What is the relationship between spreading depression of the lesioned brain and the intrinsic astrocytic Ca^{2+} signal with decreased BOLD signal? Spreading depolarization/depression can be elicited by numerous noxious triggers, such as chemical treatment with potassium and glutamate, hypoxia, and focal ischemia, as well as in the healthy intact cortex (26, 27). The persistent depression of activity and reduction of blood flow usually follows spreading depolarization in the cortex, which is also accompanied with Ca^{2+} waves propagating through the local neuronal and astrocytic network from the triggered source (28, 48, 49). However, the novel intrinsic astrocytic Ca^{2+}-mediated neurovascular coupling events showed spatiotemporal features distinct from spreading depression (*SI Appendix*, Fig. S8). First, intrinsic astrocytic Ca^{2+} signals can occur concurrently with the evoked astrocytic Ca^{2+} signal, mediating, respectively, both positive and negative BOLD fMRI signals in the brain. Although the elevated astrocytic Ca^{2+} leads to the secretion of different vasoactive agents, such as prostaglandin E2, epoxyeicosatrienoic acids, and 20-HETE, under different conditions (7, 8, 12, 37), the large-scale astrocytic Ca^{2+}-mediated vasoconstriction that is usually detected in the pathological conditions of the cortex is not accompanied by simultaneous positive events in vivo (31). Second, there was no propagation delay of the intrinsic astrocytic Ca^{2+} spikes in the two hemispheres (Fig. 4), which is different from Ca^{2+} waves traveling through the astrocytic network from the source of spreading depression (31, 32). We presented evidence that the intrinsic astrocytic Ca^{2+} signals detected instantaneously throughout the cortex (Figs. 3 and 4) were initiated by subcortical projections activating the intrinsic astrocytic Ca^{2+}-mediated neurovascular coupling events (50, 51).

The intrinsic astrocytic Ca^{2+} signal mediates the regulation of brain states through the reticular formation ascending pathway, which is known to regulate arousal (52). Although initiated in the anesthetized rat brain, the intrinsic astrocytic Ca^{2+}-mediated neuronal activity changes may shed light on the thalamic regulation of the state switch leading to arousal. The simultaneously acquired astrocytic Ca^{2+} signal led to the identification of the activated thalamic and midbrain reticular formation regions in fMRI brain mapping based on the occurrence of the intrinsic astrocytic Ca^{2+} spikes (Figs. 5 and 6, *SI Appendix*, Fig. S10, and Movie S2). Two striking features were detected: First, positive BOLD signals were detected in the thalamic regions in contrast to negative BOLD signals detected throughout the entire cortex. These results are consistent with the fMRI activity pattern reported in a recent resting-state fMRI study, showing that increased fMRI signals in the thalamus and decreased fMRI signals in the whole cortex are correlated with state fluctuation associated with arousal at eye opening (15). Optogenetic activation of the central lateral thalamus at low frequency also initiates the negative BOLD signal across the whole cortex of the anesthetized rat brain (53). Second, the increased alpha power in both the thalamus and cortex was detected before the occurrence of the intrinsic astrocytic spike, which was then followed by decreased alpha power. This could provide insights into what cortical states predispose toward the induction of these Ca^{2+} spikes. Alpha power is also reduced following eye opening (54). The regulation of alpha-power oscillation-dependent brain states is less efficient when delivered upon the high alpha-power state (55, 56). It is plausible that the intrinsic astrocytic Ca^{2+} spikes may be involved in the spontaneous fluctuation of the alpha-band EEG activity to mediate the brain excitability (56).

Two issues remain to be solved to better understand the interaction of astrocytic calcium and BOLD fMRI signal during the brain state fluctuation. The first issue is the brain state dependency and potential anesthetic effects on the correlation of astrocytic calcium signal and BOLD fMRI signal. Besides α-chloralose, the negative BOLD signal coupled to the intrinsic astrocytic Ca^{2+} spikes was observed in rats anesthetized with urethane (*SI Appendix*, Fig. S13). This result demonstrates that the negative correlation is not just caused by the α-chloralose anesthetic effect. Interestingly, the negative BOLD correlation pattern varied across different animals, indicating a potential dependency on the anesthetic effect of urethane (*SI Appendix*, Fig. S14). In a preliminary experiment, the astrocytic Ca^{2+} signal was recorded simultaneously with LFP in free-moving rats, showing the intrinsic astrocytic Ca^{2+} spikes in coincidence with the EEG state changes during sleep cycles (*SI Appendix*, Fig. S15). This preliminary result further implicates the highly correlated intrinsic astrocytic Ca^{2+} signals with brain state changes, similar to what has been reported in the urethane-anesthetized rats (9).

The second issue is to clarify the causal relationship of the intrinsic astrocytic Ca^{2+} signal to the negative BOLD signal and their underlying molecular mechanism. In the present study, both intrinsic astrocytic Ca^{2+} signal and negative BOLD signal were dampened in rats anesthetized with medetomidine, an adrenergic alpha-2 receptor agonist, which can inhibit norepinephrine effect through negative feedback (*SI Appendix*, Fig. S16). It has been shown that the locomotion- or startle-induced astrocytic Ca^{2+} signal can be blocked by trazodone or prazosin, the inhibitor or antagonist of adrenergic receptors, and abolished by neurotoxin DSP4 with local norepinephrine depletion (57, 58). These results indicate that the noradrenergic system may mediate both intrinsic astrocytic Ca^{2+} signal and vasoconstriction, respectively or sequentially (59). It is also possible that the

central thalamic nuclei and the midbrain reticular formation are directly mediated by the norepinephrine projections or are coactivated to elicit the intrinsic astrocytic Ca^{2+} signal and the negative BOLD signal in the whole cortical area (60). Optogenetic activation of the locus coeruleus or central thalamic nulcei offers further prospects for studying the causal relationship and the direct norepinephrine-driven mechanism. The simultaneous astrocytic calcium recording with fMRI could be combined with optogenetic activation to specify the molecular and circuit mechanism underlying astrocyte-mediated gliovascular interaction and correlated brain state changes.

Materials and Methods

Detailed methods are provided in *SI Appendix, SI Materials and Methods*. The study was performed in accordance with the German Animal Welfare Act (TierSchG) and Animal Welfare Laboratory Animal Ordinance (TierSchVersV). This is in full compliance with the guidelines of the EU Directive on the protection of animals used for scientific purposes (2010/63/EU). The study was reviewed by the ethics commission (§15 TierSchG) and approved by the state authority (Regierungspräsidium, Tuebingen, Baden-Württemberg, Germany). A total of 88 Sprague–Dawley rats were used in this study.

Viral vectors were directly ordered and packaged from the University of Pennsylvania Vector Core: AAV5.Syn.GCaMP6f.WPRE.SV40 and AAV5.GfaABC1D.cyto-GCaMP6f.SV40 (Addgene52925; GfaABC1D.cyto promoter for cytoplasmic expression of GCaMP6f; ref. 61).

Similar procedures of fMRI animal preparation have been previously described (62). The two-channel optical setup for fiber-optic Ca^{2+} recordings has been developed base on a previous report (Fig. 1*C*) (19). The astrocytic calcium signal-dependent event-related fMRI analysis was applied to specify the subcortical brain activity patterns from the whole brain 3D-EPI fMRI images.

A paired Student's *t* test and one-way ANOVA were performed for statistical analysis. The data with error bars are mean ± SEM in each statistic graph. In addition, the mean and 95% CIs for the distribution of LFP power spectra density, estimated onset times, amplitude of the astrocytic Ca^{2+}, and BOLD signal were calculated using the bootstrap procedure (63). The 95% CIs are equivalent to hypothesis testing with a significance level of 0.05. Both confidence intervals with (nonoverlapping CIs) and *P* values for all statistical analysis were listed in *SI Appendix*, Table S2. Sample size was not previously estimated for the animal experiments, and no blinding and randomization design was needed in this work.

ACKNOWLEDGMENTS. We thank Dr. R. Pohmann, Dr. H. Merkle, Dr. K. Buckenmaier, Dr. Y. Jiang, Ms. P. Pais, and Ms. X. Chen for technical support; Ms. H. Schulz and S. Fischer for animal maintenance support; the Analysis of Functional NeuroImages (AFNI) team for the software support; and Dr. B. S. Khakh, the Genetically-Encoded Neuronal Indicator and Effector (GENIE) Program, and the Janelia Farm Research Campus for providing the astrocyte-specific promoter and GCaMP6 plasmids. This research was supported by German Research Foundation (DFG) SPP-1655, internal funding from Max Planck Society (to X.Y.), and HHMI support (to T.J.S.).

1. Attwell D, Iadecola C (2002) The neural basis of functional brain imaging signals. *Trends Neurosci* 25:621–625.
2. Logothetis NK, Pauls J, Augath M, Trinath T, Oeltermann A (2001) Neurophysiological investigation of the basis of the fMRI signal. *Nature* 412:150–157.
3. Attwell D, et al. (2010) Glial and neuronal control of brain blood flow. *Nature* 468: 232–243.
4. Petzold GC, Murthy VN (2011) Role of astrocytes in neurovascular coupling. *Neuron* 71:782–797.
5. Nizar K, et al. (2013) In vivo stimulus-induced vasodilation occurs without IP3 receptor activation and may precede astrocytic calcium increase. *J Neurosci* 33:8411–8422.
6. Biesecker KR, et al. (2016) Glial cell calcium signaling mediates capillary regulation of blood flow in the retina. *J Neurosci* 36:9435–9445.
7. Metea MR, Newman EA (2006) Glial cells dilate and constrict blood vessels: A mechanism of neurovascular coupling. *J Neurosci* 26:2862–2870.
8. Mulligan SJ, MacVicar BA (2004) Calcium transients in astrocyte endfeet cause cerebrovascular constrictions. *Nature* 431:195–199.
9. Poskanzer KE, Yuste R (2016) Astrocytes regulate cortical state switching in vivo. *Proc Natl Acad Sci USA* 113:E2675–E2684.
10. Wang X, et al. (2006) Astrocytic Ca2+ signaling evoked by sensory stimulation in vivo. *Nat Neurosci* 9:816–823.
11. Lind BL, Brazhe AR, Jessen SB, Tan FC, Lauritzen MJ (2013) Rapid stimulus-evoked astrocyte Ca2+ elevations and hemodynamic responses in mouse somatosensory cortex in vivo. *Proc Natl Acad Sci USA* 110:E4678–E4687.
12. Zonta M, et al. (2003) Neuron-to-astrocyte signaling is central to the dynamic control of brain microcirculation. *Nat Neurosci* 6:43–50.
13. Dombeck DA, Khabbaz AN, Collman F, Adelman TL, Tank DW (2007) Imaging large-scale neural activity with cellular resolution in awake, mobile mice. *Neuron* 56:43–57.
14. Sirotin YB, Das A (2009) Anticipatory haemodynamic signals in sensory cortex not predicted by local neuronal activity. *Nature* 457:475–479.
15. Chang C, et al. (2016) Tracking brain arousal fluctuations with fMRI. *Proc Natl Acad Sci USA* 113:4518–4523.
16. Logothetis NK, et al. (2012) Hippocampal-cortical interaction during periods of subcortical silence. *Nature* 491:547–553.
17. Girouard H, Iadecola C (2006) Neurovascular coupling in the normal brain and in hypertension, stroke, and Alzheimer disease. *J Appl Physiol (1985)* 100:328–335.
18. Akerboom J, et al. (2013) Genetically encoded calcium indicators for multi-color neural activity imaging and combination with optogenetics. *Front Mol Neurosci* 6:2.
19. Schulz K, et al. (2012) Simultaneous BOLD fMRI and fiber-optic calcium recording in rat neocortex. *Nat Methods* 9:597–602.
20. Chen TW, et al. (2013) Ultrasensitive fluorescent proteins for imaging neuronal activity. *Nature* 499:295–300.
21. Adelsberger H, Garaschuk O, Konnerth A (2005) Cortical calcium waves in resting newborn mice. *Nat Neurosci* 8:988–990.
22. Lütcke H, et al. (2010) Optical recording of neuronal activity with a genetically-encoded calcium indicator in anesthetized and freely moving mice. *Front Neural Circuits* 4:9.
23. Sanganahalli BG, et al. (2016) Comparison of glomerular activity patterns by fMRI and wide-field calcium imaging: Implications for principles underlying odor mapping. *Neuroimage* 126:208–218.
24. Adelsberger H, Zainos A, Alvarez M, Romo R, Konnerth A (2014) Local domains of motor cortical activity revealed by fiber-optic calcium recordings in behaving non-human primates. *Proc Natl Acad Sci USA* 111:463–468.
25. Kim CK, et al. (2016) Simultaneous fast measurement of circuit dynamics at multiple sites across the mammalian brain. *Nat Methods* 13:325–328.
26. Dreier JP (2011) The role of spreading depression, spreading depolarization and spreading ischemia in neurological disease. *Nat Med* 17:439–447.
27. Ayata C, Lauritzen M (2015) Spreading depression, spreading depolarizations, and the cerebral vasculature. *Physiol Rev* 95:953–993.
28. Nedergaard M, Cooper AJL, Goldman SA (1995) Gap junctions are required for the propagation of spreading depression. *J Neurobiol* 28:433–444.
29. Nedergaard M, Hansen AJ (1993) Characterization of cortical depolarizations evoked in focal cerebral ischemia. *J Cereb Blood Flow Metab* 13:568–574.
30. Kuga N, Sasaki T, Takahara Y, Matsuki N, Ikegaya Y (2011) Large-scale calcium waves traveling through astrocytic networks in vivo. *J Neurosci* 31:2607–2614.
31. Chuquet J, Hollender L, Nimchinsky EA (2007) High-resolution in vivo imaging of the neurovascular unit during spreading depression. *J Neurosci* 27:4036–4044.
32. Peters O, Schipke CG, Hashimoto Y, Kettenmann H (2003) Different mechanisms promote astrocyte Ca2+ waves and spreading depression in the mouse neocortex. *J Neurosci* 23:9888–9896.
33. Poskanzer KE, Yuste R (2011) Astrocytic regulation of cortical UP states. *Proc Natl Acad Sci USA* 108:18453–18458.
34. Lee HS, et al. (2014) Astrocytes contribute to gamma oscillations and recognition memory. *Proc Natl Acad Sci USA* 111:E3343–E3352.
35. Winship IR, Plaa N, Murphy TH (2007) Rapid astrocyte calcium signals correlate with neuronal activity and onset of the hemodynamic response in vivo. *J Neurosci* 27: 6268–6272.
36. Winters WD, Spooner CE (1966) A neurophysiological comparison of alpha-chloralose with gamma-hydroxybutyrate in cats. *Electroencephalogr Clin Neurophysiol* 20: 83–90.
37. Gordon GRJ, Choi HB, Rungta RL, Ellis-Davies GCR, MacVicar BA (2008) Brain metabolism dictates the polarity of astrocyte control over arterioles. *Nature* 456: 745–749.
38. Kuchibhotla KV, Lattarulo CR, Hyman BT, Bacskai BJ (2009) Synchronous hyperactivity and intercellular calcium waves in astrocytes in Alzheimer mice. *Science* 323: 1211–1215.
39. Shmuel A, Augath M, Oeltermann A, Logothetis NK (2006) Negative functional MRI response correlates with decreases in neuronal activity in monkey visual area V1. *Nat Neurosci* 9:569–577.
40. Devor A, et al. (2007) Suppressed neuronal activity and concurrent arteriolar vasoconstriction may explain negative blood oxygenation level-dependent signal. *J Neurosci* 27:4452–4459.
41. Srinivasan R, et al. (2016) New transgenic mouse lines for selectively targeting astrocytes and studying calcium signals in astrocyte processes in situ and in Vivo. *Neuron* 92:1181–1195.
42. Di Castro MA, et al. (2011) Local Ca2+ detection and modulation of synaptic release by astrocytes. *Nat Neurosci* 14:1276–1284.
43. Mishra A, et al. (2016) Astrocytes mediate neurovascular signaling to capillary pericytes but not to arterioles. *Nat Neurosci* 19:1619–1627.
44. Srinivasan R, et al. (2015) Ca(2+) signaling in astrocytes from Ip3r2(-/-) mice in brain slices and during startle responses in vivo. *Nat Neurosci* 18:708–717.
45. Armulik A, et al. (2010) Pericytes regulate the blood-brain barrier. *Nature* 468: 557–561.
46. Hall CN, et al. (2014) Capillary pericytes regulate cerebral blood flow in health and disease. *Nature* 508:55–60.

47. Steriade M, Nuñez A, Amzica F (1993) A novel slow (< 1 Hz) oscillation of neocortical neurons in vivo: Depolarizing and hyperpolarizing components. *J Neurosci* 13: 3252–3265.
48. Nedergaard M (1994) Direct signaling from astrocytes to neurons in cultures of mammalian brain cells. *Science* 263:1768–1771.
49. Parpura V, et al. (1994) Glutamate-mediated astrocyte-neuron signalling. *Nature* 369: 744–747.
50. Hamel E (2006) Perivascular nerves and the regulation of cerebrovascular tone. *J Appl Physiol (1985)* 100:1059–1064.
51. Cauli B, et al. (2004) Cortical GABA interneurons in neurovascular coupling: Relays for subcortical vasoactive pathways. *J Neurosci* 24:8940–8949.
52. Edlow BL, et al. (2012) Neuroanatomic connectivity of the human ascending arousal system critical to consciousness and its disorders. *J Neuropathol Exp Neurol* 71:531–546.
53. Liu J, et al. (2015) Frequency-selective control of cortical and subcortical networks by central thalamus. *eLife* 4:e09215.
54. Berger H (1929) Über das Elektrenkephalogramm des Menschen. *Arch Psychiatr Nervenkr* 87:527–570.
55. Silvanto J, Muggleton N, Walsh V (2008) State-dependency in brain stimulation studies of perception and cognition. *Trends Cogn Sci* 12:447–454.
56. Romei V, et al. (2008) Spontaneous fluctuations in posterior alpha-band EEG activity reflect variability in excitability of human visual areas. *Cereb Cortex* 18:2010–2018.
57. Ding F, et al. (2013) α1-Adrenergic receptors mediate coordinated Ca2+ signaling of cortical astrocytes in awake, behaving mice. *Cell Calcium* 54:387–394.
58. Paukert M, et al. (2014) Norepinephrine controls astroglial responsiveness to local circuit activity. *Neuron* 82:1263–1270.
59. O'Donnell J, Ding F, Nedergaard M (2015) Distinct functional states of astrocytes during sleep and wakefulness: Is norepinephrine the master regulator? *Curr Sleep Med Rep* 1:1–8.
60. Carter ME, et al. (2010) Tuning arousal with optogenetic modulation of locus coeruleus neurons. *Nat Neurosci* 13:1526–1533.
61. Shigetomi E, et al. (2013) Imaging calcium microdomains within entire astrocyte territories and endfeet with GCaMPs expressed using adeno-associated viruses. *J Gen Physiol* 141:633–647.
62. Yu X, et al. (2016) Sensory and optogenetically driven single-vessel fMRI. *Nat Methods* 13:337–340.
63. Van Dort CJ, et al. (2015) Optogenetic activation of cholinergic neurons in the PPT or LDT induces REM sleep. *Proc Natl Acad Sci USA* 112:584–589.

Supporting Information

SI Materials and Methods

Animal preparation and instrument setup

Viral injection. Four-week old male Sprague-Dawley rats were used for viral injection to express GCaMP in either neurons (AAV5.Syn.GCaMP6f.WPRE.SV40) or astrocytes (AAV5.GfaABC1D.cyto-GCaMP6f.SV40 (Addgene52925; GfaABC1D.cyto promoter for cytoplasmic expression of GCaMP6f (1)). Viral vectors were directly ordered and packaged from the University of Pennsylvania Vector Core. Rats were anesthetized with 5% Isoflurane in oxygen-enhanced air (30% oxygen) in an induction box, and maintained (1.5~2%) via nosecone. The depth of anesthesia was checked by the lack of pedal withdrawal reflex. Temperature was monitored and controlled through a rectal probe and a 37°C feedback controlled heating pad. A small amount of sterile ophthalmic ointment (Puralube) was placed in eyes to protect it from drying. The animal head was secured to a stereotaxic frame by earpieces and a tooth bar. Using a dissecting microscope and a pneumatic drill, a small burr hole (up to 1.0mm diameter) was made craniotomy above the region of interest, using stereotaxic coordinates from the Paxinos & Watson rat brain atlas. The hole was made to allow the 35 gauge needle attached to a WPI syringe, lowered precisely into the region of interest, and viral vectors were delivered. AAV viral vectors (400 nL for Syn-GCaMP, 1.8ul for GFAP-GCaMP) were injected to express the GCaMP6f in either neurons or astrocytes in the rat cortex with a 10 μL WPI syringe at a rate of 100 nL/min controlled by an infusion pump (Pump11 Elite, Harvard Apparatus). Stereotaxic injections were delivered to two sites with the following coordinates: FP-S1, Rostral, 0.2 mm, lateral, 3.8 mm, ventral, 1.5~1.0 mm; BC, caudal, 2.3 mm, lateral, 4.7 mm, and ventral, 1.5~1.0 mm, respectively, from bregma. The needle was slowly withdrawn in 5 minutes after the injection. The hole on the skull was sealed by bone wax and skin was sutured. Rats were subcutaneously injected with Ketoprofen (5 mg/kg) to decrease postoperative pain. It usually takes more than 4 weeks for AAV viral vectors to express sufficient GCaMP for calcium recording. The rat brain were perfused for immunohistochemistry and fluorescent staining to examine the GCaMP expression level and cellular specificity.

Animal preparation for fMRI. Similar procedure has been previously described (2). Briefly, rats were initially anesthetized with isoflurane. Each rat was orally intubated with a mechanical ventilator (SAR-830, CWE) throughout the whole surgical and imaging procedures. Plastic catheters were inserted into the femoral artery and vein to allow monitoring of arterial blood gases and administration of drugs. After surgery, all animals were given i.v. bolus of α-chloralose (80mg/kg) and isoflurane was discontinued. Anesthesia was maintained with a constant infusion of α-chloralose (26.5mg/kg/h). The rats were placed on a heating pad to maintain rectal temperature at ~37°C while in the magnet. Each animal was secured in a head holder with a bite bar to prevent head motion. End-tidal CO_2, rectal temperature, tidal pressure of ventilation, heart rate,

and arterial blood pressure were continuously monitored during the experiment. Arterial blood gas levels were checked periodically and corrections were made by adjusting respiratory volume/rate or administering sodium bicarbonate to maintain normal levels during data acquisition. An *i.v.* infusion of pancuronium bromide (2 mg/kg/h) was delivered to reduce the motion artifacts. The rat was then implanted with the fiber optic before it was transferred to the MRI scanner for the simultaneous calcium recording and fMRI. Besides α-chloralose, urethane and Domitor (medetomidine hydrochloride) were applied to examine the astrocytic Ca^{2+} signal-mediated gliovascular interactions with fMRI, as previously reported(3, 4). For urethane anesthesia, following the similar surgical procedure with plastic catheters inserted into the femoral vein, all rats were given i.v. bolus of urethane (100-200 mg/kg) and isoflurane was discontinued. Anesthesia was maintained with a constant infusion rate (100mg/kg/h) of urethane and pancuronium bromide (1.5-2 mg/kg/h) to avoid the motion artifact during fMRI imaging. The astrocytic Ca^{2+} signal was recorded after rats were fully anesthetized in 1.5-2 hour. It is noteworthy that blood pressure and end-tidal CO_2 signal fluctuation were detected during the first 1-2 hours in rats under urethane anesthesia, coupled to astrocytic signal with varied BOLD signal changes mainly located at the sinus area in the brain. For medetomidine anesthesia, all rats were given with i.v. bolus of medetomidine (0.05 mg/kg) and maintained with a constant infusion of medetomidine (100mg/kg/h). Also, rats were first anesthetized with α-chloralose for simultaneous fMRI and fiber optic Ca^{2+} recording and then were switch to medetomidine to test the astrocytic Ca^{2+} signal-mediated gliovascular interactions.

Fiber-optic / Electrode implantation. 200um fiber optic (Thorlabs, low-OH, 200EMT) / electrode (1 MΩ, ~100 μm, Tungsten, FHC) were inserted into the deep layer of FP-S1(caudal, 0.2 mm, lateral, 4.0 mm, ventral, 1-1.2 mm, BC (rostral, 2.5 mm, lateral, 5.0 mm, ventral, 1−1.2 mm) or central thalamus (caudal, 3.2 mm, lateral, 1.5 mm, ventral, −5.5 mm). For simultaneous calcium and electrophysiological recording, the dura was carefully removed and the fiber optic and electrode were inserted into the cortex, and the reference and ground were placed on a skull screw fixed over the right cerebellum. For simultaneous calcium recording and BOLD fMRI, only the fiber optic was inserted into the FP-S1 or BC under the surgical microscope. Super glue was used to secure the fiber to the skull and the skin was sutured after the fixation for the acute terminal experiments.

Simultaneous calcium with electrophysiological recording. The anaesthetized rats were adapted in a stereotaxic device for *in vivo* recordings using similar anesthetics and surgical preparation to the fMRI experiments. Electrode was attached to the fiber optic with closely contacted fiber optic tip and electrode contacting point. The local field potential (LFP) was acquired through the EEG module of the Biopac system (gain factor, 5,000; band-pass filter, 0.02–100 Hz; sample rate, 5,000/s). The GCaMP6f-mediated fluorescent signal was acquired by the analogue input module of Biopac 150 system, which was also used to generate triggers for electrical stimulation. In parallel, the blood pressure, temperature, and heart beat signal was simultaneously recorded. Matlab scripts were developed to extract the sensory evoked potential/calcium signals, as well as

the stimulation trigger signal for signaling processing. The forepaw electrical stimulus (330 μs pulses repeated at 3 Hz, 4 s or 30 s duration) were delivered through two needles inserted into interdigital plantar muscle for the forepaw with a stimulus isolator (A365, WPI). The stimulation duration and frequency was controlled by Master-9 A.M.P.I system (Jerusalem, Israel) with the trigger directly set up by the Biopac 150 system or through the MRI scanner. Meanwhile, the simultaneous LFP and astrocytic Ca^{2+} recording in the free-moving rat. After the Fiber-optic / Electrode implantation, all rats were given a 3 days of recovery time before the recording, and the weight was monitored daily. The rat was placed in a recording box (25x25x35cm), the LFP and astrocytic Ca^{2+} signal in FP-S1 were recorded during the sleeping cycle. The recording period lasted for about 60-120 mins every day.

Immunohistochemistry. The perfused brains after imaging or recording were fixed overnight in 4% paraformaldehyde, followed by 15% and 30% sucrose in 0.1 M PBS at 4 °C until tissues sank down. The brain were sliced with 30μm thickness by cryo-microtome (CM3050S, Leica). The floating sections were blocked in a solution of 0.3% Triton X-100 (Sigma) and 20% normal goat serum (Sigma) in 0.1 M PBS for 30 min at room temperature (RT). For the detection of NeuN or GFAP, sections were incubated with primary antibodies (mouse anti-NeuN, 1:200, Merck; mouse anti-GFAP, 1:30, BD Biosciences) overnight at 4 °C, respectively. For fluorescent immunolabeling, sections were incubated for 2 hours at RT with the secondary antibodies (goat anti-mouse conjugated with CY3, 1:500; Abcam). A mounting medium with DAPI (VectaShield, vector) was used to stain the nuclei and mount the brain slice. The cell-specific GCaMP expression was co-localized with the NeuN / GFAP positive neurons or astrocytes using confocal microscope (10x, Leica Sp2) (Fig. 1). In addition, a wide-field fluorescent image was acquired to show the GCaMP expression in the FP-S1 of the whole brain slice with an Apotome microscope (Zeiss, Germany).

Two-channel optical setup for fiber optic Ca^{2+} recordings. The light path was developed base on a previous report (Fig. 1C) (5). A 473 nm laser (MBL-III, CNI) was served as the light source, then split it into two light beams for the two-channel recording by beam-splitter (30R/70T, AHF). The beams were reflected via dichroic mirrors (F48-487, reflection 471–491 nm, >94%; transmission 500–1200 nm, >93%; AHF Analysentechnik), and coupled into a multimode optical fiber (FT-200-EMT; NA = 0.39; 200μm diameter, Thorlabs) by an objective lens fixed on the fiber launch (MBT613D/M, Thorlabs), then beams were focused on the fiber optic. Laser intensity was measured at the fiber tip (~5 uW for neuronal calcium recording; or ~30 uW for astrocytic calcium recording) by an optical power meter (PM20A, ThorLabs). The emitted fluorescent signal was guided back to the optical path through the same fiber optic. After passing the dichroic mirror and optical filter (F37-516; 500-550 um band pass, AHF Analysentechnik), the GCaMP6-mediated fluorescent signal was focused by tube lens (AC254-030-A1-ML, Thorlabs) to directly project to a peltier-cooled silicon photomultiplier with trans-impedance preamplifier (MiniSM-10035-X08, SensL). The signal from photomultiplier was amplified by voltage amplifier (DHPVA-100, Femto) before detected by the analogue input module of Biopac 150 system.

MRI and fMRI procedures

Images were acquired with 14.1 T magnet (Magnex) interfaced to an Avance III console (Bruker) and equipped with a 12-cm gradient set (Resonance Research). A homemade transceiver surface coil with an internal diameter of 2.0 cm was used for rat brain imaging.

EPI fMRI. A 3D gradient-echo EPI sequence was performed with the following parameters: effective TE, 11.5 ms; effective TR, 31.25ms; total TR, 1.5 s; bandwidth, 134 kHz; flip angle, 12°; FOV, 1.92 × 1.92 × 1.92cm, isotropic resolution, 0.4 x 0.4 x 0.4mm. The paradigm consisted of 30 dummy scans to reach steady state, 10 pre-stimulation scans, 5 scans during stimulation (stimulation on period 4 s or 30 s), and 35 or 75 post-stimulation scans with total 8-12 epoch for each run.

Balanced steady state free precession fMRI (bSSFP-fMRI). A coronal slice was acquired with bSSFP sequence with following parameters: TR/TE: 4.2/2.1 ms; total TR, 200 ms; bandwidth, 19.5 kHz; flip angle, 9°; matrix, 48x48; slice thickness, 0.5 mm; in-plane resolution, 400x400 μm. The paradigm consisted of 25 dummy scans to reach steady state, 175 pre-stimulation scans, 20 scans (4 s stimulation) or 150 scan (30s stimulation) during stimulation, and 280 or 450 post-stimulation scans with total 5-8 epochs for each run, and the total acquisition time was ~10 min to ~16 min. For the resting state fMRI imaging, the paradigm consisted of 25 dummy scans to reach steady state, 175 pre-trigger scans, 3000 post-trigger scans, the trigger was used to offline synchronize the calcium with the fMRI signal.

Anatomical MRI images in the same orientation were acquired using a FLASH sequence with the following parameter: TE 2.9 ms, TR 500 ms, flip angle 30°, matrix 256×256×48. The locations of the electrode tip in central thalamus were observed using a RARE sequence with the following parameter: TE 7.0 ms, TR 1.5 s, RARE factor 4, FOV1.92 × 1.92 × 0.16 cm, matrix 256 ×256×4 (Fig. S11).

Data analysis and statistics

The Analysis of Functional NeuroImages (AFNI, NIH) and Matlab were used to process the simultaneously acquired fMRI and calcium signals. The relevant source codes can be downloaded through https://www.afni.nimh.nih.gov/afni/. Detailed description of the processing was provided in a previous study(2). For fMRI analysis, the EPI images were first aligned to anatomical dataset acquired in the same orientation. The anatomical MRI images were registered to a template across animals, as well as the EPI datasets, for group analysis. The baseline signal of EPI images were normalized to 100 for multiple trial statistical analysis of the block design EPI time-courses.

For the correlation analysis of the simultaneous fMRI with intrinsic astrocytic calcium transients detected during the resting state, an amplitude modulated response model based on the AFNI script was implemented to perform linear regression analysis (Fig. S5).

Amplitude Modulated Response Model:

$$r_{AM2}(t) = \sum_{k=1}^{k} h(t-\tau_{\mathrm{k}}) \cdot (a_k - \bar{a})$$

a_k =value of kth AIACS (Amplitude of Intrinsic Astrocytic Calcium Spike), and $\bar{a}$ is the mean AIACS value.

The hemodynamic response function (HRF) is the block function used in AFNI.

$$h(t) = \int_0^{\min(t.L)} s^4 e^{-s} / [4^4 e^{-4}]\, ds$$

Gamma variate function = s^4e^{-s} /4^4e^{-4}. L was the duration of the response. Different duration was tested to optimize the hemodynamic response modeling for the intrinsic astrocytic calcium transients, showing the most significant correlation maps at 10s duration (Fig. S5). Voxel-wise correlation was calculated between the amplitude modulated hemodynamic response and the resting state SSFP-fMRI signal, showing mean negative correlation coefficient in the whole cortex (Fig. 2).

Given the simultaneous fMRI with calcium recording, the astrocytic calcium signal was used to categorize the evoked only and concurrent (evoked + intrinsic) astrocytic calcium events at different on/off block design epochs. Two criteria were used to distinguish the two events. The concurrent event should show the peak calcium signal three times higher than the standard deviation of the calcium signal peak amplitude of events from all trials acquired for each rat. Meanwhile, the concurrent events should show intrinsic calcium spike detectable from the other non-activated cortical area, e.g. the barrel cortex (Fig. 3), or the FP-S1 of the other hemisphere (Figs. 4 and 5). In addition, for the 30 s stimulation paradigm, the concurrent events only focused on the intrinsic signal detected at the early phase of the stimulation on period (Figs. 3 and 4; Fig. S8 shows concurrent events could also occur at middle phase of stimulation or at rest of the stimulation period.). The evoked only events were collected from the same runs with concurrent events. In addition, evoked only events did not include the first epoch of each run to reduce the potential desensitization-based variability. For the EEG band power analysis between two events, to eliminate the effect of the intrinsic astrocytic calcium signal on the next epoch, we excluded the epoch immediately following the concurrent event and the epoch with the intrinsic astrocytic calcium spike detected at the inter-stimulation period. Event-relevant fMRI analysis was performed based on the two astrocytic calcium events. The HRF was estimated by the linear regression with TENT basis function(2).

$$T(x) = \begin{cases} 1-|x|, & for -1 < x < 1 \\ 0, & for\ |x| > 1 \end{cases}$$

The tent function is also called “piecewise linear spline”, which is used for deconvolution of the HRF response with magnitude estimated as beta coefficient.

$$H(t) = \sum_{k=0}^{n} \beta_k * T(\frac{t-k*L}{L}) \qquad \text{Or,}$$

$H(t)=\beta_0*T(t/L)+\beta_1*T((t-L)/L)+ \beta_2*T((t-2*L)/L)+\ldots+ \beta_k*T((t-k*L)/L)$

Here, H(t) is the HRF response, k is the total number of tent parametric fitting. β_k is response (tent height) at time t = k·L after stimulation; L: tent radius(L can be equal to TR). The beta value (β) was calculated to estimate the amplitude of fMRI response at each TR (L=TR). The beta values were calculated to estimate the amplitude of BOLD response at each TR. The time-lapsed voxel-wise beta map was presented to illustrate the spatial pattern of the fMRI response at different time points after the stimulus onset (Figs. 3*F* and 5*C*), as well as in videos (Movie S1). To illustrate the localization of BOLD signal activation of concurrent astrocytic calcium, the activation maps at 1.5 s after stimulation were overlaid onto corresponding anatomical images with the rat brain atlas (Figs. 5*C* and S10). The time courses of BOLD signal were extracted from region of interest (ROI), e.g. FP-S1, BC, entire cortex or central thalamus, which were segmented on the anatomical images base on the brain atlas (Paxinos and Watson, 2007).

Fiber optic calcium signals were low-pass filtered (at 20 Hz for neuronal calcium, at 3 Hz for Astrocytic calcium) by zero-phase shift digital filtering. Relative percentage change of fluorescence (Δ*F/F*) was defined as $(F-F_0)/F_0$, where F_0 is the baseline fluorescent signal. The amplitudes of the evoked neuronal fluorescent signal in response to each stimulus were calculated as the maximum difference in Δ*F/F* in a time window 300 ms after stimulus and the baseline is the average of signal in a 30-ms pre-stimulation window. The amplitudes of the astrocytic fluorescence signal in response to 4 s FP electric stimulus were calculated as the maximum difference in Δ*F/F* in a time window 8 s after stimulation and the baseline was the average of signal in a 2 s pre-stimulation window.

Multi-taper spectral methods were employed in calculating the spectrogram of LFP and calcium signals (1s sliding window with 0.1s steps, 9 tapers). The target spectral resolution was 0.6 Hz. The mean power spectral density was calculated from theta (4-8 Hz), alpha (8-13 Hz), and beta (13-30 Hz), respectively. To calculate the delta power in Fig 6C, the mean power spectral density was measured from 4 s windows in 0.1 s steps. The target spectral resolution was 0.15 Hz.

To compare the temporal features among the evoked BOLD and calcium spikes, as well as the intrinsic astrocytic calcium transients and correlated LFP power and resting-state fMRI signals, a two-gamma-variate fitting process was used to estimate the onset time and the full-width-of-half-maximum (FWHM) (6-8).

$$f(x) = a*(\frac{x}{p*q})^p * e^{(p-\frac{x}{q})} - b*(\frac{x}{r*s})^r * e^{(r-\frac{x}{s})}$$

(*x* is the variable; a, p, q, b, r, s are the coefficients for two-gamma-variate-function)

The onset time (T_0) was estimated as an intercept with the baseline by fitting a line to the rising slope between 20% and 80% of the peak amplitude estimated from the two-gamma-variate function (9). Alternatively, due to the difference of SNR from multi-modal signals, the signal onset estimated as the earliest time point reached 2 standard deviation of baseline was not implemented in this study (8). Also noteworthy is that the high baseline level of the optical signal recorded from

long fiber optic (8 m) vs. short fiber optic (2 m) could contribute to the difference of the onset time and the FWHM (Fig. S17).

To rule out the potential concerns of the artifacts from the hemoglobin-based intrinsic optical signal detected by fiber optic recording (10, 11), we have introduced the hyperinflation breath (HB) scheme during the calcium recordings. The hyperinflation scheme is similar to the breath holding experiments of human fMRI studies, which show strong activity-independent global BOLD signal due to hemodynamic changes(12). Fig. S18 shows no neuronal and astrocytic calcium signal changes upon the hyperinflation events delivered through the ventilator followed by blood pressure changes. Together with the distinct temporal features of the evoked neuronal and astrocytic calcium signal and BOLD fMRI signal, this control study demonstrates the hemoglobin-independent fiber optic calcium detection system, which is consistent with the previously reported calcium recording studies using fiber optometry (13, 14). In addition, the end-tidal CO_2 signal was acquired simultaneously with astrocytic calcium signals. Since we need to set up long tubing to supply air to the animals inside the MRI scanner, the end-tidal CO_2 level from the exhaled air was detected with a delay around ~22 s and no breath-dependent oscillatory readings were shown in the end-tidal trace. Figure S19 shows the recorded physiological and astrocytic calcium signals in two different conditions. Upon a manually controlled hyperinflation breath through ventilator (red arrow in Figure S19A), both blood pressure and the end-tidal CO_2 level were changed accordingly, but no astrocytic calcium signal was detected. This result indicates that the blood flow and end-tidal signal changes do not directly contribute to the astrocytic calcium signal. Secondly, we also monitored the blood pressure and end-tidal CO_2 during the forepaw electrical stimulation. As shown in the astrocytic calcium trace, both evoked only and concurrent (evoked+intrinsic) events were recorded in the stimulation on/off paradigm, but no corresponding changes were observed in blood pressure and end-tidal CO_2 traces. These results indicate that the cardiovascular or respiratory fluctuation do not cause the astrocytic calcium signal, as well as the BOLD fMRI signal detected in the brain.

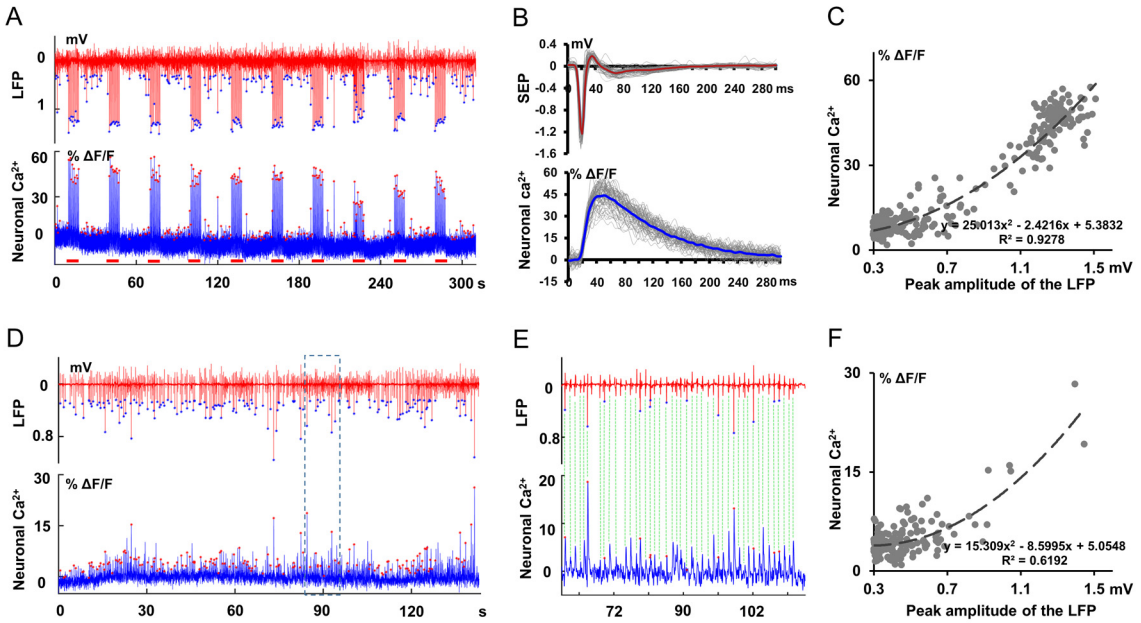

Fig. S1. Simultaneous neuronal Ca^{2+} and LFP recordings. (*A*) The representative trace of LFP (red line) and GCaMP-mediated Ca^{2+} signal in neurons (blue line) with forepaw stimulation (blue dots marks the negative peaks of the LFP burst spikes (<0.3mV); red dots mark the corresponding neuronal Ca^{2+} spike, red bars show the duration of FP stimulation). (*B*) The mean evoked LFP (red) and neuronal Ca^{2+} spikes (blue) in (*A*) (gray lines are individual trials). (*C*) The scatter plot of the LFP amplitudes vs. the corresponding neuronal Ca^{2+} spike amplitude (dashed line, the non-linear fitting). (*D*) Spontaneous LFP (red) and GCaMP-mediated Ca^{2+} signal transients in neurons (blue line). (*E*) Enlarged image in the dashed box in (*D*). (*F*) The scatter plot of the amplitude of spontaneous LFP burst spikes vs. the corresponding neuronal Ca^{2+} transients.

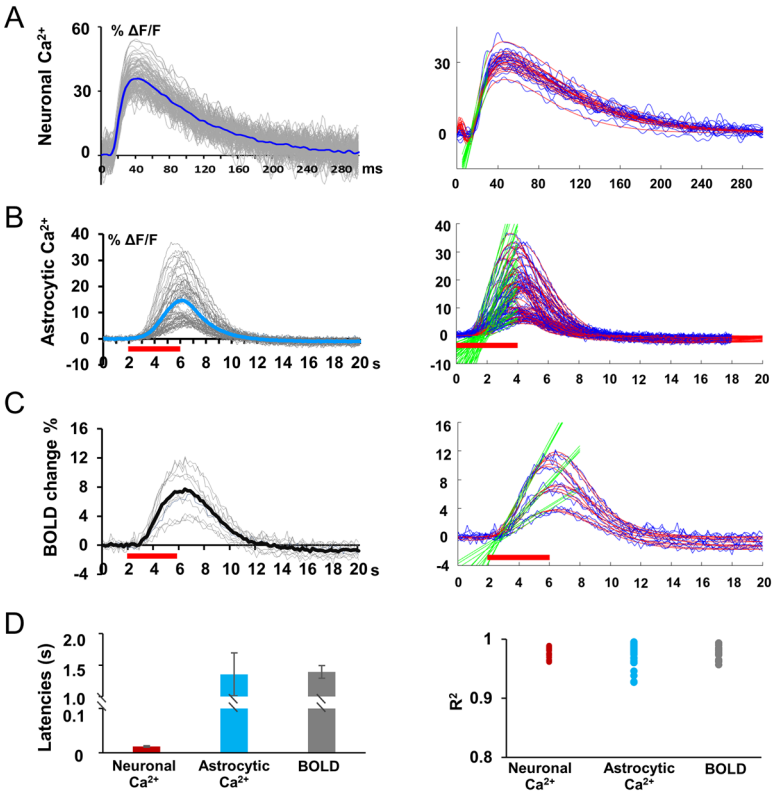

Fig. S2. The estimated latency of sensory evoked GCaMP-mediated Ca^{2+} signal and BOLD signal with two-gamma-variate fitting. The onset time (T_0) was measured as an intercept with the baseline by fitting a line to the rising slope between 20% and 80% of the peak amplitude estimated from the gamma variate function. (*A*) Representative data of the evoked GCaMP-mediated Ca^{2+} signal from neurons following individual stimulation pulses (pulse duration, 330 us, 3 Hz, 1mA; total trial #=72). Right panel is the fitting line (red) of the averaged evoked Ca^{2+} signal spikes (n_{runs}=18, from 4 rats). (*B*) Representative data of the evoked GCaMP-mediated Ca^{2+} signal from astrocytes following the forepaw stimulation train (4 s on, 1.0 mA, 3 Hz; trial#=63 from 6 rats). Red bars show the duration of forepaw stimulation. Right panel is the fitting line (red) of each evoked astrocytic Ca^{2+} spikes. (*C*) Representative data of the evoked BOLD signal from FP-S1 following the forepaw stimulation train (4 s on, 1.0 mA, 3 Hz; n_{runs}=14 from 6 rats). Red bars show the duration of forepaw stimulation. Right panel is the fitting line (red) of the averaged evoked BOLD signal. (*D*) The mean onset latency of the sensory evoked Ca^{2+} in neurons / astrocytes and the BOLD signal (left). Right panel is the R-squared values to show the goodness of fitting for each category.

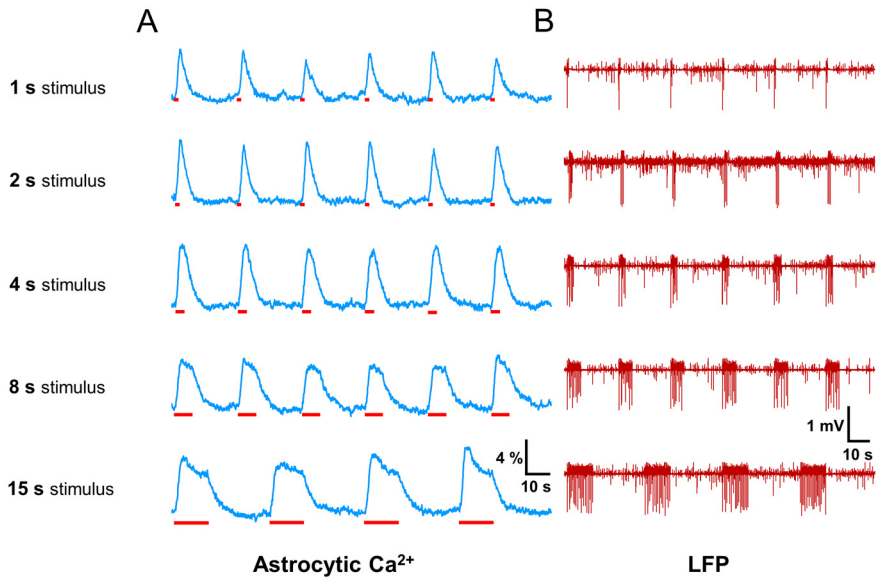

Fig. S3. The stimulation-duration dependency of simultaneous astrocytic Ca^{2+} and LFP signals. (*A*) The representative data of the GCaMP-mediated astrocytic Ca^{2+} signal at varied durations from 1 s to 15 s on/off block design with forepaw electrical stimulation (1.0 mA, 3 Hz, pulse duration, 300 μs). Red bars show the duration of forepaw stimulation (1-8 s duration with 30 s each epoch; 15 s duration with 45 s each epoch. (*B*) The simultaneous LFP signal detected with the astrocytic Ca^{2+} signal at different stimulation duration periods, showing the individual LFP spikes upon electrical stimulation pulses (3 Hz, 1-15 s stimulation on period).

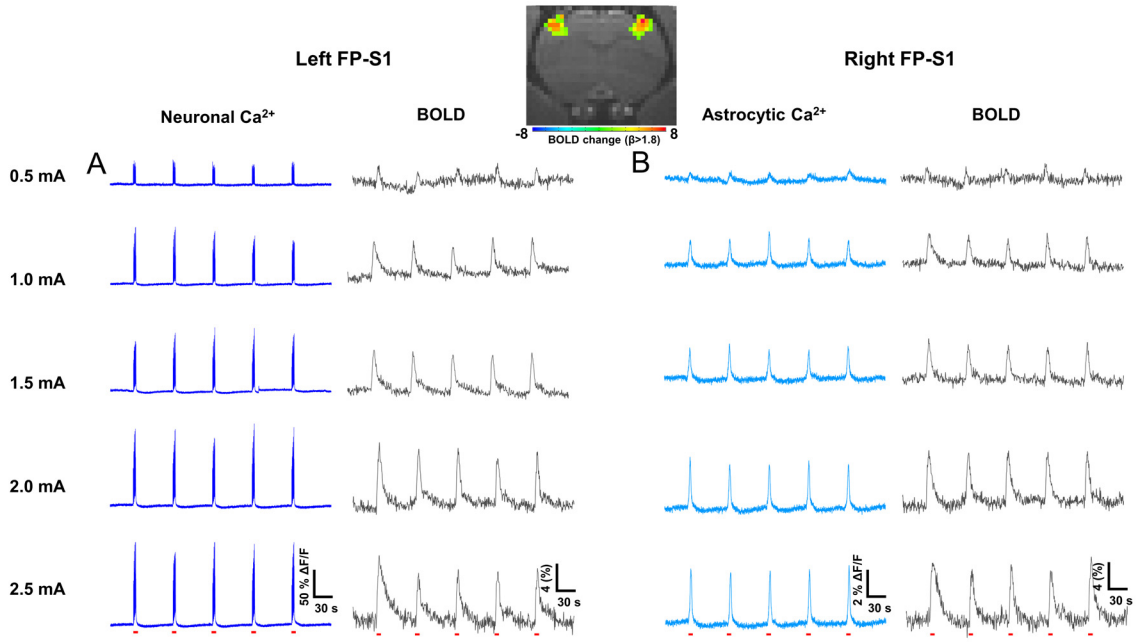

Fig. S4. The stimulation-intensity dependency of simultaneous Ca^{2+} and BOLD fMRI signals. GCaMP6f was expressed in neurons of FP-S1 of the left hemisphere and in astrocytes of FP-S1 of the right hemisphere of a representative rat. The forepaw electrical stimulation was delivered bilaterally with varied intensities (0.5, 1.0, 1.5, 2.0, 2.5 mA, 3 Hz, 4 s). (*A*) The representative traces of simultaneously recorded neuronal Ca^{2+} (left panel) and BOLD fMRI signal (right panel) from the left FP-S1 with 5 epochs, showing the amplitudes of both neuronal Ca^{2+} and BOLD signal increased as the function of the stimulation intensity. (*B*) The representative traces of simultaneously recorded astrocytic Ca^{2+} (left panel) and BOLD fMRI signal (right panel) from right FP-S1 with 5 epochs, showing the amplitudes of both astrocytic Ca^{2+} and BOLD signal increased as the function of the stimulation intensity (red bar, forepaw stimulation 4 s, 3 Hz).

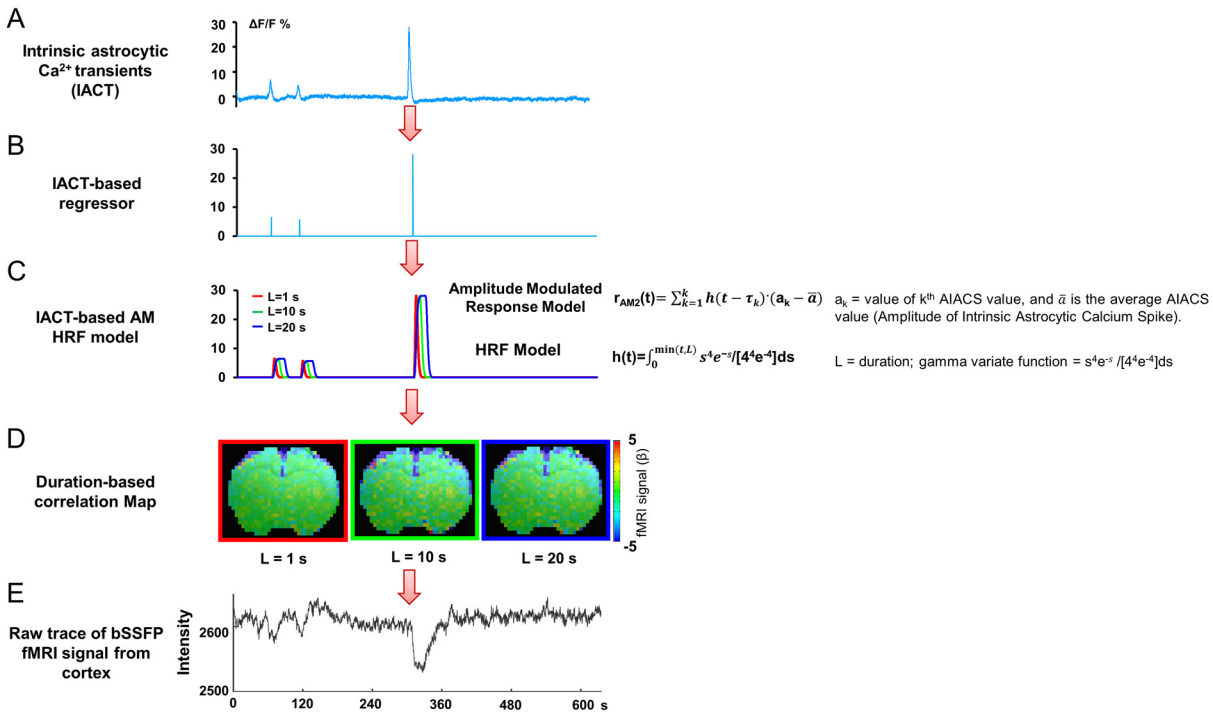

Fig. S5. The flow diagram to calculate the intrinsic astrocytic Ca^{2+} signal-based resting-state fMRI correlation map. (*A*) The astrocytic Ca^{2+} signal and bSSFP-fMRI signals were acquired simultaneously during the resting state. A representative time course of astrocytic Ca^{2+} signal was shown with intrinsic astrocytic Ca^{2+} transients (IACT). (*B*) The peak timing and amplitudes of the IACT were used to create the regressor for the resting-state fMRI correlation. (*C*) The amplitude modulated BOLD response models were generated base on the IACT-based regressor with varied duration (L, 1 s, 10 s, 20 s). The ideal functions (HRF models) of the representative time course of astrocytic Ca^{2+} signal were shown (L=1 s, red; L=10 s, green; L=20 s, blue). (*D*) The voxel-wise correlation maps of the resting-state bSSFP-fMRI signal with the simultaneously acquired astrocytic Ca^{2+} signal at varied HRF models. The duration (L=10 s) provides the optimal correlation map. (*E*) The representative time course of the bSSFP-fMRI signal from the entire cortex shows the negative fMRI signal correlated to the occurrence of the intrinsic astrocytic Ca^{2+} transients.

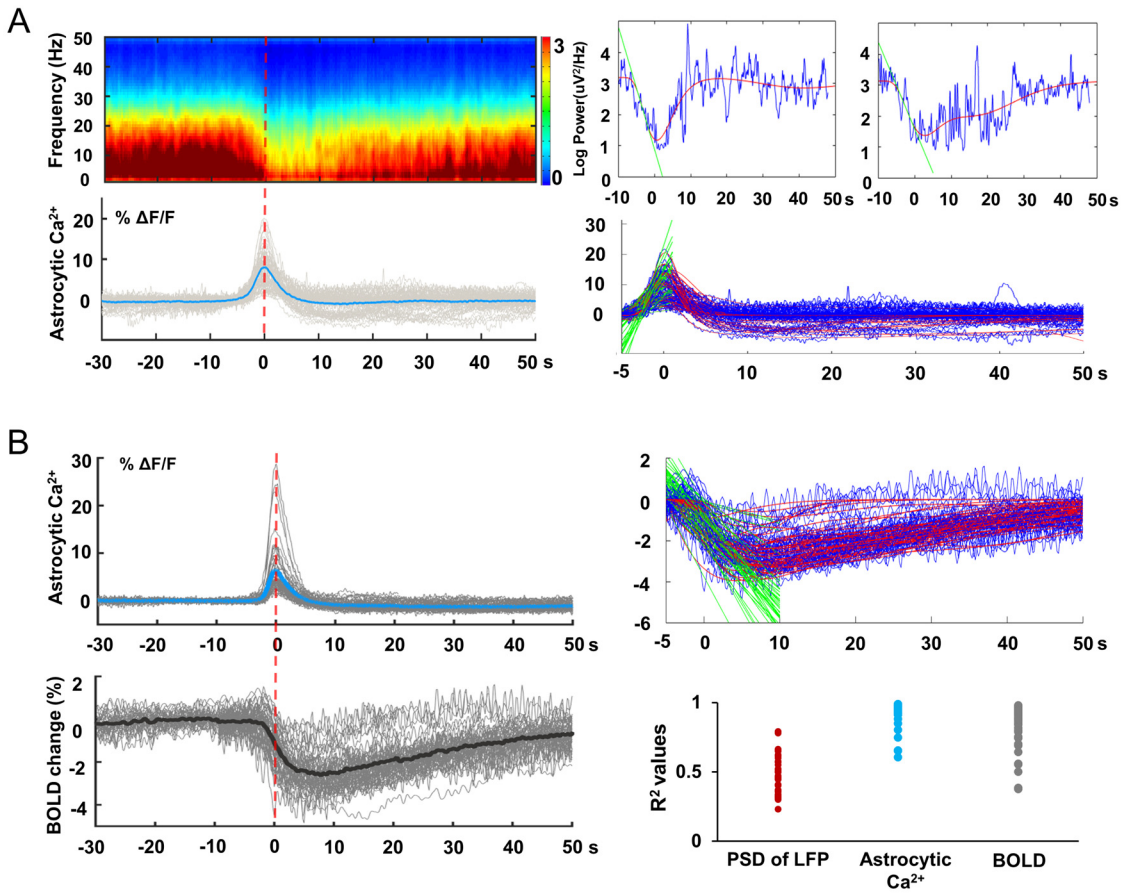

Fig. S6. The onset time estimation of LFP frequency power shift, intrinsic astrocytic Ca^{2+} transients and correlated cortical BOLD signal decrease with the two-gamma-variate fitting. All trials were aligned by the peak time of the intrinsic astrocytic calcium transients (red dashed line), which was set time zero. (*A*) Simultaneous LFP and fiber optic recording of the intrinsic astrocytic Ca^{2+} transients in FP-S1 (top panel, the averaged power spectrum density of the LFP, sampled with 500ms window in 250ms steps; lower panel, the intrinsic astrocytic Ca^{2+} transients; trial #=54, gray lines from 6 rats). Right top panel shows the representative traces of mean power profile (<30 Hz, blue) and fitting lines (red). Right bottom panel shows the corresponding traces of the intrinsic astrocytic Ca^{2+} transients and the fitting lines (red). (*B*) Simultaneous fMRI and fiber optic recording of the intrinsic astrocytic Ca^{2+} transients in FP-S1 (top panel, the intrinsic astrocytic Ca^{2+} transients; lower panel, the time course of corresponding cortical BOLD signal, trial #=52, gray lines from 6 rats). Right top panel shows the representative traces of BOLD fMRI signal and fitting lines (red). Right lower panel is R-squared values to show the goodness of fitting for each category.

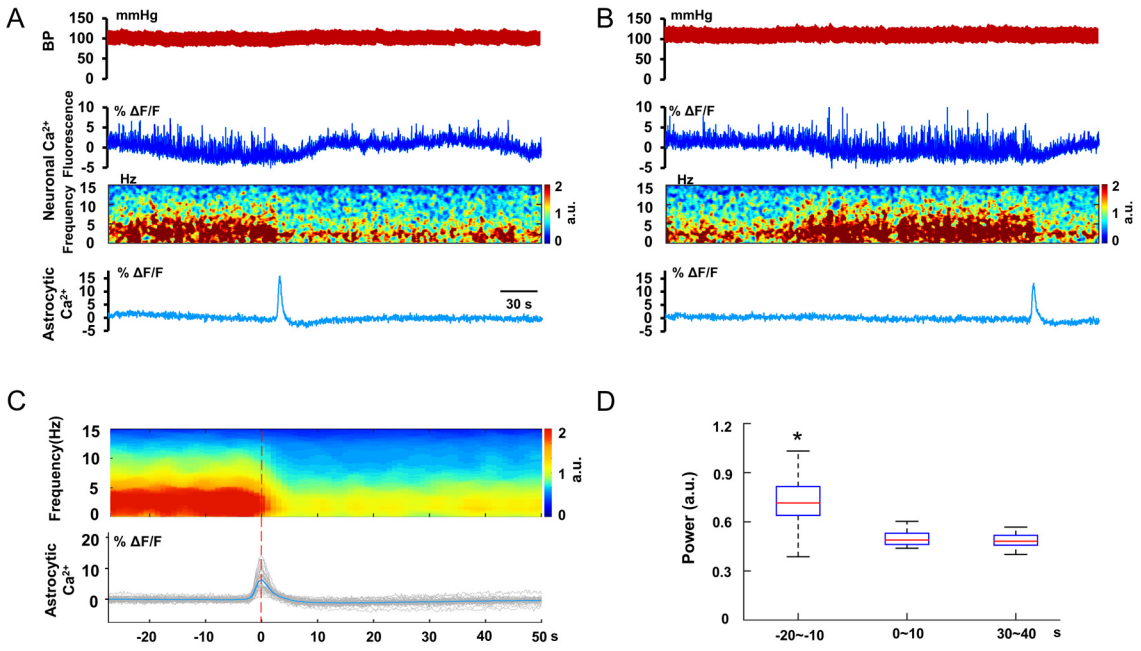

Fig. S7. Astrocytic Ca^{2+} recording with simultaneous neuronal Ca^{2+} and blood pressure monitoring. (*A* and *B*) Representative data shows intrinsic astrocytic Ca^{2+} spike occurred with a coincident depression of spontaneous neuronal Ca^{2+} activity, but not show a detectable change of blood pressure (BP). Blood pressure (red), neuronal Ca^{2+} (blue) in left FP-S1 and astrocytic Ca^{2+} (light blue) in right FP-S1 were recorded simultaneously. (*C*) Average spectrogram of the neuronal Ca^{2+} is aligned based on the simultaneously acquired peak time of the intrinsic astrocytic Ca^{2+} spikes (red dashed line as time zero). (*D*) The integrated neuronal Ca^{2+} power spectral density (0~15 Hz) at different phases according to the intrinsic astrocytic Ca^{2+} spikes (time zero at the peak time of the astrocytic Ca^{2+} spikes; one-way ANOVA followed by Tukey's multiple comparison test F = 66.13; * means p = 3.8E-19, 35 traces of 5rats).

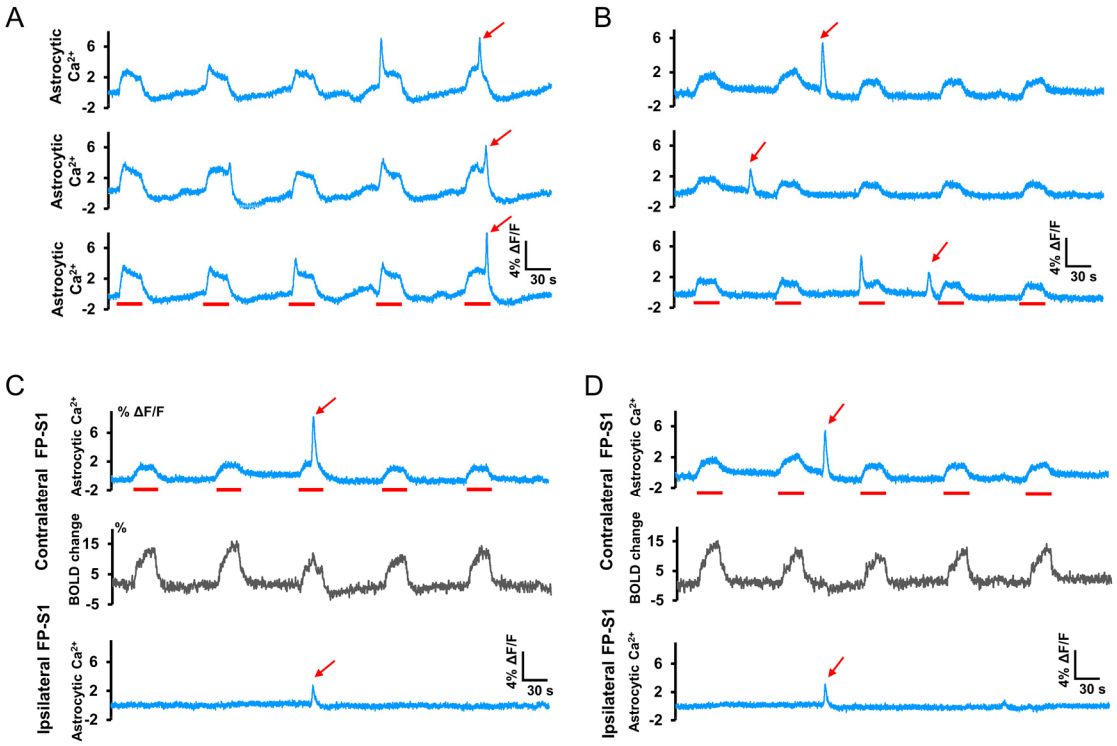

Fig. S8. Intrinsic astrocytic Ca^{2+} transients detected at different phases of the stimulation on/off block design period. (*A*) Three representative traces of the astrocytic Ca^{2+} signal show the intrinsic astrocytic Ca^{2+} transients appeared in the middle (trial 1) or later (trial 2 and 3) phases of the 30 s stimulation on period (red arrows). (*B*) Three representative traces of the astrocytic Ca^{2+} signal show the intrinsic astrocytic Ca^{2+} transients appeared in the stimulation off period (red arrows). (*C* and *D*) The representative trace of bilateral astrocytic Ca^{2+} signals and corresponding BOLD signal (30 s on/off block design paradigm). The intrinsic astrocytic Ca^{2+} transient appeared at the later phase of the 30 s stimulation on period, which was also detected in the ipsilateral FP-S1 to the stimulation side (*C*). The intrinsic astrocytic Ca^{2+} transient appeared at the stimulation off period, which was also detected in the ipsilateral FP-S1 to the stimulation side (*D*).

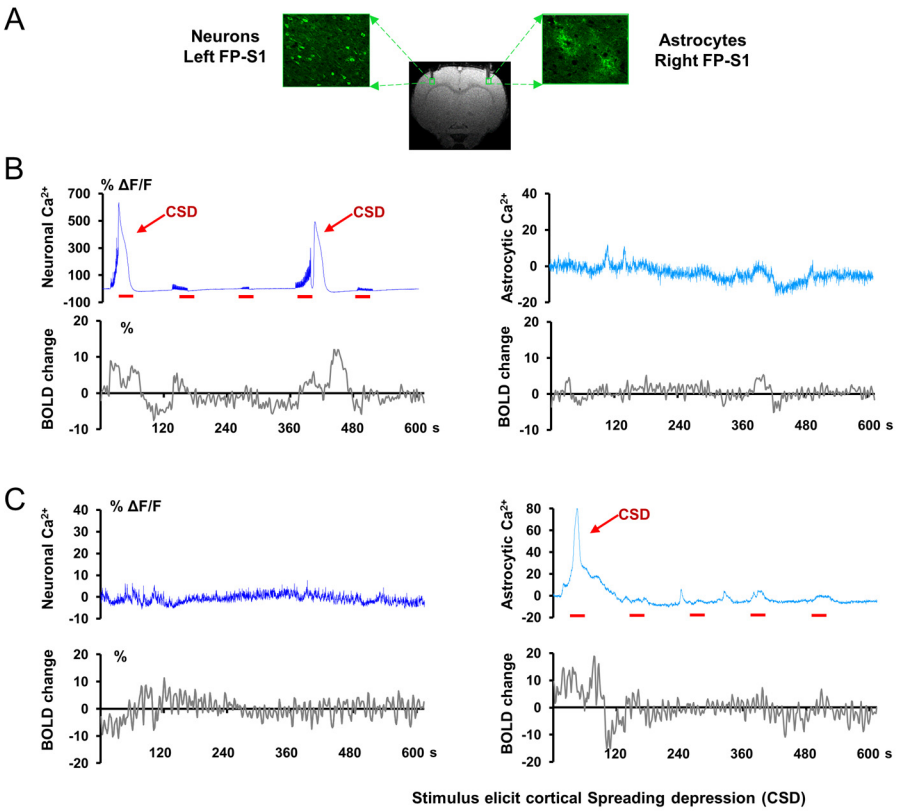

Fig. S9. Simultaneous fMRI with astrocytic Ca^{2+} signal recording during stimulation-induced spreading depression. (*A*) A 2D anatomical MR image shows the trace of inserted fibers in both FP-S1. GCaMP6f were expressed in FP-S1 neurons of the left hemisphere and FP-S1 astrocytes in the right hemisphere. (*B*) The spreading depression was elicited in the left hemisphere with 30 s forepaw electrical stimulation (2 mA, 3 Hz). The representative trace of the evoked neuronal Ca^{2+} signal showed high amplitude (>500%) at epoch 1 and 4 (red arrows), followed with depressed neuronal Ca^{2+} signal and BOLD signal in epoch 2, 3, and 5. In contrast, no astrocytic Ca^{2+} transients were detected in the non-activated FP-S1 of the right hemisphere. (*C*) The spreading depression was elicited in the right hemisphere with 30s electrical stimulation (2 mA, 3 Hz). The representative trace of the evoked astrocytic Ca^{2+} signal showed high amplitude (>80%) at epoch 1 (red arrows) with depressed Ca^{2+} signal and BOLD signal in the following epochs. In contrast, no neuronal Ca^{2+} transients were detected in the non-activated FP-S1 of the left hemisphere.

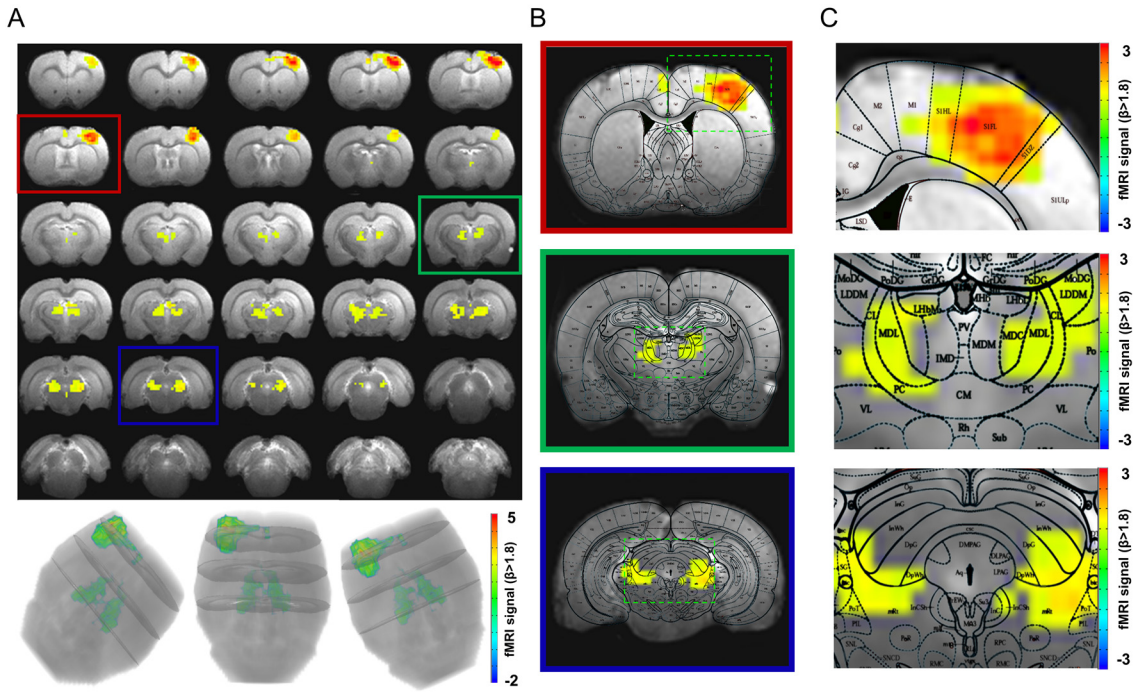

Fig. S10. Subcortical activity patterns upon the evoked intrinsic astrocytic Ca^{2+} spikes. (*A*) The time-lapsed activation maps of the concurrent events (1.5 s after stimulation onset) are overlapped on anatomical MRI images (upper panel). Low panel is the 3D rendering projection views of the activation patterns with colored-coded FP-S1 and subcortical areas. (*B*) The functional maps were overlapped with the three additional anatomical images from Fig 5, which were superimposed with the corresponding rat brain atlas. (*C*) The enlarged images of dashed boxes in (*B*) shows the activated FPI-S1, central thalamic area and the midbrain reticular formation area.

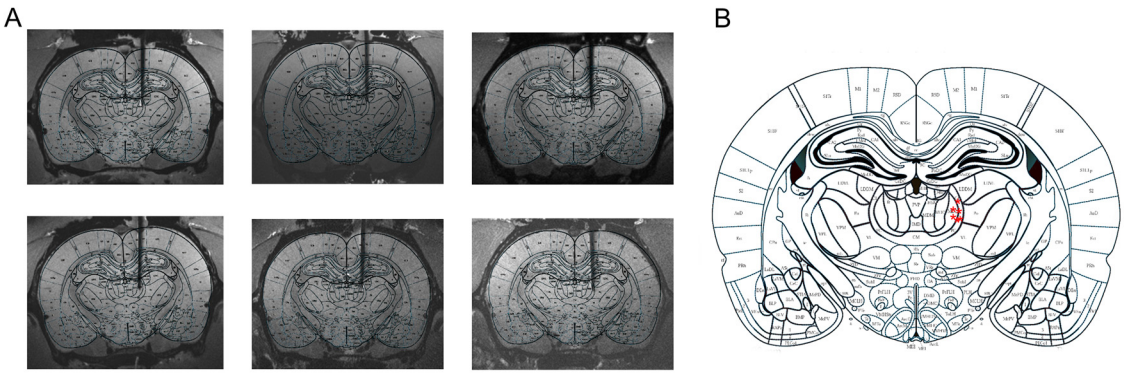

Fig. S11. Localization of the electrode tip in the central lateral thalamic nuclei with MRI. (*A*) The T2-weighted anatomical MRI images superimposed with the rat brain atlas. The electrodes were directly mapped in the MRI images as dark stripes from 6 individual rats. (*B*) The location of the electrodes tips was summarized in the rat brain atlas (red asterisks, n=6).

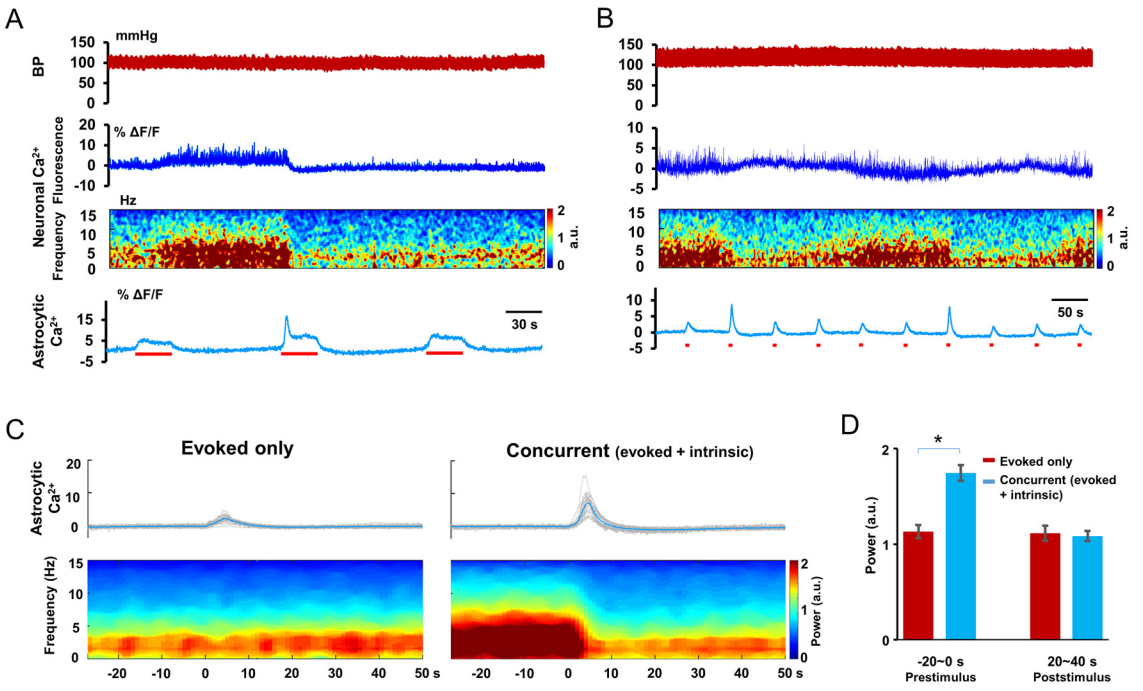

Fig. S12. Sensory evoked intrinsic astrocytic Ca^{2+} spikes was recorded with simultaneous neuronal Ca^{2+} and blood pressure monitoring. (*A* and *B*) Representative data shows left FP electric stimulation (3 Hz, 30 s duration (*A*) or 4 s duration (*B*), 1.0 mA) evoked intrinsic astrocytic Ca^{2+} spike coincide with the depression of spontaneous neuronal Ca^{2+} activity. Blood pressure (red), neuronal Ca^{2+} (blue) in left FP-S1 and astrocytic Ca^{2+} (light blue) in right FP-S1 were recorded simultaneously. Spectrogram is calculated from the neuronal Ca^{2+}. (*C*) Evoked only and concurrent events were separated to show the averaged astrocytic Ca^{2+} signal and neuronal Ca^{2+} power spectrogram (sampled with 5 s window in 1 s steps). (*D*) The integrated spectral power of neuronal Ca^{2+} (evoked only, red; concurrent, blue; trial #=24, rats, n=5) at different phases of the stimulation on/off trials (Prestimulus, -20 to 0 s; Poststimulus 20-40 s; *, p= 2.2E-06, paired t test).

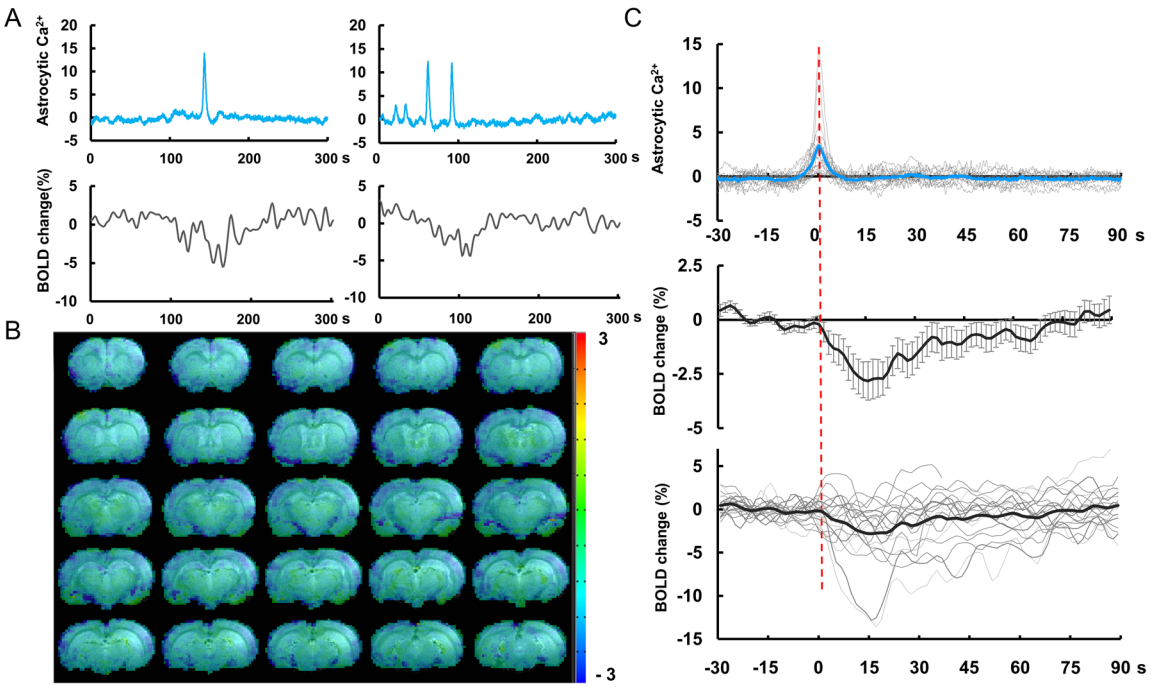

Fig. S13. Intrinsic astrocytic Ca^{2+} spikes negatively correlate with BOLD signals of rats anesthetized with urethane. (*A*) The representative traces of the intrinsic astrocytic Ca^{2+}spikes and simultaneous fMRI signal acquired from the entire cortex. (B) The averaged color-coded negative correlation map from multi-2D MR images. (*C*) The averaged time course (middle panel) of the fMRI signal (bottom panel, individual traces) is aligned based on the simultaneous acquired peak time of the intrinsic astrocytic Ca^{2+} spikes (upper, panel, individual traces, red dashed line as time zero, 15 traces in 5 rats).

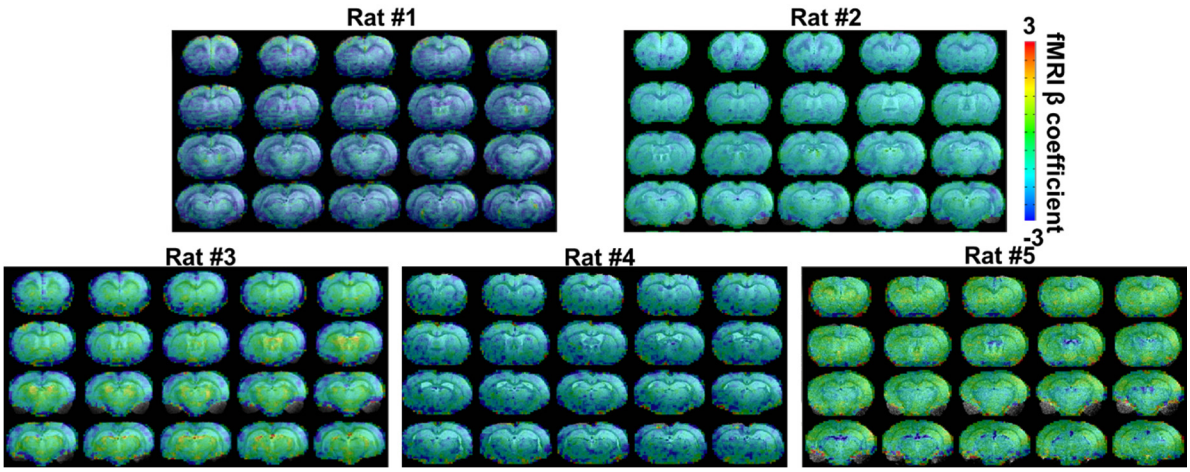

Fig. S14. The negative correlation maps of intrinsic astrocytic calcium spikes with BOLD signals of five rats anesthetized with urethane.

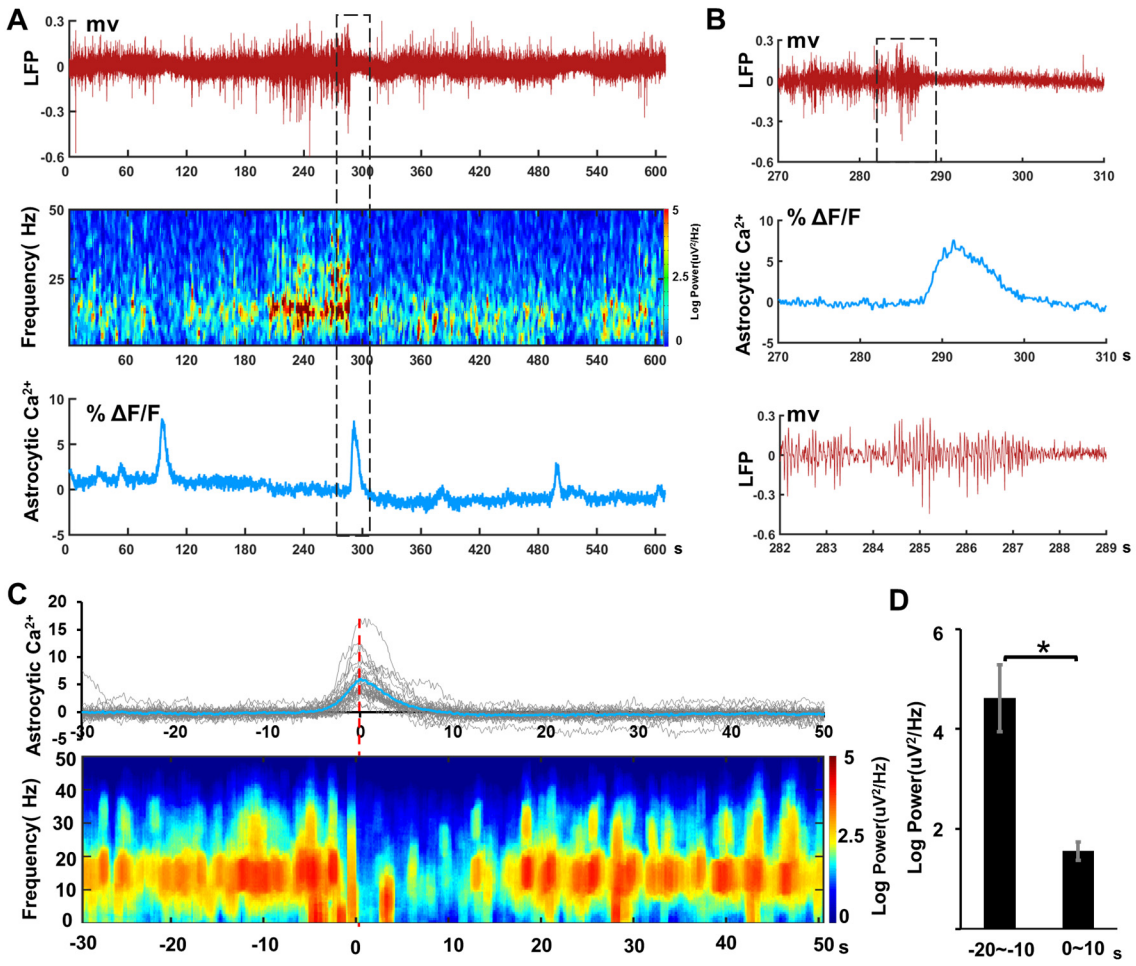

Fig S15. The simultaneous astrocytic calcium recording in rats during sleep. (A) The representative LFP trace (upper panel) and the spectrogram (middle panel) with simultaneously recorded intrinsic astrocytic calcium spikes (lower panel). The negative correlation maps of intrinsic astrocytic calcium spikes with BOLD signals of five rats anesthetized with urethane. (B) The enlarged view to highlight the changes of the EEG states in coincidence with an intrinsic astrocytic calcium spike. (black box: the spindle-like EEG activity pattern, bottom panel) (C) The mean power spectrogram graph of the LFP (bottom panel) is aligned based on the simultaneously acquired peak time (red dashed line as time zero) of the intrinsic astrocytic Ca^{2+} spike (top panel, 32 traces of 3 rats). (**F**) The power spectral density of the LFP (0~30Hz) at different phases before (-20~-10 s) or after (0-10 s) the peak time of the intrinsic astrocytic Ca^{2+} spikes (*, p= 6.3E-5, paired t-test).

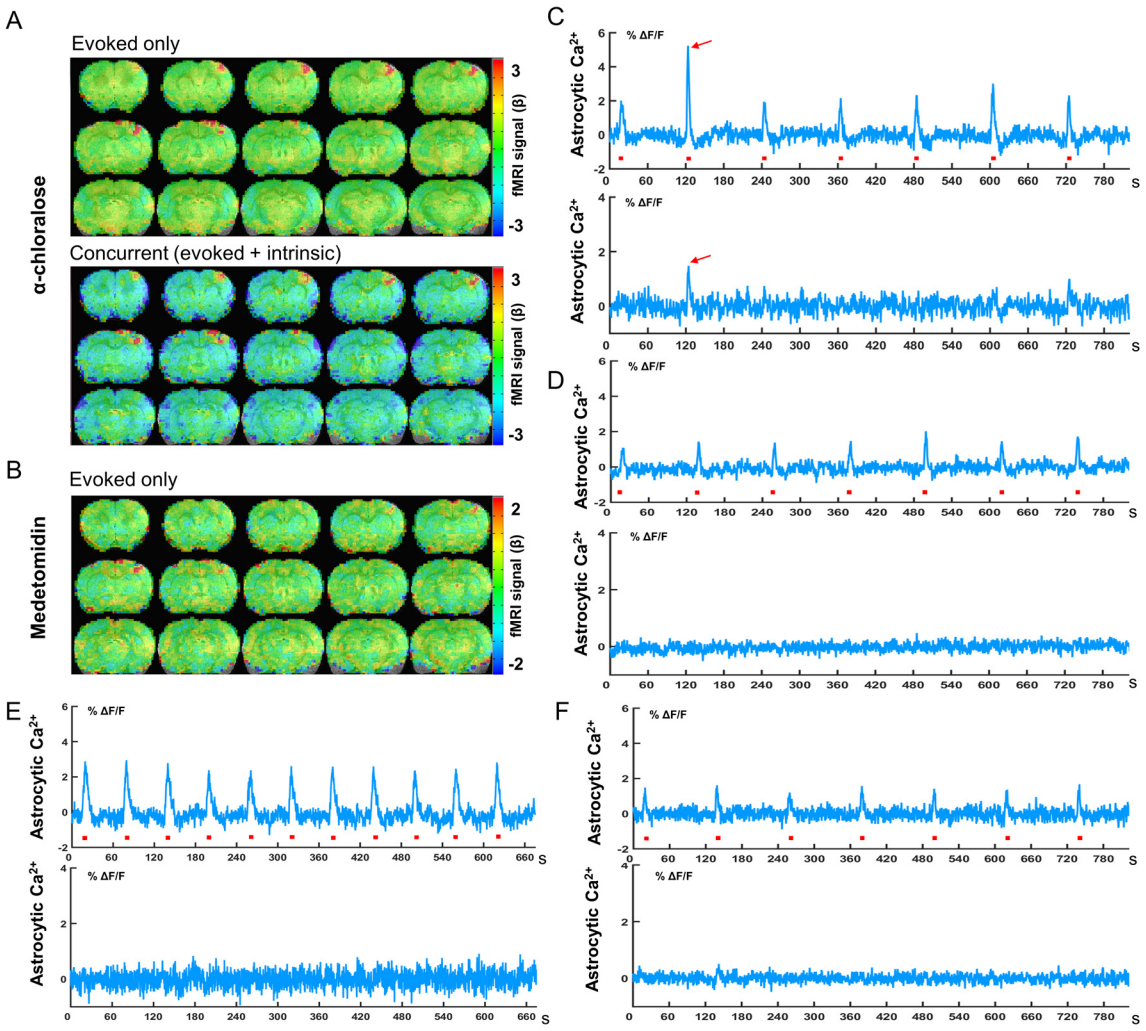

Fig S16. Simultaneous astrocytic calcium recording with BOLD fMRI in rats anesthetized with alpha-chloralose and Domitor. (A) The color-coded BOLD functional maps for evoked only and concurrent astrocytic calcium spiking events upon forepaw electrical stimulation in rats anesthetized with alpha-chloralose (Concurrent event: negative BOLD signals spread in cortex). (B) The color-coded BOLD functional maps in rats anesthetized with Domitor. (C) The representative trace of astrocytic calcium signal in rats anesthetized with alpha-chloralose (upper panel: activated FP-S1, red arrow indicates concurrent event; lower panel: the contralateral FP-S1, red arrows indicates the intrinsic astrocytic calcium spike). (D) The representative trace of astrocytic calcium signal in rats anesthetized with Domitor (upper panel: activated FP-S1, evoked only events; lower panel: the contralateral FP-S1, no intrinsic astrocytic calcium spike). (E/F) The representative traces of astrocytic calcium signal in two other rats anesthetized with Domitor.

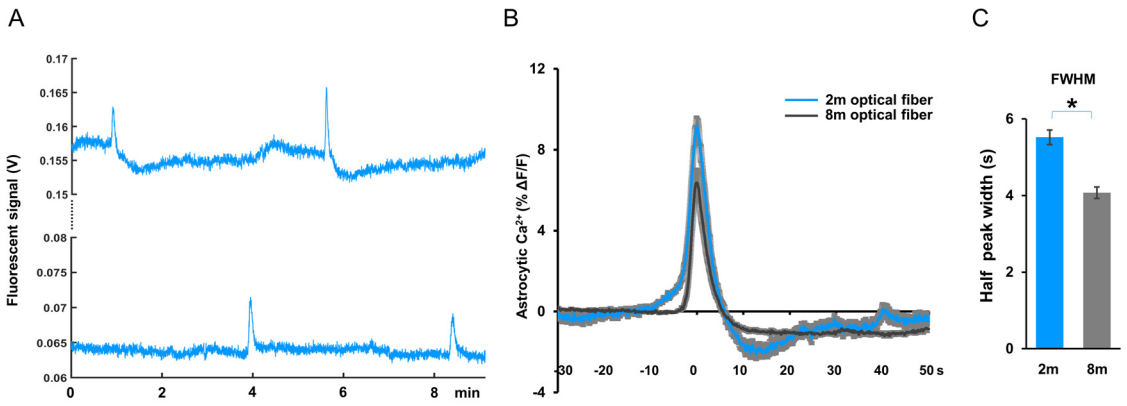

Fig. S17. The comparison of the intrinsic astrocytic ca^{2+} transients recorded by 2 m and 8 m fiber optic. (*A*) The representative traces of the intrinsic astrocytic ca^{2+} transients recorded by 2 m fiber optic (lower, for simultaneous LFP and calcium recording) or 8 m fiber optic (upper, for simultaneous BOLD fMRI and calcium recording). To keep the same output power level form the fiber tips (30 μw out of 200μm fiber tip), the baseline reading of the 2 m fiber optic is much lower than that of the 8 m fiber optic due to the compensation of the laser power and the Raman scattering (15). (*B*) The mean time courses of the intrinsic astrocytic ca^{2+} transients from 2 m (light blue, $\Delta F/F>4\%$; n= 45 from 6 rats for LFP recording) and 8 m (grey, $\Delta F/F>4\%$; n= 40 from 6 rats for BOLD-fMRI) fiber optic. The onset time of intrinsic astrocytic ca^{2+} transient can be better characterized by the 2 m fiber optic. (*C*) The full width at half maximum (FWHM) of the intrinsic astrocytic ca^{2+} transients recoded by 2 m fiber optic is significantly longer than that recorded by 8 m fiber optic(*, p= 6.26E-08, n_{2m}= 45 from 6 rats, n_{8m}= 40 from other 6 rats, two-tailed t-test).

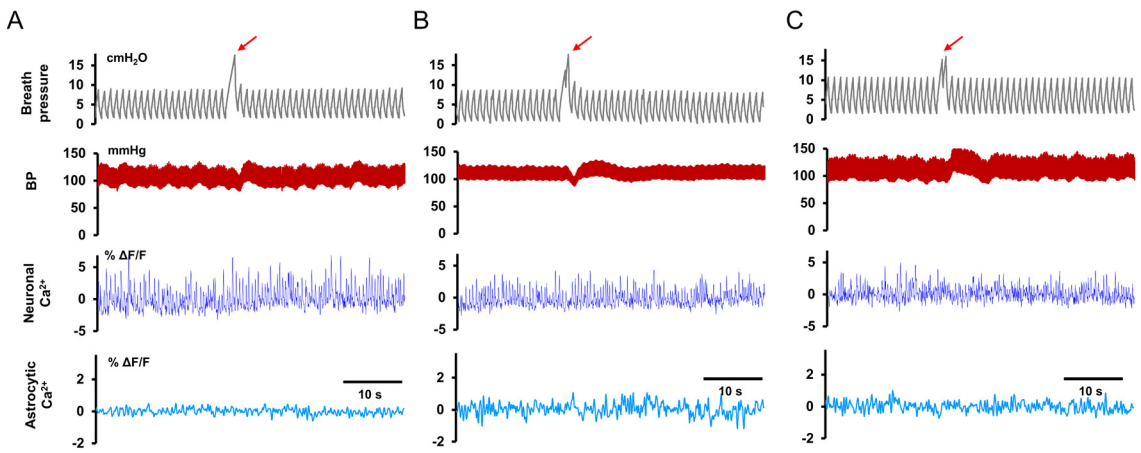

Fig. S18. The artifacts induced by manual hyperinflation breath. (*A*, *B* and *C*) Representative data from 3 rats shows manual hyperinflation breath (red arrows) altered the blood pressure, but not led to a detectable change of GCaMP signal either from neurons or astrocytes. Breath pressure (grey), arterial blood pressure (red), neuronal Ca^{2+} (blue) in left FP-S1 and astrocytic Ca^{2+} (light blue) in right FP-S1 were recorded simultaneously.

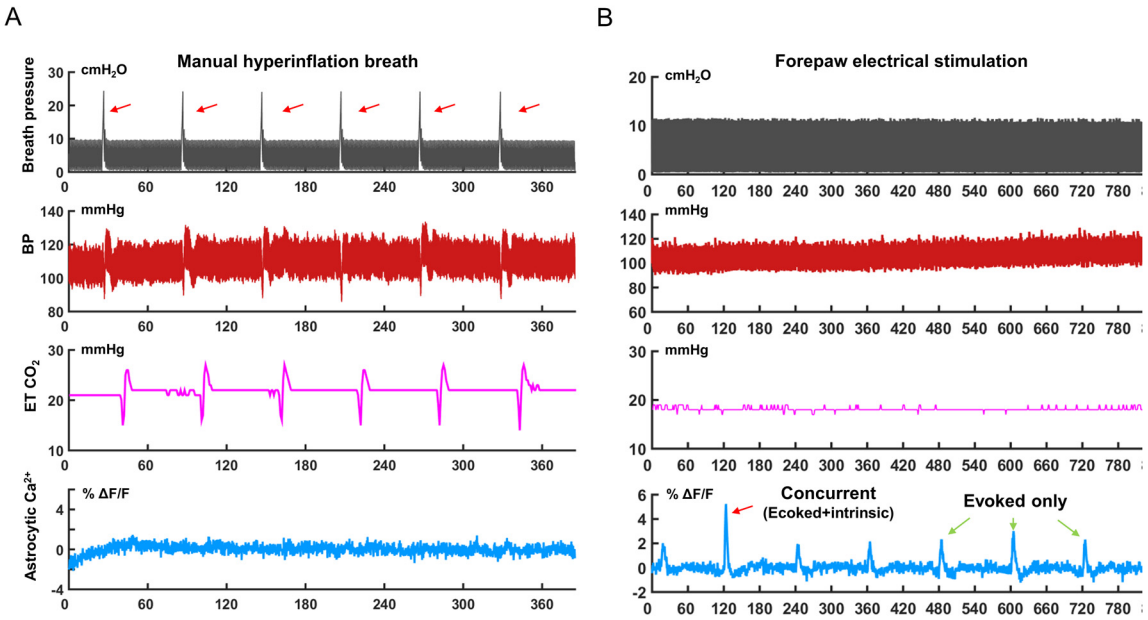

Fig. S19. The simultaneous blood pressure and end-tidal CO_2 monitoring with astrocytic calcium recording and fMRI. (A) The representative traces for breath pressure (ventilated), blood pressure, end-tidal CO_2, and astrocytic calcium signal during manually introduced hyperinflation breath (red arrows). (B) The representative traces for breath pressure (ventilated), blood pressure, end-tidal CO_2, and astrocytic calcium signal in the forepaw electrical stimulation paradigm (red arrow, concurrent event; green arrows, evoked only events).

Table S1. The occurrence rate of the intrinsic astrocytic Ca^{2+} transients

Rat No.	Total runs*	Runs with intrinsic astrocytic Ca^{2+} †	Rate of the runs with intrinsic astrocytic Ca^{2+} (%)
1	18	3	16.67
2	45	14	31.11
3	6	2	11.11
4	17	6	17.14
5	25	8	25.00
6	18	11	48.57
7	19	13	40.63
8	24	11	30.56
9	25	7	25.00
10	31	18	58.06
11	8	3	20.00
12	24	11	27.50
13	24	12	42.86
14	17	13	52.00
15	27	10	22.22
16	28	23	62.16
17	15	7	30.43
18	45	17	37.78
19	24	10	41.67
20	17	6	35.29
21	31	21	67.74
22	29	13	44.83
23	54	28	51.85
24	21	9	42.86
25	20	11	55.00
26	42	31	73.81
27	15	10	66.67
28	33	17	51.52
Total	854	351	41.10±3.20

* Total runs show the number of the run with simultaneous fMRI signal with astrocytic Ca^{2+} recording. Rats without intrinsic astrocytic Ca^{2+} detected are excluded in this table.

† Runs with intrinsic astrocytic Ca^{2+} signal show occasional spontaneous or concurrent Ca^{2+} spikes among the multiple epochs.

Table S2. The list of quantitative means with 95% confidence intervals (CIs)

	Lower CI	Mean	Upper CI	Significance	
Fig 2C (uV^2/Hz)					Paired t-test
Power(-20~-10s)	2031	2164	2315	Non-overlapping CIs	p=9.5E-22
Power(0~10s)	1339	1442	1572		
Power(30~40s)	1775	1908	2055		p=3.6E-11
Fig 2F (s)					One-way ANOVA
PSD of LFP	-5.268	-4.734	-4.240		
Astrocytic Ca^{2+}	-4.582	-4.301	-4.031	Non-overlapping CIs	p=5.1E-12
SSFP BOLD	-2.900	-2.501	-2.096		
Fig 3C (%)					Student's t-test
		Astrocytic Ca^{2+} signal			
Evoked only	5.208	6.096	7.251	Non-overlapping CIs	p=2.0E-15
Concurrent	13.70	15.85	18.12		
		BLOD, FP-S1			
Evoked only	9.696	10.58	11.40		p=0.026
Concurrent	8.340	9.285	10.21		
		BLOD in cortex except FP-S1			
Evoked only	-0.3172	0.02010	0.3539	Non-overlapping CIs	p=2.8E-07
Concurrent	-2.484	-1.986	-1.492		
Fig 4C (s)					Paired t-test
		Latency of astrocytic Ca^{2+} signal			
left FP-S1	2.129	2.291	2.460		p=0.2642
right FP-S1	2.266	2.428	2.598		
Fig 6C					Student's t-test
		PSD in FP-S1			
		Theta-before stimulation			
Evoked only	0.9603	0.9754	0.9887	Non-overlapping CIs	p=1.5E-05
Concurrent	1.012	1.025	1.039		
		Theta-after stimulation			

Evoked only	0.9923	1.012	1.042	Non-overlapping CIs	p=0.012
Concurrent	0.9226	0.9575	0.9875		
Alpha-before stimulation					
Evoked only	0.9462	0.9631	0.9788	Non-overlapping CIs	p=1.3E-07
Concurrent	1.021	1.037	1.054		
Alpha-after stimulation					
Evoked only	0.9792	1.003	1.043	Non-overlapping CIs	p=0.019
Concurrent	0.8991	0.9400	0.9791		
Beta-before stimulation					
Evoked only	0.9643	0.9763	0.9857	Non-overlapping CIs	p=1.6E-07
Concurrent	1.014	1.024	1.036		
PSD in central thalamus					
Theta-before stimulation					
Evoked only	0.9186	0.9449	0.9674	Non-overlapping CIs	p=1.8E-04
Concurrent	1.032	1.055	1.081		
Theta-after stimulation					
Evoked only	0.9551	0.9823	1.005	Non-overlapping CIs	p=2.5E-03
Concurrent	0.8756	0.9082	0.9520		
Alpha-before stimulation					
Evoked only	0.8956	0.9259	0.9514	Non-overlapping CIs	p=3.3E-05
Concurrent	1.049	1.074	1.105		
Alpha-after stimulation					
Evoked only	0.9433	0.9715	1.004	Non-overlapping CIs	p=6.8E-03
Concurrent	0.8545	0.8938	0.9422		
Beta-before stimulation					
Evoked only	0.9230	0.9465	0.9674	Non-overlapping CIs	1.0E-04
Concurrent	1.032	1.054	1.077		
Beta-during stimulation					
Evoked only	0.9747	1.022	1.078	Non-overlapping CIs	2.2E-03
Concurrent	1.103	1.166	1.234		
Beta-after stimulation					
Evoked only	0.9572	0.9827	1.011	Non-overlapping CIs	2.5E-03
Concurrent	0.8878	0.9165	0.9464		

References

1. Shigetomi E*, et al.* (2013) Imaging calcium microdomains within entire astrocyte territories and endfeet with GCaMPs expressed using adeno-associated viruses. *J Gen Physiol* 141(5):633-647.
2. Yu X*, et al.* (2016) Sensory and optogenetically driven single-vessel fMRI. *Nature methods* 13(4):337-340.
3. Ramos-Cabrer P, Weber R, Wiedermann D, & Hoehn M (2005) Continuous noninvasive monitoring of transcutaneous blood gases for a stable and persistent BOLD contrast in fMRI studies in the rat. *NMR in biomedicine* 18(7):440-446.
4. Huttunen JK, Grohn O, & Penttonen M (2008) Coupling between simultaneously recorded BOLD response and neuronal activity in the rat somatosensory cortex. *NeuroImage* 39(2):775-785.
5. Schulz K*, et al.* (2012) Simultaneous BOLD fMRI and fiber-optic calcium recording in rat neocortex. *Nature methods* 9(6):597-602.
6. Cox RW (1996) AFNI: software for analysis and visualization of functional magnetic resonance neuroimages. *Computers and biomedical research, an international journal* 29(3):162-173.
7. Madesen M (1992) A simplified formulation of the gamma variate function. *Phys. Med. Bid.* 37:1597-1600.
8. Yu X, Qian C, Chen DY, Dodd SJ, & Koretsky AP (2014) Deciphering laminar-specific neural inputs with line-scanning fMRI. *Nat Methods* 11(1):55-58.
9. Tian P*, et al.* (2010) Cortical depth-specific microvascular dilation underlies laminar differences in blood oxygenation level-dependent functional MRI signal. *Proceedings of the National Academy of Sciences of the United States of America* 107(34):15246-15251.
10. Grinvald A, Lieke E, Frostig RD, Gilbert CD, & Wiesel TN (1986) Functional architecture of cortex revealed by optical imaging of intrinsic signals. *Nature* 324(6095):361-364.
11. Cohen LB, Keynes RD, & Hille B (1968) Light scattering and birefringence changes during nerve activity. *Nature* 218(5140):438-441.
12. Thomason ME, Burrows BE, Gabrieli JD, & Glover GH (2005) Breath holding reveals differences in fMRI BOLD signal in children and adults. *NeuroImage* 25(3):824-837.
13. Kim CK*, et al.* (2016) Simultaneous fast measurement of circuit dynamics at multiple sites across the mammalian brain. *Nature methods* 13(4):325-328.
14. Adelsberger H, Garaschuk O, & Konnerth A (2005) Cortical calcium waves in resting newborn mice. *Nature neuroscience* 8(8):988-990.
15. Blow KJ & Wood D (1989) Theoretical Description of Transient Stimulated Raman-Scattering in Optical Fibers. *Ieee J Quantum Elect* 25(12):2665-2673.

Movie legends

Movie_S1 - The subcortical fMRI activation patterns underlying the intrinsic astrocytic Ca^{2+} spikes.

Upon the left forepaw electrical stimulation (epochs, 3 Hz, 4 s, 1.5 mA), the time-lapsed fMRI functional maps were analyzed based on the evoked only and concurrent events. Left shows the right FP-S1 activation for the evoked only events. Right shows the positive fMRI signal at both FP-S1 and the subcortical regions at 1.5 s after the stimulation onset, followed by the negative fMRI signal in the entire cortex except right FP-S1, as well as at ventricle areas.

Movie_S2- The 3D projection view of the subcortical fMRI activation patterns in the whole brain contour.

Left is the fMRI activation pattern based on the evoked-only events. Right is the fMRI activation pattern based on the concurrent events, showing the subcortical activation pattern.

A.2 Ultra-slow single-vessel BOLD and CBV-based fMRI spatiotemporal dynamics and their correlation with neuronal Intracellular calcium signals

Ultra-slow single-vessel BOLD and CBV-based fMRI spatiotemporal dynamics and their correlation with neuronal Intracellular calcium signals

Article

Neuron

Ultra-Slow Single-Vessel BOLD and CBV-Based fMRI Spatiotemporal Dynamics and Their Correlation with Neuronal Intracellular Calcium Signals

Graphical Abstract

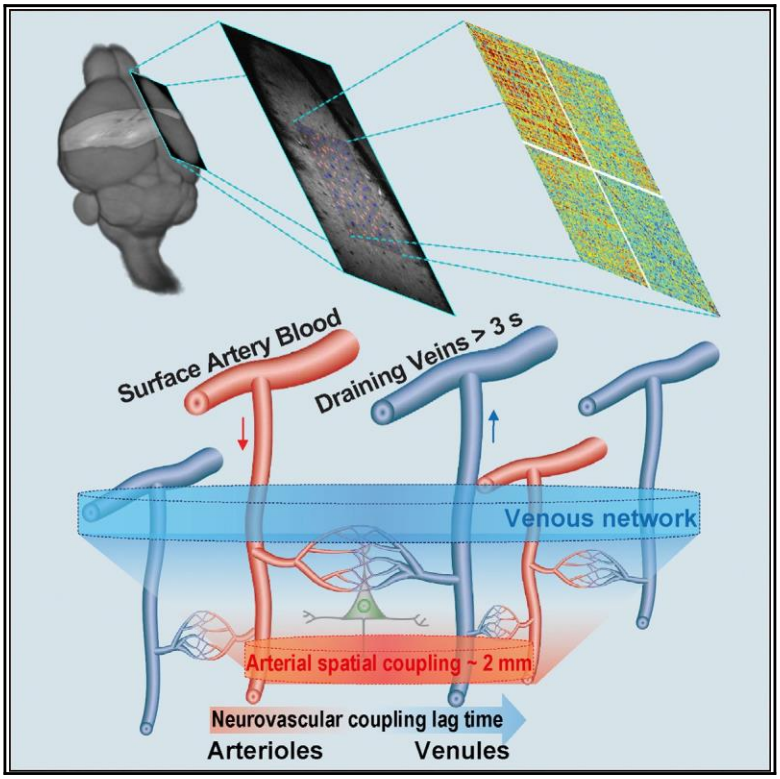

Authors

Yi He, Maosen Wang, Xuming Chen, ..., Bruce R. Rosen, David Kleinfeld, Xin Yu

Correspondence

xin.yu@tuebingen.mpg.de

In Brief

He et al. performed single-vessel fMRI in rat to map spatiotemporal correlations of ultra-slow arteriole CBV and venule BOLD fluctuations, concurrent with intracellular-calcium photometry. They find a 2 mm correlation length, which bears on the resolution of functional connectivity.

Highlights

- bSSFP-based single-vessel fMRI reveals dynamic vascular network connectivity
- Arterioles and venules showed distinct patterns of spatiotemporal correlations
- Neural Ca^{2+} ultra-slow oscillations correlate to vessel-specific fMRI fluctuations
- Human brain fMRI signal fluctuations were mapped in individual gray matter veins

He et al., 2018, Neuron 97, 1–15
February 21, 2018
https://doi.org/10.1016/j.neuron.2018.01.025

CellPress

Please cite this article in press as: He et al., Ultra-Slow Single-Vessel BOLD and CBV-Based fMRI Spatiotemporal Dynamics and Their Correlation with Neuronal Intracellular Calcium Signals, Neuron (2018), https://doi.org/10.1016/j.neuron.2018.01.025

Ultra-Slow Single-Vessel BOLD and CBV-Based fMRI Spatiotemporal Dynamics and Their Correlation with Neuronal Intracellular Calcium Signals

Yi He,[1,2] Maosen Wang,[1,2] Xuming Chen,[1,2] Rolf Pohmann,[1] Jonathan R. Polimeni,[3] Klaus Scheffler,[1,6] Bruce R. Rosen,[3] David Kleinfeld,[4,5] and Xin Yu[1,7,*]

[1]High-Field Magnetic Resonance Department, Max Planck Institute for Biological Cybernetics, 72076 Tuebingen, Germany
[2]Graduate Training Centre of Neuroscience, International Max Planck Research School, University of Tuebingen, 72074 Tuebingen, Germany
[3]MGH/MIT/HMS Athinoula A. Martinos Center for Biomedical Imaging, Department of Radiology, Harvard Medical School, Massachusetts General Hospital, Charlestown, MA 02114, USA
[4]Department of Physics
[5]Section of Neurobiology
University of California at San Diego, La Jolla, CA 92093, USA
[6]Department of Biomedical Magnetic Resonance, University of Tübingen, 72076 Tübingen, Germany
[7]Lead Contact
*Correspondence: xin.yu@tuebingen.mpg.de
https://doi.org/10.1016/j.neuron.2018.01.025

SUMMARY

Functional MRI has been used to map brain activity and functional connectivity based on the strength and temporal coherence of neurovascular-coupled hemodynamic signals. Here, single-vessel fMRI reveals vessel-specific correlation patterns in both rodents and humans. In anesthetized rats, fluctuations in the vessel-specific fMRI signal are correlated with the intracellular calcium signal measured in neighboring neurons. Further, the blood-oxygen-level-dependent (BOLD) signal from individual venules and the cerebral-blood-volume signal from individual arterioles show correlations at ultra-slow (<0.1 Hz), anesthetic-modulated rhythms. These data support a model that links neuronal activity to intrinsic oscillations in the cerebral vasculature, with a spatial correlation length of rv2 mm for arterioles. In complementary data from awake human subjects, the BOLD signal is spatially correlated among sulcus veins and specified intracortical veins of the visual cortex at similar ultra-slow rhythms. These data support the use of fMRI to resolve functional connectivity at the level of single vessels.

INTRODUCTION

The cerebral vasculature is an interconnected network that supplies metabolites to the brain and mediates chemical signaling between the brain and the body. Cerebral circulation is mediated by an electrogenic vascular system, composed of interconnected endothelial cells that transmit signals between neighboring vessels to control the tone of arteriole smooth muscle (Aydin et al., 1991; Longden et al., 2017) in addition to forming the lumen of the vessels. The vascular system exhibits a number of rhythms of neurological and vascular origin (Obrig et al., 2000; Tak et al., 2015; Zhu et al., 2015). Respiratory- and cardiac-based rhythmic components can be regressed out of the fMRI data. Yet an ultra-low frequency (0.1 Hz) fluctuation in the diameter of arterioles, known as vasomotion (Intaglietta, 1990), remain. Far from a confounding factor (Murphy et al., 2013), these fluctuations form the basis of resting-state fMRI (Biswal et al., 1995; Fox and Raichle, 2007). Critically, vasomotion has been shown to be entrained by similarly ultra-slow oscillations in neuronal signaling (Mateo et al., 2017). It has been hypothesized that these covaried vasomotion and oscillatory neuronal patterns may contribute to the physiological basis of the resting-state fMRI connectivity mapping. This would provide the underpinning to observations of concurrent ultra-slow neuronal and hemodynamic signals, acquired optically (Schulz et al., 2012; Du et al., 2014; Ma et al., 2016) and electrophysiologically (Shmuel and Leopold, 2008; Schölvinck et al., 2010).

It is an open challenge to merge the optically acquired neuronal and vessel-specific hemodynamic signaling events with fMRI recordings to directly interpret the vascular basis of the resting-state fMRI signal (Logothetis et al., 2001). In most past work, the resting-state fMRI signal is acquired from large brain voxels (He et al., 2008; Shmuel and Leopold, 2008; Schölvinck et al., 2010). However, more recently high-resolution fMRI has allowed us to map vessel-specific hemodynamic signal from distinct vessel-dominated versus parenchyma-dominated voxels enriched with capillaries in animal brains with either cerebral blood volume (CBV) fMRI or blood-oxygen-level-dependent BOLD (fMRI) (Yu et al., 2012; Moon et al., 2013; Poplawsky et al., 2017). Using line-scanning fMRI methods, the iron oxide particle-based CBV-weighted signal is localized at penetrating arterioles (Yu et al., 2016), while the BOLD signal is detected at penetrating venules (Mansfield et al., 1976; Silva and Koretsky, 2002; Yu et al., 2012, 2014). Thus, the high-resolution fMRI will

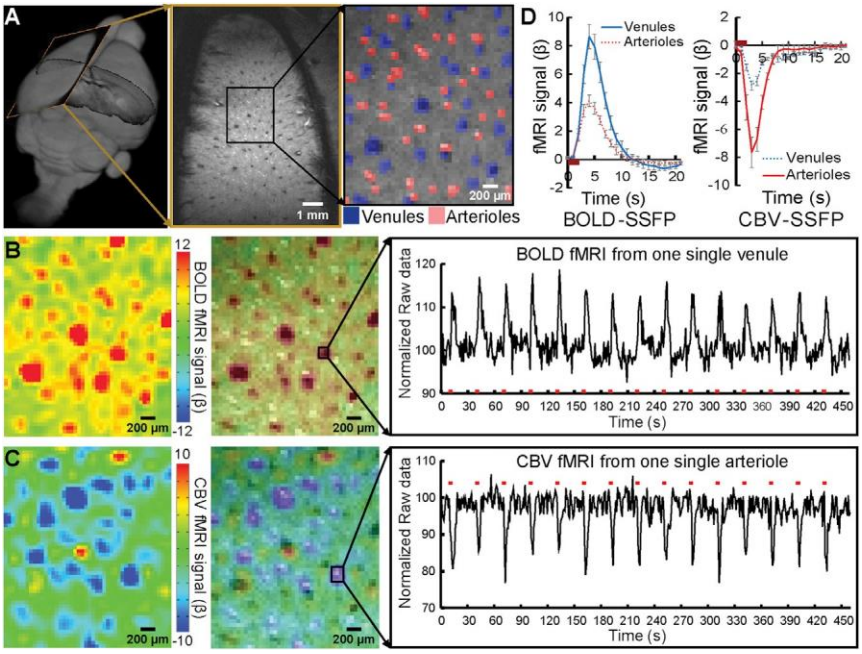

Figure 1. Balanced Steady-State Free Precession-Based Task-Related Single-Vessel BOLD and CBV fMRI

(A) An A-V map shows individual venules (dark dots, blue markers) and arterioles (bright dots, red markers) in a 2D slice.

(B) The BOLD fMRI map (left) and the semi-transparent map overlaid on the A-V map demonstrate the venule-dominated peak BOLD signal with the on/off block time series from a single venule ROI.

(C) The CBV fMRI map (left) and the semi-transparent map overlaid on the A-V map show the arteriole-dominated peak CBV signal with the on/off block time series from a single arteriole ROI.

(D) The averaged BOLD (left)/CBV (right) fMRI response function from venule (blue) and arteriole (red) voxels (n = 5, mean ± SEM).

See also Figures S1 and S4 and Table S1.

permit us to follow neurovascular-coupled hemodynamic signals as they propagate from the arteriolar network, e.g., in terms of a CBV-weighted signal that will be sensitive to changes in vascular diameter, to the venous network, e.g., in terms of the BOLD signal, to gain a vascular-specific view of hemodynamic signaling with fMRI.

The technical goal of this work is 2-fold. The first is to detect the vessel-specific fluctuations in fMRI signals during the resting state. This goal must be accomplished across a plane through cortex with sufficient speed to accurately determine the magnitude and phase of correlation mediated by vasomotor fluctuations across vessels. The second is to measure these fluctuations concurrent with calcium signal recordings from neighboring neurons. Our approach builds on our ability to identify brain arterioles from venules with MRI and our line-scanning method to map the single-vessel hemodynamic signal (Yu et al., 2016). The line-scanning scheme reshuffled the k-space acquisition so that each image was reconstructed from data acquired along the entire experimental time series with a fast sampling rate, but not in real time (Silva and Koretsky, 2002; Yu et al., 2016). Here, we develop a single-vessel resting-state fMRI mapping method to specify the unique temporal dynamic features of neurovascular oscillatory signals, as well as to characterize the spatial distribution of fluctuations in the fMRI signal in both arteriolar and venous networks. We ask: (1) can the balanced steady-state free precession (bSSFP) method be used to detect vessel-specific fMRI signal fluctuations during resting state? The bSSFP method has higher SNR per time unit than the line-scanning method and presents less image distortion with reduced extravascular effect than the echo-planar imaging (EPI) method for high-field rat brain fMRI (Scheffler and Lehnhardt, 2003). (2) Can both BOLD and CBV signals be detected at the scale of penetrating vessels, the finest spatial scale within the brain in real time? This has not been feasible for the previously established line-scanning single-vessel fMRI method (Yu et al., 2016). (3) As a means to connect neural activity with hemodynamics, does the neuronal calcium signal at the location of cortical vessels studied with fMRI match all or part of the fMRI signal with the context of low-frequency fluctuations in brain state (Schulz et al., 2012; Du et al., 2014; Ma et al., 2016)? (4) Lastly, can the single-vessel fMRI scheme be extended to map the vessel-specific long-range correlation patterns in the gray matter of the human brain?

RESULTS

Single-Vessel Mapping of the Evoked BOLD and CBV-Weighted Signal with bSSFP-fMRI

Balanced steady-state free precession (bSSFP) single-vessel fMRI was implemented to map the evoked BOLD and CBV-weighted fMRI signal in the forepaw region of primary sensory (S1) cortex rats under a-chloralose anesthesia. Although anesthesia will alter brain rhythms, and lower the ultra-slow fluctuations to below their awake, resting-state value of rv0.1 Hz (Chan et al., 2015), the use of anesthesia is currently necessary for stability in these initial single-vessel fMRI measurements. Our stimulus was transient electrical stimulation of the forepaw. To acquire a high spatial resolution 2D bSSFP image, we acquired each spin echo every 7.8 ms to shorten the total acquisition time for each 2D image, comprising a 96 × 128 matrix (FOV, 9.6 × 12.8 mm) for an in-plane resolution of 100 × 100 mm, to a TR of 1 s. As described previously (Yu et al., 2016), a multi-gradient-echo (MGE) sequence was used to distinguish among individual arterioles (bright dots, due to the inflow effect) and venules (dark dots, due to fast T2* decay of deoxygenated blood) from the anatomical single-vessel 2D images, i.e., the arteriole-venule (A-V) map (Figure 1A). Also noteworthy is that the A-V ratio is 0.85 ± 0.04 (Table S1), demonstrating more penetrating veins than arteries, which is consistent with what has been previous reported in rodents (Hirsch et al., 2012; Blinder et al., 2013).

Further, the sensory-evoked single-vessel BOLD and CBV-weighted fMRI signal was detected by the bSSFP single-vessel fMRI before and after iron oxide particle injection. The data of Figure 1B show that the peak BOLD signals are primarily located at the venule voxels with the time course of the positive BOLD signal from a selected venule (Figure S1). After an injection of iron oxide particles, the bSSFP fMRI signal was acquired in the same 2D slice and shows that the evoked CBV-weighted signal corresponds to a decreased T2*-weighted MR signal (Figure 1C). Note that the T2*-weighted signal drops since activity-evoked vasodilation leads to an increased blood volume with more iron oxide particles in a given voxel, which shortens the magnitude of T2* and diminishes the signal (Mandeville et al., 1998). The peak CBV-weighted signal was mainly located at individual arterioles with the time course of the negative CBV-weighted signal originated from a selected arteriole (Figures 1C and S1). The averaged hemodynamic time courses from regions of interest of venule and arteriole voxels showed that the positive BOLD signal is much higher in venule than arteriole voxels (Figure 1D). Similarly, the negative CBV-weighted signal is much lower in arteriole than venule voxels (Figure 1D). Interestingly, the CBV-weighted signal in arteriole voxels returned to baseline faster than that in venules. An extended temporal response for the CBV-weighted signal in venules has been previously reported for CBV-based fMRI studies (Mandeville et al., 1999; Silva et al., 2007; Drew et al., 2011) and may be inferred from optical imaging (Drew et al., 2011). These results demonstrate the feasibility of bSSFP-fMRI for real-time single-vessel hemodynamic mapping from arterioles. They complement the venule-dominated approach for the positive BOLD signal mainly in terms of oxy/deoxy-hemoglobin ratio changes.

Single-Vessel bSSFP fMRI Mapping the Resting-State BOLD and CBV-Weighted Signals

Moving beyond the evoked single-vessel fMRI mapping, the ultra-slow resting-state hemodynamic signal was directly mapped with the bSSFP single-vessel fMRI method. Individual arterioles or venules identified from the A-V map were selected as seed voxels to calculate the correlation maps of both BOLD and CBV-based fluctuations in the fMRI signal (Figure 2); the frequency range was 0.01 to 0.1 Hz. As shown in the example data of Figure 2B, venule voxels were highly correlated to each other but less correlated for arterioles in the resting-state BOLD correlation maps (Movie S1). In contrast, as shown in the example data of Figure 2C, arteriole voxels were highly correlated but venules essentially uncorrelated in the resting-state CBV-weighted correlation maps (Movie S2). The power spectral density shows that the venule-specific BOLD and arteriole-specific CBV-weighted fMRI signal fluctuate within the ultra-slow frequency range of 0.01 to 0.04 Hz (Figure 2D). Similar to the evoked fMRI maps, the significant BOLD signal correlations were primarily located at venule voxels, i.e., the venule-specific connectivity map, and the significant CBV-weighted signal correlation were primarily located at arteriole voxels, i.e., the arteriole-specific connectivity map, during the resting state.

To better characterize the spatial and temporal features of the single-vessel fMRI fluctuations, the vessels identified in the A-V map were paired to calculate correlation coefficients (Figure 3A). First, the values of the correlation coefficient for all vessel pairs (arteriole pairs: A-A; venule pairs: V-V) were plotted as the function of inter-vessel distance. For the BOLD signal fluctuation, V-V pairs show a stronger correlation than that of A-A pairs in the large field-of-view, up to 5 3 5 mm. This highlights the large-scale extent of the BOLD-based venule functional connectivity (Figures 3B and 3F). In contrast to the case for BOLD, a stronger correlation was detected for the A-A pairs than the V-V pairs for the CBV-weighted signal fluctuations. These correlations diminished over a vessel separation distance of 2 mm (Figures 3C and 3G). This spatial scale is consistent with the scale for correlations in vasomotion across arterioles, as detected by two-photon imaging of vessel diameter (Mateo et al., 2017). This spatial scale also corresponds to the rv2 mm electrotonic length for conduction through endothelial cells (Segal and Duling, 1989). The color-coded correlation matrices showed higher BOLD values of correlation in V-V pairs than the other pairs (Figure 3D) and higher CBV-weighted values of correlation in A-A pairs than the other pairs (Figure 3E), which is quantitatively represented as the function of vessel pair distance (Figures 3F and 3G).

Next, Spectral coherence analysis from paired venules or arterioles was performed to characterize the full frequency spectrum of the vessel-specifi fMRI signal fl ctuation during the resting state. The coherent oscillation was mainly distributed in the 0.01–0.04 Hz frequency range for both BOLD and CBV-weighted fMRI signal fl (Figures 3H and 3I, similar to the spectral power, Figure 2D). Quantitative analysis demonstrates that the coherence coeffi of venule pairs is signifi antly higher than that of arteriole pairs for the BOLD signal fluctuation. In contrast, for the CBV-weighted signal fluctuation, the coherence coefficient of arteriole pairs is signifi higher than that of venule pairs for the 0.01–1.4 Hz frequency bandwidth (Figures 3J and 3K). In addition to the seed-based analysis, independent component analysis (ICA) was used to determine the venule-specifi dynamic connectivity for BOLD signal fluctuation and the arteriole-specifi dynamic connectivity for CBV-weighted signal fl (Figures S2A–S2G). One component appeared specifi for vessel-specifi BOLD ultra-slow oscillations and another for CBV-weighted the ultra-slow oscillations (Figures S2F and S2G). These results confi m distinct vessel-specific correlation patterns for BOLD and CBV-weighted signal fl

Vessel-specific BOLD correlation maps were detected in rats anesthetized with isoflurane (<1.2% [v/v]) (Figures S2H–S2M). The frequency range of oscillations extended to rv0.1 Hz with peak power levels at 0.01–0.04 Hz, similar to those observed with rats anesthetized with a-chloralose (Figure 2). This result suggests that while oscillation at frequencies above rv0.1 Hz may vary depending on the anesthetized or awake brain state (Obrig et al., 2000; Du et al., 2014; Ma et al., 2016; Mateo et al., 2017), the ultra-slow frequencies are fairly stable (<0.1 Hz) under uniform ventilation. It is noteworthy that blood pressure was acquired simultaneously with fMRI, but no clear ultra-slow frequency fluctuation was observed from either of the physiological parameters (Figure S3).

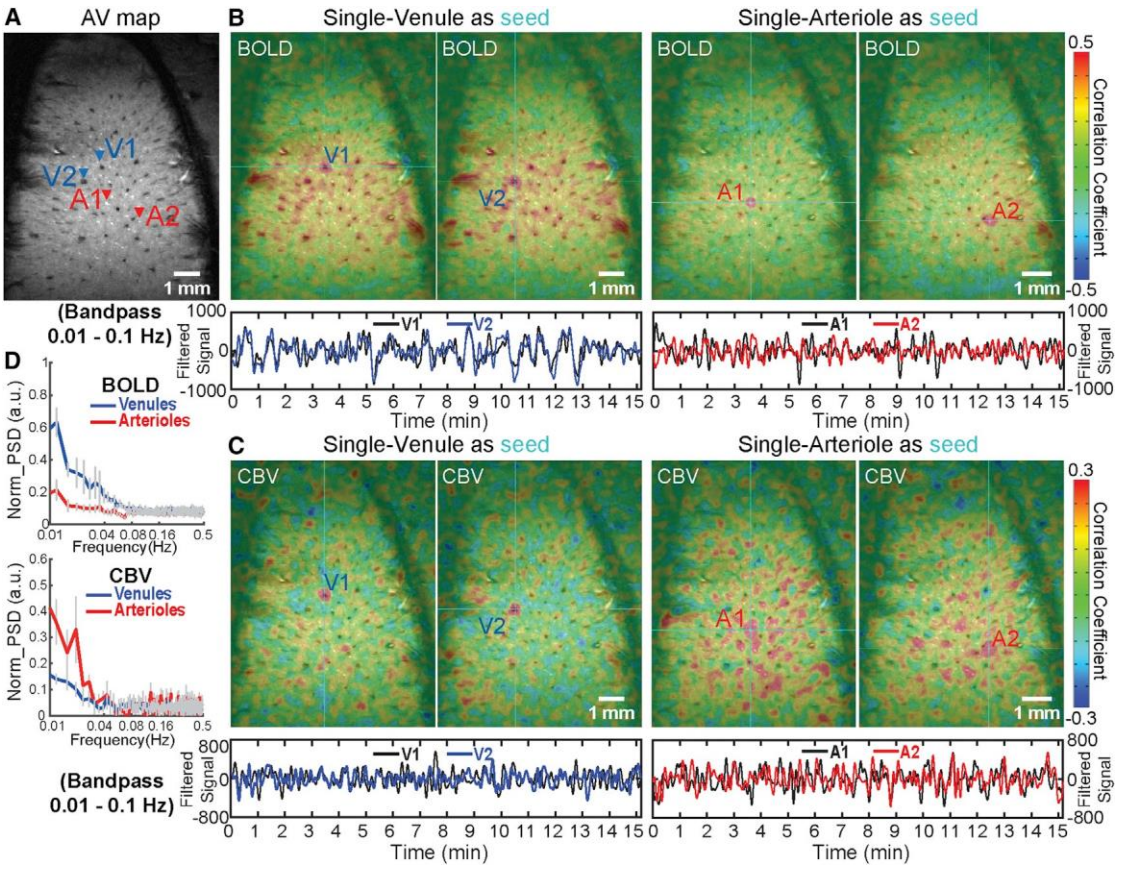

Figure 2. Using bSSFP-Based rs-fMRI to Map Vascular-Specific Correlation Patterns

(A) The A-V map shows individual penetrating arterioles and venules (blue arrowheads, venules; red arrowheads, arterioles).

(B) The seed-based BOLD rs-fMRI correlation maps (0.01–0.1 Hz; seeds: cyan crosshairs) of two venule seeds (V1 and V2; left) and CBV rs-fMRI correlation maps (0.01–0.1 Hz; seeds: cyan crosshairs) of two arteriole seeds (A1 and A2; right). The lower panel is the BOLD signal time course of the two venule seed ROIs and two arteriole seed ROIs.

(C) The seed-based CBV rs-fMRI correlation maps (0.01–0.1 Hz; seeds: cyan crosshairs) of two venule seeds (V1 and V2; left) and CBV rs-fMRI correlation maps (0.01–0.1 Hz; seeds: cyan crosshairs) of two arteriole seeds (A1 and A2; right). The lower panel is the CBV signal time course of the two venule seed ROIs and two arteriole seed ROIs.

(D) The power spectral density (PSD: arbitrary unit [a.u.]) of the venule and arteriole-specific resting-state BOLD (upper) and CBV (lower) fMRI time courses.

See also Figures S2 and S3.

Comparison of Vessel-Specific BOLD and CBV fMRI Signals with Simultaneous Neuronal Calcium Recording

To characterize the potential neural correlates of the vessel-specific fMRI signal fluctuation, a genetically encoded calcium indicator, GCaMP6f, was expressed in neurons of forepaw S1 or vibrissa S1 cortex for simultaneous intracellular [Ca^{2+}] recording and fMRI (Figure S4); immunostaining verified the GCaMP expression in cortical neurons (Figure S4B). Evoked and spontaneous intracellular [Ca^{2+}] transients were recorded in the deep layers with fiber photometry concurrent with the local field potential (LFP) (Figures 4A and S4C–S4F). Evoked [Ca^{2+}] spikes were acquired simultaneously with single-vessel bSSFP-fMRI for comparison with the venule-specific positive BOLD signal and arteriole-specific negative CBV-weighted signal (Figures S4E and S4F). These results demonstrate the feasibility of simultaneous single-vessel fMRI with intracellular [Ca^{2+}] fiber optic recording.

We sought to characterize the potential neuronal origin of the vessel-specific fMRI signal fluctuation. We first considered the correlation between changes in intracellular [Ca^{2+}] in the 0.01 to 0.1 Hz band and the resting-state BOLD signal. It shows vessel-specific positive correlation patterns that are similar to the venule-seed based correlation maps from rats anesthetized with a-chloralose (Figures 4B and 4C); time courses of representative venules (V1, V2), and changes in intracellular [Ca^{2+}] are shown in Figure 4D. The correlation coefficient between the intracellular [Ca^{2+}] and the venule BOLD signal (Ca^{2+}-V) was significantly higher than that with the arteriole BOLD signal (Ca^{2+}-A) (Figure 4F). Cross-correlation analysis between the changes in intracellular [Ca^{2+}] and the venule-specific BOLD signal showed a positive peak at the averaged lag time of 2.3 ± 0.2 s (Figures 4E and 4G). The vessels at the cortical surface had the longest lag, up to 3–5 s (Figure 4C), which agrees with the lag reported previously by cross-correlation analysis of the

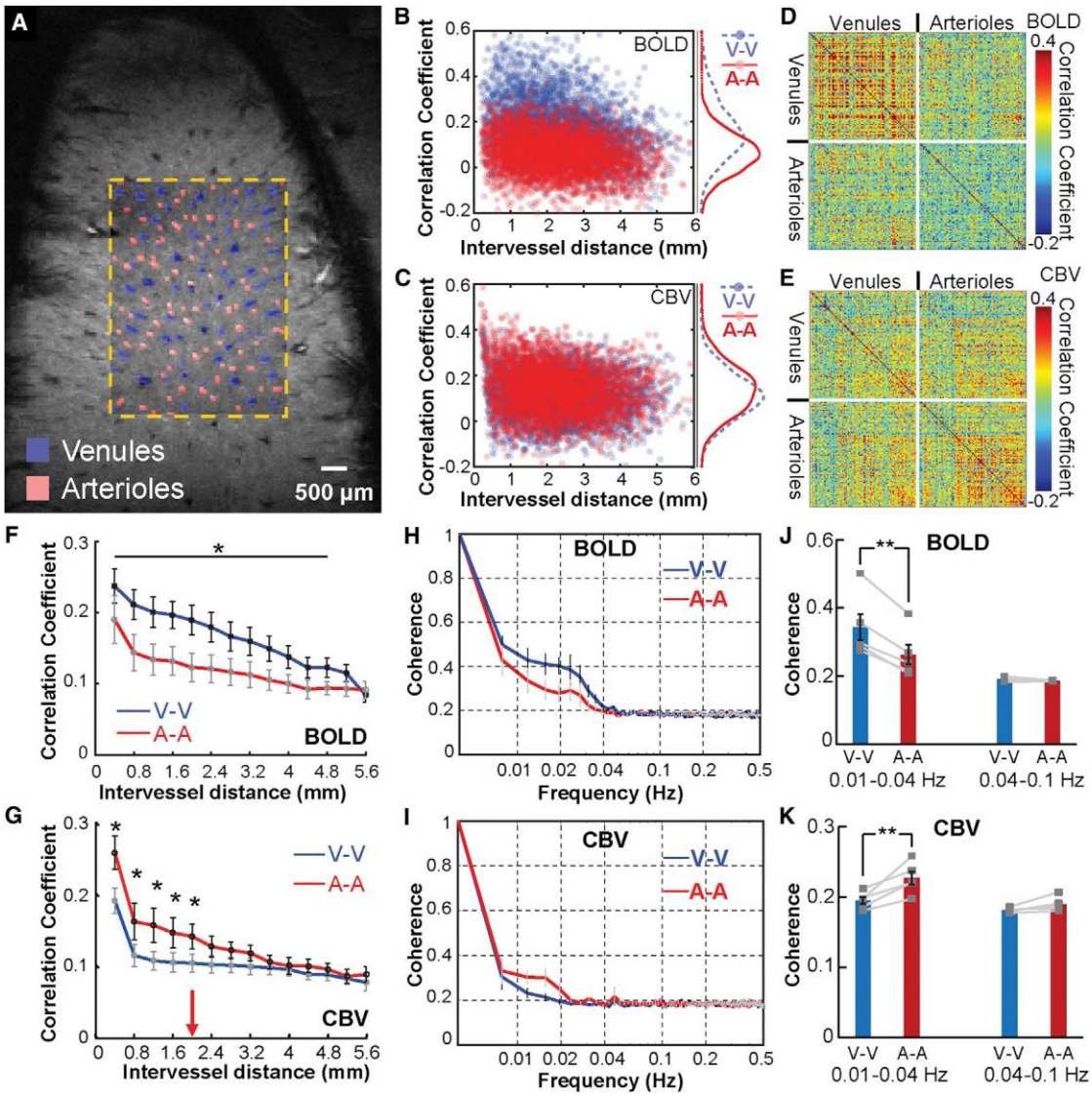

Figure 3. Vascular Dynamic Network Connectivity in Rats at 14.1T

(A) The A-V map of one representative rat (arteriole ROIs in red and venule ROIs in blue).

(B and C) Scatterplots of the correlation coefficient (CC) of BOLD (B) and CBV (C) fMRI from venule-to-venule (V-V) pairs, arteriole-to-arteriole (A-A) pairs as the function of the inter-vessel distance from one representative rat.

(D and E) The correlation matrices of all vessel pairs for the BOLD (D) and CBV (E) fMRI from one representative rat.

(F and G) The mean CC value of the BOLD signal from the venule pairs is significantly higher than that of the arteriole pairs with large spatial inter-vessel distance (>5 mm) (F, n = 5, mean ± SEM, *, paired t test, $p < 0.03$). In contrast, the mean CC value of the CBV signal from the arteriole pairs is significantly higher than that of the venule pairs with small spatial inter-vessel distance (rv2 mm) (G, n = 5, mean ± SEM, *, paired t test, $p < 0.03$).

(H and I) The averaged coherence graph of paired venules and arterioles from BOLD/CBV fMRI (H), BOLD fMRI, n = 5, (I), CBV fMRI, n = 5 rats, mean ± SEM.

(J) The mean BOLD coherence coefficient of the venule pairs is significantly higher than that of arteriole pairs at the low-frequency range (0.01–0.04 Hz) (n = 5, paired t test, **p = 0.0009).

(K) The mean CBV coherence value of paired venules is significantly lower than that of paired arterioles at the low-frequency range (0.01–0.04 Hz) (n = 5 rats, paired t test, **p = 0.007).

See also Figures S2 and S3.

calcium signal and hemoglobin-based intrinsic optical signal (Du et al., 2014).

We next considered the correlation of the calcium signal in the 0.01–0.1 Hz band with the single-vessel CBV-weighted fMRI signal obtained after the injection of iron oxide particles. Similar to the arteriole-seed based CBV correlation maps (Figure 4I), the highly correlated voxels with changes in intracellular $[Ca^{2+}]$ were located mainly at arterioles, but with negative values of the correlation coefficient (Figure 4J); the time courses of representative arterioles (A1, A2) and the calcium signal are shown in Figure 4K.

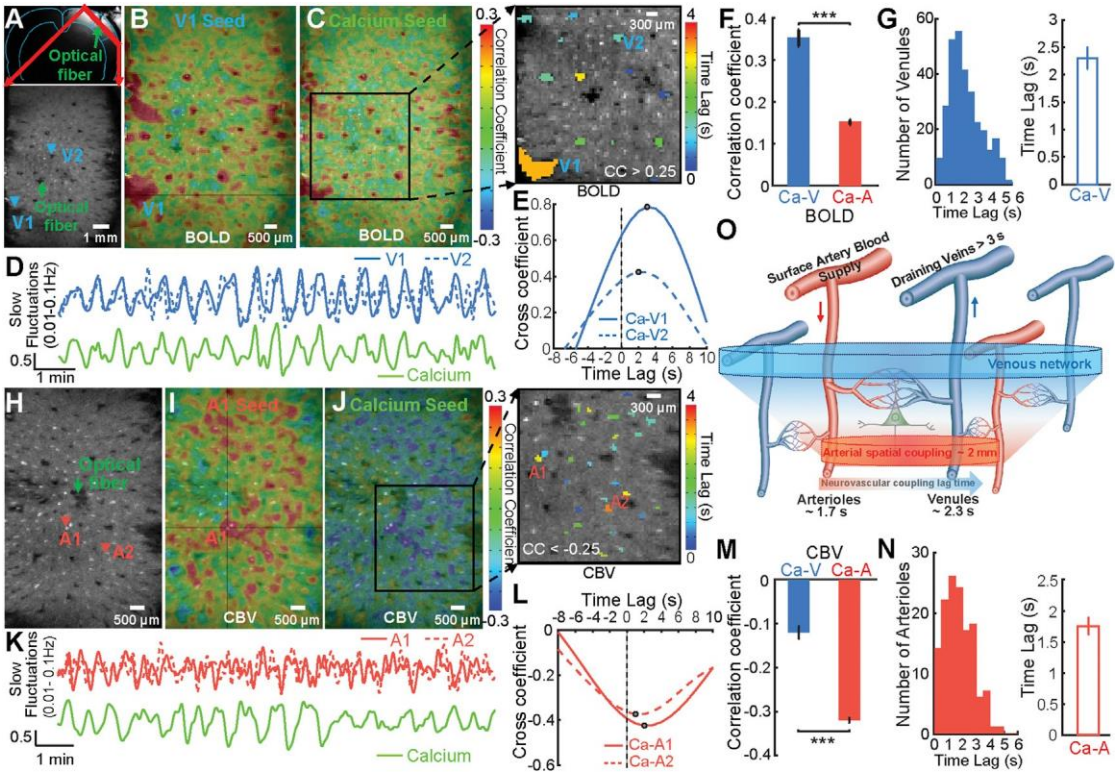

Figure 4. Correlation Analysis of the Single-Vessel BOLD/CBV fMRI with GCaMP6f-Mediated Calcium Signal

(A) The coronal view of the anatomical MR image with the optic fiber targeting the vibrissa S1 (upper). The A-V map from a 2D slice covering the deep cortical layer (lower).

(B) The seed-based BOLD correlation maps from one representative venule voxels (V1) overlaid on the A-V map.

(C) The correlation map between the BOLD fMRI signal and the calcium signal (band-pass filter: 0.01–0.1 Hz). Inset is a representative color-coded lag time map between the calcium signal with the BOLD fMRI of individual venules (CC > 0.25).

(D) The time courses of the BOLD fMRI signal from vessel voxels (V1: blue, solid line; V2: blue, dotted line) and the slow oscillation calcium signal (green).

(E) The cross-correlation function of the calcium signal and BOLD fMRI signal of two representative venules (Ca-V1 and Ca-V2) with positive peak coefficients at the lag time 2–3 s.

(F) The mean correlation coefficient of the calcium signal with the BOLD fMRI signal of venules is significantly higher than that of arterioles (n = 7 rats, mean ± SEM, paired t test, ***$p = 2.5 \times 10^{-5}$).

(G) The histogram of venules with lag times varied from 0.5 to 6 s (CC > 0.25) and mean lag time at 2.30 ± 0.19 s. (n = 7, mean ± SEM).

(H) The A-V map with the markers of arterioles (arteriole 1: A1, arteriole 2: A2, red arrowheads) and optical fiber (green arrowhead).

(I) The seed-based correlation maps of CBV fMRI from one arterioles voxel (A1) overlaid on the A-V map.

(J) The correlation map between the CBV fMRI and calcium signal (band-pass filter: 0.01–0.1 Hz). Inset is a representative color-coded lag time map between the calcium signal and the CBV fMRI signal of individual arterioles (CC < -0.25).

(K) The time course of the CBV fMRI signal from arteriole voxels (red, solid and dotted lines) and the slow oscillation calcium signal (green).

(L) The cross-correlation function of the calcium signal and CBV fMRI signal of two representative arterioles (Ca-A1 and Ca-A2) with negative peak coefficients at the lag time 1–2 s.

(M) The mean correlation coefficient of the calcium signal with the CBV fMRI signal of arterioles is significantly higher than that of venules (n = 4, mean ± SEM, paired t test, ***p = 0.0002).

(N) The histogram of arterioles with lag times varied from 0.5 to 5 s (CC < -0.25). The mean lag time is 1.76 ± 0.14 s (n = 4, mean ± SEM), which is significantly shorter than the lag times of the calcium and venule BOLD signal (BOLD, n = 7, CBV, n = 4, t test, p = 0.025).

(O) The schematic drawing of the spatial and temporal correlation patterns of the slow oscillation signal coupling from neurons to vessels.

See also Figures S4–S7 and S10 and Table S2

Quantitative analysis showed that the correlation between the intracellular [Ca^{2+}] and the CBV-weighted signal of arterioles (Ca^{2+}-A) was significantly higher than that of venules (Ca^{2+}-V) (Figure 4M). The oscillation in intracellular [Ca^{2+}] also led the arteriole-specific CBV-weighted signal fluctuations, as observed by the cross-correlations of two representative arterioles as the function of lag time (Figure 4L). Different arterioles showed varied lags with a mean value at 1.8 ± 0.2 s (Figure 4N). Cross-correlation of the intracellular [Ca^{2+}] with the arteriole CBV-weighted signal showed a shorter lag time than that with the venule BOLD signal (Figures 4G and 4N). Meanwhile, the oscillation in intracellular [Ca^{2+}] was found to be correlated with the CBV-weighted signal of a few venules with lag time of 5–10 s (Figure S5). This result indicates the passive venule dilation usually

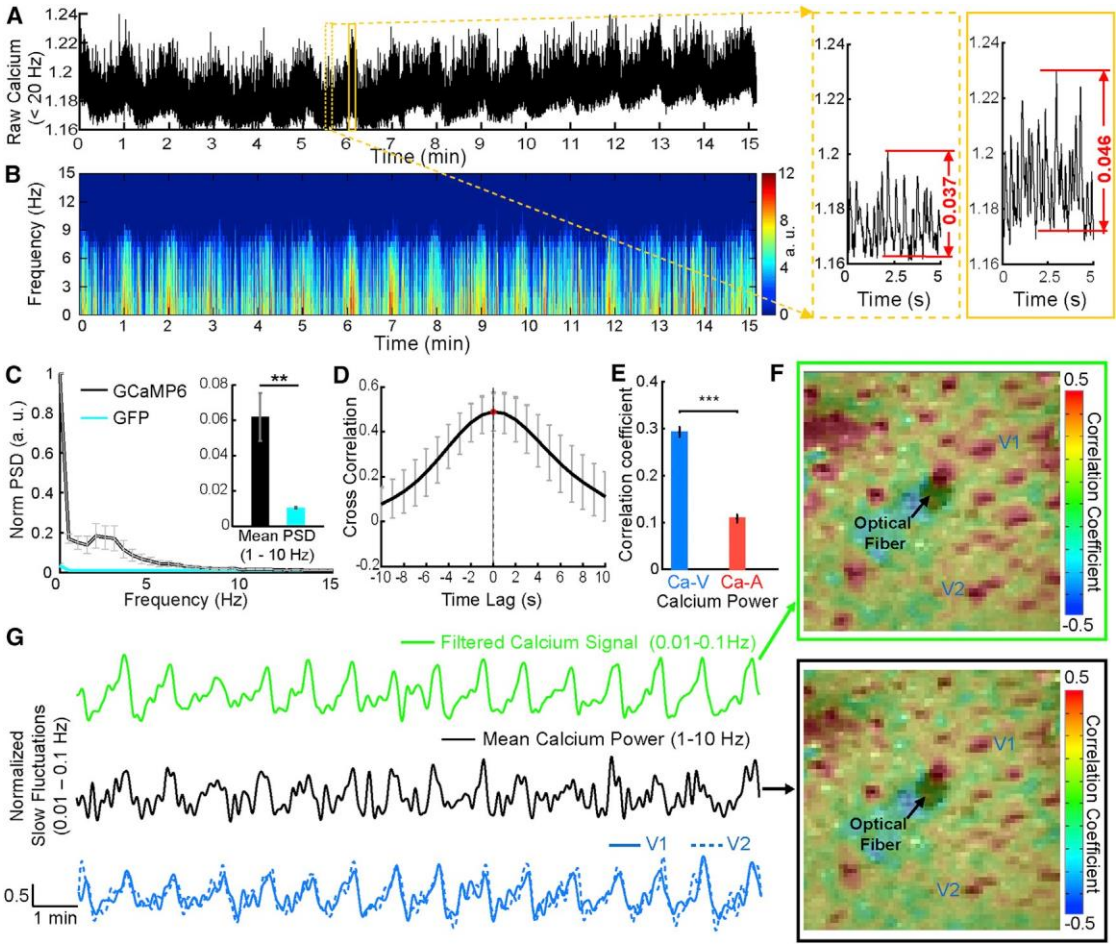

Figure 5. The Correlation between the Calcium Power Spectral Profile with Vessel-Specific fMRI Signal

(A) The time course of the calcium signal (low-pass filter: 20 Hz) from one representative rat at the resting state with enlarged 5 s windows of the calcium spikes identified at different periods (dotted and solid yellow boxes).

(B) The time-varying power spectrogram of the calcium signal is plotted as the function of time from 0.5 to 15 Hz (discrete Fourier transform in 1 s Hamming window; the sampling rate is 1 Hz to match the TR of fMRI signal).

(C) The normalized PSD from the rats with GCaMP6 (black, n = 5) or GFP (cyan, n = 4) indicates the mean PSD (1–10 Hz) of GCaMP6 is significantly higher than that of GFP (**p = 0.001, t test).

(D) The cross-correlation function of the calcium signal and the averaged power (1–10 Hz) profile from the calcium spectrogram (band-pass filter with 0.01–0.1 Hz) illustrates the peak cross-correlation coefficient at 0 s lag time (n = 4, mean ± SEM).

(E) The mean correlation coefficients of the averaged calcium power signal with the BOLD fMRI signal of venules are significantly higher than that of arterioles (***$p = 1.9 \times 10^{-4}$, pair t test, n = 4, mean ± SEM).

(F) The correlation maps between the SSFP-based BOLD fMRI signal and the slow oscillation calcium signal (band-pass filter: 0.01–0.1 Hz, upper) and the mean calcium power spectral profile (1–10 Hz, lower) show similar venule-specific correlation patterns.

(G) The time series (band-pass filter: 0.01–0.1 Hz) of the slow oscillation calcium signal (green), the mean calcium spectral power profile (1–10 Hz) (black), the BOLD fMRI signal from two venules (V1, V2; blue, solid and dotted blue lines).

See also Figure S6.

detected as the post-stimulus undershoot of the evoked BOLD signal results from increase blood flow following prolonged stimulation (Buxton et al., 1998; Silva et al., 2007; Drew et al., 2011).

Besides the ultra-slow oscillation, the GCaMP6-mediated calcium signal exhibited EEG-like rhythmic neuronal activity, showing significantly higher spectral power at the 1–10 Hz frequency range than that of the fluorescent signal detected from the GFP-expressing cortex of control rats (Figures 5A–5C). Cross-correlation of the spectral power in the 1–10 Hz and ultra-slow oscillatory calcium signal fluctuation (0.1–0.01 Hz) showed peak positive correlation coefficient at zero time lag (Figure 5D). In addition, the spectral power in 1–10 Hz was correlated to the vessel-specific BOLD signal, showing the correlation coefficient of spectral power with the venule BOLD signal is significantly higher than that of the spectral power with the arteriole BOLD signal, similar to the ultra-slow oscillatory calcium signal fluctuation (Figures 4B–4D and 5E–5G). This result further demonstrates the neuronal correlates of the vessel-specific fMRI

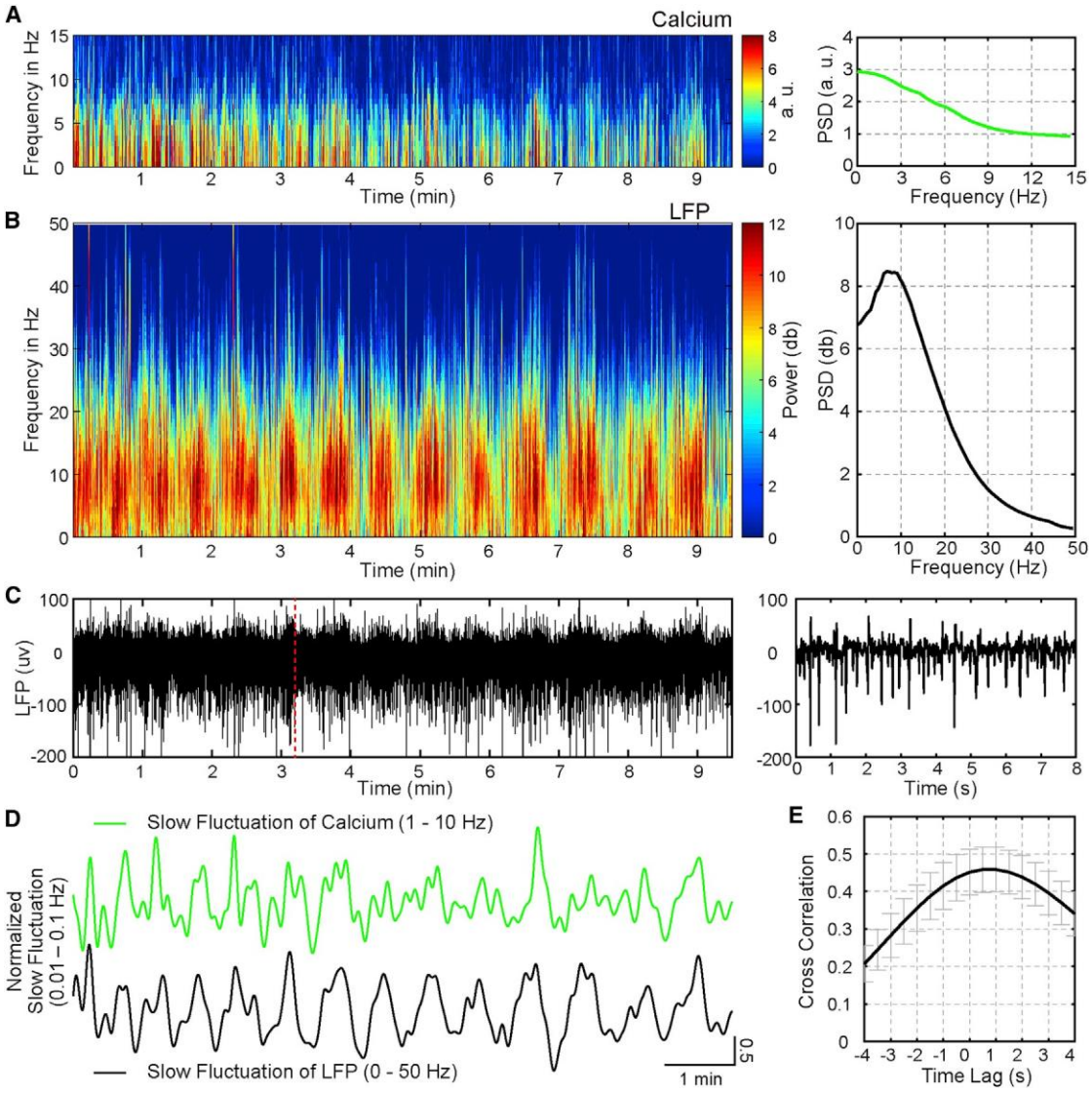

Figure 6. The Spectrogram of Simultaneous Calcium and Electrophysiological Signal under A-chloralose Anesthesia

(A) Spectrogram of calcium signal during light anesthesia.

(B) Spectrogram of local field potential (LFP) at light anesthesia from multi-taper spectral estimates (1 s sliding window with 0.1 s steps, 9 tapers). The right panel shows the averaged power spectral density (PSD).

(C) The time course of the LFP signal under light anesthesia.

(D) The mean calcium spectral power profile (band-pass filter: 0.01–0.1 Hz of 1–10 Hz, green) and the mean LFP spectral power profile (0–50 Hz, black) at light anesthesia.

(E) The cross-correlation function of the averaged LFP power (0–50 Hz) from LFP spectrogram and the averaged calcium power (1–10 Hz) profile from the calcium spectrogram (band-pass filter with 0.01–0.1 Hz) illustrates the peak cross-correlation coefficient at 0.8 s lag time at light anesthesia (n = 4, mean ± SEM).

See also Figures S5 and S6.

signal fluctuation in the cerebrovascular network. Finally, the cartoon of Figure 4O summarizes the spatial and temporal patterns of neurovascular hemodynamic signal fluctuation from arteriolar to venous networks.

Also noteworthy is that the power spectral density shows elevated power at frequencies below 0.1 Hz for the venule BOLD and arteriole CBV-weighted signal, as well as for the simultaneously acquired calcium signal at the light anesthesia (Figures 2D and S6). In contrast, at the deep anesthesia level with a-chloralose, the ultra-slow oscillation pattern was undetectable for both fMRI and changes in $[Ca^{2+}]$ concentration in the same rats (Figure S6), but the evoked BOLD and CBV fMRI signals and changes in $[Ca^{2+}]$ concentration remained (Figures S4E and S4F). This result further supports the neural correlates of the single-vessel fMRI signal fluctuation. Meanwhile, simultaneous LFP and intracellular $[Ca^{2+}]$ recording was performed to specify the ultra-slow oscillatory signal at different anesthesia levels (Figures 6 and S7). The spectrogram of the spontaneous

LFP and intracellular [Ca^{2+}] signal showed similar ultra-slow oscillation patterns in rats under the light anesthesia level (Figures 6A–6D). Cross-correlation of the LFP and intracellular [Ca^{2+}] signal power profile showed positive correlation coefficients (0.46 ± 0.06) at the time lag (0.73 ± 0.13 s), showing the ultra-slow oscillatory LFP signal leads the intracellular [Ca^{2+}] signal (Figure 6E). Similar to the single-vessel fMRI data, these results showed consistent correlation features at the light anesthesia level (Figure 5) but not at the deep anesthesia (Figures S7A–S7E). In addition, the ultra-slow oscillatory correlation of the LFP power profile and intracellular [Ca^{2+}] fluctuations were detected in rats anesthetized with 1.2% (v/v) isoflurane (Figures S7F–S7I). These results suggest that the neuronal and vascular hemodynamic oscillations are highly correlated in the anesthetized brain and that the correlation is dampened when the neural activity is suppressed with deep anesthesia.

Mapping Vascular Network Connectivity in the Human Brain under 3T and 9.4T

The single-vessel mapping scheme was implemented to characterize the prospects for vessel-specific fMRI correlation patterns in awake human subjects. Although bSSFP shows great advantage for the high-field fMRI in the rat brain as a consequence of decreased distortion and reduced extravascular effect compared to the EPI method, the single-echo bSSFP method acquires single k-space line per echo and takes longer time than the EPI method to acquire multi-slice high-resolution images (Budde et al., 2014). We established single-vessel fMRI human brain mapping with the EPI method. First, the fMRI signal of sulcus veins in the occipital lobe was mapped using EPI-fMRI at 3T. Upon the checkerboard visual stimulation, the evoked BOLD signal was located primarily at venous voxels with a sparsely distributed patchy pattern that was previously reported (Menon et al., 1993) (Figures 7A–7C and 7F; Movie S3). Besides the task-related functional maps, the seed-based correlation maps from resting-state fMRI demonstrated vein-dominated correlation spatial patterns (Figures 7D and 7G; Movie S4). The coherence analysis of paired venous voxels showed coherent ultra-slow oscillation of the awake human subjects up to rv0.1 Hz (Figure 7H), which was much higher than the oscillation frequency detected in anesthetized rats (Figure 3H). The correlation coefficients of paired venous voxels were plotted as the function of the intra-hemispheric and inter-hemispheric vessel distances (Figure 7I). The values of the correlation decreased as the function of the intra-hemispheric vessel distance but showed significantly higher values for the inter-hemispheric venous voxel pairs (Figure 7J), similar to previously established spatial vasomotion correlation patterns in awake mice (Mateo et al., 2017). The low-frequency oscillation around 0.1 Hz has been previously reported in the visual cortex of the human brain with conventional resting-state fMRI method (Mitra et al., 1997). Also, when EPI images were spatially smoothed with different kernels from 1 to 5 mm, the vessel-specific spatial patterns merged to functional blobs similar to the conventional functional connectivity maps (Biswal et al., 1995; Smith et al., 2009) (Figures 7K and 7L).

The seed-based analysis was performed before and after the regression of respiration and heartbeat relevant temporal artifacts (Figures S8A–S8F), showing the little difference in the vessel-specific spatial patterns (Figures S8G–S8M). In addition, ICA analysis specified the highly correlated venous voxels at multiple slices, showing a 3D vascular dynamic correlation structure through the main branches of cerebral vasculature (Figures S9A–S9D; Movie S5). These results demonstrate that the hemodynamic fMRI signals from central veins through sulci or at the gyrus surface are highly correlated, representing large-scale vascular dynamic network connectivity detectable with the 3T MR scanner.

To characterize the hemodynamic signal fluctuation in vessels penetrating cortical gray matter, we mapped the single vessel-based resting-state fMRI signal at 9.4T. The multiple 2D EPI images were acquired with an in-plane resolution of 500 × 500 mm^2 and 800 mm thickness at a TR of 1 s. In parallel, a single-vessel A-V map was acquired to better characterize the location of individual sulcus arteries and veins, as well as a few intracortical veins (Figures 8A–8C). Similarly, the BOLD signal was highly correlated on venous voxels, but not on artery voxels (Figures 8D and 8E). In the enlarged correlation maps, a few intracortical veins penetrating the gray matter could be spotted on the A-V map, given their unique vascular orientation through the 2D slice, showing a strong correlation to each other (Figures 8B, 8C, S9E, and S9F). Furthermore, coherence analysis of paired veins showed a coherent frequency range less than rv0.1 Hz, which is consistent with previous brain ultra-slow oscillation studies (Obrig et al., 2000) (Figure 8G). This result provides a good example for the illustration of vascular correlation of the selected intracortical veins penetrating cortical gray matter at 9.4T. This result shows the translational potential of high-resolution single-vessel fMRI to associate anatomical vascular biomarkers with prognostic dynamic indicators of neurovascular disease and vascular dementia in the brain.

DISCUSSION

We have demonstrated that a single-vessel fMRI mapping scheme reveals the spatial and temporal features of vessel-to-vessel hemodynamic correlations in anesthetized rats and in awake human subjects. With regard to rats, BOLD-specific venous signals and the CBV-specific arteriolar signals evolve at ultra-slow timescales, with frequency components between 1.1 and 0.04 Hz (Figure 3). Both signals show a causal relationship to the simultaneously acquired calcium signal (Figure 4). With regard to humans, the ultra-slow oscillation was observed in the BOLD signal for frequencies up to 0.1 Hz and vessel-to-vessel correlations are strong (Figure 8). This work demonstrates the feasibility to apply a multi-modal fMRI platform to measure the neuronal correlates of resting-state hemodynamic signal fluctuation from arteriolar to venous networks at the scale of individual vessels.

Technical Advances

The attainment of single-vessel imaging with high SNR was achieved based on three factors: a high magnetic field to enhance the transverse signal; a bSSFP sequence with high SNR efficiency per time unit; and a small radio frequency coil with appropriate sample loading to optimize the detection from local cortical regions. These factors ensured that the temporal

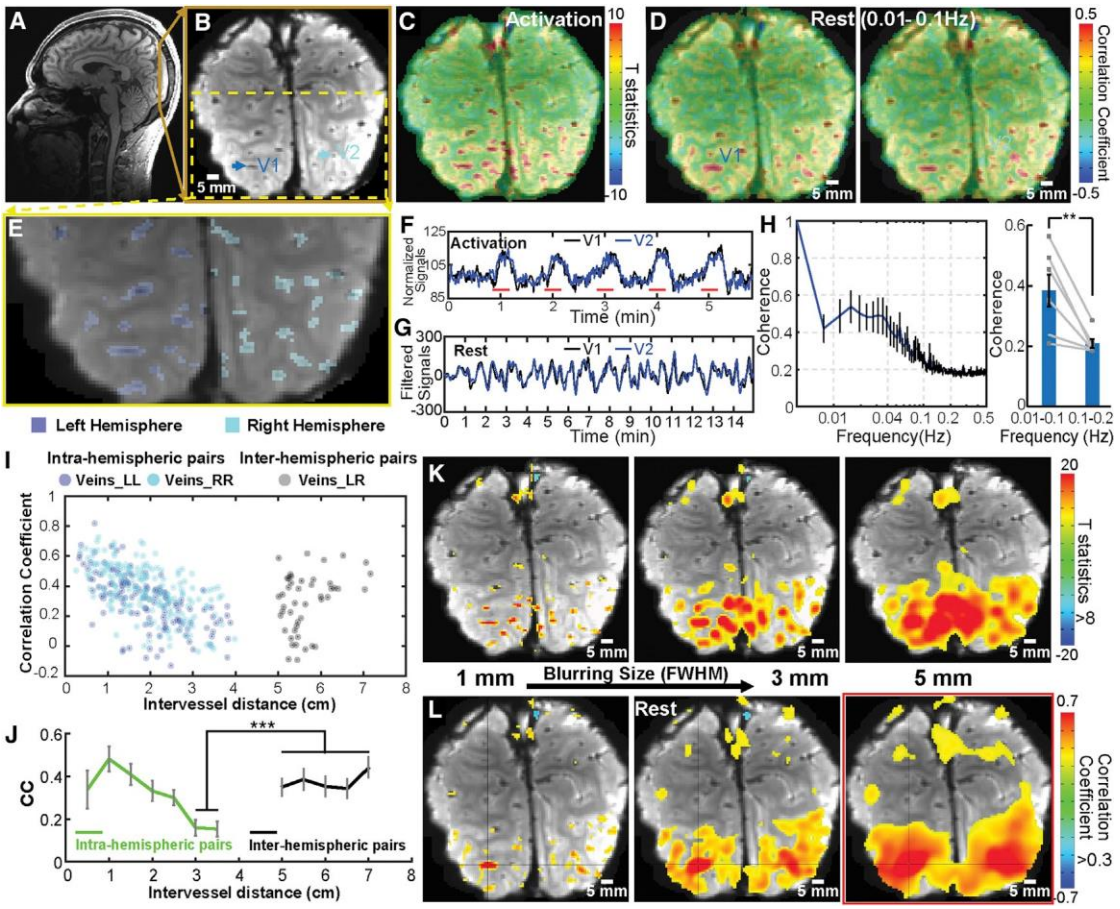

Figure 7. The Task-Related and Resting-State Single-Vessel fMRI Mapping in Awake Human Subjects at 3T

(A) A sagittal view of the human brain with a 2D EPI slice located in the occipital lobe.

(B) An averaged EPI image shows the pial veins in sulci as dark dots.

(C) The checkerboard visual stimulation-evoked BOLD functional map with peak BOLD signals located at pial veins.

(D) The seed-based BOLD correlation maps (0.01–0.1 Hz; seeds: two veins [V1 and V2]) demonstrate vessel-dominated patterns.

(E) The magnified view of the averaged EPI image from one representative subject (vein ROIs, left hemisphere, blue, right hemisphere, cyan).

(F and G) The time courses of two veins in the task-related (F) and resting-state (G) (0.01–0.1 Hz) conditions.

(H) The coherence graph of paired veins exhibits coherent oscillation at the frequency range of 0.01–0.1 Hz significantly higher than the higher frequency range (0.1–0.2 Hz; n = 6, mean ± SEM, **, paired t test, p = 0.008).

(I) The scatterplot of the correlation coefficient (CC) from intra and inter-hemispheric vein pairs.

(J) The mean CC of inter-hemispheric vein pairs with the intervessel distance between 5–7 cm is significantly higher than that of intra-hemispheric vein pairs with distance between 3–3.5 cm. (***, n = 6, mean ± SEM, t test, p = 0.0002).

(K and L) The evoked functional (K) and resting-state correlation (L) maps were smoothed from 1 mm to 5 mm (FWHM).

See also Figures S8 and S9.

fluctuation of the vessel-specific fMRI signal was not dominated by machine-based technical noise, but rather represented the physiological state of the brain. This issue was further verified by the anesthetic dose-dependent study, which indicated that the vessel-specific fMRI signal fluctuation could be dampened even though the SNR remained unchanged (Figure S6). Besides the technical noise, artifacts from physiological motion can be erroneously intrinsically linked to the functional connectivity (Hu et al., 1995; Murphy et al., 2013). Numerous strategies have been developed to regress out the potential artifacts, or identify the functional node-specific component using ICA analysis (Glover et al., 2000; McKeown et al., 2003). Nonetheless, a lack of standard criteria to distinguish the contribution from brain signal fluctuation versus physiological motion artifacts limits the reliability of functional connectivity. We nominally expect that the pattern of correlations should be insensitive to global motion artifacts. Further, the enhanced correlations in the BOLD response for pairs of venules versus arterioles (Figures 3F, 3H, 3J, and 8F) and the enhanced correlations in the CBV response for arterioles versus venules (Figures 3G, 3I, and K) as a function of frequency are highly unlikely to result from known artifacts.

The detected bSSFP signal change is a mixture of intravascular and extravascular contributions. The intravascular signal is given by the steady-state contrast of passband bSSFP, which

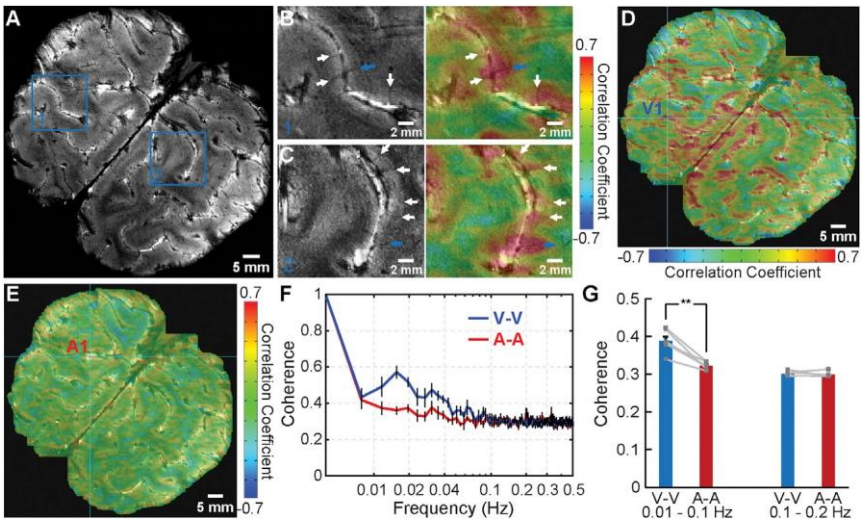

Figure 8. The Intracortical Vascular Dynamic Mapping with 9.4T

(A) The A-V map is acquired from a 2D slice across the occipital lobe.

(B and C) The intra-cortical veins (arrows) in the magnified view of region 1 and region 2 in the A-V map (left). The right panel shows the correlation map based on the selected seeds (the intracortical veins: blue arrows) with highly correlated voxels detected on the other intracortical veins (white arrows) in the gray matter.

(D and E) The seed-based correlation maps with vein 1 (V1), artery 1 (A1) as seeds, respectively (seeds: cyan crosshairs).

(F) The coherence graph of paired veins (blue) and arteries (red) identified by the AV map demonstrates the slow fluctuations from 0.01 to 0.1 Hz.

(G) The mean coherence coefficients of the paired veins are significantly higher than that of the paired arteries at low frequency (0.01–0.1 Hz) ($n = 6$, mean ± SEM, paired t test, $^{**}p = 0.0009$).

See also Figure S9.

is proportional to $T = T$ (Scheffler and Lehnhardt, 2003). Given the high spatial resolution of the bSSFP fMRI imaging, the BOLD contrast from venules and the CBV-based contrast from arterioles of vessel voxels remained highly T2-weighted because of the fast T2 decay of deoxygenated venule blood and iron oxide enriched arteriole blood (Lee et al., 1999; Blockley et al., 2008). The extravascular contribution depends on the vessel size. As for spin echoes, the rapid refocusing in bSSFP produces dynamic averaging that reduces the extravascular effects of the cortical penetrating vessels larger than 10–20 mm (Bieri and Scheffler, 2007; Scheffler and Ehses, 2016). Therefore, the observed signal changes with high spatial resolution bSSFP were mainly intravascular. It is noteworthy that the blood flow could contribute to the BOLD fMRI signal fluctuation based on the in-flow effect, given the short TR of the bSSFP sequence at a given flip angle (Kim et al., 1994). This is especially true for arterioles. However, the BOLD signal fluctuation in arterioles showed significantly lower correlation than that of venules, indicating that the in-flow effect is not the primary contributor to the vascular dynamic correlation patterns (Figures 2 and 3).

BOLD versus CBV-Weighted fMRI Signals

In contrast to the venus BOLD signal, for the CBV signal fluctuation, the arteriole-dominated CBV-signal results from vasomotor fluctuations in vessel diameter. The vasomotion signal shows ultra-slow oscillation with a broader frequency band centered at 0.1 Hz in the anesthetized rat brain (Mayhew et al., 1996; Kleinfeld et al., 1998) and 0.1 Hz in awake mice (Drew et al., 2010). Although in the present study arteriole CBV signal fluctuations were detected at a frequency band of <0.04 Hz in a-chloralose anesthetized rats, it is likely that this hemodynamic signal corresponds to vasomotion. Further to this point, beyond the neuronal effects of anesthetics (Brown et al., 2011; Mateo et al., 2017), anesthetics may directly affect vasomotion and directly contribute to the temporal dynamic patterns detected by fMRI in anesthetized animals (Colantuoni et al., 1984; Hundley et al., 1988). In addition, future studies will compare the arteriole-specific fMRI signal fluctuation in rat under anesthesia and wakefulness to specify the dynamic patterns driven by vasomotion. Lastly, our result is also consistent with the ''bagpipe'' model of active arteriole dilation with increased neuronal activity, where arteriole dynamics dominate both spontaneous and evoked blood volume changes in the brain (Drew et al., 2011). Following the net increase of the arteriole blood reservoir, venules drain the blood with a delayed passive dilation, which is consistent with undershoot of the evoked BOLD fMRI signal (Mandeville et al., 1999).

The ultra-slow passive venule dilation was detected by single-vessel CBV-bSSFP fMRI when iron oxide particles were delivered at a lower than normal dosage so that the venule fMRI signal was not completely dampened due to shortened T2* decay (Figure S5). This observation also explains the small number of venules highlighted by the arteriole-seed-based CBV correlation maps (Figure 2C), which showed much longer lag time than arterioles when analyzing the simultaneously acquired calcium ultra-slow oscillation signal via cross-correlation (Figure S5). All told, single-vessel bSSFP-fMRI detects distinct spatial and temporal patterns of vessel-specific dynamic connectivity in the anesthetized rat brain.

Correlates of Neuronal [Ca^{2+}] and Single-Vessel fMRI

A key observation was the correlation of ultra-slow calcium oscillation with single-vessel fMRI signal fluctuation. Prior combined fMRI and electrophysiological studies show that the resting-state BOLD signal correlates with neuronal activity oscillation (He et al., 2008; Shmuel and Leopold, 2008; Schölvinck et al., 2010; Pan et al., 2013). The present study extends the spatial resolution of resting-state fMRI down to single vessels. The coherence of the ultra-slow oscillations from both intracellular [Ca^{2+}] and vessel-specific fMRI signals demonstrates a potential link of the two events, with the calcium event leading the vascular fluctuation (Figures 4E and 4L). In particular, the BOLD signal from individual venules and the CBV-weighted signal detected primarily from arterioles showed

varied lag times, ranging from 0.5 to 6 s, relative to the calcium signal (Figures 4G and 4N).

Previous studies reported only long, i.e., 5 to 6 s, lag times by cross-correlation of the change in g-band power and the resting-state BOLD signal (Schö lvinck et al., 2010). This long lag time could be caused by signal fluctuations in large voxels, with primary weighting on surface draining veins. In the present study, the fMRI signal from draining veins also showed longer lag time, which is consistent with the lag time between the calcium and hemoglobin signal oscillation (rv0.1 Hz) detected from the cortical surface (Du et al., 2014). In contrast to surface draining veins, penetrating vessels at the deep cortical layers showed shorter lag times of 1.8 ± 0.2 s for the arteriole CBV signal and 2.3 ± 0.2 s for the venule BOLD signal (Figure 4), which is in coincordance with the signaling order of arteriole dilation followed by oxygen saturation changes in venules for neurovascular coupling (Devor et al., 2003; Iadecola, 2004).

The arterio-venous (A-V) transit time of the resting-state hemodynamic signal was calculated based on the cross-correlation lag times of the BOLD and CBV-weighted signals to the simultaneously recorded calcium signal (Figure S10 and Table S2). The resting-state A-V transit time of 0.61 s at the deep cortical layers is slighter shorter than the transit time of 0.8–1.2 s, calculated by the time to half-maximal, $t_{1/2}$, from surface arterioles to venules (Hutchinson et al., 2006). This further supports the vessel-specific hemodynamic signal propagation. Also noteworthy is that the variability of the measured resting-state transit time is relatively higher than that of the evoked A-V hemodynamic transit time (Yu et al., 2016) (Figure S10), indicating a more heterogeneous hemodynamic coupling during the resting state. Lastly, cortical calcium waves have been observed in the newborn and adult rodent brain (Adelsberger et al., 2005; Ma et al., 2016) and can propagate through the cortex at a fast speed (Stroh et al., 2013). It will be interesting to determine whether these drive propagating vascular events.

Single-Vessel Human Maps

Vascular dynamic network connectivity was directly mapped in awake human subjects to demonstrate the translational potential of single-vessel fMRI mapping. The vessel-specific ultra-slow oscillation shares a similar frequency range to that of the long-distance functional nodes detected by conventional resting-state fMRI, as well as the spontaneous oscillation of the cerebral hemodynamic signal detected by near-infrared spectroscopy (Obrig et al., 2000). In addition, the smoothed single-vessel correlation maps represented similar functional connectivity maps in the visual area as detected by the conventional resting-state fMRI (Smith et al., 2009) (Figures 7K and 7L). Together with the rat data that show highly correlated calcium and single-vessel fMRI signal fluctuation, the vascular dynamic network connectivity could represent the hemodynamic vascular correlation coupled to neuronal signal oscillation in both anesthetized and awake conditions. Interestingly, a recent resting-state fMRI study showed that the connectivity strength of a given voxel among the ''default mode'' and other networks is inversely proportional to its vascular volume fraction (Tak et al., 2015). This observation indicates that functional connectivity of long-range nodes in the brain may be driven independently of the vascular-specific hemodynamic fluctuation. Given the highly correlated calcium signal to the hemodynamic signal fluctuation, one possible explanation for this discrepancy is that vascular dynamic network connectivity represents the whole brain state fluctuation with less region specificity (Chang et al., 2016), but the functional connectivity may specify the network pattern of long-distance functional nodes (Biswal et al., 1995; Smith et al., 2009). Alternatively, because the vascular volume fraction was calculated from the largest extracerebral vessels detected by MRI images, it is also possible that the reduced connectivity may be caused by the low SNR of voxels occupied by these extracerebral vessels.

Given the cerebral folds and fissures of the human brain, single-vessel EPI-fMRI mapping mainly detects the central pial veins through the sulci with diameters of a few hundred micrometers based on the T2*-weighted partial volume effect. Single-vessel fMRI with 9.4T at high spatial resolution. i.e., 500 3 500 3 800 mm^3, showed the correlation patterns of the intracortical penetrating veins in the human brain (Duvernoy et al., 1981) (Figure 8). In contrast to studies focusing on excluding the venous BOLD signal to improve spatial specificity for brain function and connectivity mapping (Barth and Norris, 2007; Curtis et al., 2014), this work specifies the vascular network connectivity in gray matter of the human brain with the potential clinical application of illustrating hemodynamic features of vascular dementia (O'Brien et al., 2003; Iadecola, 2013). Specifically, the neural correlates of the vascular dynamic network connectivity detected in the rodent brain display great potential for clinical applications such as the diagnosis of cognitive impairments in patients with cerebral small vessel diseases or degenerative diseases such as Alzheimer's disease (Schaefer et al., 2014). The ability to specify the direct linkage of vascular pathology to dysfunction of the neurovascular network remains elusive (Stevens et al., 2014). The ability to map the hemodynamic origin of the BOLD signal from anatomically distinguishable vessels in human gray matter provides a key step to link vascular biomarkers, e.g., microbleeds (Poels et al., 2012) or cortical microinfarcts (van Veluw et al., 2013; van Rooden et al., 2014), with dynamic indicators in patients with small vessel or Alzheimer's disease.

Caveats Going Forward

We developed the single-vessel fMRI resting-state mapping scheme to characterize the spatial and temporal hemodynamic signals in arteriolar and venous networks, concurrent with photometric calcium recording. The high field MRI scanner, 14T for animals and 9.4T for humans, achieves sufficient SNR and high BOLD contrast for high-resolution fMRI imaging. A redesign of the radio frequency detection coil will be needed to extend the single-vessel fMRI method to broader application with lower magnetic field scanners. Toward this goal, a super-conducting coil has been developed to boost the SNR of MRI images (Ratering et al., 2008). Also, instead of the current 32- or 64-channel coils for human brain imaging, region-specific array coils can be developed to cover focal cortical areas with optimized geometry to increase the SNR. This step will help further resolve individual intracortical vessels in gray matter of normal human

subjects as well as patients with neurovascular dysfunction due to vascular dementia.

STAR+METHODS

Detailed methods are provided in the online version of this paper and include the following:

- KEY RESOURCES TABLE
- CONTACT FOR REAGENT AND RESOURCE SHARING
- EXPERIMENTAL MODELS AND SUBJECT DETAILS
  - Animals
  - Human Subjects
- METHODS DETAILS
  - Animal experiments
  - MRI image acquisition from rats
  - MRI image acquisition from humans (3T)
  - MRI image acquisition from humans (9.4 T)
  - Data processing
  - Immunohistochemistry
- QUANTIFICATION AND STATISTICAL ANALYSIS

SUPPLEMENTAL INFORMATION

Supplemental Information includes ten figures, three tables, and five movies and can be found with this article online at https://doi.org/10.1016/j.neuron.2018.01.025.

ACKNOWLEDGMENTS

Q1 This research was supported by Germany Research Foundation (DFG) SPP-1655 and internal funding from Max Planck Society for X.Y. and NIH grants R35NS097265 for D.K. and NIMH BRAIN grant R01MH111438 for D.K. and B.R.R. We thank Dr. H. Merkle and Dr. K. Buckenmaier for technical support, Ms. H. Schulz and Ms. S. Fischer for animal maintenance support, the AFNI team for the software support, and Dr. L. Looger and the Janelia Research Campus of HHMI for kindly providing viral vectors.

AUTHOR CONTRIBUTIONS

X.Y., D.K., and B.R.R. designed the research, Y.H., X.Y., M.W., and X.C. performed animal experiments, Y.H., X.Y., and R.P. acquired data, X.Y. supervised the research, Y.H. analyzed data, K.S., R.P., J.R.P., and M.W. provided key technical support, and X.Y., D.K., and Y.H. wrote the manuscript.

DECLARATION OF INTERESTS

The authors declare no competing interests.

Received: June 26, 2017
Revised: November 14, 2017
Accepted: January 10, 2018
Published: February 1, 2018

REFERENCES

Adelsberger, H., Garaschuk, O., and Konnerth, A. (2005). Cortical calcium waves in resting newborn mice. Nat. Neurosci. *8*, 988–990.

Aydin, F., Rosenblum, W.I., and Povlishock, J.T. (1991). Myoendothelial junctions in human brain arterioles. Stroke *22*, 1592–1597.

Barth, M., and Norris, D.G. (2007). Very high-resolution three-dimensional functional MRI of the human visual cortex with elimination of large venous vessels. NMR Biomed. *20*, 477–484.

Bell, A.J., and Sejnowski, T.J. (1995). An information-maximization approach to blind separation and blind deconvolution. Neural Comput. *7*, 1129–1159.

Bieri, O., and Scheffler, K. (2007). Effect of diffusion in inhomogeneous magnetic fields on balanced steady-state free precession. NMR Biomed. *20*, 1–10.

Biswal, B., Yetkin, F.Z., Haughton, V.M., and Hyde, J.S. (1995). Functional connectivity in the motor cortex of resting human brain using echo-planar MRI. Magn. Reson. Med. *34*, 537–541.

Blinder, P., Tsai, P.S., Kaufhold, J.P., Knutsen, P.M., Suhl, H., and Kleinfeld, D. (2013). The cortical angiome: an interconnected vascular network with noncolumnar patterns of blood flow. Nat. Neurosci. *16*, 889–897.

Blockley, N.P., Jiang, L., Gardener, A.G., Ludman, C.N., Francis, S.T., and Gowland, P.A. (2008). Field strength dependence of R1 and R2* relaxivities of human whole blood to ProHance, Vasovist, and deoxyhemoglobin. Magn. Reson. Med. *60*, 1313–1320.

Brown, E.N., Purdon, P.L., and Van Dort, C.J. (2011). General anesthesia and altered states of arousal: a systems neuroscience analysis. Annu. Rev. Neurosci. *34*, 601–628.

Budde, J., Shajan, G., Zaitsev, M., Scheffler, K., and Pohmann, R. (2014). Functional MRI in human subjects with gradient-echo and spin-echo EPI at 9.4 T. Magn. Reson. Med. *71*, 209–218.

Buxton, R.B., Wong, E.C., and Frank, L.R. (1998). Dynamics of blood flow and oxygenation changes during brain activation: the balloon model. Magn. Reson. Med. *39*, 855–864.

Chan, A.W., Mohajerani, M.H., LeDue, J.M., Wang, Y.T., and Murphy, T.H. (2015). Mesoscale infraslow spontaneous membrane potential fluctuations recapitulate high-frequency activity cortical motifs. Nat. Commun. *6*, 7738.

Chang, C., Leopold, D.A., Schölvinck, M.L., Mandelkow, H., Picchioni, D., Liu, X., Ye, F.Q., Turchi, J.N., and Duyn, J.H. (2016). Tracking brain arousal fluctuations with fMRI. Proc. Natl. Acad. Sci. USA *113*, 4518–4523.

Chen, T.W., Wardill, T.J., Sun, Y., Pulver, S.R., Renninger, S.L., Baohan, A., Schreiter, E.R., Kerr, R.A., Orger, M.B., Jayaraman, V., et al. (2013). Ultrasensitive fluorescent proteins for imaging neuronal activity. Nature *499*, 295–300.

Colantuoni, A., Bertuglia, S., and Intaglietta, M. (1984). Effects of anesthesia on the spontaneous activity of the microvasculature. Int. J. Microcirc. Clin. Exp. *3*, 13–28.

Cox, R.W. (1996). AFNI: software for analysis and visualization of functional magnetic resonance neuroimages. Comput. Biomed. Res. *29*, 162–173.

Curtis, A.T., Hutchison, R.M., and Menon, R.S. (2014). Phase based venous suppression in resting-state BOLD GE-fMRI. Neuroimage *100*, 51–59.

Delorme, A., and Makeig, S. (2004). EEGLAB: an open source toolbox for analysis of single-trial EEG dynamics including independent component analysis. J. Neurosci. Methods *134*, 9–21.

Devor, A., Dunn, A.K., Andermann, M.L., Ulbert, I., Boas, D.A., and Dale, A.M. (2003). Coupling of total hemoglobin concentration, oxygenation, and neural activity in rat somatosensory cortex. Neuron *39*, 353–359.

Drew, P.J., Duyn, J.H., Golanov, E., and Kleinfeld, D. (2008). Finding coherence in spontaneous oscillations. Nat. Neurosci. *11*, 991–993.

Drew, P.J., Shih, A.Y., Driscoll, J.D., Knutsen, P.M., Blinder, P., Davalos, D., Akassoglou, K., Tsai, P.S., and Kleinfeld, D. (2010). Chronic optical access through a polished and reinforced thinned skull. Nat. Methods *7*, 981–984.

Drew, P.J., Shih, A.Y., and Kleinfeld, D. (2011). Fluctuating and sensory-induced vasodynamics in rodent cortex extend arteriole capacity. Proc. Natl. Acad. Sci. USA *108*, 8473–8478.

Du, C., Volkow, N.D., Koretsky, A.P., and Pan, Y. (2014). Low-frequency calcium oscillations accompany deoxyhemoglobin oscillations in rat somatosensory cortex. Proc. Natl. Acad. Sci. USA *111*, E4677–E4686.

Duvernoy, H.M., Delon, S., and Vannson, J.L. (1981). Cortical blood vessels of the human brain. Brain Res. Bull. *7*, 519–579.

Fox, M.D., and Raichle, M.E. (2007). Spontaneous fluctuations in brain activity observed with functional magnetic resonance imaging. Nat. Rev. Neurosci. *8*, 700–711.

Glover, G.H., Li, T.Q., and Ress, D. (2000). Image-based method for retrospective correction of physiological motion effects in fMRI: RETROICOR. Magn. Reson. Med. *44*, 162–167.

He, B.J., Snyder, A.Z., Zempel, J.M., Smyth, M.D., and Raichle, M.E. (2008). Electrophysiological correlates of the brain's intrinsic large-scale functional architecture. Proc. Natl. Acad. Sci. USA *105*, 16039–16044.

Hirsch, S., Reichold, J., Schneider, M., Szé kely, G., and Weber, B. (2012). Topology and hemodynamics of the cortical cerebrovascular system. J. Cereb. Blood Flow Metab. *32*, 952–967.

Hu, X., Le, T.H., Parrish, T., and Erhard, P. (1995). Retrospective estimation and correction of physiological fluctuation in functional MRI. Magn. Reson. Med. *34*, 201–212.

Hundley, W.G., Renaldo, G.J., Levasseur, J.E., and Kontos, H.A. (1988). Vasomotion in cerebral microcirculation of awake rabbits. Am. J. Physiol. *254*, H67–H71.

Hutchinson, E.B., Stefanovic, B., Koretsky, A.P., and Silva, A.C. (2006). Spatial flow-volume dissociation of the cerebral microcirculatory response to mild hypercapnia. Neuroimage *32*, 520–530.

Iadecola, C. (2004). Neurovascular regulation in the normal brain and in Alzheimer's disease. Nat. Rev. Neurosci. *5*, 347–360.

Iadecola, C. (2013). The pathobiology of vascular dementia. Neuron *80*, 844–866.

Intaglietta, M. (1990). Vasomotion and flowmotion: physiological mechanisms and clinical evidence. Vasc. Med. Rev. *1*, 101–112.

Kim, S.G., Hendrich, K., Hu, X., Merkle, H., and Uğurbil, K. (1994). Potential pitfalls of functional MRI using conventional gradient-recalled echo techniques. NMR Biomed. *7*, 69–74.

Kleinfeld, D., Mitra, P.P., Helmchen, F., and Denk, W. (1998). Fluctuations and stimulus-induced changes in blood flow observed in individual capillaries in layers 2 through 4 of rat neocortex. Proc. Natl. Acad. Sci. USA *95*, 15741–15746.

Lee, S.P., Silva, A.C., Ugurbil, K., and Kim, S.G. (1999). Diffusion-weighted spin-echo fMRI at 9.4 T: microvascular/tissue contribution to BOLD signal changes. Magn. Reson. Med. *42*, 919–928.

Logothetis, N.K., Pauls, J., Augath, M., Trinath, T., and Oeltermann, A. (2001). Neurophysiological investigation of the basis of the fMRI signal. Nature *412*, 150–157.

Longden, T.A., Dabertrand, F., Koide, M., Gonzales, A.L., Tykocki, N.R., Brayden, J.E., Hill-Eubanks, D., and Nelson, M.T. (2017). Capillary K+-sensing initiates retrograde hyperpolarization to increase local cerebral blood flow. Nat. Neurosci. *20*, 717–726.

Ma, Y., Shaik, M.A., Kozberg, M.G., Kim, S.H., Portes, J.P., Timerman, D., and Hillman, E.M. (2016). Resting-state hemodynamics are spatiotemporally coupled to synchronized and symmetric neural activity in excitatory neurons. Proc. Natl. Acad. Sci. USA *113*, E8463–E8471.

Mandeville, J.B., Marota, J.J., Kosofsky, B.E., Keltner, J.R., Weissleder, R., Rosen, B.R., and Weisskoff, R.M. (1998). Dynamic functional imaging of relative cerebral blood volume during rat forepaw stimulation. Magn. Reson. Med. *39*, 615–624.

Mandeville, J.B., Marota, J.J., Ayata, C., Zaharchuk, G., Moskowitz, M.A., Rosen, B.R., and Weisskoff, R.M. (1999). Evidence of a cerebrovascular postarteriole windkessel with delayed compliance. J. Cereb. Blood Flow Metab. *19*, 679–689.

Mansfield, P., Maudsley, A.A., and Baines, T. (1976). Fast Scan Proton Density Imaging by Nmr. J. Phys. E Sci. Instrum. *9*, 271–278.

Mateo, C., Knutsen, P.M., Tsai, P.S., Shih, A.Y., and Kleinfeld, D. (2017). Entrainment of arteriole vasomotor fluctuations by neural activity is a basis of blood-oxygenation-level-dependent "resting-state" connectivity. Neuron *96*, 936–948.e3.

Mayhew, J.E., Askew, S., Zheng, Y., Porrill, J., Westby, G.W., Redgrave, P., Rector, D.M., and Harper, R.M. (1996). Cerebral vasomotion: a 0.1-Hz oscillation in reflected light imaging of neural activity. Neuroimage *4*, 183–193.

McKeown, M.J., Hansen, L.K., and Sejnowsk, T.J. (2003). Independent component analysis of functional MRI: what is signal and what is noise? Curr. Opin. Neurobiol. *13*, 620–629.

Menon, R.S., Ogawa, S., Tank, D.W., and Uğurbil, K. (1993). Tesla gradient recalled echo characteristics of photic stimulation-induced signal changes in the human primary visual cortex. Magn. Reson. Med. *30*, 380–386.

Mitra, P.P., Ogawa, S., Hu, X., and Uğurbil, K. (1997). The nature of spatiotemporal changes in cerebral hemodynamics as manifested in functional magnetic resonance imaging. Magn. Reson. Med. *37*, 511–518.

Moon, C.H., Fukuda, M., and Kim, S.G. (2013). Spatiotemporal characteristics and vascular sources of neural-specific and -nonspecific fMRI signals at submillimeter columnar resolution. Neuroimage *64*, 91–103.

Murphy, K., Birn, R.M., and Bandettini, P.A. (2013). Resting-state fMRI confounds and cleanup. Neuroimage *80*, 349–359.

O'Brien, J.T., Erkinjuntti, T., Reisberg, B., Roman, G., Sawada, T., Pantoni, L., Bowler, J.V., Ballard, C., DeCarli, C., Gorelick, P.B., et al. (2003). Vascular cognitive impairment. Lancet Neurol. *2*, 89–98.

Obrig, H., Neufang, M., Wenzel, R., Kohl, M., Steinbrink, J., Einhäupl, K., and Villringer, A. (2000). Spontaneous low frequency oscillations of cerebral hemodynamics and metabolism in human adults. Neuroimage *12*, 623–639.

Pan, W.J., Thompson, G.J., Magnuson, M.E., Jaeger, D., and Keilholz, S. (2013). Infraslow LFP correlates to resting-state fMRI BOLD signals. Neuroimage *74*, 288–297.

Poels, M.M., Ikram, M.A., van der Lugt, A., Hofman, A., Niessen, W.J., Krestin, G.P., Breteler, M.M., and Vernooij, M.W. (2012). Cerebral microbleeds are associated with worse cognitive function: the Rotterdam Scan Study. Neurology *78*, 326–333.

Poplawsky, A.J., Fukuda, M., Kang, B.M., Kim, J.H., Suh, M., and Kim, S.G. (2017). Dominance of layer-specific microvessel dilation in contrast-enhanced high-resolution fMRI: Comparison between hemodynamic spread and vascular architecture with CLARITY. NeuroImage. Published online August 16, 2017. https://doi.org/10.1016/j.neuroimage.2017.1008.1046.

Ratering, D., Baltes, C., Nordmeyer-Massner, J., Marek, D., and Rudin, M. (2008). Performance of a 200-MHz cryogenic RF probe designed for MRI and MRS of the murine brain. Magn. Reson. Med. *59*, 1440–1447.

Schaefer, A., Quinque, E.M., Kipping, J.A., Arélin, K., Roggenhofer, E., Frisch, S., Villringer, A., Mueller, K., and Schroeter, M.L. (2014). Early small vessel disease affects frontoparietal and cerebellar hubs in close correlation with clinical symptoms–a resting-state fMRI study. J. Cereb. Blood Flow Metab. *34*, 1091–1095.

Scheffler, K., and Ehses, P. (2016). High-resolution mapping of neuronal activation with balanced SSFP at 9.4 tesla. Magn. Reson. Med. *76*, 163–171.

Scheffler, K., and Lehnhardt, S. (2003). Principles and applications of balanced SSFP techniques. Eur. Radiol. *13*, 2409–2418.

Schölvinck, M.L., Maier, A., Ye, F.Q., Duyn, J.H., and Leopold, D.A. (2010). Neural basis of global resting-state fMRI activity. Proc. Natl. Acad. Sci. USA *107*, 10238–10243.

Schulz, K., Sydekum, E., Krueppel, R., Engelbrecht, C.J., Schlegel, F., Schröter, A., Rudin, M., and Helmchen, F. (2012). Simultaneous BOLD fMRI and fiber-optic calcium recording in rat neocortex. Nat. Methods *9*, 597–602.

Segal, S.S., and Duling, B.R. (1989). Conduction of vasomotor responses in arterioles: a role for cell-to-cell coupling? Am. J. Physiol. *256*, H838–H845.

Shajan, G., Kozlov, M., Hoffmann, J., Turner, R., Scheffler, K., and Pohmann, R. (2014). A 16-channel dual-row transmit array in combination with a 31-element receive array for human brain imaging at 9.4 T. Magn. Reson. Med. *71*, 870–879.

Shmuel, A., and Leopold, D.A. (2008). Neuronal correlates of spontaneous fluctuations in fMRI signals in monkey visual cortex: Implications for functional connectivity at rest. Hum. Brain Mapp. *29*, 751–761.

Silva, A.C., and Koretsky, A.P. (2002). Laminar specificity of functional MRI onset times during somatosensory stimulation in rat. Proc. Natl. Acad. Sci. USA *99*, 15182–15187.

Silva, A.C., Koretsky, A.P., and Duyn, J.H. (2007). Functional MRI impulse response for BOLD and CBV contrast in rat somatosensory cortex. Magn. Reson. Med. *57*, 1110–1118.

Smith, S.M., Fox, P.T., Miller, K.L., Glahn, D.C., Fox, P.M., Mackay, C.E., Filippini, N., Watkins, K.E., Toro, R., Laird, A.R., and Beckmann, C.F. (2009). Correspondence of the brain's functional architecture during activation and rest. Proc. Natl. Acad. Sci. USA *106*, 13040–13045.

Stevens, R.D., Hannawi, Y., and Sair, H. (2014). Small vessel disease and the resting functional architecture of the brain. J. Cereb. Blood Flow Metab. *34*, 1089–1090.

Stroh, A., Adelsberger, H., Groh, A., Rühlmann, C., Fischer, S., Schierloh, A., Deisseroth, K., and Konnerth, A. (2013). Making waves: initiation and propagation of corticothalamic Ca2+ waves in vivo. Neuron *77*, 1136–1150.

Tak, S., Polimeni, J.R., Wang, D.J., Yan, L., and Chen, J.J. (2015). Associations of resting-state fMRI functional connectivity with flow-BOLD coupling and regional vasculature. Brain Connect. *5*, 137–146.

van Rooden, S., Goos, J.D., van Opstal, A.M., Versluis, M.J., Webb, A.G., Blauw, G.J., van der Flier, W.M., Scheltens, P., Barkhof, F., van Buchem, M.A., and van der Grond, J. (2014). Increased number of microinfarcts in Alzheimer disease at 7-T MR imaging. Radiology *270*, 205–211.

van Veluw, S.J., Zwanenburg, J.J., Engelen-Lee, J., Spliet, W.G., Hendrikse, J., Luijten, P.R., and Biessels, G.J. (2013). In vivo detection of cerebral cortical microinfarcts with high-resolution 7T MRI. J. Cereb. Blood Flow Metab. *33*, 322–329.

Wang, L., Saalmann, Y.B., Pinsk, M.A., Arcaro, M.J., and Kastner, S. (2012). Electrophysiological low-frequency coherence and cross-frequency coupling contribute to BOLD connectivity. Neuron *76*, 1010–1020.

Yu, X., Wang, S.M., Chen, D.Y., Dodd, S., Goloshevsky, A., and Koretsky, A.P. (2010). 3D mapping of somatotopic reorganization with small animal functional MRI. NeuroImage *49*, 1667–1676.

Yu, X., Glen, D., Wang, S., Dodd, S., Hirano, Y., Saad, Z., Reynolds, R., Silva, A.C., and Koretsky, A.P. (2012). Direct imaging of macrovascular and microvascular contributions to BOLD fMRI in layers IV-V of the rat whisker-barrel cortex. Neuroimage *59*, 1451–1460.

Yu, X., Qian, C., Chen, D.Y., Dodd, S.J., and Koretsky, A.P. (2014). Deciphering laminar-specific neural inputs with line-scanning fMRI. Nat. Methods *11*, 55–58.

Yu, X., He, Y., Wang, M., Merkle, H., Dodd, S.J., Silva, A.C., and Koretsky, A.P. (2016). Sensory and optogenetically driven single-vessel fMRI. Nat. Methods *13*, 337–340.

Zhu, D.C., Tarumi, T., Khan, M.A., and Zhang, R. (2015). Vascular coupling in resting-state fMRI: evidence from multiple modalities. J. Cereb. Blood Flow Metab. *35*, 1910–1920.

STAR+METHODS

KEY RESOURCES TABLE

REAGENT or RESOURCE	SOURCE	IDENTIFIER
Antibodies		
Anti NeuN antibody	Merck	RRID: AB_2298772, Cat# MAB377
Secondary antibody (Goat Anti-Mouse)	Abcam	RRID: AB_10680176, Cat# ab97035
Bacterial and Virus Strains		
AAV5.Syn.GCaMP6f.WPRE.SV40	PENN Vector Core	Cat# AV-5-PV2822
Chemicals, Peptides, and Recombinant Proteins		
Isoflurane	CP-Pharma	Cat# 1214
Iron oxide nanoparticle: Molday ION	BioPhysics Assay Laboratory (BioPAL)	Cat# CL-30Q02-2
a-chloralose	Sigma-Aldrich	Cat# C0128-25G;RRID
pancuronium bromide	Inresa Arzneimittel	Cat# 34409.00.00
VECTASHIELD Antifade Mounting Medium with DAPI	Vector Laboratories	RRID: AB_2336790, Cat# H-1200
Phosphate Buffered Saline (PBS)	GIBCO	Cat# 10010-023
Experimental Models: Organisms/Strains		
Rat: Sprague Dawley rat	Charles River Laboratories	N/A
Software and Algorithms		
MATLAB	MathWorks	RRID:SCR_001622, https://www.mathworks.com/
AFNI	Cox, 1996	RRID: SCR_005927, http://afni.nimh.nih.gov
EEGLAB	Delorme and Makeig, 2004	RRID: SCR_007292, https://sccn.ucsd.edu/eeglab/index.html
Group ICA Of fMRI Toolbox (GIFT)	Medical Image Analysis Lab	RRID:SCR_001953, GIFT 4.0, http://mialab.mrn.org/software/gift/
Excel 2013	Microsoft	https://products.office.com/en-us/excel
Adobe Illustrator CC	Adobe	RRID: SCR_010279, http://www.adobe.com/products/illustrator.html
Other		
Biopac MP150 System	Biopac	RRID: SCR_014829
AcqKnowledge Software	Biopac	RRID: SCR_014279, https://www.biopac.com/product/acqknowledge-software/
Master-9	A.M.P.I	N/A
Nanoliter Injector	World Precision Instruments	Cat# NANOFIL
Laser (473 nm)	CNI	Cat# MBL-III
Dichroic mirrors	AHF Analysentechnik	Cat# F48-487
Fiber launch	Thorlabs	Cat# MBT613D/M
Optical fiber	Thorlabs	Cat# FT-200-EMT
Optical power meter	Thorlabs	Cat# PM20A
Optical filter	AHF Analysentechnik	Cat# F37-516
Silicon photomultiplier	SensL	Cat# MiniSM-10035-X08
Voltage amplifier	Femto	Cat# DHPVA-100
Tungsten Microelectrode	FHC	Cat# UEWSDDSMCN1M

CONTACT FOR REAGENT AND RESOURCE SHARING

Further information and requests for resources and reagents should be directed to and will be fulfilled by the Lead Contact, Dr. Xin Yu (xin.yu@tuebingen.mpg.de).

EXPERIMENTAL MODELS AND SUBJECT DETAILS

Animals

All experimental procedures were approved by the Animal Protection Committee of Tuebingen (Regierungspräsidium Tuebingen) and performed in accordance with the guidelines. Thirty-five male Sprague-Dawley rats were employed in all experiments. Littermates of the male rats (age: 2 - 3 months) were randomly assigned to experimental groups. Both evoked and resting-state bSSFP-fMRI data with A-V maps were acquired from five of nine rats under alpha-chloralose anesthesia, of which both BOLD and CBV signals were acquired under the same A-V map. To verify the effect of different drugs on vascular dynamic network connectivity, five rats were utilized for resting-state BOLD bSSFP-fMRI data under isoflurane anesthesia. In addition, the rats (BOLD: seven of eight, CBV: four of eight) with calcium indicator were employed for the statistics of simultaneous BOLD/CBV rsfMRI and fiber-optic calcium recording studies. Some rats were excluded from statistical analysis due to the large SSFP image distortion introduced by the optical fiber insertion. In addition, seven rats were employed to acquire simultaneous local field potential (LFP) and calcium signal.

Human Subjects

All human subject experiments follow the guidelines of the regulation procedure in the Max Planck Institute, and the informed consents were obtained from all human volunteers. For 3T MRI image acquisition, six healthy adult subjects (female, n = 3; male, n = 3; age: 20 - 35 years) were employed to obtain rsfMRI. For 9.4T MRI image acquisition, six healthy adult subjects (female, n = 2; male, n = 4; age: 20 - 35 years) were examined with Echo-planar imaging (EPI) sequence.

METHODS DETAILS

Animal experiments

Animal preparation

All procedures were described in a previous study (Yu et al., 2010). Rats were initially anesthetized with isoflurane (5% induction, 1.5% maintenance). Each rat was orally intubated and placed on a mechanical ventilator (SAR-830/AP, CWE). Plastic catheters were inserted into the right femoral artery and vein to allow monitoring of arterial blood gasses and administration of anesthetics. Two different anesthesia treatments were delivered during fMRI (Table S3). For alpha-chloralose anesthesia, after surgery, each rat was given an intravenous bolus of α-chloralose (60 mg/kg) and isoflurane was discontinued. Anesthesia was maintained with two constant infusion rates of α-chloralose (15 and 26.5 mg/kg/hr) in combination with pancuronium bromide (4 mg/kg/hr) to reduce motion artifacts. For isoflurane anesthesia, the ventilator maintained the rats breathing under isoflurane 1.2% in the magnet. The rats' rectal temperature was maintained at around 37°C. To prevent head motion, rats were secured in a head holder with a bite bar. All relevant physiological parameters (end-tidal CO2, rectal temperature, heart rate, and arterial blood pressure) were continuously monitored during imaging (Figure S3, blood pressure and heart rate). The pulse sequence–based trigger and stimulation control were established using the BioPac system (Goleta, USA) and Master-9 A.M.P.I system (Jerusalem, Israel).

Viral vector injection and optical fiber implantation

The viral vectors (AV-1-PV2822 AAV5.Syn.GCaMP6f.WPRE.SV40) were procured from University of Pennsylvania Vector Core (Chen et al., 2013). Viral vectors were injected in the barrel cortex (BC) or the forepaw region of the primary somatosensory cortex (S1FL) of 3 to 4 week old rats. For the stereotactic injection procedure, rats were initially anesthetized with isoflurane. After exposing the skull, a small bur hole was drilled. A nanoliter injector (WPI, FL) was used to place a 35-gauge needle at the proper coordinates in the stereotactic frame. Injections were performed slowly over 5–6 min and the needle was slowly removed after being kept in the injection site for 10 min after finishing the injection. The injection sites of BC were as follows with stereotactic coordinates: AP = -2.35 mm; ML: 4.8 mm; DV = 2; injections each 400 nL at 1.2 mm and 0.7 mm. The injection sites of S1FL were as follows: AP = 0.2 mm; ML = 3.7 mm; DV = 2 injections each 400 nL at 1.2 mm and 0.7 mm. After 6-8 weeks of viral expression, a 200-mm optical fiber (7 m length) was inserted through the burr holes on the skull into the BC (stereotactic coordinates: AP = -2.7 mm; ML = 5.1 mm; DV = 1.3 mm; tilt, 4°) or S1FL (AP = 0.2 mm; ML = 4 mm; DV = 1.3 mm). The optical fiber was fixed on the skull with glue. Then, the skin was sutured to cover the glue with the optical fiber extending outside of the rat head.

Simultaneous rsfMRI and calcium recording

The optical setup for calcium signal recording was built up based on a previous study (Schulz et al., 2012; M.W., Y.H., T.J. Sejnowski, and X.Y., unpublished data). As shown in Figure S4A, a 473 nm laser (MBC-III, CNI) was set to deliver the fluorescent excitation light. The laser beam was first aligned by a reflection mirror to a correct angle better deflect off a dichroic beam-splitting mirror (BS R488: reflection 471 - 491 nm, >94%; transmission 500 - 1200 nm, >93%; AHF Analysentechnik), which was coupled into a multimode fiber (FT200EMT: NA = 0.48, 230 mm cladding diameter; Thorlabs) via amplifying lens (RMS4X; Thorlabs). Fluorescence excitation occurred in the vicinity of the fiber tip inside the MRI scanner and the emitted fluorescence light was collected and guided back to the optical setup through the same fiber. The emitted fluorescent signal from the fiber passed a lens, dichroic mirror, and an emission filter (Semrock Razoredge; 488 Long Pass; AHF Analysentechnik), and was finally focused by a tube lens (AC254-030-A1-ML; Thorlabs) onto a peltier-cooled silicon photomultiplier with transimpedance preamplifier (MiniSM-10035-X08; SensL). The signal from the photomultiplier was amplified by voltage amplifier (DHPVA-100; Femto) and acquired by the analog input module of a Biopac

MP 150 system (5-K sampling rate). Triggers from the MRI scanner were also recorded by the Biopac system and used to synchronize calcium to BOLD fMRI offline. Laser intensity was measured at the fiber tip for neuronal calcium (rv5 uW) to avoid phototoxicity for long-term recording by optical power meters (PM20A; ThorLabs).

Simultaneous calcium with electrophysiology recording

The anesthetized rats were adapted in a stereotaxic device for *in vivo* recordings using similar anesthetics and surgical preparation to the fMRI experiments. Tungsten microelectrode (1 MU, rv100 mm, Tungsten, FHC) was bonded to an optical fiber with closely contacted fiber optic tip and electrode contacting point. The local field potential (LFP) was recorded through the EEG module of the Biopac system (gain factor, 5,000; band-pass filter, 0.02 - 100 Hz; sample rate, 5,000/s). In addition, calcium data and blood pressure were digitized and recorded with Biopac MP150 system at a sampling rate of 5 kHz. The spectrogram of LFP was calculated through multi-taper spectral estimation. (Figure 6, and S7, 1 s sliding window with 0.1 s steps, 9 tapers)

MRI image acquisition from rats

All images from rats were acquired with a 14.1 T/26 cm horizontal bore magnet (Magnex) interfaced to an Avance III console (Bruker). A transceiver surface coil with a 6-mm diameter was used to acquire images.

bSSFP-fMRI

Balanced Steady-State Free Precession was implemented with the following parameters: TE, 3.9 ms; TR, 7.8 ms; flip angle (FA), 12°; matrix, 96 3 128; FOV, 9.6 3 12.8 mm; slice thickness = 400 mm; in-plane resolution = 100 3 100 mm^2, resulting in one slice repetition time of 1 s. The block design was 2 s stimulation and 28 s inter-stimulus interval. The duration of each trial of rsfMRI was 15 min, and 2 - 5 trails of BOLD/CBV rsfMRI were acquired for each rat. CBV fMRI signals were acquired after intravenous injection of 15 - 20 mg of Fe/kg dextran-coated iron oxide (BioPAL, MA).

Single-vessel MGE imaging in rats

The imaging protocol was similar with our previous paper (Yu et al., 2016). To recognize individual arterioles and venules, we employed a 2D Multiple Gradient-Echo (MGE) sequence with the following parameters: TR = 50 ms; TE = 2.5, 5, 7.5, 10, 12.5 and 15 ms; flip angle = 40°; matrix = 192 3 192; in-plane resolution = 50 3 50 mm^2; slice thickness = 500 mm. We averaged the MGE images from the second echo to the fourth echo and created an arteriole-venule (A-V) map, where the venule voxels display as dark dots (blue marks) because of the fast T_2* decay but arteriole voxels remain bright (red marks) owing to the in-flow effect (Figure 1A).

MRI image acquisition from humans (3T)

All measurements were performed on a 3-T Siemens Prisma with a 20-channel receive head coil. Six healthy adult subjects (female, n = 3; male, n = 3; age: 20 - 35 years) were employed to obtain a BOLD signal using EPI with the following parameters: TR = 1,000 ms; TE = 29 ms; FA = 60°; matrix = 121 3 119; in-plane resolution = 840 mm x 840 mm; 9 slices with thicknesses of 1.5 mm. Parallel imaging (GRAPPA factor: 3) and partial Fourier (6/8) were employed to accelerate image acquisition. The visual stimulation consisted of a circular black and white checkerboard. For the resting state fMRI, the duration of each trial of rs-fMRI was 15 min with the eyes-closed condition. The Siemens physiologic Monitoring Unit (PMU) was used to monitor the respiration and pulse oximetry simultaneously. Both PMU physiological log files and EPI data contain time tags, which were utilized to synchronize the temporal profile for statistical analysis.

MRI image acquisition from humans (9.4 T)

All images were acquired with a 9.4-T MRI scanner (Siemens Healthcare, Erlangen, Germany) with a home-built 16-channel transmit/31-channel receive head coil (Shajan et al., 2014). All the imaging protocols follow those of the 3-T scanner but at a higher resolution. Six healthy subjects (female, n = 2; male, n = 4; age: 20 - 35 years) were examined with EPI sequence: TR = 1,000 ms; TE = 22 ms; FA = 50°; matrix = 300 3 300; in-plane resolution = 500 mm 3 500 mm; 9 slices a thicknesses of 0.8 mm. Parallel imaging (GRAPPA factor: 4) and partial Fourier (5/8) were utilized to accelerate image acquisition.

Single-vessel MGE imaging in humans

We utilized a 2D MGE sequence with the following parameters: TR = 61 ms; TE = 5.99, 10.39, 14.79, 19.19, 23.59, 27.99, 32.39, 36.79, 41.19, 45.59 ms; flip angle = 60°; matrix = 896 3 896; in-plane resolution = 19 3 19 mm^2; slice thickness = 1,000 mm. An arteriole-venule (A-V) map was acquired by averaging of the MGE images from the second echo to the ninth echo (Figure 8A).

Data processing

All data processing was performed using Analysis of Functional NeuroImages (AFNI) software (Cox, 1996) and MATLAB. The relevant fMRI analysis source codes can be downloaded through https://www.afni.nimh.nih.gov/afni/. A detailed description of the processing procedure conducted is provided in a previous study (Yu et al., 2012). To register the single-vessel functional map with the A-V map, the tag-based registration method was applied, which carried out ten to twelve tags (venule voxels) of the averaged bSSFP fMRI images corresponding to those of the A-V map. No additional smoothing step was applied. For evoked fMRI analysis, images were normalized by scaling the baseline to 100. Linear regression analysis was applied to estimate the hemodynamic response function. The beta estimates were used to indicate the amplitude of the BOLD response in the beta maps.

Definition of the individual vessel

The individual vessel voxels in A-V map were identified by the following algorithm: the intensities of arteriole/artery voxels are higher than the mean signal intensities plus two times the standard deviation (s.d.) of the local area in a 5 3 5 kernel, while the intensities of venule/vein voxels are lower than the mean signal intensities minus two times the s.d. of local area, as shown in Figure 1A (Yu et al., 2016). The locations of individual vessel voxels defined in the A-V map were employed to extract the time courses from BOLD/CBV fMRI of individual vessels.

Resting state fMRI analysis

The preprocessing analysis was performed using a modified AFNI resting state fMRI processing protocol (afni_proc.py). The time courses of the vessel seed voxels were chosen for correlation analysis. The vessel voxels from both arteriole and venules were determined based on the A-V map. The detailed image processing procedure utilized was described previously (Yu et al., 2016). Then the 3dTcorr1D function in AFNI was employed to generate the correlation map. In addition, ICA analysis was also performed to characterize the vessel specific correlation maps with the Independent Component Analysis (ICA) Toolbox (GIFT 4.0, MIND Research Network). The ICA toolbox employed principal component analysis (PCA) to realign the data at a lower dimensionality (or reduced variance in a simplified dimensional space). ICA was utilized to generate ten independent components using Infomax algorithms, which specialize in the separation of super-Gaussian sources (Bell and Sejnowski, 1995). After the back reconstruction step, the spatial maps and time courses of components were scaled using Z-scores. Finally, a RETROICOR algorithm (Glover et al., 2000) was implemented to correct physiological motion effects (Figure S8).

Power spectrum analysis

Depending on data format, power spectrum analysis was performed in AFNI (image format) or MATLAB (text format). In AFNI, a 3dPeriodogram function was utilized to compute the power spectrum of time courses in all individual voxels. Then the averaged power spectral density was calculated in venule voxels or arteriole voxels, respectively (FFT length: 256, Figures S6B and S6D). In MATLAB, we employed Fast Fourier Transform (FFT) to calculate the power spectral density of the physiologic data (respiration/pulse oximetry) (Figure S8F) and calcium data (Figure S6F). The calcium signals under light/deep anesthesia were sampled at 1 Hz and calculated by Welch's power spectral density estimate method (FFT length: 256, the overlap: 50%).

Coherence analysis

Previously, coherence analysis was implemented to identify the functional connectivity between different brain areas (Drew et al., 2008; Wang et al., 2012). For this study, to investigate the interactions of paired vessels, coherence analysis was employed as an indicator of functional interactions and indicator of how well the seed vessel corresponds to other vessel voxels at different frequency ranges. The definition of coherence is as follows:

$$Coh_{xy}(f) = \frac{t \quad t}{t P_{xy}(f) t_2}{P_{xx}(f) P_{yy}(f)}$$

where x indicates the fMRI signal from one seed vessel, y represents the fMRI time course from another vessel. $P_{xx}(f)$ and $P_{yy}(f)$ are the power spectral densities of x and y, respectively, and $P_{xy}(f)$ is the cross power spectral density of x and y. The coherence was calculated by using Welch's overlapped averaged periodogram method with FFT (256-point length) and a 256 s Hamming window, which divides x and y into equal overlapping sections (240-point overlap, >90% overlap). The frequency resolution of coherence is 1 / 256 s = 0.0039 Hz which provides enough resolution to observe the slow frequency range.

The calcium data analysis

The calcium signal was down-sampled to one TR per sample. Next, zero-phase digital filtering (0.01 - 0.1 Hz) was employed to obtain the slow fluctuation of the calcium signal (filtfilt function in MATLAB). In addition, a cross-correlation between the slow fluctuation of the calcium signal and individual venules was performed using the MATLAB function xcorr (Figures 4E and 4L). A 3ddelay function from the AFNI library was utilized to estimate the time lag map between the slow fluctuation of the calcium signal with BOLD fMRI of venules (CC > 0.25) (Figure 4C, inset) or CBV fMRI of arterioles (CC < -0.25) (Figure 4J, inset). For the spectrogram of the calcium signal, a function timefreq from EEGLAB (Delorme and Makeig, 2004) was employed to get the averaged power of the spontaneous calcium spikes (Figures 5B and 6A). A time-varying power spectrogram of calcium signal was computed by using the discrete Fourier transform with a sliding Humming window. The sliding window was 1000 ms without overlap to match one TR of BOLD fMRI data.

Immunohistochemistry

After the conclusion of the fMRI experiments, the rat brain tissues were perfused using a 4% paraformaldehyde fixative. The tissues were then transferred the to 15% sucrose in PBS and keep overnight at 4°C. Next, the prefixed tissues were moved to 30% sucrose in PBS. After sinking, the tissues were stored at -80°C until use. The tissues were also utilized to prepare coronal sequential brain sections (30-mm thickness, -20°C using Leica CM3050S microtome). The sections were incubated overnight at 4°C with primary antibodies: mouse anti-NeuN (1:200; Merck). Afterward, sections were washed five times with PBS and incubated for 60 min with the secondary antibodies: goat anti-mouse conjugated with CY3 (1:500; Abcam). Finally, mounting medium with DAPI (VectaShield, vector) was utilized to protect the fluorescence signal and reveal nuclei. The expression position of GCaMP was confirmed by colocalization with NeuN using a fluorescence microscope (ApoTome, Zeiss).

QUANTIFICATION AND STATISTICAL ANALYSIS

A paired Student's t test was performed to compare the coherence values of paired venules/veins and paired arterioles/arteries in the rat and human resting-state fMRI data. The data with error bars are displayed as the means ± SEM. The p values < 0.05 were considered statistically significant. The sample size for animal experiments was not previously estimated. The sample size for human experiments was estimated based on the statistical parameters derived from the animal data using G* power analysis. No blinding and randomization design was needed in this work.

Movie legend

MovieS1: The seed-based bSSFP BOLD rs-fMRI in the anesthetized rat brain. (Related to Figure 2)

The white arrow indicates the location of the seed (radius:150μm). When the seed is moved to dark dots (venulevoxels), most venule voxels are highly correlated but less so for arteriole voxels.

MovieS2: The seed-based bSSFP CBV rs-fMRI in the anesthetized rat brain. (Related to Figure 2)

The white arrow indicates the position of the seed (radius:150μm). When the seed is moved to bright dots (arteriolevoxels), most arteriole voxels are highly correlated but less so for venule voxels.

MovieS3: The evoked BOLD fMRI signal with voxel-wise time courses in the human brain. (Related to Figure 5)

With the visual stimulation (8Hz checker board stimulation), the voxel-wise BOLD fMRI signal changes (leftpanel) are shown from 5x5 voxel matrix covering one individual vein through sulcus (the dark voxel in the green square, middle panel). The red cursor in the timecourse is corresponding to the color-coded BOLD functional movie time (rightpanel).

MovieS4:The seed-based rs-fMRI in the human brain. (Related to Figure 5)

The white arrow indicates the location of the seed (radius:1mm). The seed-based correlation maps by the resting-state fMRI demonstrates vein-dominated correlation spatial patterns.

MovieS5: Vascular dynamic network connectivity using ICA Analysis in human at restingstate. (Related to Figure 5)

The left panel exhibits the ICA-based correlation maps with the averaged EPI images as the background (dark voxels as veins). The video demonstrates the highly correlated venous voxels at multiple slices, showing a 3D vascular dynamic correlation structure (Z-scores>1.5) through the main branches of the cerebral vasculature.

A.3 Sensory and optogenetically driven single-vessel fMRI

Sensory and optogenetically driven single-vessel fMRI

Sensory and optogenetically driven single-vessel fMRI

Xin Yu[1], Yi He[1], Maosen Wang[1], Hellmut Merkle[2], Stephen J Dodd[2], Afonso C Silva[2] & Alan P Koretsky[2]

Magnetic resonance imaging (MRI) sensitivity approaches vessel specificity. We developed a single-vessel functional MRI (fMRI) method to image the contribution of vascular components to blood oxygenation level–dependent (BOLD) and cerebral blood volume (CBV) fMRI signal. We mapped individual vessels penetrating the rat somatosensory cortex with 100-ms temporal resolution by MRI with sensory or optogenetic stimulation. The BOLD signal originated primarily from venules, and the CBV signal from arterioles. The single-vessel fMRI method and its combination with optogenetics provide a platform for mapping the hemodynamic signal through the neurovascular network with specificity at the level of individual arterioles and venules.

MAIN TEXT

fMRI maps brain activity by means of tight coupling of hemodynamic responses in the local vasculature to neural activity[1–4]. However, this neurovascular coupling limits fMRI specificity, because of the complexity of the hemodynamic response[3,5–7]. Given the large voxel size (on the order of millimeters) and slow acquisition time (on the order of seconds) of conventional fMRI, detailed high-resolution hemodynamic responses are usually not sampled[2–4]. The spatial discrepancy between the vascular origin of the fMRI signal and the neural source that produces the vascular response remains a concern for fMRI brain mapping.

Recently, high magnetic field strengths have made it possible to acquire high-spatiotemporal-resolution fMRI images with increased signal-to-noise ratios[8,9]. These increased signal-to-noise ratios have been used to improve spatial and/or temporal resolution in order to localize BOLD signal to venules in the rat somatosensory cortex[10] and correlate a punctate pattern of CBV signal to arterioles in the cat visual cortex[11]. Furthermore, very high-temporal-resolution fMRI has detected fMRI onset at specific cortical layers coinciding with neural projection inputs[5]. In human brains, layer-dependent fMRI signal was mapped by gradient-echo BOLD and vascular space occupancy–based CBV methodologies at submillimeter resolution[12]. However, no study has mapped the fMRI signal from individual vessels in deep cortical layers with sampling rates sufficient to define the response. Here we developed a strategy to enable direct imaging of both arteriole and venule responses to neural activity at 100-ms resolution.

Previously, a conventional fMRI–echo-planar imaging (EPI) method[13] was used to characterize BOLD signal from distinct vascular components in midcortical layers of the rat somatosensory cortex[10]. One can map different vascular responses by CBV fMRI with iron oxide–particle injection using the EPI method (**Supplementary Fig. 1** and **Supplementary Note 1**). Recently we adapted a line-scanning scheme to the fast low-angle shot (FLASH) fMRI method and achieved very high temporal resolution[5,9] (**Supplementary Fig. 2**). We used the FLASH fMRI method to map BOLD and CBV fMRI signal from 2D slices acquired perpendicular to the vessels penetrating the midcortical layers of somatosensory cortex of anesthetized rats (**Supplementary Figs. 3–5**, **Supplementary Video 1** and **Supplementary Note 1**). In contrast to the positive BOLD signal, which was mainly due to the increased ratio of oxygenated to deoxygenated blood in venules, the negative CBV signal was caused by activity-evoked vasodilation leading to increased blood volume, more iron oxide particles, a shorter T2* relaxation time and, therefore, less signal in the imaged vessels. Vasodilation has been attributed to arterioles, and there are reports of vein and venule dilation as well[14]. In addition, changes in capillary diameter could be a major contributor to or initiator of changes in cerebral blood volume[15]. To detect single-vessel responses driven by sensory (i.e., electrical stimulation of the forepaw or whisker pad) or optogenetic stimulation through a fiber optic directly targeting the cortex, we used a multigradient-echo (MGE) sequence to anatomically map individual arterioles and venules penetrating the midcortical layers of somatosensory cortex. The blood flow delineates vessels: unsaturated MRI signal from blood flowing into a slice can be detected as brighter signal in vessels[16]. In this study, the specific in-flow effect resulted in brighter signal in both arterioles and venules compared with surrounding voxels (**Fig. 1a**). The deoxygenated blood in venules has a shorter T2* than surrounding tissues and arterioles, which leads to less signal only in venules at longer TE (time to echo). Here arterioles and surrounding tissues had a similar but longer T2*, and thus brighter signal, compared with venules (**Fig. 1a** and **Supplementary Fig. 6**), consistent with previous results[17]. MGE images acquired at different TEs enabled us to create an anatomical map of penetrating arterioles and venules (A-V map) (**Fig. 1b**). Using the FLASH fMRI method, we were able to detect both BOLD and CBV fMRI signal from the same 2D slice for the A-V map. The peak BOLD signal overlapped primarily with penetrating venule regions of interest (ROIs), and the peak CBV signal overlapped primarily with penetrating arteriole ROIs (**Fig. 1c** and **Supplementary Videos 2–9**). 3D and 2D plots of the vessel-specific spatial distribution of BOLD and CBV fMRI signal as a function of the normalized signal intensity of individual voxels from the A-V map showed peak CBV signal on arteriole voxels, whereas the peak BOLD signal was on venule voxels (**Fig. 1d**,**e**

[1]High Field Magnetic Resonance Department, Max Planck Institute for Biological Cybernetics, Tuebingen, Germany. [2]Laboratory of Functional and Molecular Imaging, National Institute of Neurological Disorders and Stroke, US National Institutes of Health, Bethesda, Maryland, USA. Correspondence should be addressed to X.Y. (xin.yu@tuebingen.mpg.de) or A.P.K. (korestkya@mail.nih.gov).

RECEIVED 29 MAY 2015; ACCEPTED 7 JANUARY 2016; PUBLISHED ONLINE 8 FEBRUARY 2016; CORRECTED ONLINE 29 FEBRUARY 2016 (DETAILS ONLINE); DOI:10.1038/NMETH.3765

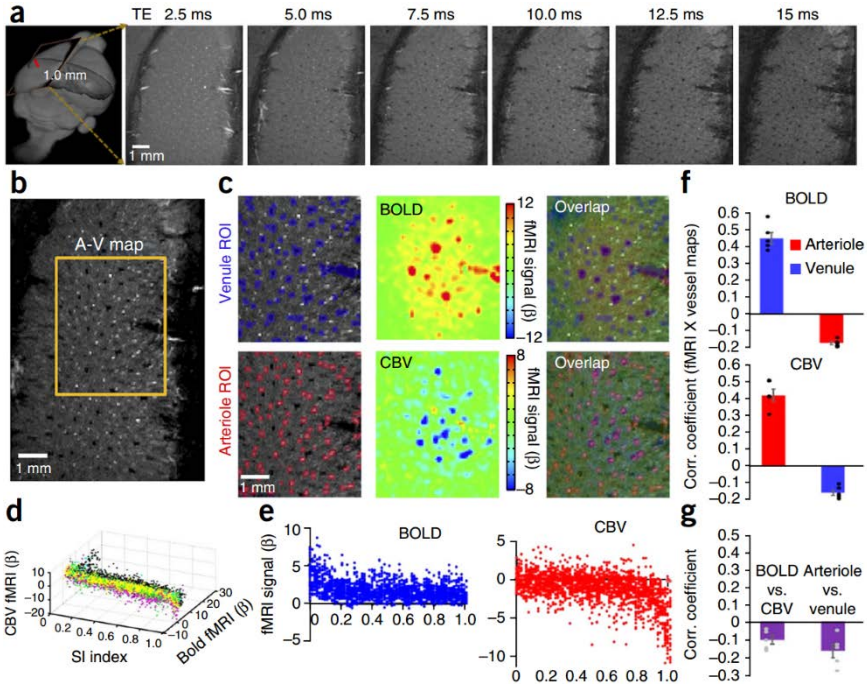

Figure 1 | Single-vessel fMRI overlaps with the A-V map. (**a**) 2D MGE slices from a deep layer of the forepaw S1 cortex (1.0–1.5 mm, left) at different TEs (representative images from experiments with seven rats). (**b**) The A-V map derived from the images in **a**. Arterioles and venules appear as bright and dark voxels, respectively. (**c**) Zoomed views of the area outlined in **b** with venule and arteriole ROIs highlighted, BOLD and CBV fMRI maps of the same 2D slice, and overlap (active voxels are in purple in overlap images). **(d)** Distribution of BOLD and CBV signals as a function of voxel normalized signal intensity (SI) in A-V maps ($n = 5$, denoted by different colors of plotted points). (**e**) A 2D plot of BOLD and CBV fMRI signals from individual voxels as a function of voxel signal intensity in A-V maps (representative of one data set from **d**). (**f**) The spatial correlation (Corr.) coefficients of BOLD and CBV functional maps with represent the coefficients of individual rats ($n = 5$); mean ± s.e.m.). Significant differences were noted between arterioles and venules for both signals (BOLD, $P = 0.00002$; CBV, $P = 0.0003$; Student's *t*-test). (**g**) The spatial correlation coefficients of the functional maps (BOLD versus CBV) and the single-vessel ROI maps (arteriole versus venule) (mean ± s.e.m.). Gray dots represent the coefficients of individual rats ($n = 5$). In **a** and **c**, scale bar applies to all images in the panel.

and **Supplementary Video 10**). The spatial correlation coefficient of BOLD functional maps with venule ROI maps was significantly higher than that with arteriole ROI maps, whereas the opposite was true for CBV functional maps (**Fig. 1f**). Spatial correlation was negative for BOLD with arterioles and for CBV with venules. Negative spatial correlation coefficients were also detected for BOLD versus CBV functional maps and for arteriole versus venule ROI maps (**Fig. 1g**), indicating that most of the BOLD responses came from venules (in agreement with recent work[10]) and that most of the CBV responses came from arterioles[11,12]. Thus the single-vessel method made it possible to identify the hemodynamic signal from individual arterioles and venules.

The discovery of channelrhodopsin 2 (ChR2) as a light-sensitive cation membrane channel has made it possible to control neural activity optogenetically by targeting specific cell types in neural circuits[18,19]. Optogenetics has been used to initiate fMRI signals[20]. The temporal and spatial features of the hemodynamic signal evoked by optogenetic stimulation were assessed by optical measurement of oxygenated versus deoxygenated hemoglobin in the somatosensory cortex[21], as well as with BOLD fMRI[22,23], although not at the single-vessel level. To determine whether the hemodynamic features of such fMRI signals are similar to those of signals evoked with more physiological stimulation, we optogenetically evoked neural activity with a fiber optic inserted into rat whisker barrel cortex expressing ChR2 (**Fig. 2a**). Recordings of the local field potential indicated robust responses upon optical stimulation (**Supplementary Fig. 7**). We mapped BOLD and CBV signal with EPI-fMRI in the region close to the tip of the fiber optic (**Fig. 2b** and **Supplementary Fig. 8**) and aligned the A-V map to specify individual arterioles and venules near the tip (**Fig. 2c**). The light-driven BOLD signal was located primarily at venule voxels, whereas the CBV signal was located primarily at arteriole voxels (**Fig. 2d** and **Supplementary Videos 11** and **12**). The average time courses of BOLD and CBV signal from venule and arteriole ROIs showed similar temporal patterns with both sensory and optogenetic stimuli (**Fig. 2e**,**f**).

To quantitatively compare optogenetically activated and sensory-evoked hemodynamic signals, we fit BOLD and CBV signals from individual arterioles and venules to estimate the onset time (t_0), the time to peak (ttp) and the full-width at half-maximum (FWHM) (**Supplementary Figs. 9**–**11**). The CBV signals of individual arterioles showed earlier onset (t_0) and ttp than did the BOLD signals of individual venules for both sensory stimulation and optogenetics (**Fig. 3a** and **Supplementary Fig. 9**). However, there were a few very early BOLD responding venules and a few arterioles with late onset of CBV signal (**Supplementary Fig. 12** and **Supplementary Note 1**). We analyzed the BOLD signals from individual arterioles (**Supplementary Fig. 10**) and the CBV signals from individual venules (**Supplementary Fig. 11**) to characterize specific vascular contributions to BOLD and CBV fMRI signal, respectively (discussed in **Supplementary Note 1**). The t_0, ttp and FWHM plots of the single-vessel BOLD and CBV signals readily separated into distinct clusters of arterioles and venules (**Fig. 3b**,**c** and **Supplementary Videos 13** and **14**). The temporal parameters of the optogenetically activated fMRI signal showed little difference in comparison to the sensory stimulation–evoked fMRI signal acquired via either 11.7-T or 14-T MRI (**Supplementary Fig. 13** and **Supplementary Table 1**; Student's *t*-test). Thus, the temporal features of hemodynamic signal propagating through the cerebrovascular network were similar for optogenetic and sensory stimulation–evoked neural activity.

Two-photon microscopy is increasingly used to image vessels in the cortex[24–26]. The single-vessel fMRI method has three potential benefits as compared to optical imaging. First, we were able to detect fMRI signal from individual penetrating vessels in midcortical layers. Using this strategy, it should be possible to map single vessels located in subcortical brain regions such as the hippocampus. Second, it is possible to use the full range of MRI techniques to enable

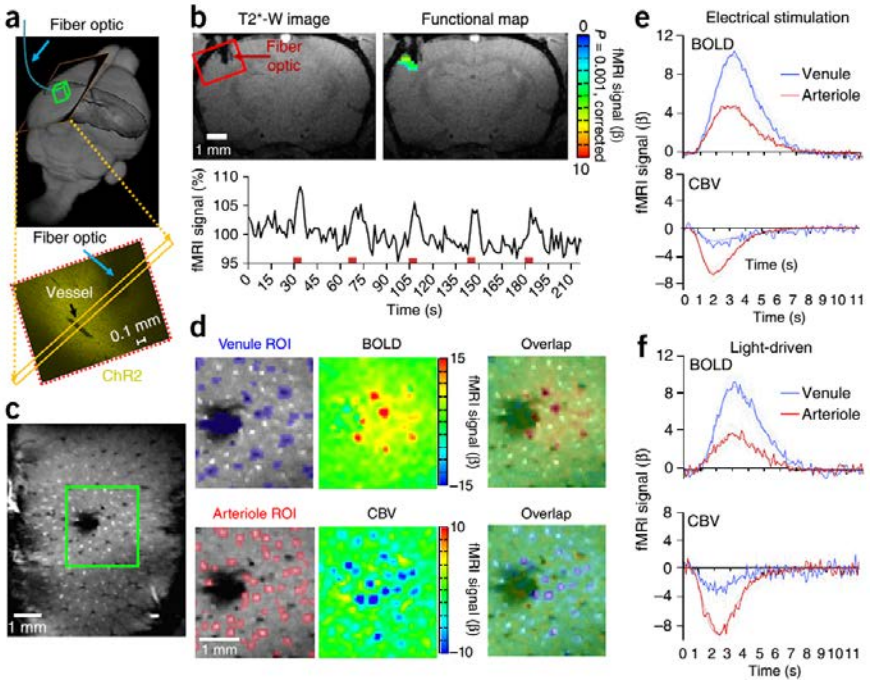

Figure 2 | Optogenetically induced fMRI signal from single vessels penetrating the barrel cortex. (**a**) Overview of optogenetically driven single-vessel fMRI and a histological section (from the boxed area in **b**) showing ChR2 expression. The blue arrows show the ic entry point; the black arrow points out a penetrating vessel. The yellow rectangle encloses the area imaged by single-vessel fMRI. Images are representative of experiments with nine rats. (**b**) Top left, T2*-weighted (T2*-W) image with the fiber optic inserted into the barrel cortex. Top right, overlay of the optogenetically induced fMRI signal on the T2*-weighted image. The average time course from the indicated cortical area (bottom) shows corresponding fMRI signal changes with the block-design paradigm (illumination: 5 s on/30 s off, 5 epoch, 20-ms light pulse, 10 Hz, 3.2 mw). (**c**) A-V map with venule (bright) and arteriole (dark) voxels. The dark area in the center indicates the position of the fiber optic. The green box outlines the area shown in **d**. (**d**) Venule and arteriole ROIs on the A-V maps (left) , BOLD and CBV fMRI maps (center) and overlap (BOLD, top; CBV, bottom). (e) The average BOLD and CBV fMRI time courses from individual arterioles and venules after sensory stimulation of the forepaw. (BOLD, $n = 7$ rats; CBV, $n = 5$ rats; all ROIs were averaged for each rat. The mean values shown are of the averages for all rats in each group; gray region denotes error (±s.e.m.).) (f) The average BOLD and CBV fMRI time courses from individual arterioles and venules driven by optogenetic stimulation of the barrel cortex ($n = 4$ rats; gray region denotes error (±s.e.m.); illumination: 20 ms, 10 Hz, 3.2 mw (light pulse on for 2 s)). In **b** and **d**, scale bar applies to all images in the panel.

coregistration of anatomy, connectivity and fMRI in order to obtain complementary information. It might even become possible to extend the single-vessel mappings to the human brain as sensitivity increases with the emerging high-field MRI. Third, fMRI can be performed without any invasive procedures on animal subjects, as opposed to optical imaging, which requires window or thin skull preparations and possibly the insertion of optical equipment into the brain. Moreover, the fMRI signal could be acquired with temporal resolution similar to that of optical microscopy. In the current study we acquired data at a 100-ms temporal interval, which represents a sampling rate similar to that of optical brain imaging methods, in which the temporal resolution ranges from 9–18 Hz for fields of view on the submillimeter scale.

A question that arose during this work was how well individual penetrating arterioles and venules were characterized in the cortex. The average distance between venule voxels measured in the present work was 372 ± 33 μm, and that between arterioles was 286 ± 15 μm (mean ± s.e.m.). These values are in agreement with the known spacing of these vessels, indicating that the majority of penetrating vessels were detected[26]. The established size of penetrating vessels separated by a few hundred micrometers ranges from 30 to 70 μm (ref. 26). We acquired the A-V map with an in-plane resolution of 75 × 75 μm or 50 × 50 μm, which is close to the mean size of the main penetrating vessels (**Fig. 2** and **Supplementary Fig. 8**). The brightest voxels of A-V maps were usually detected within a 2 × 2 voxel matrix, implying that the in-flow effect was sufficient to highlight individual arterioles smaller than the voxels. Darker voxels representing penetrating venules were larger than the actual venules because of the extravascular dephasing effect of deoxygenated hemoglobin in venule blood[27]. Different vessel sizes with potentially different orientation angles probably led to variation in the signal intensity of vessel voxels. The arterioles and venules were identified on the basis of a nearest-neighbor variation analysis; however, it is likely that some smaller penetrating vessels were not identified. It is important to note that in this study, "single vessel" refers to the arteriole or venule voxels in the A-V map that could be detected under the imaging condition used.

This work shows that the peak BOLD signal aligned with venule voxels and the peak CBV signal aligned with arteriole voxels. The t_0 and ttp of the CBV signal from arterioles was comparable to the temporal-onset estimates of arteriole dilation detected with two-photon microscopy at a 0.5-mm cortical depth[25]. This observation was also consistent with BOLD and CBV studies performed in cats[11] and humans[12] to show the early onset of CBV signals. The mean t_0 of BOLD signal in venules (0.96 ± 0.04 s, mean ± s.e.m.) was slightly faster than what was previously reported for macrovenules detected by EPI-fMRI methods[10]. In a previous study, Hutchinson *et al.* measured[24] the transit time (calculated using the time to half-maximum ($t_{1/2}$)) from surface arterioles to venules as 0.8–1.2 s with two-photon microscopy. The average transit time estimated in the present study was ~0.8 s on the basis of the mean time-to-peak difference from arteriole CBV to venule BOLD signal in the mid-cortical layers (**Supplementary Note 1**). The MRI-defined transit time was on the lower end of the range of transit times measured by optical microscopy[24], which may be explained by differences in the induction of vessel dilation, in the imaged capillary network and in the definition of transit time. The estimated transit time based on comparison of arteriole and venule fMRI signals illustrates that vessel-specific hemodynamic signal propagation can be measured with the single-vessel fMRI method.

In conclusion, we were able to characterize distinct arteriole CBV and venule BOLD signals with 100-ms temporal resolution. The vascular kinetics of light-driven and sensory-evoked fMRI

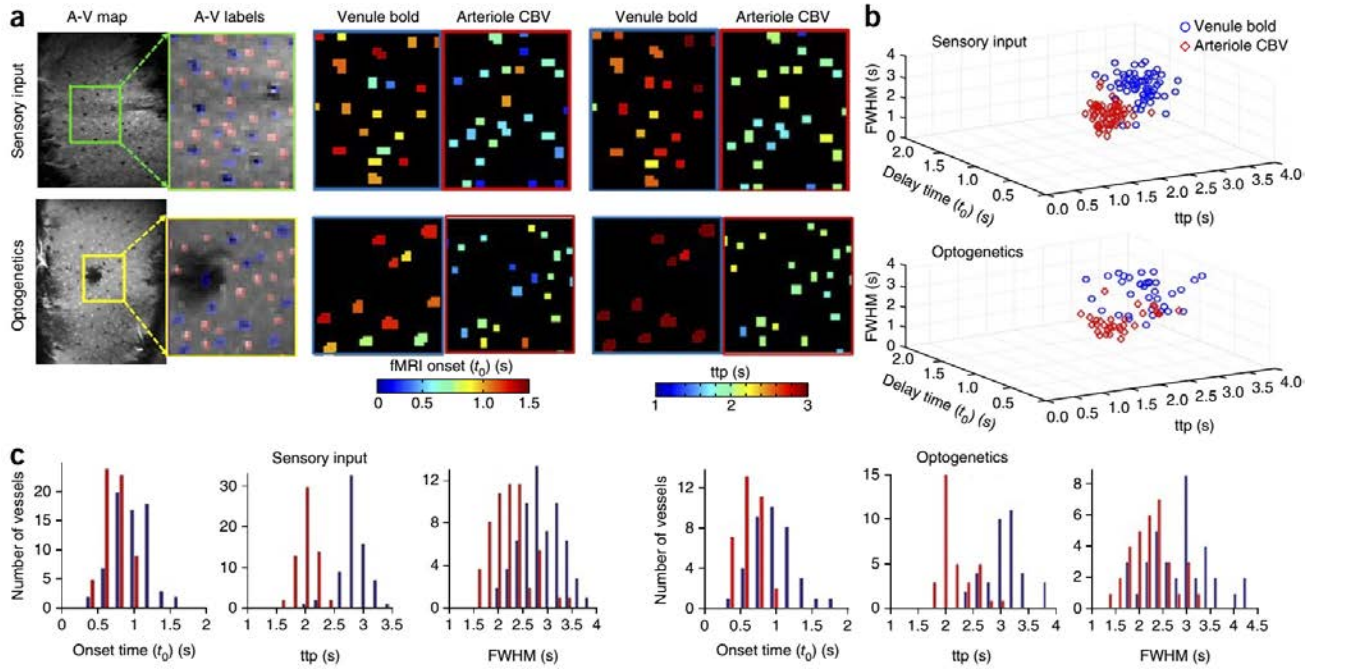

Figure 3 | Temporal features of sensory and optogenetically driven BOLD and CBV fMRI signals from individual arterioles and venules. (**a**) A-V maps of individual arteriole (red) and venule (blue) voxels, t_0 maps and ttp maps of a representative rat, each for either sensory stimulation ($n = 5$ rats) or fiber optic–mediated optical stimulation ($n = 4$ rats). (**b**) 3D plots of t_0, ttp and FWHM of sensory-evoked fMRI signal from individual arteriole ($n = 61$, $r^2 > 0.4$) and venule ($n = 69$, $r^2 > 0.5$) voxels ($n = 5$ rats) and of light-driven fMRI signal from individual arteriole ($n = 33$, $r^2 > 0.3$) and venule ($n = 37$, $r^2 > 0.35$) voxels ($n = 4$ rats). (**c**) Distribution of the number of venule (blue) and arteriole (red) voxels with different t_0, ttp and FWHM in rats with sensory stimulation ($n = 5$) or fiber optic–mediated optical stimulation by optogenetics ($n = 4$ rats).

signals in the deep cortical layers were similar, consistent with previous optogenetic fMRI studies[22,23], which we extended to the single-vessel level in the present study. The single-vessel fMRI method and its combination with optogenetics should enable researchers to decipher individual vascular coupling events in the neuron-glia-vessel network in both normal and diseased brain states.

METHODS

Methods and any associated references are available in the online version of the paper.

Note: Any Supplementary Information and Source Data files are available in the online version of the paper.

ACKNOWLEDGMENTS

This research was supported by the Intramural Research Program of the US National Institutes of Health, the US National Institute of Neurological Disorders and Stroke and internal funding from the Max Planck Society. We thank H. Schulz, S. Fischer, K. Sharer and N. Bouraoud for technical support and A. Bonci for help with the optogenetic setup.

AUTHOR CONTRIBUTIONS

X.Y. and A.P.K. initiated the work, developed the method and wrote the paper. A.C.S. and S.J.D. helped setup the *k*-space reconstruction. H.M. and S.J.D. designed the radiofrequency coil. X.Y. performed MRI experiments at 11.7 T and 14 T. Y.H. and M.W. helped with 14-T MRI data acquisition and analysis.

COMPETING FINANCIAL INTERESTS

The authors declare no competing financial interests.

1. Belliveau, J.W. *et al. Science* **254**, 716–719 (1991).
2. Ogawa, S. *et al. Proc. Natl. Acad. Sci. USA* **89**, 5951–5955 (1992).
3. Kwong, K.K. *et al. Proc. Natl. Acad. Sci. USA* **89**, 5675–5679 (1992).
4. Bandettini, P.A., Wong, E.C., Hinks, R.S., Tikofsky, R.S. & Hyde, J.S. *Magn. Reson. Med.* **25**, 390–397 (1992).
5. Yu, X., Qian, C., Chen, D.Y., Dodd, S.J. & Koretsky, A.P. *Nat. Methods* **11**, 55–58 (2014).
6. Logothetis, N.K., Pauls, J., Augath, M., Trinath, T. & Oeltermann, A. *Nature* **412**, 150–157 (2001).
7. Uğurbil, K., Toth, L. & Kim, D.S. *Trends Neurosci.* **26**, 108–114 (2003).
8. Duyn, J.H. *Neuroimage* **62**, 1241–1248 (2012).
9. Silva, A.C. & Koretsky, A.P. *Proc. Natl. Acad. Sci. USA* **99**, 15182–15187 (2002).
10. Yu, X. *et al. Neuroimage* **59**, 1451–1460 (2012).
11. Moon, C.H., Fukuda, M. & Kim, S.G. *Neuroimage* **64**, 91–103 (2013).
12. Huber, L. *et al. Neuroimage* **107**, 23–33 (2015).
13. Jezzard, P. *et al. NMR Biomed.* **7**, 35–44 (1994).
14. Lee, S.P., Duong, T.Q., Yang, G., Iadecola, C. & Kim, S.G. *Magn. Reson. Med.* **45**, 791–800 (2001).
15. Hall, C.N. *et al. Nature* **508**, 55–60 (2014).
16. Wedeen, V.J. *et al. Science* **230**, 946–948 (1985).
17. Bolan, P.J., Yacoub, E., Garwood, M., Ugurbil, K. & Harel, N. *Neuroimage* **32**, 62–69 (2006).
18. Boyden, E.S., Zhang, F., Bamberg, E., Nagel, G. & Deisseroth, K. *Nat. Neurosci.* **8**, 1263–1268 (2005).
19. Zhao, S. *et al. Nat. Methods* **8**, 745–752 (2011).
20. Lee, J.H. *et al. Nature* **465**, 788–792 (2010).
21. Vazquez, A.L., Fukuda, M., Crowley, J.C. & Kim, S.G. *Cereb. Cortex* **24**, 2908–2919 (2014).
22. Iordanova, B., Vazquez, A.L., Poplawsky, A.J., Fukuda, M. & Kim, S.G. *J. Cereb. Blood Flow Metab.* **35**, 922–932 (2015).
23. Kahn, I. *et al. J. Neurosci.* **31**, 15086–15091 (2011).
24. Hutchinson, E.B., Stefanovic, B., Koretsky, A.P. & Silva, A.C. *Neuroimage* **32**, 520–530 (2006).
25. Tian, P. *et al. Proc. Natl. Acad. Sci. USA* **107**, 15246–15251 (2010).
26. Blinder, P., Shih, A.Y., Rafie, C. & Kleinfeld, D. *Proc. Natl. Acad. Sci. USA* **107**, 12670–12675 (2010).
27. Boxerman, J.L., Hamberg, L.M., Rosen, B.R. & Weisskoff, R.M. Magn. Reson. Med. 34, 555–566 (1995).

ONLINE METHODS

MRI image acquisition. All images were acquired with an 11.7 T/31 cm and 14.1 T/26 cm horizontal bore magnet (Magnex) interfaced to an Avance III console (Bruker) and equipped with a 12-cm gradient set capable of providing 100 G/cm with a rise time of 150 μs (Resonance Research). For the 11.7-T scanner, a custom-built 9-cm-diameter quadrature transmitter coil was placed in the gradient. Surface receive-only coils were used during image acquisition. For the 14-T scanner, a transceiver surface coil with a 6-mm diameter was used to acquire fMRI images.

Line-scanning fMRI. A 2D FLASH sequence was used to map the fMRI signal with the following parameters: TE, 4 ms (CBV) or 16 ms (BOLD); repetition time (TR), 100 ms; matrix, 80 × 32 (11.7 T) or 96 × 64 (14 T); in-plane resolution, 150 × 150 μm (11.7 T) or 100 × 100 μm (14 T); slice thickness, 500 μm; flip angle, 20°. As previously described[5,9], the single *k*-space line was acquired for each image of the block-design stimulation pattern. The on/off stimulation trials were repeated for the number of phase-encoding steps (**Supplementary Fig. 2**). The field of view (FOV) along the phase-encoding direction was aligned to cover the deep layers of the cortical regions of interest (**Supplementary Fig. 2b**) as previously described[10]. To reduce the potential aliasing effect along the phase-encoding direction, we used two saturation slices to nullify the signal out of the FOV as previously established for line-scanning fMRI[5]. The 2D FLASH slice image was reconstructed from the reshuffled *k*-space data with a 100-ms sampling rate[9]. As described previously[10], the in-flow effect contributes little to the BOLD signal detected from individual venules. For CBV fMRI signal, the in-flow effect from blood with a high concentration of iron oxides would likely be negligible.

Single-vessel MGE imaging. To detect individual arterioles and venules, we used a 2D MGE sequence with the following parameters for 11.7 T: TR, 30 ms; TE, 1.8, 4.3, 6.8 or 9.3 ms; flip angle, 50°; matrix, 160 × 128; in-plane resolution, 75 × 75 μm; slice thickness, 500 μm. The following parameters were used for 14 T: TR, 50 ms; TE, 2.5, 5, 7.5, 10, 12.5 or 15 ms; flip angle, 40°; matrix, 192 × 128; in-plane resolution, 50 × 50 μm; slice thickness, 500 μm. A single-vessel map is acquired by averaging of the MGE images acquired from the second echo to the forth echo, where the venule voxels show as dark dots because of the fast T2* decay but arteriole voxels remain bright owing to the in-flow effect.

EPI fMRI. For the EPI sequence, FASTMAP shimming, adjustments to echo spacing and symmetry, and B_0 compensation were set up first. Using the single surface coil, we ran a single shot sequence with a 64 × 64 matrix with the following parameters: effective TE, 18/9.6 ms; TR, 0.8 s; bandwidth, 138/300 kHz; flip angle, 45°; in-plane resolution, 150 × 150; slice thickness, 500 μm. A 3D gradient-echo EPI sequence with a 64 × 64 × 32 matrix was run with the following parameters: effective TE, 16 ms; TR, 1.5 s; bandwidth, 170 kHz; flip angle, 12°; FOV, 1.92 × 1.92 × 0.96 cm. For fMRI studies, we placed electrodes on the forepaw or whisker pads of rats to deliver a 2.0-mA pulse sequence (300-μs duration repeated at 3 Hz) via an isolated stimulator[10] (A360LA; WPI). For optical stimulation, we used a 473-nm laser (CNI, China) with a built-in FC/PC coupler to deliver the light pulse. The light pulse was triggered through an analog module to deliver optical stimulation with different durations ranging from 0.3 ms to 20 ms. The multimode optical fiber was 200 μm (FT200EMT; ThorLabs). The light power from the fiber tips was calibrated using optical power meters (PM20A; ThorLabs) and was controlled from 0.3 to 10 mw. The power levels used for light-driven fMRI studies (2 s or 5 s, 10 Hz, 20-ms light pulse, 3.2 mw) did not induce pseudo-BOLD signal due to heating effects, as shown by testing in cortical regions both without and with ChR2 expression after the rats died.

The 2D slice covered the forepaw and barrel S1 areas as defined by the Paxinos atlas[28]. The horizontal slice angle was set at 15° and 40°, and the center of the slice was positioned 1 mm from the cortical surface to cover layers 4 and 5. For FLASH fMRI, the forepaw and whisker pad stimulation experiment consisted of 60 dummy scans to reach steady state followed by 10 prestimulation scans, 20 scans during electrical stimulation, and 100 scans after stimulation (a total of 13 s for each on/off epoch for three times). The total time for each trial was 42 min. Each trial was repeated three or four times for both BOLD and CBV fMRI mapping. After the second trial for the CBV fMRI study, a small dosage of iron oxide particles (3–4 mg/kg) was injected to compensate for the potential washout of iron particles from the blood. The single-vessel map was acquired at the same slice orientation for further imaging registration. For EPI-fMRI, the forepaw and whisker stimulation experiment consisted of 10 dummy scans to reach steady state followed by 10 prestimulation scans, 3 scans during stimulation and 12 interstimulation scans for 8 epochs or 20 prestimulation scans, 5 scans during stimulation and 20 inter- stimulation scans for 5 epochs. The pulse sequence–based trigger and stimulation control was established using the BioPac system (Goleta, USA) and AD instruments (Oxford, UK).

Animal surgeries. All animal work was performed according to the guidelines of the Animal Care and Use Committee and the Animal Health and Care Section of the National Institute of Neurological Disorders and Stroke, National Institutes of Health (NIH; Bethesda, MD, USA), and the protocol was approved by the Animal Protection Committee of Tuebingen (Regierungspräsidium Tuebingen). A total of 24 male Sprague-Dawley rats were imaged at 2–3 months of age. Eight rats were imaged under 11.7 T (both BOLD and CBV FLASH fMRI data with A-V maps were acquired from five of eight rats) at NIH, seven rats were imaged under 14 T at the Max Planck Institute (both BOLD and CBV FLASH fMRI data with A-V maps were acquired from four of seven rats), and nine rats were imaged for optogenetic studies (both BOLD and CBV FLASH fMRI data with A-V maps were acquired from four of nine rats). The number of animals to be used was calculated by a power analysis with parameters acquired from our previous studies[5,10]. If a rat died during an fMRI experiment, the data acquired for that rat were not included in the statistical analysis.

Animal preparation for fMRI. The detailed procedure is described elsewhere[29]. Briefly, rats were initially anesthetized with isoflurane. Each rat was orally intubated with a mechanical ventilator throughout the surgical and imaging procedures. Plastic catheters were inserted into the right femoral artery and vein to allow monitoring of arterial blood gases and administration of drugs (anesthetics and iron oxide particles). After catheterization, all rats were given an i.v. bolus of α-chloralose (80 mg/kg). Isoflurane was discontinued after 3–5 min. Constant infusion of α-chloralose was set with a rate of 26.5 mg/kg/h. The rats' rectal temperature was maintained at ~37 °C while they were in

the magnet. Rats were secured in a head holder with a bite bar to prevent head motion. All relevant physiological parameters, such as end-tidal CO_2, rectal temperature, heart rate, and arterial blood pressure, were continuously monitored during imaging. Arterial blood gas contents were checked regularly, and adjustments were made by tuning respiratory volume or administering sodium bicarbonate to maintain normal pH levels when required. An i.v. injection of pancuronium bromide (4 mg/kg) was administrated to reduce motion artifacts upon request. BOLD and CBV fMRI were performed on α-chloralose anesthetized rats. CBV fMRI was performed directly after BOLD fMRI. CBV-weighted signals were obtained after intravenous administration of 15 mg of Fe/kg dextran-coated iron oxide (Biopal, MA).

Viral vector injection and fiber optic implantation. The viral vectors (AAV5.CaMKIIa.hChR2 (H134R)-eYFP.WPRE.hGH) were obtained from the University of Pennsylvania Vector Core. Three- to four-week-old rats were injected with 200 nl of original viral vector solution in the barrel cortex with stereotactic coordinates: bregma, −2.35 mm; lateral, −4.8 mm; and ventral, 1.5 and 0.7 mm. For the stereotactic injection procedure, rats were initially anesthetized with isoflurane. A small burr hole was drilled after the skull was exposed. A nanoliter injector (WPI, FL) was used to place the 35-gauge needle at the proper coordinates in the stereotactic frame. Injections were performed slowly over 5–6 min, and the needle was slowly removed after being kept in the injection site for 10 min after the end of the injection. Within 5–6 weeks after the viral injection, a 200-μm fiber optic was inserted into the rat barrel cortex at stereotactic coordinates: bregma, −2.7 mm; lateral, −5.1 mm; ventral, 1.3 mm; tilt, 4°. The fiber optic was glued to the skull, and the skin around it was sutured after the glue had solidified (20–30 min).

In vivo electrophysiological recordings: Rats were placed in a stereotaxic frame for the in vivo recordings under similar anesthesia and surgical procedures to the fMRI experiments. The 200μm fiber optic was first inserted to target the barrel cortex previously injected with AVV viral vectors. The electrodes (Plastics One Inc, Roanoke, VA) was positioned to the barrel cortex (Bregma -2.7, lateral −5.1, and ventral 0.8 mm, tilt 5-6°). The intact whisker pad was electrically stimulated at 2.0mA (3Hz, 300μs) by an isolated stimulator (A360LA, WPI). Or, the barrel cortex was directly activated by the light pulse exposure (0.3-20ms, 1, 3Hz, 10Hz, and 0.3 to 20mw). Stimulation trigger were delivered through the M150 Biopac system using the STM100C stimulator module with 10K sampling rate. The evoked potential was acquired through the EEG module of the Biopac system (gain factor: 5000, the band-pass filter 0.1-100 Hz). Mean profiles of evoked potential responses were subsequently obtained by averaging over the entire series with a time-window step of 300ms (synchronized to the start of a stimulation pulse). AcqKnowledge software package (Biopac Systems) was used to calculate the averaged profiles of evoked potential responses.

Animal perfusion and brain slice microscopic imaging: Immediately after the fMRI imaging, rats were deeply anesthetized with sodium pentobarbital (60mg/kg, per rat, subcutaneous admin- istration)). Then, animals were secured dorsally, and an incision was made along the chest. The heart was exposed, by incising through the rib cage and diaphragm. The left ventricle was be punctured with a sterile catheter, the right atrium was cut to allow fluid to drain, and heparanized saline was fed into the heart with a

doi:10.1038/nmeth.3765

perfusion pump. After the saline, 4% paraformaldehyde, 10% buff- ered formalin was fed into the heart. After perfusion, the brain was carefully extracted from the skull and frozen. A 30-μm brain slice was cut from the frozen rat brain using a cryostat (Leica-CM1860, Wetzlar, Germany). The floating slice was mounted on a glass slide with a coverslip. Fluorescent imaging was done using a Zeiss Axio Imager 2 (Zeiss, Göttingen, Germany).

Image processing and statistical analysis. Data analysis for both FLASH and EPI-fMRI data was performed using Analysis of Functional NeuroImages (AFNI) software (NIH)[30]. The relevant source codes can be downloaded at http://afni.nimh.nih. gov/afni/. A detailed description of the processing is provided elsewhere[10].

The FLASH fMRI data stored in the *k*-space format (**Supplementary Fig. 2**) were first reshuffled with a Matlab script for reconstruction using the built-in function of the Bruker Paravision software. For the AFNI analysis, a 2D registration function was first applied to register the reconstructed FLASH images to a template for multiple data sets acquired with the same orientation setup. To register the FLASH fMRI images with the single-vessel maps, we used the tag-based registration method. Ten to twelve tags were chosen from venule voxels distributed around the 2D slices of FLASH and single-vessel images. We normalized all time-series FLASH fMRI images by scaling the baseline images to 100. Multiple trials of block-design time courses were averaged for each animal. No smoothing procedure was included in the image-processing steps so that the single-vessel fMRI signal could be determined from the high-resolution FLASH fMRI images. The hemodynamic response function (HRF) was derived via linear regression using a tent function.

$$f(x) = \begin{cases} 1 - |x| \; for - 1 < \; x < 1 \\ 0 \; for \; \; |x| > 1 \end{cases}$$

The tent function is also called “piecewise linear spline”, which is used for deconvolution of the HRF response with magnitude estimated as beta coefficient.

$$H(t) = \sum_{k=0}^{n} \left(\beta_k * (\frac{t - k * L}{L}) \right)$$

Or,

$$\mathrm{H(t)} = \beta_0 \times T(t/L) + \beta_1 \times T((t-L)/L) + \beta_2 \times T((t-2L)/L) + \cdots + \beta_k \times T((t-kL)/L)$$

Here $H(t)$ is the HRF response, k is the total number of tent parametric fittings, β_k is the response (tent height) at time $t = kL$ after stimulation, and L is the tent radius (L can be equal to TR). The value of β was calculated to estimate the amplitude of the fMRI response at each TR (L = TR). The voxel-wise β-map is presented to illustrate the spatial pattern of the fMRI response at different time points after the stimulus onset.

The individual arterioles and venules were characterized on the basis of the signal intensity of the voxels detected in the single-vessel map. We created the single-vessel map by averaging the MGE images from the second echo to the forth echo. The individual

doi:10.1038/nmeth.3765

vessel voxels were determined on the basis of their signal intensity, interpreted as either higher (arterioles) than the mean signal intensity plus two times the s.d. or lower (venules) than the mean signal intensity minus two times the s.d. of the local area in a 5 × 5 kernel[31] (**Supplementary Fig. 6a**). A 3dLocalstat function from the AFNI library was used to normalize the signal intensity of single-vessel maps. This allowed us to plot the BOLD and CBV β-values of all voxels to the normalized signal intensity of A-V maps (**Fig. 1d**,**e**). In addition, we performed a 2D spatial correlation between the single-vessel maps and the corresponding BOLD and CBV fMRI functional maps using the Matlab script corr2. The fMRI onset profile was determined on the basis of the full hemodynamic response function. As previously reported, a two-gamma-variate fitting step was applied to estimate the onset time from the averaged and normalized fMRI signal[5,30,32].

$$f(x) = \mathrm{a}\left(\frac{x}{pq}\right)^{p} \times e^{(p-(x/q))} - \mathrm{b}\left(\frac{x}{rs}\right)^{r} \times e^{(r-(x/s))}$$

where x is the variable and a, p, q, b, r and s are the coefficients for the two-gamma-variate function.

The two-gamma-variate function with optimized coefficients was fit to the hemodynamic responses of individual voxels. The fitting curve was plotted with the raw BOLD and CBV hemodynamic signals from individual vessels (**Fig. 3** and **Supplementary Figs. 9**–**12**). The mean r^2 value for each individual fitting of venule BOLD and arteriole CBV signal is shown for individual rats in a scatter plot (**Supplementary Fig. 13**). The ttp and FWHM were estimated from the fitting function. The onset time was derived from a t_0 coefficient from the modified two-gamma-variate function (3dNLfim function with ConvDiffGram module), which showed a reliable estimate of the hemodynamic signal onset in comparison to the noise threshold–based onset estimates[5].

Finally, Student's *t*-test was performed for group analysis; error bars indicate the standard error of the mean in graphs. No blinding design was needed in this work.

28. Paxinos, G. & Watson, C. The Rat Brain in Stereotaxic Coordinates 6th edn. (Academic Press, 2006).
29. Yu, X. et al. Neuroimage 49, 1667–1676 (2010).
30. Cox, R.W. Comput. Biomed. Res. 29, 162–173 (1996).
31. Qian, C. et al. Am. J. Physiol. Renal Physiol. 307, F1162–F1168 (2014).
32. Madesen, M. Phys. Med. Biol. 37, 1597–1600 (1992).

26. *ereotaxic Coordinates* 6th edn.

Supplementary Figures (13)

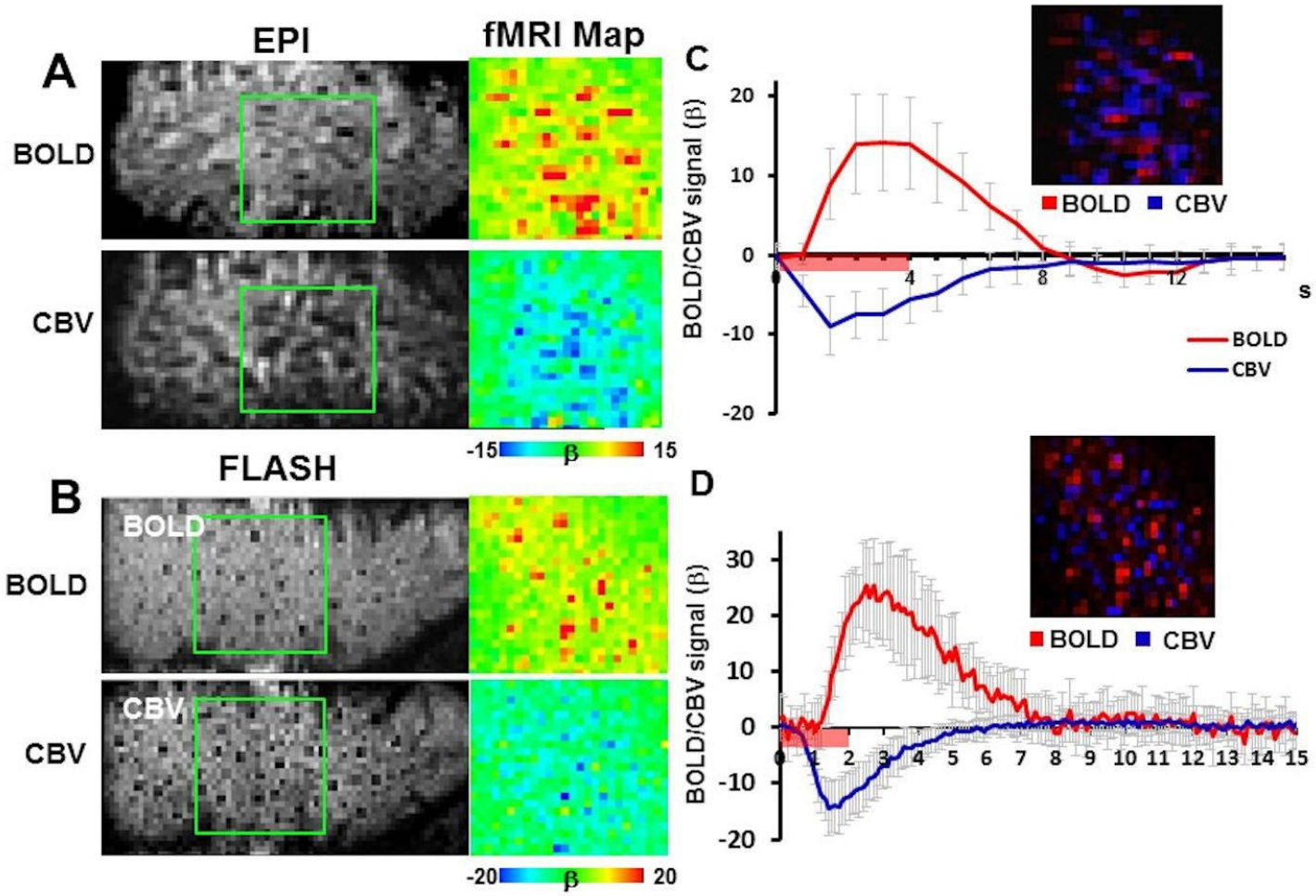

Supplementary Figure 1

BOLD and CBV functional maps showing EPI versus line-scanning FLASH fMRI.

A. Colored BOLD and CBV functional maps are shown in the highlighted window (green frame) of the raw EPI images (representative of 3 rats). **B**. Colored BOLD and CBV functional maps are shown in the highlighted window (green frame) of the raw FLASH images (representative of 5 rats). **C and D**. The BOLD (red) and CBV (blue) fMRI time courses were averaged from the sparsely distributed voxels with β values at thresholds (BOLD, β ≥ 5; CBV, β ≤ -5, mean±SD).

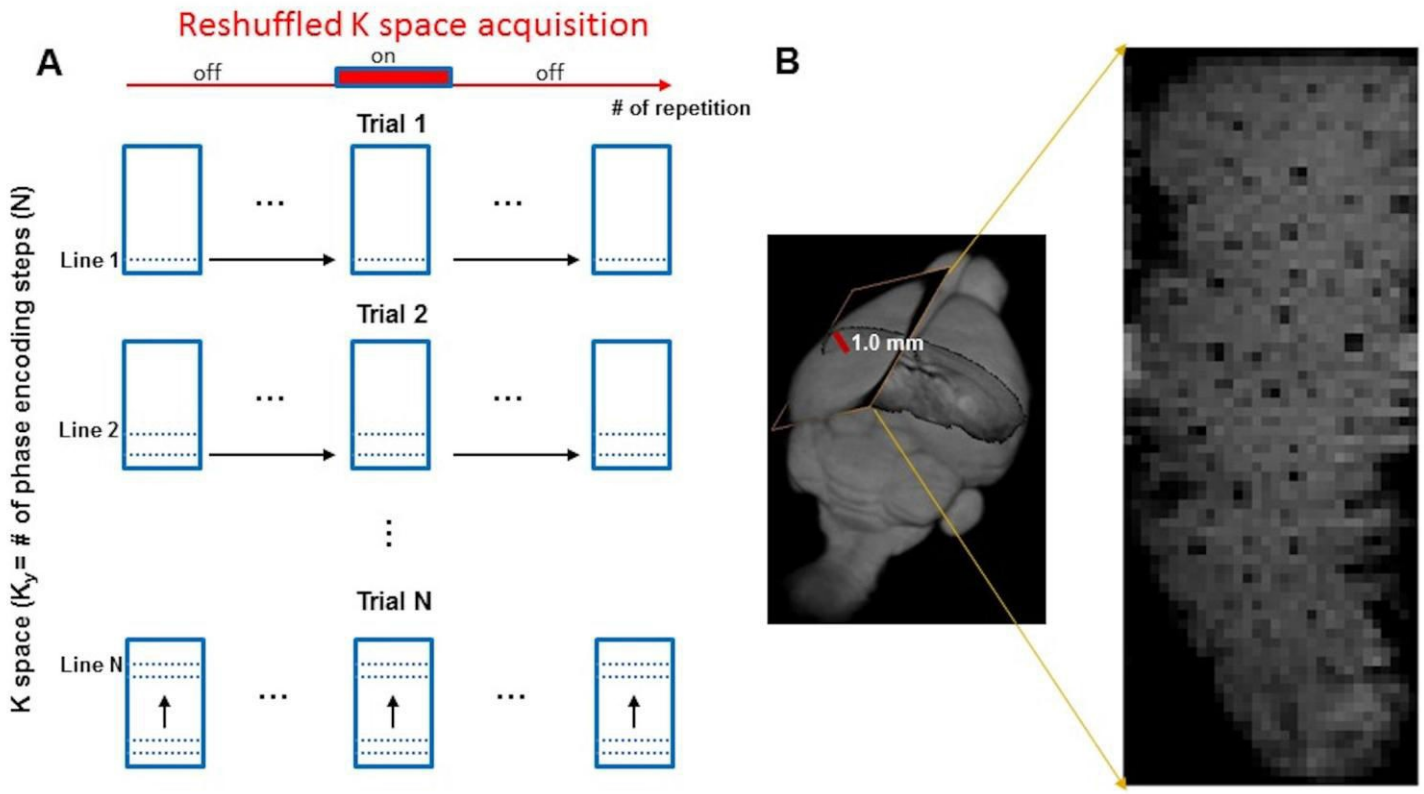

Supplementary Figure 2

The line-scanning–based FLASH fMRI method.

A. The overall view on the k-space acquisition of the FLASH-fMRI method. At each trial of the block-design experiment (red line), one k space line was acquired for each image. The k space for each image was filled with one line at each trial. Experimental trials were repeated for the number of phase-encoding steps (N=32/64). **B**. The k space map was reconstructed to produce the 2D image, which was located at the deep layer cortex (1.0mm to the cortical surface) covering the primary somatosensory cortex.

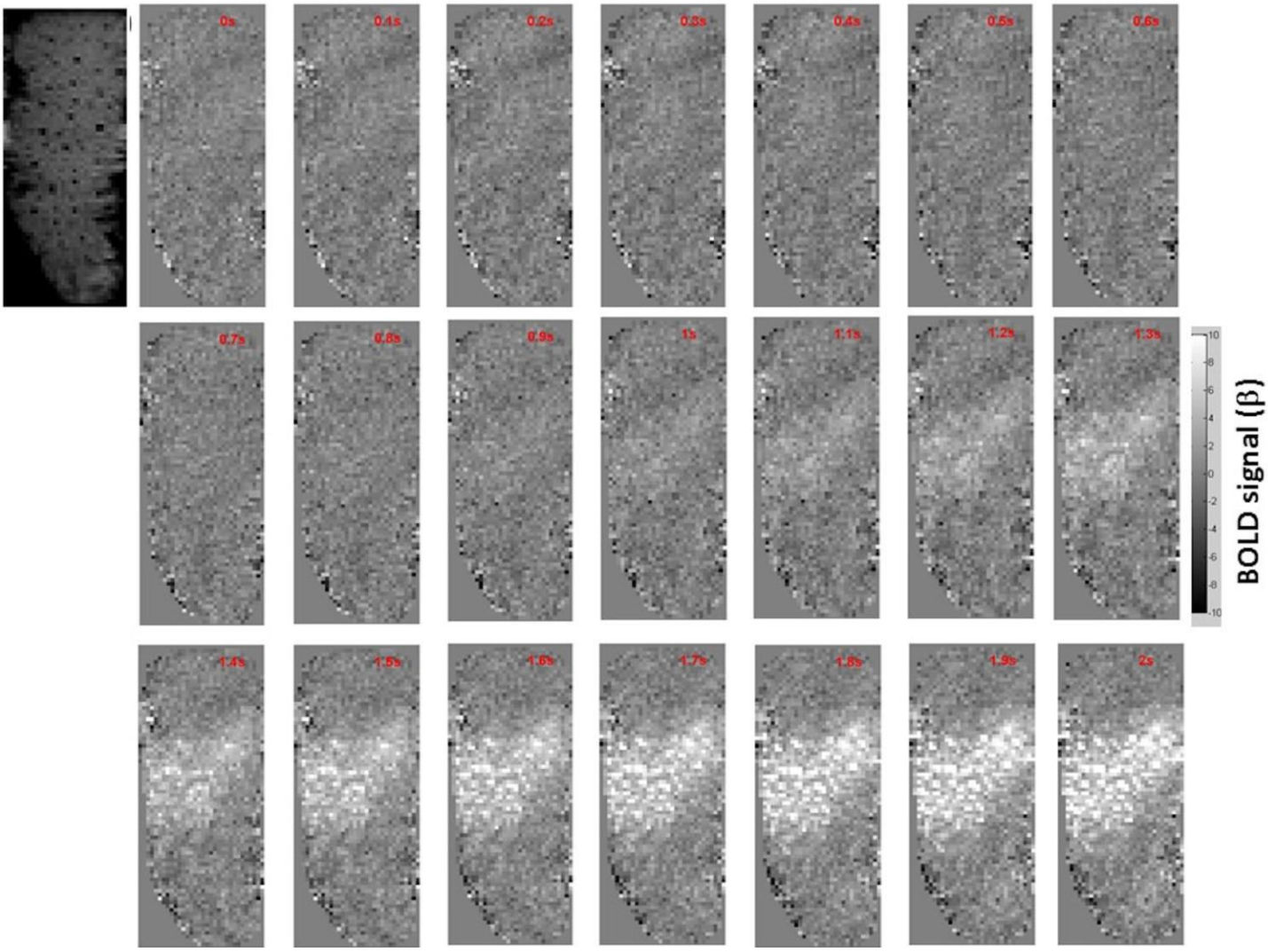

Supplementary Figure 3

Time-lapsed BOLD fMRI images with line-scanning fMRI.

The grey-scale BOLD functional maps are shown as the function of time at every 100ms from 0s to 2s following the stimulus onset. The raw image is shown in the upper left corner.

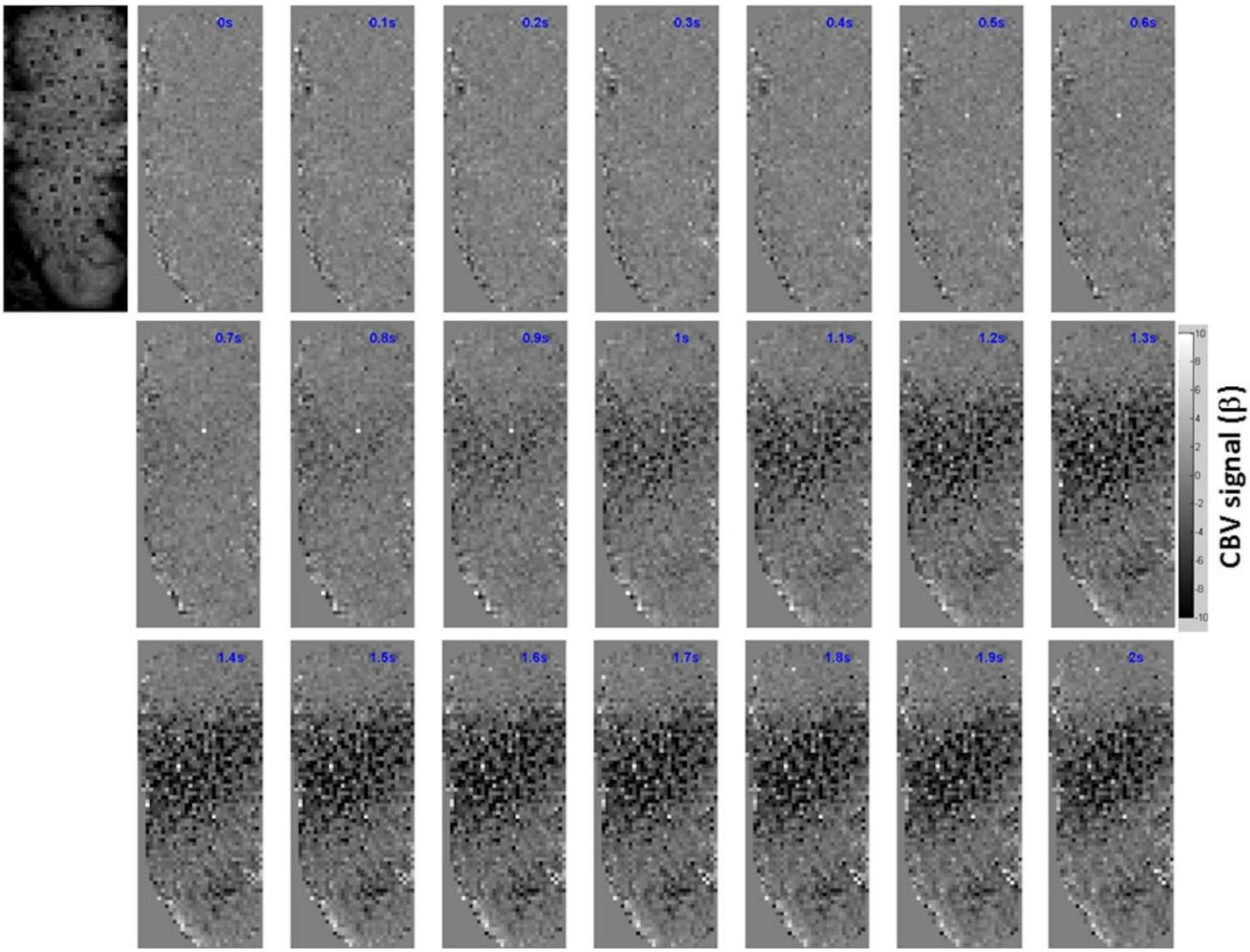

Supplementary Figure 4

Time-lapsed CBV fMRI images with line-scanning fMRI.

The grey-scale CBV functional maps are shown as the function of time at every 100ms from 0s to 2s following the stimulus onset. The raw image (after iron injection) is shown in the upper left corner.

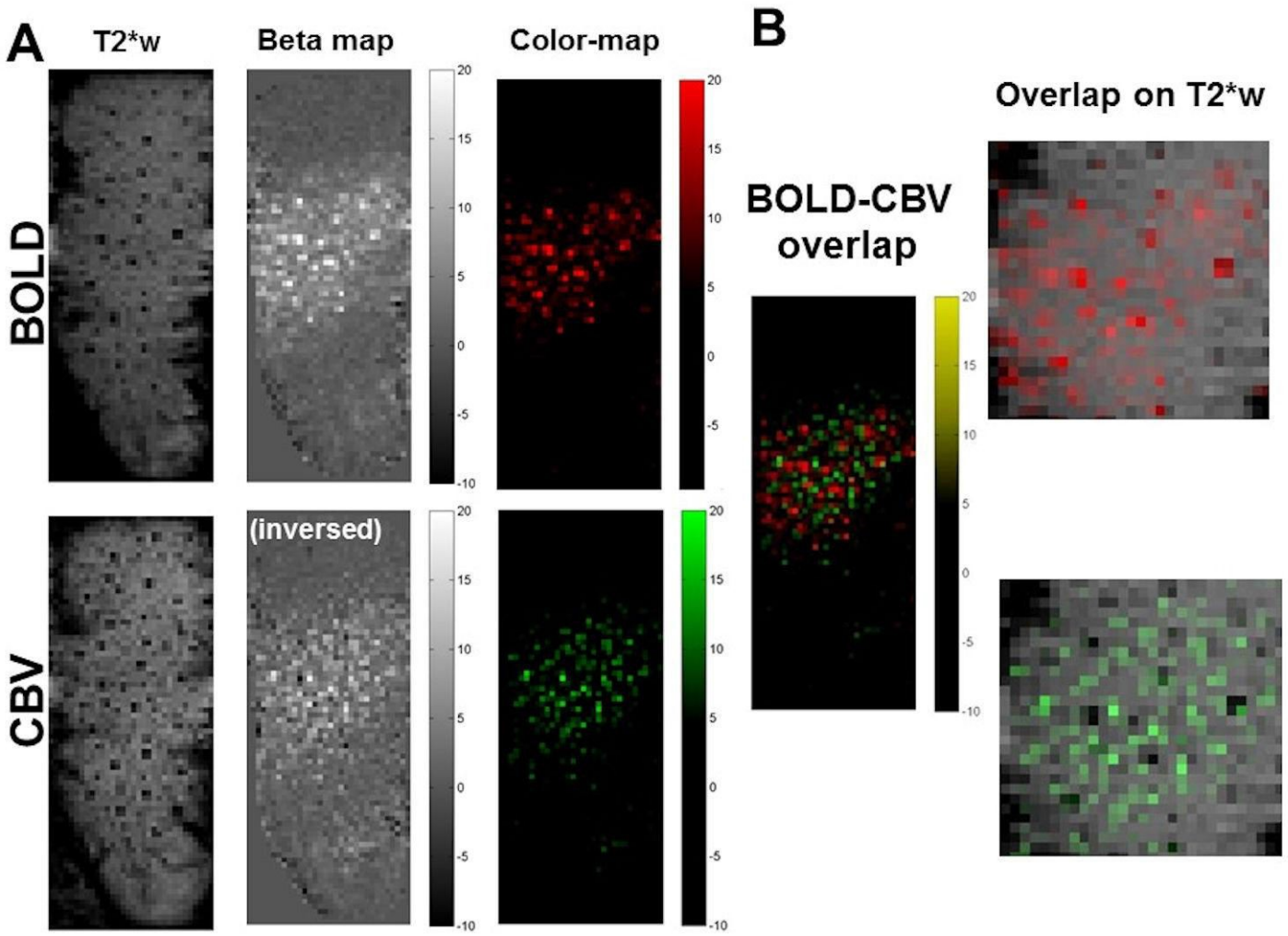

Supplementary Figure 5

Localization of BOLD and CBV fMRI voxels.

A. BOLD and CBV functional maps from the 2D anatomical image (T2*w) in gray-scale (middle) and color-scale (right; BOLD, red; CBV, green, inversed). **B.** The BOLD and CBV functional color-maps overlapped with the sparsely distributed active voxels in the same 2D slice (left). Both enlarged functional maps were overlapped on the anatomical T2*W images (right).

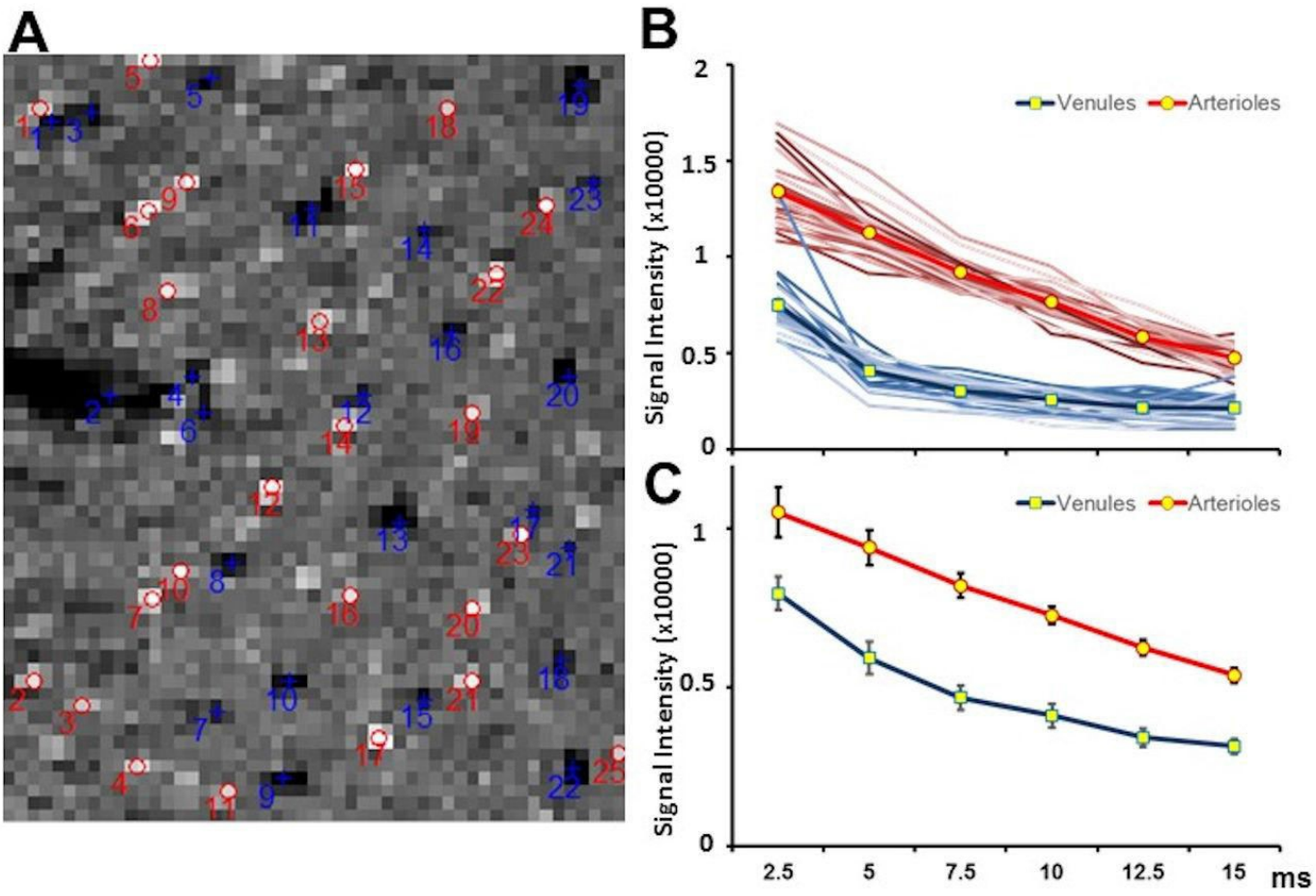

Supplementary Figure 6

The detection of individual penetrating arterioles and venules in the deep layer cortex.

A. The representative A-V map from 6 rats. The individual venules are shown as dark voxels (blue crosses). The individual arterioles are shown as bright voxels (red circles). **B.** The signal intensity of the venule (23) and arteriole (25) voxels was plotted as the function of different TEs from 2.5ms to 15ms (one representative rat from A. **C**. The averaged signal intensity of all venule and arteriole voxels was plotted as the function of different TEs (n=6, rats, mean±SEM).

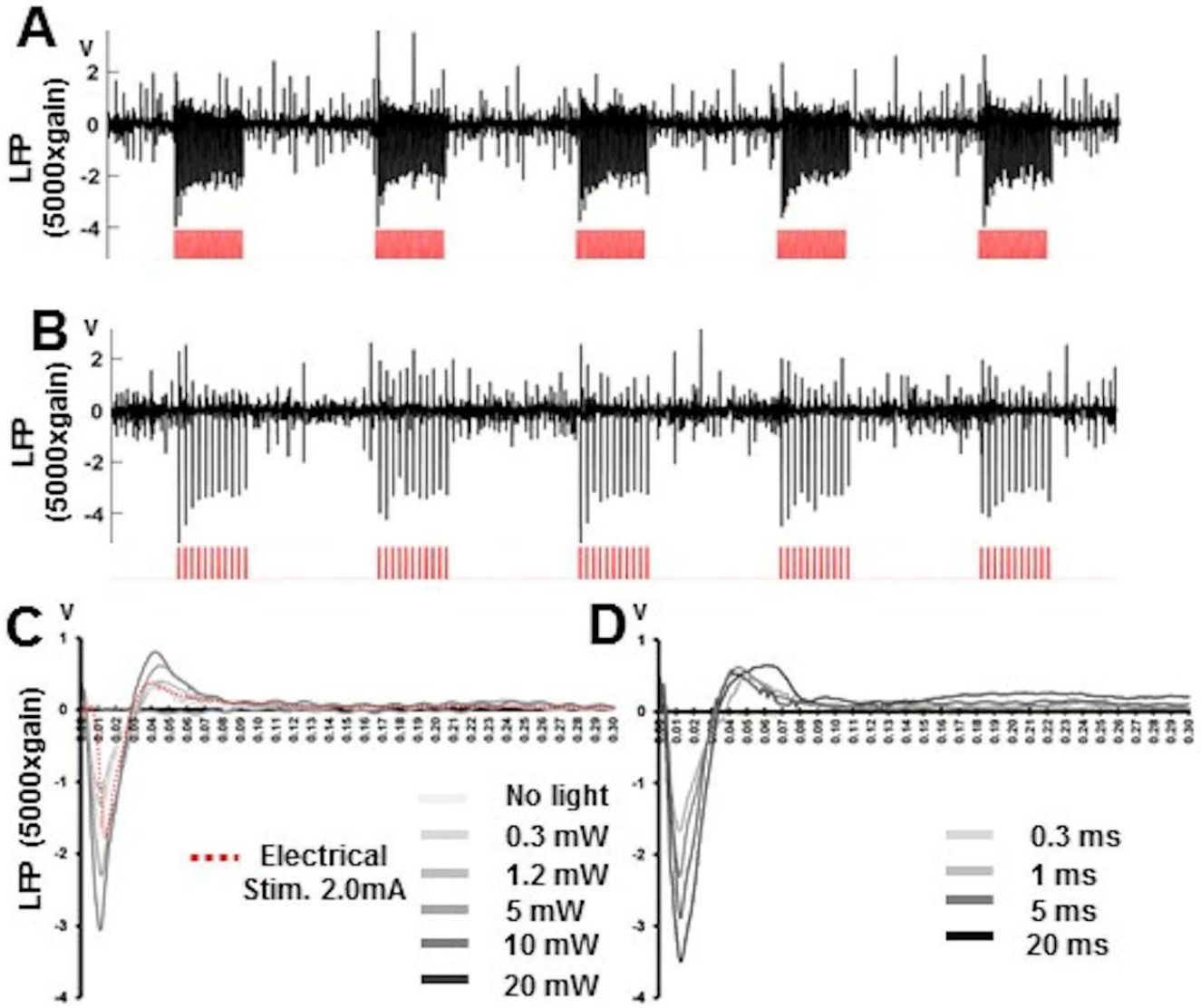

Supplementary Figure 7

The light-driven local field potential (LFP) by optogenetics.

A. The LFP trace by optical stimulation (upper panel: 1ms light pulse, 3Hz, 10mw; lower panel, 20ms light pulse, 1Hz, 10mw). **B**. The averaged LFP driven by 1ms light pulse at different power (0, 0.3, 1.2, 5, 10, 20 mw) and by electrical stimulation of the whisker barrel (2.0mA, 3Hz, 0.3ms, red dotted line). **C**. The averaged LFP driven by light pulse at different duration (0.3, 1, 5, and 20ms; 3Hz, 10mw).

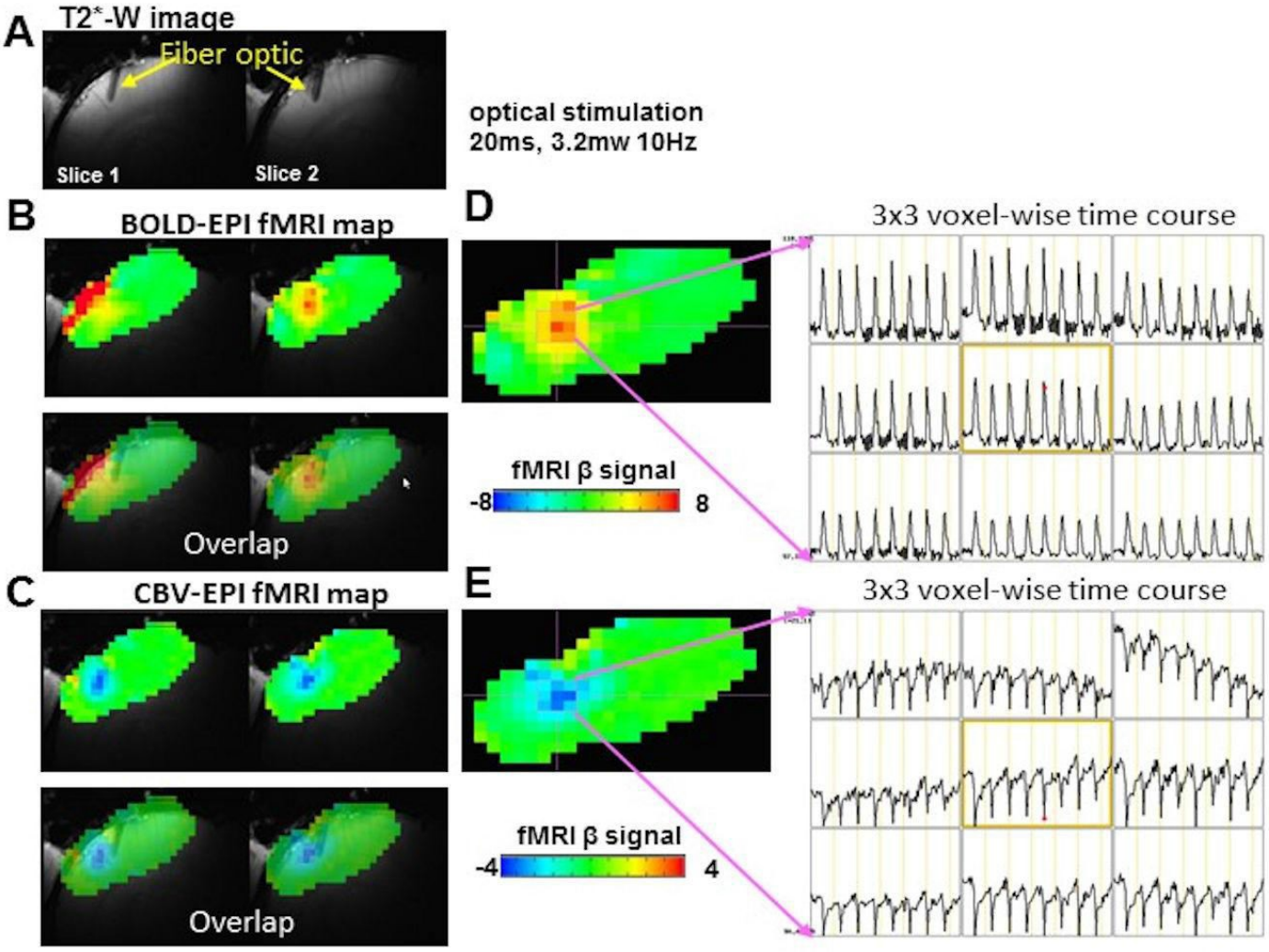

Supplementary Figure 8

Light-driven BOLD and CBV fMRI signal acquired by EPI methods.

A. The T2*-weighted images with the fiber optic inserted to target the barrel cortex in two consecutive slices. **B**. The colored BOLD fMRI maps show the most active voxels close to the fiber tip (upper panel) with anatomical image overlay (lower panel). **C**. The colored CBV fMRI maps show the most active voxels close to the fiber tip after iron oxide particle injection (upper panel) with anatomical image overlay (lower panel). **D**. The voxel-wise BOLD fMRI time courses (2s on/ 20s off, 8 epochs) plotted in a 3x3 matrix (the voxel position is shown in the colored BOLD-fMRI map, left). **E**. The voxel-wise CBV fMRI time courses (2s on/ 20s off, 8 epochs) plotted in a 3x3 matrix (the voxel position is shown in the colored CBV-fMRI map, left).

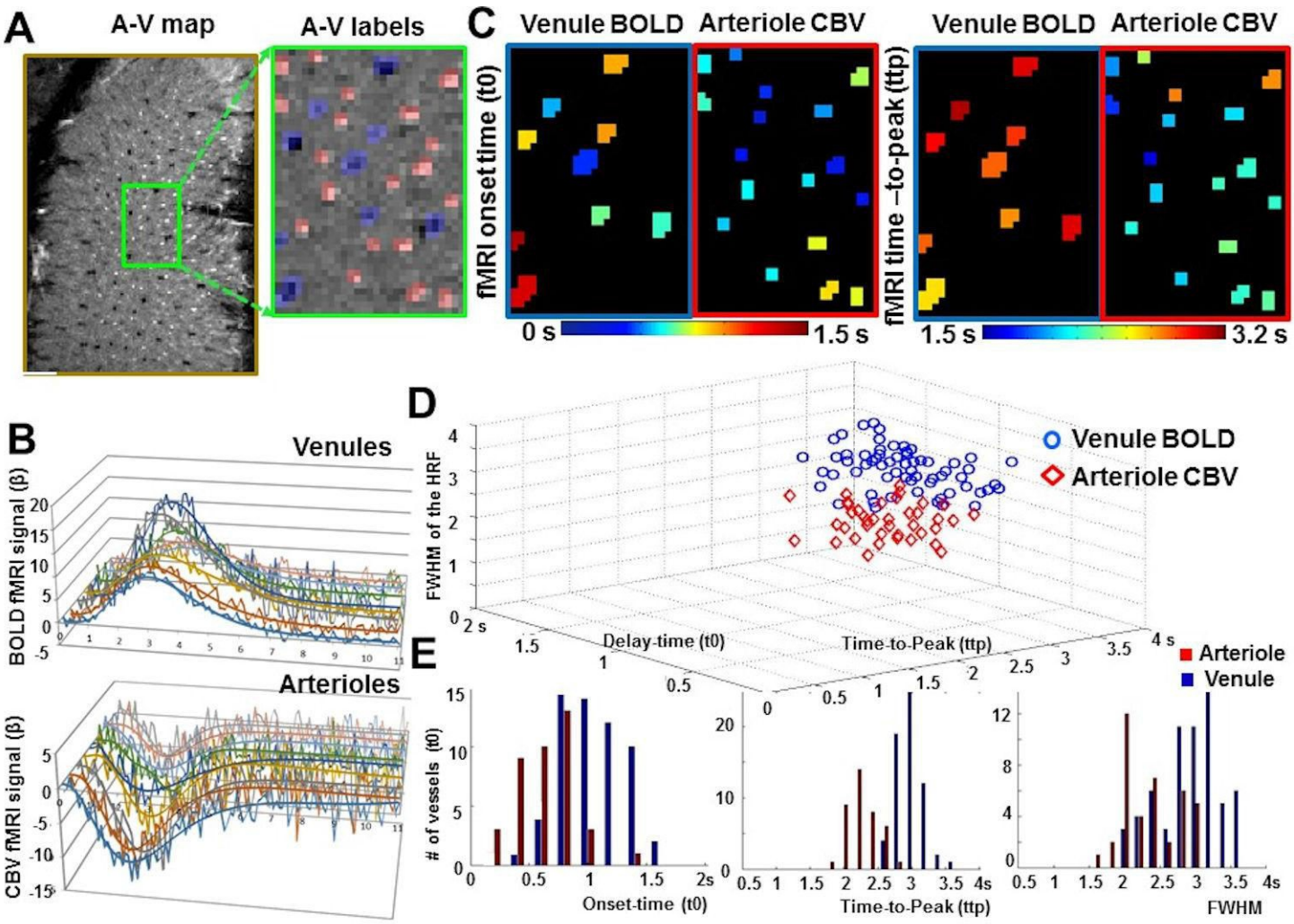

Supplementary Figure 9

The BOLD and CBV fMRI signal from individual arterioles and venules under 14.1 T.

A. A representative A-V map from 4 rats. The individual arteriole and venule voxels were detected with different signal intensity (venule voxels, blue; arteriole voxels, red). **B**. The BOLD fMRI time courses (raw data and fitting curves) from individual venule voxels(upper panel) and the CBV fMRI time courses (raw data and fitting curves) from individual arteriole voxels (lower panel). **C**. The fMRI onset time (t0) maps (left panel) and time-to-peak (ttp) maps (right panel) of a representative rat. **D**. 3d plots of the onset-time (t0), time-to-peak (ttp), and full-width-of-half-maximum (FWHM) of fMRI signal from individual arteriole (red diamonds, 39, r^2>0.4) and venule (blue circles, 63, r^2>0.5) voxels from 4 rats. **E**. Distribution of number of venule (blue) and arteriole (red) voxels with different t0, ttp and FWHM.

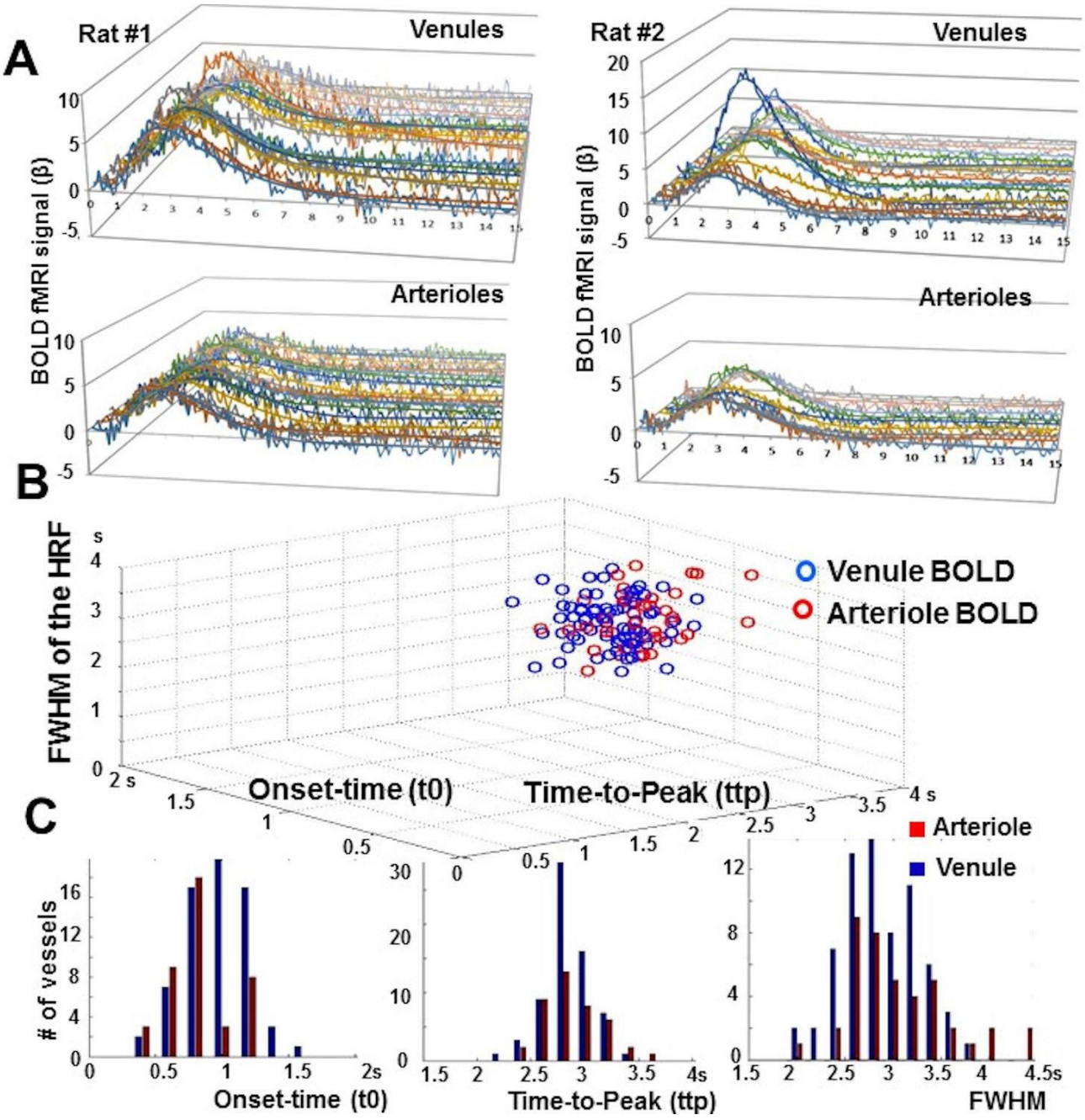

Supplementary Figure 10

The BOLD fMRI signal from individual arterioles and venules.

A. The BOLD fMRI time courses (raw data and fitting curves) of two representative rats from total 5 rats (venules, upper panel; arterioles, lower panel). **B**. 3d plot of the onset-time (t0), time-to-peak (ttp), and full-width-of-half-maximum (FWHM) of fMRI signal from individual arteriole (red circles, 41, r^2>0.4) and venule (blue circles, 71, r^2>0.5) voxels from 5 rats. **C**. Distribution of the number of venule (blue) and arteriole (red) voxels with different t0, ttp and FWHM.

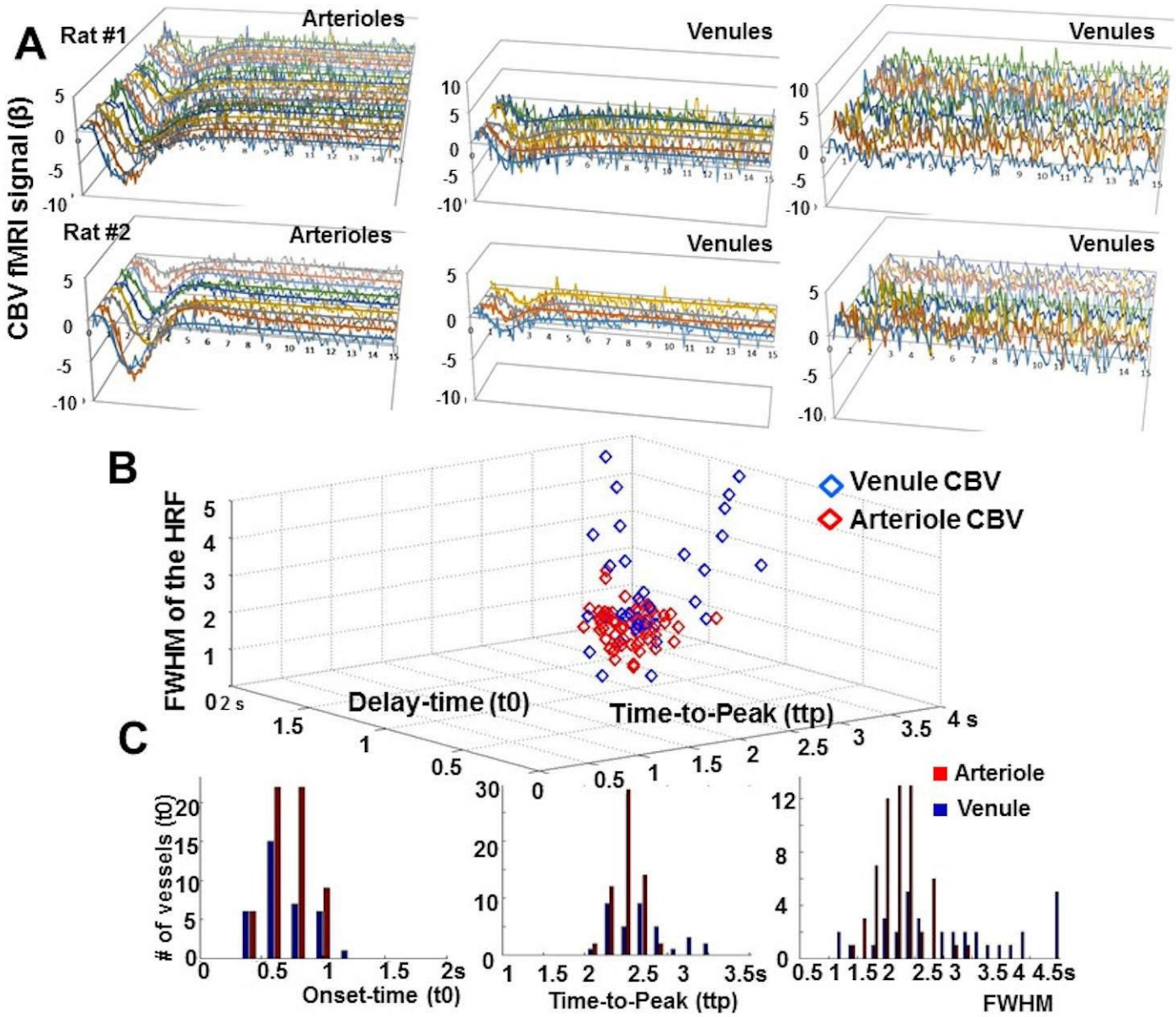

Supplementary Figure 11

The CBV fMRI signal from individual arterioles and venules.

A. The CBV fMRI time courses (raw data and fitting curves) of two representative rats from total five rats (arterioles, left; venules, middle, r^2>0.2, right, r^2 ≤0.2). **B**. 3d plot of the onset-time (t0), time-to-peak (ttp), and full-width-of-half-maximum (FWHM) of fMRI signal from individual arteriole (red diamonds, 59, r^2>0.4) and venule (blue circles, 35, r^2>0.2) voxels from 5 rats. **C**. Distribution of number of venule (blue) and arteriole (red) voxels with different t0, ttp and FWHM.

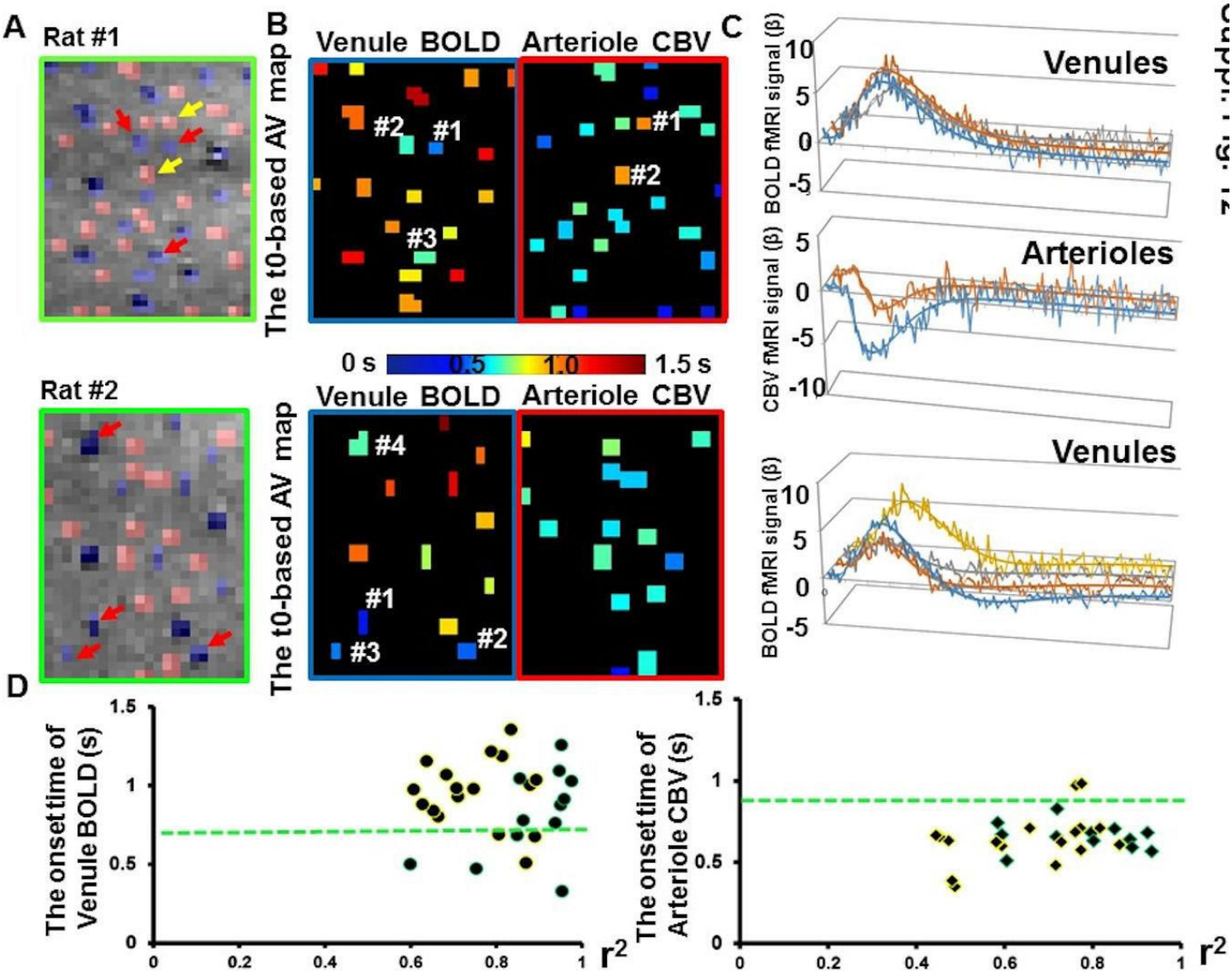

Supplementary Figure 12

The spatial and temporal characterization of the outlier vessel hemodynamic signal.

A. The A-V maps of two representative rats (red arrows for venule outliers, yellow arrows for arteriole outliers). **B**. The onset-time (t0) based A-V maps showed the BOLD t0 values of different venules and CBV t0 values of different arterioles of two representative rats (the outlier vessels are marked in numerical numbers). **C**. The time course of the hemodynamic signal from the outlier vessel voxels and their fitting curves. **D**. The scatter plot of the venule BOLD (left, dots, green line: 0.7s) and arteriole CBV (right, diamonds, green line: 0.9s) t0 values with the fitting r^2 values (rat #1, yellow borders, rat #2, blue borders).

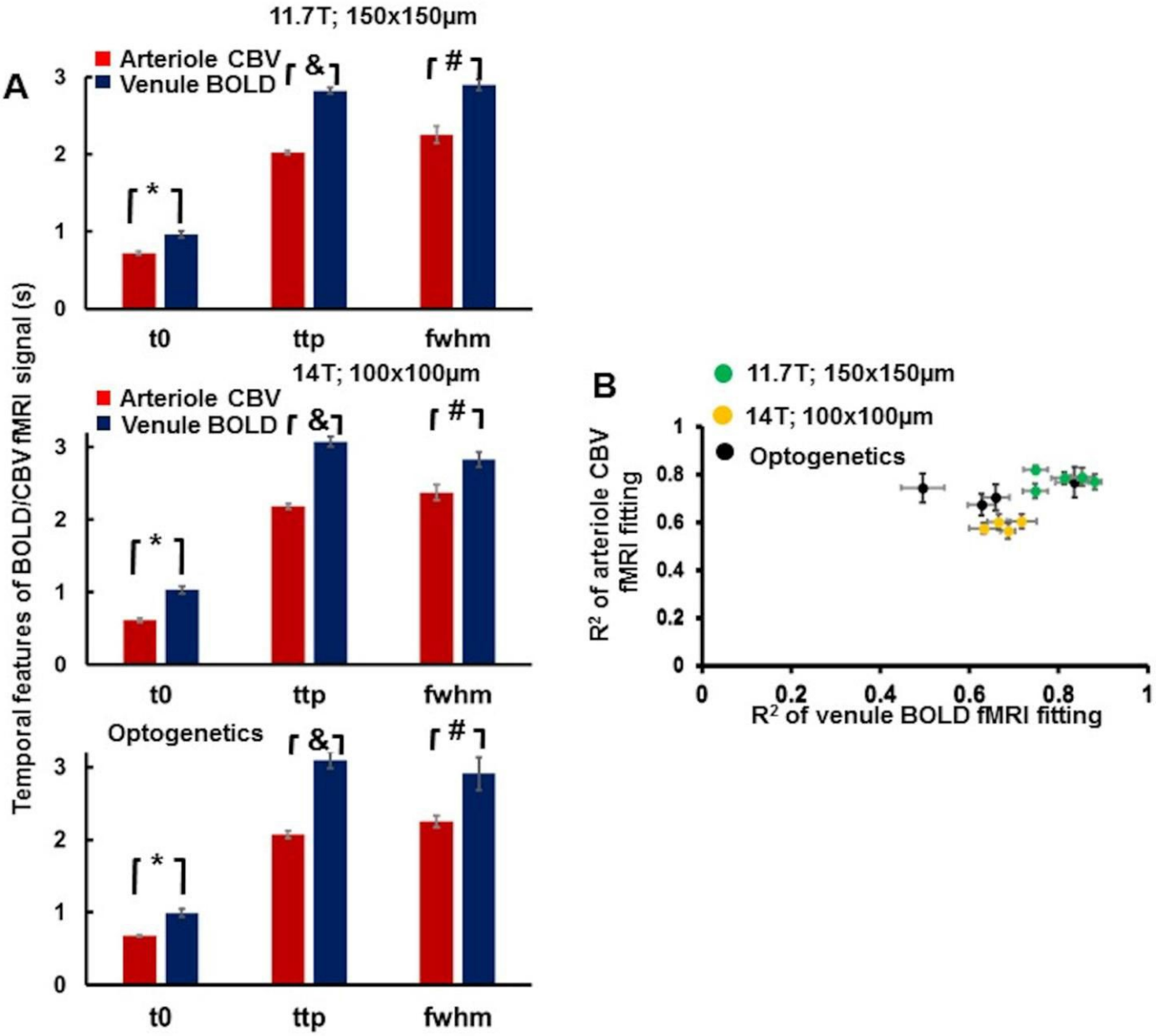

Supplementary Figure 13

Group analysis of BOLD and CBV fMRI signals from individual vessels.

A. The averaged onset time(t0), time-to-peak (ttp), and full-width-of-half-maximum (FWHM) from arteriole CBV signal (red) and venule BOLD signal (blue) acquired from 11.7T (top panel; n=5; * p=0.002; & p=0.00001, # p=0.002), 14.1T (middle panel, n=4; * p=0.002; &, p=0.0006; # p=0.01), and driven by optogenetic method under 14.1T (bottom panel; n=4; * p=0.01; & p=0.002, # p=0.04. **B**. The averaged r^2 values of all individual vessels were plotted for each rat of two experiments (11.7T: green, n=5, 14.1T: yellow, n=4; optogenetics: dark, n=4; error bar is ±SEM). Students't-test was used for statistical analysis.

Supplementary Table

MR Scanner	Experiments	Vessels	Onset time (t0)	Time-to-Peak (ttp)	Full width of half Maximum (FWHM)
11.7T	Sensory input (n=5)	Venules	0.96 ± 0.04s	2.82 ± 0.04s	2.90 ± 0.07s
		Arterioles	0.72 ± 0.02s	2.02 ± 0.03s	2.26 ± 0.11s
14T	Sensory input (n=4)	Venules	1.03 ± 0.05s	3.08 ± 0.07s	2.83 ± 0.10s
		Arterioles	0.63 ± 0.03s	2.29 ± 0.03s	2.27 ± 0.11s
	Optogenetics (n=4)	Venules	0.99 ± 0.06s	3.10 ± 0.11s	2.91 ± 0.22s
		Arterioles	0.67 ± 0.01s	2.07 ± 0.05s	2.25 ± 0.08s

Supplementary Table 1. The mean t0, ttp and FWHM of hemodynamic signal evoked by sensory stimulation and optical stimulation with optogenetics. The values are mean ± SEM.

Supplementary Note

Supplementary results

In Supplementary Figure 1, cerebral blood volume (CBV) fMRI signal was acquired with EPI, after injecting iron oxide particles, to compare to BOLD signal. In the mid-cortical layers mapped with the same slice orientation, the most active CBV voxels did not overlap with active BOLD voxels, which were previously assigned to the penetrating venules (Supplementary Fig 1A). This preliminary result indicated that CBV signal originated from different vascular components than the BOLD signal from mid-cortical layers of somatosensory cortex. However, there are limitations to distinguishing vessel-specific BOLD and CBV signals using the long echo train of EPI due to image distortion. In addition, the short TR to get high temporal sampling leads to low signal-to-noise ratios (SNR) with long TE after the injection of iron oxide particles. To overcome these limitations, a single k-space line scanning technique was used to build up high resolution anatomical and functional images[1].

Here, the line-scanning based FLASH-fMRI method was used to map BOLD and CBV fMRI signal from a 2D slice perpendicular to the vessels penetrating the mid-cortical layers of somatosensory cortex (Supplementary Figure 2, Supplementary video 1). The short TE (~4ms) used for detection of CBV with iron oxide particles reduced the field distortion by the iron particles in the blood to get more accurate anatomical images. This short TE remains sensitive to T2*-weighted signal changes at the high field used. The CBV and BOLD signal can be mapped directly onto the anatomical images due to less distortion from the FLASH acquisition as compared to the EPI images (Supplementary Figure 3, 4). The spatial pattern of the most active CBV voxels was clearly separated from the most active BOLD voxels from penetrating venules(Supplementary Figure 5). However, the anatomical source of the active CBV voxels has not been clarified. This work motivated us to develop the single-vessel fMRI method to clearly map the fMRI signal from individual arterioles or venules penetrating the deep layer cortex.

The detailed discussion of the vessel-specific hemodynamic signal detected by single vessel fMRI method.

An issue for this work is how to best extract individual vessel-specific hemodynamic signals. In addition to averaging all venule or arteriole voxels from multiple subjects (Supplementary Figure 13), the individual vessel responses and their spatial and temporal hemodynamic features could be characterized directly (Fig 3). Of the measures made arterioles could be very well separated from venules based on the time-to-peak differences of CBV in arterioles vs. BOLD in venules. Interestingly, there were a few venules that showed very fast BOLD onset times. As shown in Supplementary Figure 12, there were seven venules from two rats with onset times (t0) estimated shorter than 0.7s. In addition, there were two arterioles with onset times longer than 0.9s. These specific vessel onsets might be due to misassignment of the types of vessels. Re-examination of the signal in the anatomical images used to label the A-V map indicated that two of the seven venules showed only slightly lower signal intensity than the surrounding voxels just passing the threshold for identification as venules. However, the other five venule voxels demonstrated large signal drops in the A-V maps, indicating that they were likely assigned correctly. In addition, the two arterioles voxels with slow onset times were readily identified by bright spots in the A-V map. The r^2 of the hemodynamic signal fitting of the total nine vessels fell within the normal distribution of the r^2 of all the vessels detected indicating that the parameters extracted came from good fits to the data. Therefore, the fast onset venules and slow onset arterioles were not likely due to incorrect localization of the venule or arteriole voxels or to poor data fitting. Fast onset times of venules are likely due to a short capillary distance from arteriole to venule or to fast responding arterioles that feed the fast responding venules. It is clear that the temporal characteristics of vessel responses to neural activity can be measured and opens the possibility of studying changes due to aging and disease such as stroke or Alzheimer's disease.

The final challenging issue raised by the work is to understand the extravascular effects on single-vessel fMRI mapping that are well known to occur with BOLD and CBV fMRI signals. It is unclear whether the BOLD signal detected from the arteriole voxels arose from the arterioles or were due to extravascular effects from nearby venule BOLD signals. Similarly, any CBV detected on venule voxels could be due to extravascular effects from arterioles. Since very few venules showed any CBV effect at all this is a smaller problem with CBV. One way to distinguish whether signals are independent is to analyze time courses to compare different vessel types (Supplementary Figure 10, 11). The vessel t0 distribution histogram showed that 75% of the arterioles analyzed had a BOLD onset time shorter than 1s, but 60% of the venules had a BOLD onset time equal or longer than 1s. The group analysis of the mean t0 of arteriole and venules BOLD showed that the arteriole BOLD was significantly shorter than the venule BOLD (Mean t0: arteriole, 0.82±0.03s; venules, 0.96±0.04s, p=0.035, two-tail paired t-test, n=5). This result indicated that there was likely some BOLD effect in arterioles. This result of a shorter BOLD onset in arteriole voxels compared to venule voxels is consistent with a previous report showing that the tissue voxels (arterioles and capillaries) had earlier onset than the macro-venule voxels[2]. However, it could be that the 40% venule voxels with earlier onset time than 1s contributed to the arteriole BOLD signal through extravascular effects. Therefore, it is difficult to conclusively assign the early BOLD onset signal from the present study. It should be possible to do quantitative modeling based on the geometry of the vessel and the data to be more quantitative about the origins of the BOLD signals in non-venule voxels. It was observed that the majority of venule voxels did not show any CBV signal in response to the relatively short stimuli used in this study. Only a few venules had a CBV response (Supplementary Figure 11). The venule CBV signal could come from extravascular effects from nearby arterioles. There is evidence that longer stimulation leads to a venous balloon effect and so it may be that a longer duration of stimulation would lead to changes in venule CBV with different temporal features[3, 4]. In addition, the SNR of the venule voxels after injection of iron particles is significantly reduced and the fitting r^2 value for

venule CBV signal (r^2>0.2) is much lower than the fitting to other data (Supplementary Figure 13). The large variability of the FWHM can be caused by the low contrast-noise-ratio of the venule CBV signal. An alternative methodological improvement for CBV studies is to implement the arterial spin labeling or VASO approaches so CBV could be measured without introducing iron oxide particles and T2* extravascular effects would be minimized[5-8]. However, blood spin labeling approaches are predicted to give smaller signal changes and would not give the vessel size amplification that T2* based methods give making it challenging to image arterioles. Nevertheless, the fact that in-flow effects could be used to assign arterioles does give some hope to using VASO or other arterial spin labeling strategies.

Reference

1. Yu, X., Qian, C., Chen, D.Y., Dodd, S.J. & Koretsky, A.P. Deciphering laminar-specific neural inputs with line-scanning fMRI. *Nature methods* **11**, 55-58 (2014).
2. Yu, X. et al. Direct imaging of macrovascular and microvascular contributions to BOLD fMRI in layers IV-V of the rat whisker-barrel cortex. *Neuroimage* **59**, 1451-1460 (2012).
3. Silva, A.C., Koretsky, A.P. & Duyn, J.H. Functional MRI impulse response for BOLD and CBV contrast in rat somatosensory cortex. *Magnetic resonance in medicine : official journal of the Society of Magnetic Resonance in Medicine / Society of Magnetic Resonance in Medicine* **57**, 1110-1118 (2007).
4. Buxton, R.B. Dynamic models of BOLD contrast. *NeuroImage* **62**, 953-961 (2012).
5. Lu, H. & van Zijl, P.C. A review of the development of Vascular-Space-Occupancy (VASO) fMRI. *NeuroImage* **62**, 736-742 (2012).
6. Moon, C.H., Fukuda, M. & Kim, S.G. Spatiotemporal characteristics and vascular sources of neural-specific and -nonspecific fMRI signals at submillimeter columnar resolution. *NeuroImage* **64**, 91-103 (2013).
7. Huber, L. et al. Cortical lamina-dependent blood volume changes in human brain at 7 T. *NeuroImage* **107**, 23-33 (2015).
8. Detre, J.A., Leigh, J.S., Williams, D.S. & Koretsky, A.P. Perfusion imaging. *Magnetic resonance in medicine : official journal of the Society of Magnetic Resonance in Medicine / Society of Magnetic Resonance in Medicine* **23**, 37-45 (1992).

A.4 Directly mapping the single-vessel hemodynamic signal with Multi-echo Line-scanning fMRI (MELS-fMRI)

Directly mapping the single-vessel hemodynamic signal with Multi-echo Line-scanning fMRI (MELS-fMRI)

Directly mapping the single-vessel hemodynamic signal with Multi-echo Line-scanning fMRI (MELS-fMRI)

Yi He[1,2], Maosen Wang[1,2], Xin Yu[1*]

[1]Translational Neuroimaging and Neural Control Group, High Field Magnetic Resonance Department Max Planck Institute for Biological Cybernetics, Tuebingen, 72076, Germany
[2]Graduate Training Centre of Neuroscience, International Max Planck Research School, University of Tuebingen, Tuebingen, 72074, Germany

* Corresponding author: Dr. Xin Yu, Email: xin.yu@tuebingen.mpg.de.

Acknowledgments

This research was supported by funding of the DFG SPP 1665 and internal funding from the Max Planck Society. We thank Dr. Pohmann, R., Dr. Merkle H., and Buckenmaier, K. for technical support. We thank Ms. Schulz, H. and Fischer, S. for animal maintenance support. We thank Schluesner J. and Pais-Roldán P for proofreading the manuscript. We thank the AFNI team for the software support.

Keywords:

BOLD, single-vessel fMRI, vascular dynamics, hemodynamic signal, arterioles, neurovascular coupling

Abbreviations:

fMRI, functional magnetic resonance imaging; BOLD, blood oxygen level dependent; EPI, echo planar imaging; CNR, contrast to noise ratios; DTI, diffusion tensor imaging; TE, echo time; T0, Onset-time; TTP, Time-to-Peak; FWHM, full-width-of-half-maximum; MELS-fMRI, Multi-Echo Line-Scanning fMRI; A-V, Arteriole-Venule; peri-arteriole, peripheral-arteriole; peri-venule, peripheral-venule.

ABSTRACT

Besides mapping large-scale functional activity, fMRI detects the vascular dynamics of distinct cerebrovascular components in brains noninvasively. Here, a 2D multi-echo line-scanning fMRI (MELS-fMRI) method has been modified to distinguish the hemodynamic features of the fMRI signal from individual arterioles and venules penetrating the deep layer cortex. The fMRI signal is acquired at different echo-times (TE, 3-30 ms) with a 100 ms sampling rate. Venule voxels dominate the T_2*-weighted blood-oxygen-level-dependent (BOLD) signal, indicating the increased extravascular effect as the function of TE. Arteriole voxels show the T_1-weighted fMRI signal at 3 ms TE with earlier onset than venules voxels, which could be caused by the increased blood inflow and volume effects. At longer TEs, arteriole and peri-arteriole voxels illustrate a positive fMRI signal because the arteriole-specific BOLD and the extravascular effect from neighboring venules overcome the intrinsic negative effect of arteriole dilation. Meanwhile, by measuring the T_2* value from multi-echoes, the T_2*-based fMRI signal reveals the earlier fMRI onset and time-to-peak of arteriole than venule voxels. The MELS-fMRI method detects the vessel-specific TE-dependent fMRI signal, which extends the single-vessel dynamic mapping in small animals and assists the optimization of quantitative fMRI modeling of the human brain.

INTRODUCTION

High-field fMRI is utilized to map brain function non-invasively (Ogawa et al., 1990; Belliveau et al., 1991; Bandettini et al., 1992; Kwong et al., 1992; Ogawa et al., 1992; Kim and Ugurbil, 2003). High spatial resolution MR images are acquired under high magnetic field with sufficient signal-to-noise ratio (SNR) to better locate the fMRI signal coupled with brain function (Yacoub et al., 2001; Hu and Norris, 2004; Harel et al., 2010; Duyn, 2012). This advantage inherent in high field fMRI makes it possible to detect functional cortical columns (Menon et al., 1997; Grinvald et al., 2000; Kim et al., 2000; Cheng et al., 2001; Duong et al., 2001; Fukuda et al., 2006; Yacoub et al., 2008), as well as the laminar specific fMRI signal in animal and human brains (Polimeni et al., 2010; Siero et al., 2011; Goense et al., 2012; Yu et al., 2012; Moon et al., 2013; Shih et al., 2013; Yu et al., 2014; Huber et al., 2015; Heinzle et al., 2016). Recently, high field fMRI studies have mapped the fMRI signal from individual vessels penetrating the cortex of rat and cat brains in the deep cortical layers (Yu et al., 2012; Moon et al., 2013). In contrast to the BOLD signal primarily located at penetrating venules, the iron oxide particle-based cerebral blood volume (CBV) fMRI signal is detected mainly at penetrating arterioles (Yu et al., 2016). These studies indicate that fMRI can be used to directly map the vessel-specific hemodynamic signal in the cerebrovascular network.

The hemodynamic microvascular origin of fMRI signal has been better characterized by optical methods in small animals. By measuring the absorption spectral changes of oxy-deoxyhemoglobin (Malonek and Grinvald, 1996), the blood oxygen content changes of cortical vessels closely correlate with the evoked neural activity (Devor et al., 2003). Using two-photon microscopic imaging, the laminar and temporal features of neural activity-coupled arteriole dilation or pericyte-controlled capillary dilation can be further linked to the fMRI signal (Tian et al., 2010; Hall et al., 2014; Uhlirova et al., 2016). Recently, the BOLD fMRI signal was quantitatively modeled by measuring the oxygen saturation distribution from reconstructed 3D cerebrovasculature of rodent brains (Gagnon et al., 2015), showing a step forward in the interpretation of a fMRI signal based on hemodynamic signal propagation. However, few measurements directly link fMRI signal to its microvascular origin close to the neuronal source. The concurrent optical measurement of the hemodynamic responses with fMRI has revealed strong temporal correlation, but it is limited to the surface cortical vessels (Jezzard et al., 1994; Kennerley et al., 2005). In contrast, the high-resolution single-vessel fMRI method could directly characterize the vascular hemodynamic features of the fMRI signal, indicating great potential to decipher the neurovascular signaling through the cerebrovasculature directly by using fMRI.

In this study, a multi-echo acquisition scheme was implemented to the line-scanning fMRI method, i.e. multi-echo line-scanning fMRI (MELS-fMRI). The line-scanning method originates from the pioneer work of Mansfield *et al*(Mansfield et al., 1976). To construct MR images, each k-space line is acquired consecutively along the block design paradigm and the on/off stimulation trials are repeated for the number of phase-encoding steps (Silva and Koretsky, 2002; Yu et al., 2016). Since only one k-space line is acquired per echo, the acquisition window could be significantly reduced to 1-2 ms, which is much shorter than the readout echo train (10-20 ms) of the EPI method. The short acquisition window not only avoids the long echo train-induced extra T_2*-weighting under the high magnetic field, but also shortens the minimal TE(Lee et al., 1999; Hyde et al., 2001; Duong et al., 2003; Goense and Logothetis, 2006; Yu et al., 2012; Budde et al., 2014). Thus, the MELS-fMRI method can sample the T_1 or T_2* weighted fMRI signal at different TEs, as well as examine temporal features of the T_2*-based fMRI signal at the single vessel level. The vessel-specific fMRI signal could lead to better verification and optimization of fMRI quantitative models for human brain mapping.

MATERIALS AND METHODS

Animal preparation

All animal experiments were performed according to a protocol approved by the animal protection committee (Regierungspräsidium Tuebingen). FMRI experiments were performed on five male Sprague Dawley rats. All procedures are described in a previous study (Yu et al., 2010). Rats were initially anesthetized with isoflurane (5% induction, 1.5% maintenance). Each rat was orally intubated and placed on a mechanical ventilator (SAR-830/AP, CWE Inc.). Plastic catheters were inserted into the right femoral artery and vein to allow monitoring of arterial blood gasses and administration of anesthetics. After surgery, each rat was given an intravenous bolus of α-chloralose (80 mg/kg) and isoflurane was discontinued. Anesthesia was maintained with a constant infusion of α-chloralose (26.5 mg/kg/h). The animals were placed on a heated pad to maintain rectal temperature at 37 °C while in the magnet. Each animal was secured in a head holder with a tooth-bar to prevent head motion. End-tidal CO_2, rectal temperature, tidal pressure of ventilation, heart rate, and arterial blood pressure were continuously monitored during the experiment. Arterial blood gas levels were checked periodically and corrections were made by adjusting the respiratory volume or administering sodium bicarbonate to maintain blood gas levels when required. An intravenous injection of pancuronium bromide (4 mg/kg) was given once per hour to reduce motion artifacts. Voluntary respiration-induced resonance

offset reduced significantly following the administration of the pancuronium injection.

MRI image acquisition

All images were acquired with a 14.1 T / 26 cm horizontal bore magnet (Magnex), interfaced to an AVANCE III console (Bruker, Germany) and equipped with a 12 cm gradient set, capable of providing 100 G/cm with a rise time of 150 μs (Resonance Research). A transceiver surface coil with 6 mm diameter was used to acquire images.

Multi-Echo Line-Scanning fMRI (MELS-fMRI): A 2D Multiple Gradient Echo (MGE) sequence was modified to perform multi-echo line-scanning fMRI with the following parameters: TEs, 3 ms, 6.5 ms, 10 ms, 13.5 ms, 17 ms, 20.5 ms, 24 ms, 27.5 ms, 31 ms; TR, 100 ms; flip angle, 22°; matrix, 96 x 64; slice thickness, 400 μm; in-plane resolution, 100 x 100 μm. Two saturation slices were applied to suppress signal out of the Field of view (FOV) to reduce the potential aliasing effect along the phase-encoding direction. The frequency-encoding direction was set along the z0 direction towards the lung to reduce the respiration-induced resonance offset. The block-design stimulation paradigm was used in the MELS-fMRI experiment. The electrical stimulation was delivered by a stimulation isolator (AD Instruments) (2.0 mA, 300 μs pulses repeated at 3 Hz) through two needle electrodes that were inserted between digits of the forepaw. The block-design paradigm consisted of 60 dummy scans to reach steady state, followed by 10 pre-stimulation scans, 20 scans during electrical stimulation, and 100 scans post-stimulation (with a total of 13 s for each on/off stimulation experiment). For image acquisition, only one single-phase k-space line was acquired at each TE per 100 ms before the second set of k-spaces was filled during the block design trial (Supplementary Figure 1). Each trial consisted of 3 epochs of stimulation on/off design with total 390 TRs. The trials were repeated for the number of phase-encoding steps. The total duration was 40 minutes, and 3 - 6 MELS-fMRI trials were acquired for each rat.

The single-vessel Arteriole-Venule (A-V) map: A 2D Multiple Gradient Echo (MGE) sequence was used to detect individual arterioles and venules with the following parameters: TR, 50 ms; TEs, 2.5 ms, 5 ms, 7.5 ms, 10 ms, 12.5 ms, 15 ms, 17.5 ms; flip angle, 40°; matrix, 192 × 128; in-plane resolution, 50 μm × 50 μm; slice thickness, 400 μm. This slice orientation was perpendicular to the penetrating vessels and covered forepaw S1 areas based on the Paxinos atlas. The horizontal slice angle was set at 15° and the center of the slice was positioned 1.2 mm from the cortical surface to cover layer 5 (Fig. 1 A). Similar to the previous study (Yu et al., 2016), by averaging the MGE images acquired from the second echo to the fourth echo, the single-vessel A-V map showed the venule voxels as dark dots due to fast T_2* dephase, while

arteriole voxels remained bright dots due to the in-flow effect. The individual vessel voxels were determined based on their signal intensity as either higher than the mean signal intensity plus 3 times standard deviation (arterioles) or lower than the mean signal intensity minus 3 times the standard deviation (venules) of the local areas in a 7x7 kernel. The venule voxels were colored blue while the arterial voxels were colored red (Fig. 1 A). After the vessel voxels were characterized, an “imdilate” Matlab function was used to select the voxels surrounding the vessel voxels specifically. To avoid the overlap of peri-vessel voxels from different vessel voxels, a dilating factor of 2 was chosen so as to set the expanded peri-vessel ROI with a width of 2 voxels (Fig. 2 C).

Image processing and statistical analysis

MELS-fMRI data analysis was performed using the “Analysis of Functional NeuroImages” (AFNI) (Cox, 1996) software (NIH) and MATLAB. The detailed description of the processing is provided in a previous study (Yu et al., 2014).

MELS-fMRI preprocessing: The MELS-fMRI 2D k-space data were first reordered with a Matlab script, and then reconstructed to MELS-fMRI images using a built-in function of Bruker Paravision software. For AFNI analysis, a 2D registration function was applied to align all MELS-fMRI images to a template for multiple datasets acquired in the same orientation setup. To register the MELS-fMRI images with the single-vessel map, a tag-based registration method was applied. Ten to twelve tags were chosen from the venule voxels distributed around the 2D slices of MELS-fMRI and single-vessel images. The baseline level of MELS-fMRI images was scaled to 100 and multiple trials of block-design time courses were averaged for statistical analysis. The hemodynamic response function (HRF) was estimated by the linear regression using tent basis function as previously reported(Yu et al., 2016).

T_2 Mapping*: T_2* values were calculated in voxel-wise by fitting the following exponential decay equation:

$$f(t) = S_0 \times \exp\left(-t / T_2^*\right) \quad [1]$$

Where t is the time variable and S_0 is the initial signal intensity. T_2*-based fMRI signal was estimated based on the percentage change of the T_2* value from the baseline level scaled to 100.

Contrast-to-Noise Ratio (CNR): CNR (Geissler et al., 2007) was estimated based on the following equation:

$$CNR = (S_P - S_B) / \sigma_B \quad [2]$$

Where S_P is the peak amplitude, S_B is the mean of baseline signal, and σ_B is the standard deviation of the baseline signal, respectively. The CNR of the fMRI signal at

different echoes and T_2*-based fMRI signal were analyzed with one-way ANOVA followed by Tukey's multiple comparison tests.

Estimation of the hemodynamic temporal features of vessel-specific fMRI signal: A two-gamma-variate fitting process was used to fit the fMRI signal acquired from individual vessel voxels (Madsen, 1992).

$$F(t) = a \times (t/(p \times q))^p \times e^{p-t/q} - b \times (t/(r \times s))^r \times e^{r-t/s} \quad [3]$$

Where t is the temporal variable and a, p, q, b, r and s are the coefficients for two-gamma-variate-function. The onset time (T0) was measured as an intercept with the baseline by fitting one line to the rising slope between 20% and 80% of the peak amplitude estimated from the two-gamma-variate-function(Tian et al., 2010). The time-to-peak (TTP) and the full-width-of-half-maximum (FWHM) were estimated directly from the two-gamma-variate-function (Supplementary Figure 2).

A paired Student's t-test was performed to compare the mean signal intensity, T0, TTP, and FWHM of T_2* fMRI signal from the venule voxels and arteriole voxels. The error bar in each graph represents the standard error of the mean (s.e.m).

RESULTS

Mapping the T_2-weighted fMRI signal from arterioles and venules with MELS-fMRI*

Previously, the line-scanning method was applied to acquire a single k-space line along the on/off block design to map the fMRI signal with high spatial and temporal resolution(Silva and Koretsky, 2002; Yu et al., 2014; Yu et al., 2016). Here, multi-gradient echoes were implemented into the single-vessel fMRI method. In contrast to the multi-echo EPI-fMRI and FLASH-fMRI method (Menon et al., 1993; Chen and Wyrwicz, 1999; Weiskopf et al., 2005; Poser et al., 2006), the MELS-fMRI acquired only one k-space line for each echo at every TR during an on/off stimulation block design trial and the k-space was filled sequentially by repeating the fMRI block-design stimulation trials for the number of phase-encoding steps (Fig. 1 C). This acquisition scheme sampled fMRI signals from multiple echoes ranging from 3 ms to 30 ms at every 100 ms with an acquisition window for each echo in less than 1-2 ms.

The individual arterioles and venules penetrating the deep layer cortex could be directly mapped by an inflow based multi-gradient echo (MGE) sequence (Yu et al., 2016), which had been previously proposed for the human brain mapping to identify pial arteries and veins (Menon et al., 1993). For shorter TEs, both arterioles and venules with fast blood flow were detected as brighter voxels due to the inflow effect. In contrast, only venules were detected as darker voxels at the longer TE due to the

fast T_2* decay of the deoxygenated venule blood at the longer TEs, but not the arterioles because of the similar susceptibility of the oxygenated blood to the surrounding parenchyma voxels. MGE images at different TEs were integrated into the arteriole-venule (A-V) map, demonstrating arterioles as bright dots and venules as dark dots (Fig. 1A). The size of penetrating vessels detected with the A-V map ranged from 30 to 70 microns (Yu et al., 2016). The vessel diameter was previously estimated based on vessel distance of the A-V map in comparison to the mean distance of penetrating vessels in the 3D reconstruction of the vascular network characterized by two-photon imaging (Blinder et al., 2010; Keller et al., 2011; Gagnon et al., 2015).

The same slice orientation was applied for both MELS-fMRI images and the A-V map so that the vessel-specific fMRI signal could be identified for individual arteriole and venule voxels penetrating the deep layer cortex. The primary somatosensory (S1) cortex was covered in the A-V map (Fig. 1A). Electrical stimulation of the forepaw elicited the fMRI signal, which could be detected by the MELS-fMRI method. Fig. 1B illustrates the T_2* decay curves of arteriole and venule voxels as a function of TE, which were acquired every 100 ms along the on/off block design. Fig. 1 D shows a 3d plot of decay curves along the stimulation on/off period during the block design (Supplementary Movie 1). At the stimulation-on period, the T_2*-weighted signal at different TEs of the decay curves increased, indicating that fMRI signal changes could be directly characterized through the multiple echoes with MELS-fMRI.

The detailed functional patterns were characterized with TEs from 3 ms to 20.5 ms with MELS-fMRI (Fig. 2 A, B, Supplementary Movie 2). The peak fMRI signal acquired at different echoes was located primarily on venule voxels. This was also demonstrated by comparing the peak amplitude of fMRI time courses detected from arteriole and venule voxels (Fig. 2 C). The other voxels, enriched with capillaries or small vessels not identified by the A-V map, showed higher fMRI peak amplitude than arteriole voxels, but lower than venule voxels at different TEs (Supplementary Figure 3). To better characterize the fMRI signal at different vascular components, the non-vessel voxels were further distinguished as parenchyma voxels surrounding arterioles, i.e. peri-arteriole voxels, and parenchyma voxels surrounding venules, i.e. peri-venule voxels. At short TEs, the peak fMRI signal matched well with the venules voxels detected in the A-V map, which could be caused by the oxy/deoxy-hemoglobin changes of the venule blood, i.e. the BOLD effect, since the venule blood has very short T_2 (Lee et al., 1999; Blockley et al., 2008). In contrast, the BOLD fMRI signal spread to peri-venule voxels due to the increased extravascular effect at the longer TE. The multi-echo scheme of MELS-fMRI made it possible to specify the extravascular effect on the functional patterns with different T_2* weighting, as well as

the potential contribution from the T_1-weighted signal due to cerebral blood flow changes from arterioles. The peak fMRI signal from peri-arteriole and peri-venule voxels was extracted to compare with the arteriole and venule fMRI signal at different TEs (Fig. 2 C). Quantitative analysis demonstrated that the peak fMRI signal from peri-venule voxels was significantly higher than that of the peri-arteriole voxels at longer TEs from 10 to 20 ms (Fig. 2 D). In addition, the TE-dependent fMRI peak signal of the other non-vessel voxels showed similar amplitude to that of the peri-venule voxels (Supplementary Figure 4). These results indicated that the extravascular effect from venules could be directly measured from the peri-venule voxels and the other non-vessel voxels enriched with capillaries or small vessels using the MELS-fMRI method. In contrast, the peak fMRI signal of arterioles was significantly higher than that of the peri-arteriole voxels for shorter TEs (3 and 6.5 ms), but not for longer TEs (Fig. 2 E). This result indicated that the inflow effect due to activity-coupled cerebral blood flow and volume changes might directly contribute to the fMRI signal acquired at short TEs. Besides the peak fMRI signal, the fMRI signal acquired from 1 s to 2 s following stimulus onset was compared among arteriole, venule, peri-arteriole and peri-venule voxels at the short TE (3 ms) (Supplementary Figure 5). The early fMRI signal (e.g. 1 s, 1.2 s after stimulus onset) from arteriole voxels was significantly higher than that of the other voxels. These results indicated that the CBF/CBV dependent arteriole-specific fMRI signal could be detected by MELS-fMRI, which was independent of the BOLD effect dominating fMRI signal detected in venule voxels.

Analysis of the T_2*-based fMRI signal from arterioles and venules with MELS-fMRI

Besides the T_2*-weighted fMRI signal at each TE, the T_2* decay curves were fitted to estimate the T_2* value for each voxel at every 100ms. Fig. 3 B demonstrates the T_2* maps acquired at 2 s and 3 s after the stimulus onset. The estimated T_2* values of venules voxels were much lower than the arteriole and non-vessel parenchyma voxels due to the high susceptibility of the deoxy-hemoglobin of venule blood. In contrast, the arteriole and non-vessel parenchyma voxels showed similar T_2* values because of the similar susceptibility of arteriole blood with high concentration of oxy-hemoglobin to that of non-vessel parenchyma voxels enriched with capillaries or small vessels. Fig. 3 C illustrates the averaged time courses of T_2* values of arteriole and venule voxels, which were highly consistent through the fitting curves from 6 to 10 TEs. Furthermore, similar to previous multi-echo EPI studies(Chen and Wyrwicz, 1999; Poser and Norris, 2009; Kundu et al., 2013), the contrast-to-noise ratios (CNR) of the T_2* based fMRI signal changes were significantly higher than the

T_2*-weighted fMRI signal changes acquired at each echo for both arteriole and venule voxels (Fig. 3 D, E). In addition, the T_2*-based fMRI signal showed similar or higher CNR than that of the averaged T_2*-weighted image acquired at all TEs (Fig. 3 D, E). In contrast to the line-scanning single-vessel fMRI method, the multi-echo acquisition of MELS-fMRI allowed us to achieve higher CNR of the fMRI signal to better characterize the temporal hemodynamic features of individual arterioles and venules penetrating the somatosensory cortex.

The T_2*-based fMRI signal changes were characterized from individual arteriole and venule voxels. Similar to the T_2*-weighted functional maps acquired at different TEs (Fig. 2), the peak T_2*-based fMRI signal was primarily located at the penetrating venules (Fig. 4 B, Supplementary Movie 3). The vessel-specific temporal features of the T_2*-based fMRI signal could be characterized with the MELS-fMRI method. The time courses of T_2*-based fMRI signal with fitting curves were plotted from individual arteriole and venule voxels (Fig. 4 C). The averaged time courses of the T_2*-based fMRI signal showed an earlier onset from arteriole than venule voxels (Fig. 4 D). The T_2* value of arteriole voxels detected at 0.8 s after stimulus onset was significantly higher than that of venule voxels, which was reversed at later time points, e.g. at 1.8 s after the stimulus onset (Fig. 4 E, F). This result was consistent with a previous study using EPI-fMRI method to decipher the distinct vascular components contributing to BOLD-fMRI signal (Yu et al., 2012). The onset time (T0), time-to-peak (TTP) and full-width-of-half-maximum (FWHM) plots of the T_2*-based fMRI signal readily separated arteriole and venule responses into distinct clusters (Fig. 4 G). The T0 and TTP of the arteriole voxels were significantly shorter than those of the venule voxels (Fig. 4 H), demonstrating the potential hemodynamic signal propagation through the cerebrovasculature directly mapped by MELS-fMRI. Therefore, MELS-fMRI makes it possible to extract the unique hemodynamic features of the fMRI signal detected from individual arteriole and venules in the deep layer cortex.

DISCUSSION

The MELS-fMRI method offers two unique features when mapping the fMRI signal in the individual vessels in the brain. First is the very short acquisition window (1-2 ms) due to the single-phase line acquired per TR, which significantly shortens the minimal TE and excludes additional T_2* dephasing during echo acquisition. The other is the detection of vessel-specific fMRI signal from multi-echoes with high spatiotemporal resolution. In this study, the fMRI signal was acquired with the sampling rate at 10 Hz over a field of view up to 9 x 6 mm of the rat cortex. Although only penetrating vessels (>30 μm) were identified from the A-V map (Blinder et al.,

2010; Keller et al., 2011), the vessel-specific fMRI signal could be directly mapped in the deep layer cortex up to 1-1.5 mm, which was beyond the conventional optical penetration depth(Yu et al., 2016). MELS-fMRI further extended the single-vessel mapping scheme to acquire fMRI signal at different TEs so that unique hemodynamic response features could be directly detected from fMRI signal with either T_1 or T_2* weighting. Although the line-scanning scheme elongated the total imaging time making it less practical for human brain mapping, the vessel-specific fMRI signal acquired at different TEs provided first-hand experimental data to optimize the vessel-specific quantitative modeling of the fMRI signal (Gagnon et al., 2015).

The MELS-fMRI method better characterized the intravascular and extravascular effect from the vessel and the surrounding parenchyma at different TEs. Consistent with previous experimental and model prediction studies (Yacoub et al., 2003; Jochimsen et al., 2004; Uludag et al., 2009; Gagnon et al., 2015), the extravascular effect from venules increased as the function of TE, which could be directly detected as largely spread fMRI signal from venules voxels to the surrounding voxels (Fig 2). In addition, the peak CNR of T_2*-weighted fMRI signal at venule voxels was detected at the TE similar to the T_2* value of venule voxels (Fig. 3E). The arteriole T_2* value did not match the TE with peak CNR of T_2*-weighted fMRI, which could be deviated by the extravascular effect of nearby venule voxels. In contrast to the extravascular effect, the direct measurement of the intravascular effect was more challenging given the limit of spatial resolution. The penetrating vessel size, characterized in the cortex by the single-vessel fMRI method or two-photon microscopy, ranged from 30 to 70 microns(Blinder et al., 2010; Yu et al., 2016). Despite the high spatial resolution, the fMRI signal from designated single-vessel voxels contained a good portion of partial volume effects from surrounding non-vessel parenchyma. Thus, the peak fMRI signal detected from the venule voxels remained partially extravascular-driven (Yu et al., 2012). However, for very short TEs, the intravascular effect from the venule blood could be approximately characterized given the very short T_2* value of the deoxygenated blood (Lee et al., 1999; Blockley et al., 2008; Gagnon et al., 2015). Though the fMRI signal detected at short TE might not be as specific as in the spin-echo scheme to exclude the extravascular effect by the refocusing pulse (Duong et al., 2003; Ugurbil et al., 2003; Yacoub et al., 2003; Jochimsen et al., 2004), the intravascular effect contribution to the venule voxels could be much higher for shorter TEs than for longer TEs. This intravascular effect could be better visualized on the venule voxels, showing a strong fMRI signal at the 3ms TE (Fig. 2).

One novel application of MELS-fMRI is to detect fMRI signal changes from individual arterioles at different TEs. In contrast to the BOLD signal acquisition with

EPI-fMRI, the direct CBV and CBF-based signal was not detectable without a specific mapping sequence, e.g. arterial spin labeling (Detre et al., 1992; Kim et al., 2007a) or vascular space occupancy (Lu et al., 2003), or injection with contrast agent for CBV (Belliveau et al., 1991; Lee et al., 2001; Kim and Kim, 2011). The fMRI signal detected by MELS-fMRI at short TEs from 3 ms to 6.5 ms depended more on the T_1-weighted effect for voxels covering parenchyma enriched with capillaries or small arterioles with oxygenated blood. The vessel-specific inflow signal over the saturation effect due to the lack of full relaxation under the short TR (100 ms) of MELS-fMRI led to significantly higher fMRI signal from the arteriole voxels compared to the peri-arteriole voxels (Fig. 2 E) (Kim et al., 1994). This could be directly caused by the increased CBF/CBV (Kim et al., 2007b) upon stimulation. Interestingly, even at the long TE we did not observe the CBV-induced decrease of BOLD-fMRI signal either at the arteriole or peri-arteriole voxels from the averaged time courses as suggested for fMRI predictive models(Uludag et al., 2009). The negative extravascular effect of arterioles on the BOLD signal was suggested to be caused by the susceptibility difference of arteriole blood from the surrounding tissue parenchyma (the baseline oxygen level of arteriole blood (95%) has similar susceptibility to surrounding tissue(Spees et al., 2001; Blockley et al., 2008), but evoked neural activity increases oxygen level of arteriole blood to induce susceptibility difference from surrounding tissue, which leads to decreased BOLD fMRI signal)(Uludag et al., 2009; Vazquez et al., 2010a). There are a few possible explanations to explain the discrepancy. First, Gagnon et al. detected that the oxygen levels of penetrating arterioles varied from 70 to 95% (Gagnon et al., 2015). Upon stimulation, the changes of susceptibility difference may vary from individual arterioles since not all arterioles with baseline oxygen level have similar susceptibility to surrounding tissues, which could cancel out the expected negative extravascular effect of arterioles. Second, the arteriole dilation could increase the volume contribution of blood with increased oxygen levels upon stimulation. The signal changes of the arteriole voxels are determined by both the susceptibility difference of arteriole blood from surrounding tissue and the susceptibility changes of arteriole blood with increased oxygen levels. Thirdly, the negative BOLD signal from arteriole or peri-arteriole voxels can also be concealed by the highly spread extravascular effect of venules as presented in Fig. 2. Altogether, multiple effects from the arteriole blood oxygen content, particle volume contribution, and the extravascular effects of nearby venules could lead to the lack of negative CBV contribution to the BOLD-fMRI signal detected in the present study.

Similar to previous multi-echo EPI studies (Chen and Wyrwicz, 1999; Poser and Norris, 2009; Kundu et al., 2013), the T_2*-based functional map showed much higher

CNR than the T_2*-weighted functional maps acquired at each TE (Fig. 3 D, E). The temporal features of the vessel specific hemodynamic signal can be better characterized to show earlier onset time of the arteriole T_2*-based fMRI signal (0.92 ± 0.03 s) than that of the venule T_2*-based fMRI signal (1.14 ± 0.03 s). The T_2*-based fMRI functional mapping represented more significant vessel-specific onset time difference compared to previous single-vessel T_2*-weighted fMRI studies (Yu et al., 2016), which could be due to the better CNR of the T_2*-based fMRI signal. Also noteworthy is that the time-to-peak of the T_2*-based fMRI signal from arterioles was significantly shorter than that of the venules. The T_2*-based early arteriole fMRI signal onset and time-to-peak could result from the oxy/deoxy-hemoglobin ratio changes detected in arterioles (Berwick et al., 2005; Hillman et al., 2007; Vazquez et al., 2010b), as well as from the CBF/CBV contribution at short TEs (Supplementary Figure 5). The onset time of fMRI signal detected by MELS-fMRI is similar to previous studies, indicating BOLD signal increased as early as 1s after stimulus onset in both cat and human visual cortex (Lin et al., 2013; Moon et al., 2013). Meanwhile, Silva *et al*. used an M-sequence and showed faster BOLD-fMRI onset with a mean time-to-peak less than 2.5s due to the short stimulation duration(Silva et al., 2007). Thus, the T_2*-based MELS-fMRI could better differentiate the temporal features of fMRI signal from arteriole and venule voxels than the T_2*-weighted fMRI acquired from the single echo (Yu et al., 2012; Yu et al., 2016).

In contrast to the EPI-fMRI with conventional Cartesian or Spiral trajectory to cover k-space, MELS-fMRI was less efficient and highly sensitive to motion artifacts. This is because the MELS-fMRI k-space was filled inconsecutively through the time series of the on/off block design. This line-scanning scheme leads to a great number of averaging of the fMRI signal across multiple blocks. Therefore, signal acquisition in real time in MELS-fMRI differed from multi-echo EPI-fMRI, and MELS-fMRI could not be used for non-BOLD component correction for the resting-state fMRI study(Kundu et al., 2012). This implies that the MELS-fMRI method would be less practical for human brain mapping and awake animal fMRI. However, this method could be readily used for ventilated and head-fixed animals under anesthesia. In addition, MELS-fMRI was less sensitive to the field inhomogeneity and fluctuation. It was less dependent on gradient performance and had shorter readout times than EPI-fMRI. These features allowed MELS-fMRI to acquire images with a much higher spatiotemporal resolution than EPI-fMRI to directly decipher distinct vascular contributions to the fMRI signal with different hemodynamic features. This method provided a unique advantage to characterize the vessel-specific neurovascular signaling events in the normal and diseased states, e.g. stroke or vascular/neuronal dementia, of animal models.

Acknowledgments

This research was supported by funding of the DFG SPP 1665 and internal funding from the Max Planck Society. We thank Dr. Pohmann, R., Dr. Merkle H., and Buckenmaier, K. for technical support. We thank Ms. Schulz, H. and Fischer, S. for animal maintenance support. We thank Schluesner J. and Pais-Roldán P for proofreading the manuscript. We thank the AFNI team for the software support.

Conflict of Interest: The authors declare that no competing interests exist.

Authors' contributions

XY designed the research. YH, MW performed animal experiments; YH, XY acquired and analyzed data; XY, YH wrote the paper.

REFERENCES

Bandettini, P.A., Wong, E.C., Hinks, R.S., Tikofsky, R.S., and Hyde, J.S. (1992). Time course EPI of human brain function during task activation. Magn Reson Med 25, 390-397.

Belliveau, J.W., Kennedy, D.N., Jr., McKinstry, R.C., Buchbinder, B.R., Weisskoff, R.M., Cohen, M.S., Vevea, J.M., Brady, T.J., and Rosen, B.R. (1991). Functional mapping of the human visual cortex by magnetic resonance imaging. Science 254, 716-719.

Berwick, J., Johnston, D., Jones, M., Martindale, J., Redgrave, P., McLoughlin, N., Schiessl, I., and Mayhew, J.E. (2005). Neurovascular coupling investigated with two-dimensional optical imaging spectroscopy in rat whisker barrel cortex. Eur J Neurosci 22, 1655-1666.

Blinder, P., Shih, A.Y., Rafie, C., and Kleinfeld, D. (2010). Topological basis for the robust distribution of blood to rodent neocortex. Proc Natl Acad Sci U S A 107, 12670-12675.

Blockley, N.P., Jiang, L., Gardener, A.G., Ludman, C.N., Francis, S.T., and Gowland, P.A. (2008). Field strength dependence of R1 and R2* relaxivities of human whole blood to ProHance, Vasovist, and deoxyhemoglobin. Magnetic resonance in medicine : official journal of the Society of Magnetic Resonance in Medicine / Society of Magnetic Resonance in Medicine 60, 1313-1320.

Budde, J., Shajan, G., Zaitsev, M., Scheffler, K., and Pohmann, R. (2014). Functional MRI in human subjects with gradient-echo and spin-echo EPI at 9.4 T. Magnetic resonance in medicine : official journal of the Society of Magnetic Resonance in Medicine / Society of Magnetic Resonance in Medicine 71, 209-218.

Chen, N.K., and Wyrwicz, A.M. (1999). Correction for EPI distortions using multi-echo gradient-echo imaging. Magn Reson Med 41, 1206-1213.

Cheng, K., Waggoner, R.A., and Tanaka, K. (2001). Human ocular dominance columns as revealed by high-field functional magnetic resonance imaging. Neuron 32, 359-374.

Cox, R.W. (1996). AFNI: software for analysis and visualization of functional magnetic resonance neuroimages. Computers and biomedical research, an international journal 29, 162-173.

Detre, J.A., Leigh, J.S., Williams, D.S., and Koretsky, A.P. (1992). Perfusion imaging. Magn Reson Med 23, 37-45.

Devor, A., Dunn, A.K., Andermann, M.L., Ulbert, I., Boas, D.A., and Dale, A.M. (2003). Coupling of total hemoglobin concentration, oxygenation, and neural activity in rat somatosensory cortex. Neuron 39, 353-359.

Duong, T.Q., Kim, D.S., Ugurbil, K., and Kim, S.G. (2001). Localized cerebral blood flow response at submillimeter columnar resolution. Proc Natl Acad Sci U S A 98, 10904-10909.

Duong, T.Q., Yacoub, E., Adriany, G., Hu, X., Ugurbil, K., and Kim, S.G. (2003). Microvascular BOLD contribution at 4 and 7 T in the human brain: gradient-echo and spin-echo fMRI with suppression of blood effects. Magn Reson Med 49, 1019-1027.

Duyn, J.H. (2012). The future of ultra-high field MRI and fMRI for study of the human brain. NeuroImage 62, 1241-1248.

Fukuda, M., Moon, C.H., Wang, P., and Kim, S.G. (2006). Mapping iso-orientation columns by contrast agent-enhanced functional magnetic resonance imaging: reproducibility, specificity, and evaluation by optical imaging of intrinsic signal. J Neurosci 26, 11821-11832.

Gagnon, L., Sakadzic, S., Lesage, F., Musacchia, J.J., Lefebvre, J., Fang, Q., Yucel, M.A., Evans, K.C., Mandeville, E.T., Cohen-Adad, J.*, et al.* (2015). Quantifying the microvascular origin of BOLD-fMRI from first principles with two-photon microscopy and an oxygen-sensitive nanoprobe. J Neurosci 35, 3663-3675.

Geissler, A., Gartus, A., Foki, T., Tahamtan, A.R., Beisteiner, R., and Barth, M. (2007). Contrast-to-noise ratio (CNR) as a quality parameter in fMRI. J Magn Reson Imaging 25, 1263-1270.

Goense, J., Merkle, H., and Logothetis, N.K. (2012). High-resolution fMRI reveals laminar differences in neurovascular coupling between positive and negative BOLD responses. Neuron 76, 629-639.

Goense, J.B., and Logothetis, N.K. (2006). Laminar specificity in monkey V1 using high-resolution SE-fMRI. Magn Reson Imaging 24, 381-392.

Grinvald, A., Slovin, H., and Vanzetta, I. (2000). Non-invasive visualization of cortical columns by fMRI. Nat Neurosci 3, 105-107.

Hall, C.N., Reynell, C., Gesslein, B., Hamilton, N.B., Mishra, A., Sutherland, B.A., O'Farrell, F.M., Buchan, A.M., Lauritzen, M., and Attwell, D. (2014). Capillary pericytes regulate cerebral blood flow in health and disease. Nature 508, 55-60.

Harel, N., Bolan, P.J., Turner, R., Ugurbil, K., and Yacoub, E. (2010). Recent advances in high-resolution MR application and its implications for neurovascular coupling research. Frontiers in neuroenergetics 2.

Heinzle, J., Koopmans, P.J., den Ouden, H.E., Raman, S., and Stephan, K.E. (2016). A hemodynamic model for layered BOLD signals. NeuroImage 125, 556-570.

Hillman, E.M., Devor, A., Bouchard, M.B., Dunn, A.K., Krauss, G.W., Skoch, J., Bacskai, B.J., Dale, A.M., and Boas, D.A. (2007). Depth-resolved optical imaging and microscopy of vascular compartment dynamics during somatosensory stimulation. NeuroImage 35, 89-104.

Hu, X.P., and Norris, D.G. (2004). Advances in high-field magnetic resonance imaging. Annu Rev Biomed Eng 6, 157-184.

Huber, L., Goense, J., Kennerley, A.J., Trampel, R., Guidi, M., Reimer, E., Ivanov, D., Neef, N., Gauthier, C.J., Turner, R., and Moller, H.E. (2015). Cortical lamina-dependent blood volume changes in human brain at 7 T. NeuroImage 107, 23-33.

Hyde, J.S., Biswal, B.B., and Jesmanowicz, A. (2001). High-resolution fMRI using multislice partial k-space GR-EPI with cubic voxels. Magn Reson Med 46, 114-125.

Jezzard, P., Heineman, F., Taylor, J., DesPres, D., Wen, H., Balaban, R.S., and Turner, R. (1994). Comparison of EPI gradient-echo contrast changes in cat brain caused by respiratory challenges with direct simultaneous evaluation of cerebral oxygenation via a cranial window. NMR Biomed 7, 35-44.

Jochimsen, T.H., Norris, D.G., Mildner, T., and Moller, H.E. (2004). Quantifying the intra- and extravascular contributions to spin-echo fMRI at 3 T. Magn Reson Med 52, 724-732.

Keller, A.L., Schuz, A., Logothetis, N.K., and Weber, B. (2011). Vascularization of cytochrome oxidase-rich blobs in the primary visual cortex of squirrel and macaque monkeys. J Neurosci 31, 1246-1253.

Kennerley, A.J., Berwick, J., Martindale, J., Johnston, D., Papadakis, N., and Mayhew, J.E. (2005). Concurrent fMRI and optical measures for the investigation of the hemodynamic response function. Magn Reson Med 54, 354-365.

Kim, D.S., Duong, T.Q., and Kim, S.G. (2000). High-resolution mapping of iso-orientation columns by fMRI. Nat Neurosci 3, 164-169.

Kim, S.G., Hendrich, K., Hu, X., Merkle, H., and Ugurbil, K. (1994). Potential pitfalls of functional MRI using conventional gradient-recalled echo techniques. NMR in biomedicine 7, 69-74.

Kim, S.G., and Ugurbil, K. (2003). High-resolution functional magnetic resonance imaging of the animal brain. Methods 30, 28-41.

Kim, T., Hendrich, K.S., Masamoto, K., and Kim, S.G. (2007a). Arterial versus total blood volume changes during neural activity-induced cerebral blood flow change: implication for BOLD fMRI. J Cereb Blood Flow Metab 27, 1235-1247.

Kim, T., Hendrich, K.S., Masamoto, K., and Kim, S.G. (2007b). Arterial versus total blood volume changes during neural activity-induced cerebral blood flow change: implication for BOLD fMRI. J Cerebr Blood F Met 27, 1235-1247.

Kim, T., and Kim, S.G. (2011). Temporal dynamics and spatial specificity of arterial and venous blood volume changes during visual stimulation: implication for BOLD quantification. Journal of cerebral blood flow and metabolism : official journal of the International Society of Cerebral Blood Flow and Metabolism 31, 1211-1222.

Kundu, P., Brenowitz, N.D., Voon, V., Worbe, Y., Vertes, P.E., Inati, S.J., Saad, Z.S., Bandettini, P.A., and Bullmore, E.T. (2013). Integrated strategy for improving functional connectivity mapping using multiecho fMRI. Proc Natl Acad Sci U S A 110, 16187-16192.

Kundu, P., Inati, S.J., Evans, J.W., Luh, W.M., and Bandettini, P.A. (2012). Differentiating BOLD and non-BOLD signals in fMRI time series using multi-echo EPI. NeuroImage 60, 1759-1770.

Kwong, K.K., Belliveau, J.W., Chesler, D.A., Goldberg, I.E., Weisskoff, R.M., Poncelet, B.P., Kennedy, D.N., Hoppel, B.E., Cohen, M.S., Turner, R., and et al. (1992). Dynamic magnetic resonance imaging of human brain activity during primary sensory stimulation. Proc Natl Acad Sci U S A 89, 5675-5679.

Lee, S.P., Duong, T.Q., Yang, G., Iadecola, C., and Kim, S.G. (2001). Relative changes of cerebral arterial and venous blood volumes during increased cerebral blood flow: implications for BOLD fMRI. Magn Reson Med 45, 791-800.

Lee, S.P., Silva, A.C., Ugurbil, K., and Kim, S.G. (1999). Diffusion-weighted spin-echo fMRI at 9.4 T: microvascular/tissue contribution to BOLD signal changes. Magnetic resonance in medicine : official journal of the Society of Magnetic Resonance in Medicine / Society of Magnetic Resonance in Medicine 42, 919-928.

Lin, F.H., Witzel, T., Raij, T., Ahveninen, J., Tsai, K.W., Chu, Y.H., Chang, W.T., Nummenmaa, A., Polimeni, J.R., Kuo, W.J.*, et al.* (2013). fMRI hemodynamics accurately reflects neuronal timing in the human brain measured by MEG. NeuroImage 78, 372-384.

Lu, H., Golay, X., Pekar, J.J., and Van Zijl, P.C. (2003). Functional magnetic resonance imaging based on changes in vascular space occupancy. Magn Reson Med 50, 263-274.

Madsen, M.T. (1992). A simplified formulation of the gamma variate function. Physics in Medicine and Biology 37, 1597.

Malonek, D., and Grinvald, A. (1996). Interactions between electrical activity and cortical microcirculation revealed by imaging spectroscopy: implications for functional brain mapping. Science 272, 551-554.

Mansfield, P., Maudsley, A.A., and Baines, T. (1976). Fast Scan Proton Density Imaging by Nmr. J Phys E Sci Instrum 9, 271-278.

Menon, R.S., Ogawa, S., Strupp, J.P., and Ugurbil, K. (1997). Ocular dominance in human V1 demonstrated by functional magnetic resonance imaging. J Neurophysiol 77, 2780-2787.

Menon, R.S., Ogawa, S., Tank, D.W., and Ugurbil, K. (1993). Tesla gradient recalled echo characteristics of photic stimulation-induced signal changes in the human primary visual cortex. Magnetic resonance in medicine : official journal of the Society of Magnetic Resonance in Medicine / Society of Magnetic Resonance in Medicine 30, 380-386.

Moon, C.H., Fukuda, M., and Kim, S.G. (2013). Spatiotemporal characteristics and vascular sources of neural-specific and -nonspecific fMRI signals at submillimeter columnar resolution. NeuroImage 64, 91-103.

Ogawa, S., Lee, T.M., Kay, A.R., and Tank, D.W. (1990). Brain magnetic resonance imaging with contrast dependent on blood oxygenation. Proc Natl Acad Sci U S A 87, 9868-9872.

Ogawa, S., Tank, D.W., Menon, R., Ellermann, J.M., Kim, S.G., Merkle, H., and Ugurbil, K. (1992). Intrinsic signal changes accompanying sensory stimulation: functional brain mapping with magnetic resonance imaging. Proc Natl Acad Sci U S A 89, 5951-5955.

Polimeni, J.R., Fischl, B., Greve, D.N., and Wald, L.L. (2010). Laminar analysis of 7T BOLD using an imposed spatial activation pattern in human V1. NeuroImage 52, 1334-1346.

Poser, B.A., and Norris, D.G. (2009). Investigating the benefits of multi-echo EPI for fMRI at 7 T. NeuroImage 45, 1162-1172.

Poser, B.A., Versluis, M.J., Hoogduin, J.M., and Norris, D.G. (2006). BOLD contrast sensitivity enhancement and artifact reduction with multiecho EPI: parallel-acquired inhomogeneity-desensitized fMRI. Magn Reson Med 55, 1227-1235.

Shih, Y.Y., Chen, Y.Y., Lai, H.Y., Kao, Y.C., Shyu, B.C., and Duong, T.Q. (2013). Ultra high-resolution fMRI and electrophysiology of the rat primary somatosensory cortex. NeuroImage 73, 113-120.

Siero, J.C., Petridou, N., Hoogduin, H., Luijten, P.R., and Ramsey, N.F. (2011). Cortical depth-dependent temporal dynamics of the BOLD response in the human brain. J Cereb Blood Flow Metab 31, 1999-2008.

Silva, A.C., and Koretsky, A.P. (2002). Laminar specificity of functional MRI onset times during somatosensory stimulation in rat. Proceedings of the National Academy of Sciences of the United States of America 99, 15182-15187.

Silva, A.C., Koretsky, A.P., and Duyn, J.H. (2007). Functional MRI impulse response for BOLD and CBV contrast in rat somatosensory cortex. Magnetic resonance in medicine : official journal of the Society of Magnetic Resonance in Medicine / Society of Magnetic Resonance in Medicine 57, 1110-1118.

Spees, W.M., Yablonskiy, D.A., Oswood, M.C., and Ackerman, J.J. (2001). Water proton MR properties of human blood at 1.5 Tesla: magnetic susceptibility, T(1), T(2), T*(2), and non-Lorentzian signal behavior. Magn Reson Med 45, 533-542.

Tian, P., Teng, I.C., May, L.D., Kurz, R., Lu, K., Scadeng, M., Hillman, E.M., De Crespigny, A.J., D'Arceuil, H.E., Mandeville, J.B.*, et al.* (2010). Cortical depth-specific microvascular dilation underlies laminar differences in blood oxygenation level-dependent functional MRI signal. Proc Natl Acad Sci U S A 107, 15246-15251.

Ugurbil, K., Toth, L., and Kim, D.S. (2003). How accurate is magnetic resonance imaging of brain function? Trends Neurosci 26, 108-114.

Uhlirova, H., Kilic, K., Tian, P., Thunemann, M., Desjardins, M., Saisan, P.A., Sakadzic, S., Ness, T.V., Mateo, C., Cheng, Q.*, et al.* (2016). Cell type specificity of neurovascular coupling in cerebral cortex. Elife 5.

Uludag, K., Muller-Bierl, B., and Ugurbil, K. (2009). An integrative model for neuronal activity-induced signal changes for gradient and spin echo functional imaging. NeuroImage 48, 150-165.

Vazquez, A.L., Fukuda, M., Tasker, M.L., Masamoto, K., and Kim, S.G. (2010a). Changes in cerebral arterial, tissue and venous oxygenation with evoked neural stimulation: implications for hemoglobin-based functional neuroimaging. J Cereb Blood Flow Metab 30, 428-439.

Vazquez, A.L., Fukuda, M., Tasker, M.L., Masamoto, K., and Kim, S.G. (2010b). Changes in cerebral arterial, tissue and venous oxygenation with evoked neural stimulation: implications for hemoglobin-based functional neuroimaging. Journal of cerebral blood flow and metabolism : official journal of the International Society of Cerebral Blood Flow and Metabolism 30, 428-439.

Weiskopf, N., Klose, U., Birbaumer, N., and Mathiak, K. (2005). Single-shot compensation of image distortions and BOLD contrast optimization using multi-echo EPI for real-time fMRI. NeuroImage 24, 1068-1079.

Yacoub, E., Duong, T.Q., Van De Moortele, P.F., Lindquist, M., Adriany, G., Kim, S.G., Ugurbil, K., and Hu, X. (2003). Spin-echo fMRI in humans using high spatial resolutions and high magnetic fields. Magn Reson Med 49, 655-664.

Yacoub, E., Harel, N., and Ugurbil, K. (2008). High-field fMRI unveils orientation columns in humans. Proceedings of the National Academy of Sciences of the United States of America 105, 10607-10612.

Yacoub, E., Shmuel, A., Pfeuffer, J., Van De Moortele, P.F., Adriany, G., Andersen, P., Vaughan, J.T., Merkle, H., Ugurbil, K., and Hu, X. (2001). Imaging brain function in humans at 7 Tesla. Magn Reson Med 45, 588-594.

Yu, X., Glen, D., Wang, S., Dodd, S., Hirano, Y., Saad, Z., Reynolds, R., Silva, A.C., and Koretsky, A.P. (2012). Direct imaging of macrovascular and microvascular contributions to BOLD fMRI in layers IV-V of the rat whisker-barrel cortex. NeuroImage 59, 1451-1460.

Yu, X., He, Y., Wang, M., Merkle, H., Dodd, S.J., Silva, A.C., and Koretsky, A.P. (2016). Sensory and optogenetically driven single-vessel fMRI. Nature methods 13, 337-340.

Yu, X., Qian, C., Chen, D.Y., Dodd, S.J., and Koretsky, A.P. (2014). Deciphering laminar-specific neural inputs with line-scanning fMRI. Nature methods 11, 55-58.

Yu, X., Wang, S.M., Chen, D.Y., Dodd, S., Goloshevsky, A., and Koretsky, A.P. (2010). 3D mapping of somatotopic reorganization with small animal functional MRI. NeuroImage 49, 1667-1676.

Main Figures (4)

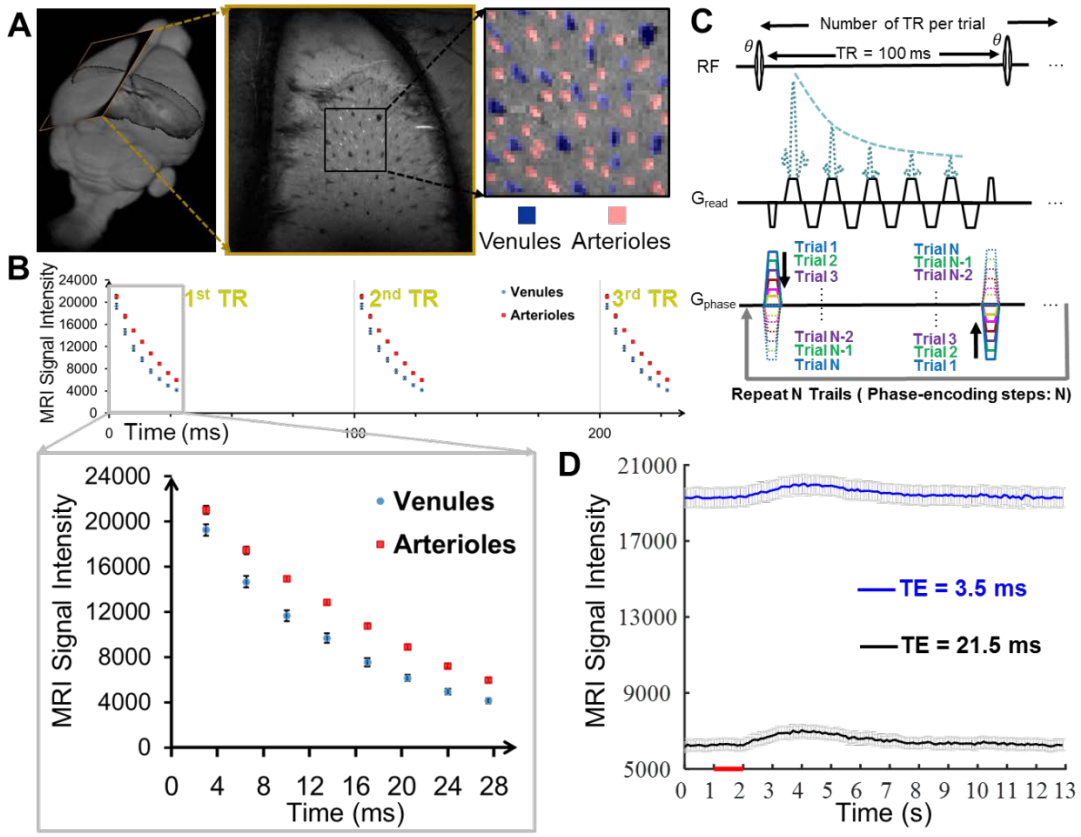

Figure 1. Map the single-vessel fMRI signal with the MELS-fMRI method. (**A**) The 2D slice position of the A-V map is shown in the 3D rat brain (left panel). The arteriole voxels were marked in red ROIs and the venule voxels were marked as blue ROIs (right panel). (**B**). The signal intensity of venule voxels (blue circles) and arteriole voxels (red squares) is shown at different echo time from three consecutive TR (100ms). The enlarged data showed that the venule voxels has faster decay curve than the arteriole voxels (one representative rat from five rats, venules: n = 25, arteriole: n = 35, mean ± s.e.m) **(C)**. MELS-fMRI pulse sequence diagram. Only one phase-encoding step was employed at each trial. The trials were repeated for the number of phase-encoding steps to fill up the k-space. (**D**). The signal intensity of long TE (21.5 ms) and short TE (3.5 ms) from venule voxels (n = 25, mean ± s.e.m) as the function of the on/off block design time (1s off, 2s on, and 10 s off).

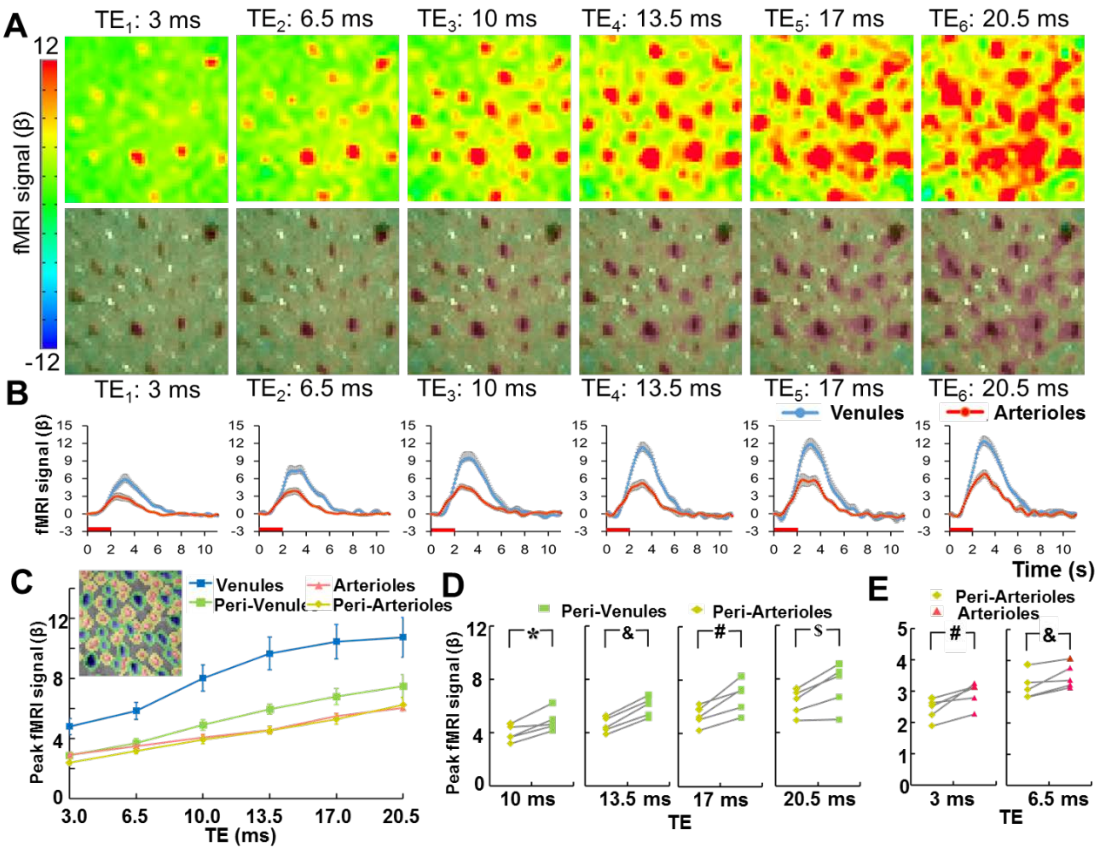

Figure 2. The vessel-specific fMRI patterns acquired at different TEs. (**A**) The color-coded fMRI maps are shown at six different TEs (up) and the overlapped images with the A-V map represent the venule-dominated peak fMRI signal distribution (bottom). (**B**) The averaged time courses of fMRI signal from venule (blue) and arteriole (red) voxels (n = 5 rats, the graphs show the mean ± s.e.m). (**C**) The peak amplitudes of fMRI signal from arteriole (red), venule (blue), peri-venule (green), and peri-arteriole (yellow) voxels are shown at different TEs (n = 5 rats, mean ± s.e.m). The inset is an A-V map demo to show the definition of different ROIs. (**D**) The peak fMRI signal of peri-venule voxels are significantly higher than that of the peri-arteriole voxels acquired at TEs ranging from 10ms to 20.5ms (n=5, *, p = 0.007, &, p = 0.0001, #, p = 0.005, $, p = 0.012, paired t-test). (**E**) The peak fMRI signal of arteriole voxels are significantly higher than that of the peri-arteriole voxels acquired at TEs 3 ms and 6.5ms (#, p = 0.012; &, p = 0.017, paired t-test, n = 5).

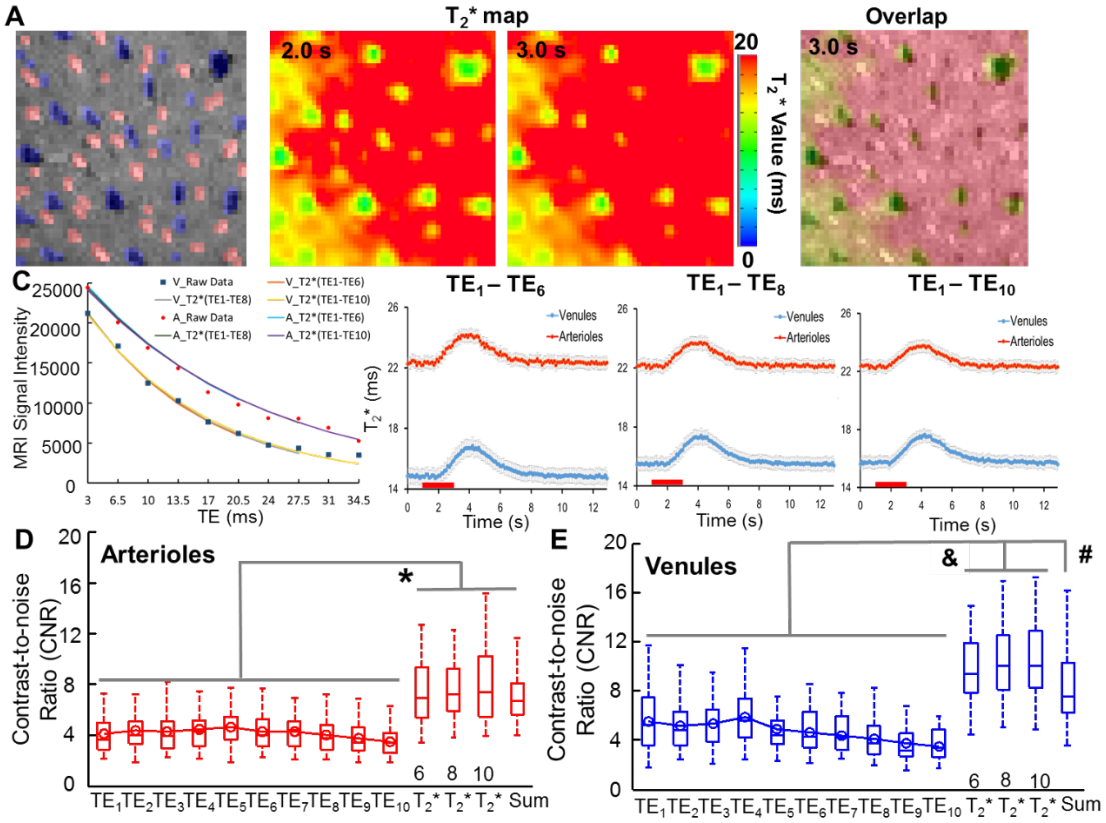

Fiugre 3. The vessel-specific T_2* map with the MELS-fMRI method. (A) A-V map **(B)** The T_2* maps of the 2D slice acquired at 2s and 3s after stimulus onset (left and middle panel). The T_2* map (3s) is overlapped with the A-V map, showing all venules voxels have shorter T_2* decay time than the surrounding parenchyma and arteriole voxels (right). **(C)** The decay curves were fitted to the MR signal detected at different TEs of one venule voxel and one arterial voxel. The averaged time course of T_2*-value (TE1-TE6, TE1-TE8, TE1-TE10) based fMRI signal from most activated venules (blue) and arterioles ROIs (n = 48 arterioles, red, 36 venules, blue, mean ± s.e.m.). **(D-E)** The Contrast-to-noise Ratios (CNR) of T_2*-weight fMRI signal acquired at different TEs are significantly lower than the CNR of the T_2*-based fMRI signal from arteriole and venule voxels (*, F=36.81, p<0.00001, &, F=33.03, p<0.00001, one-way ANOVA followed by Tukey's multiple comparison test).

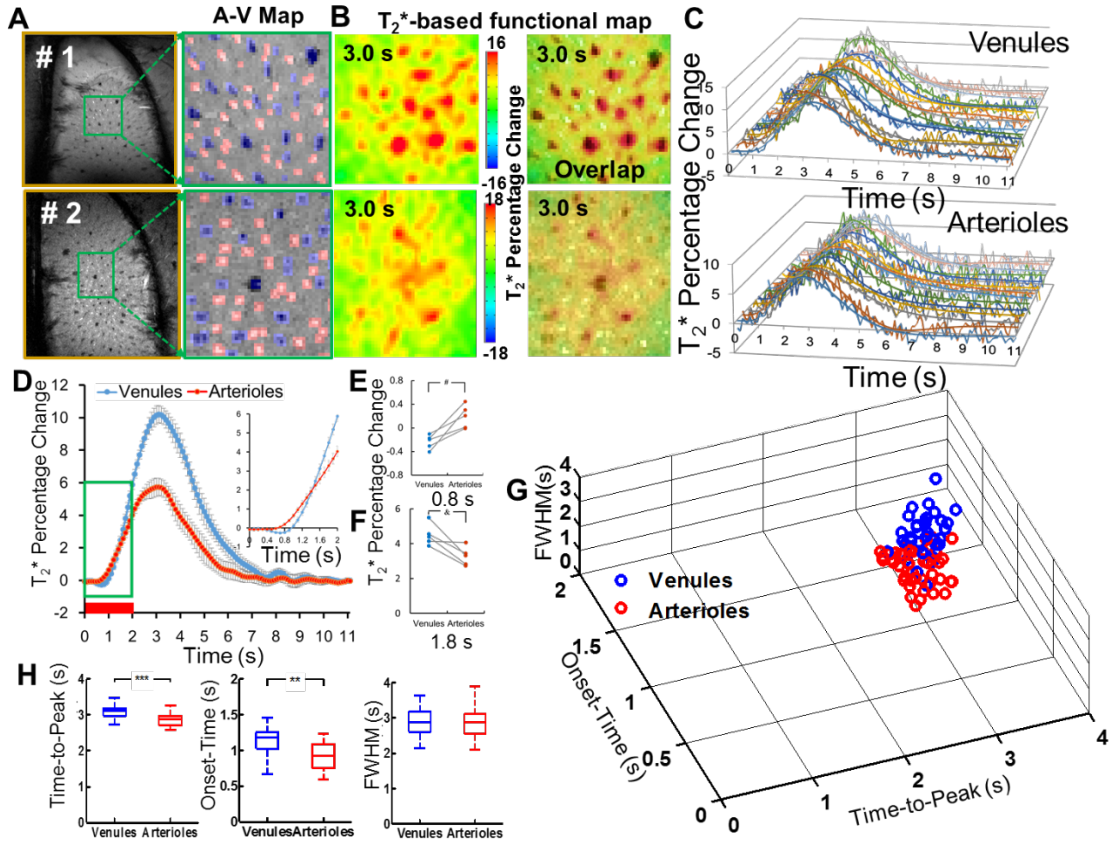

Figure 4. The hemodynamic feature of the T_2*-based fMRI signal with the MELS-fMRI method. (**A**) The A-V maps from two representative rats of five rats show arteriole (red) and venule (blue) ROIs. (**B**) T_2*-based fMRI maps at 3.0s after stimulation and the overlap images with A-V maps. (**C**) The time course (raw data and fitting curves) of T_2*-based fMRI signal from individual venule voxels (upper panel) and individual arteriole voxels (lower panel) of one representative rat. (**D**) The averaged time course of T_2* fMRI signal from venule (blue) and arteriole (red) voxels (n = 5 rats, mean ± s.e.m). The inset is the enlarged time course from 0 s to 2.0 s after stimulus onset. (**E-F**) T_2* fMRI signal percentage changes from arteriole and venule ROIs are shown at 0.8 s and 1.8 s after stimulation onset from individual rats (#, p = 0.006; &, p = 0.012, paired t-test, n = 5). (**G**) The 3d plot of Onset-time (T0), Time-to-Peak (TTP), and the full-width-of-half-maximum (FWHM) of T_2* fMRI signal from individual arteriole (red circles, 34, $r^2 > 0.8$) and venule (blue circles, 43, $r^2 > 0.7$) voxels demonstrates two distinct clusters. (**H**). The boxplot of TTP, T0 from venule voxels (blue) is significantly higher than that from arteriole voxels (red) (*, p = 6.2×10^{-8}, &, p = 8.1×10^{-9}, unpaired t-test, arteriole voxels, 34, venule voxels, 43). The boxplot shows no significant difference on FWHM of the venule and arteriole voxels (right panel).

Supplementary Figures (5)

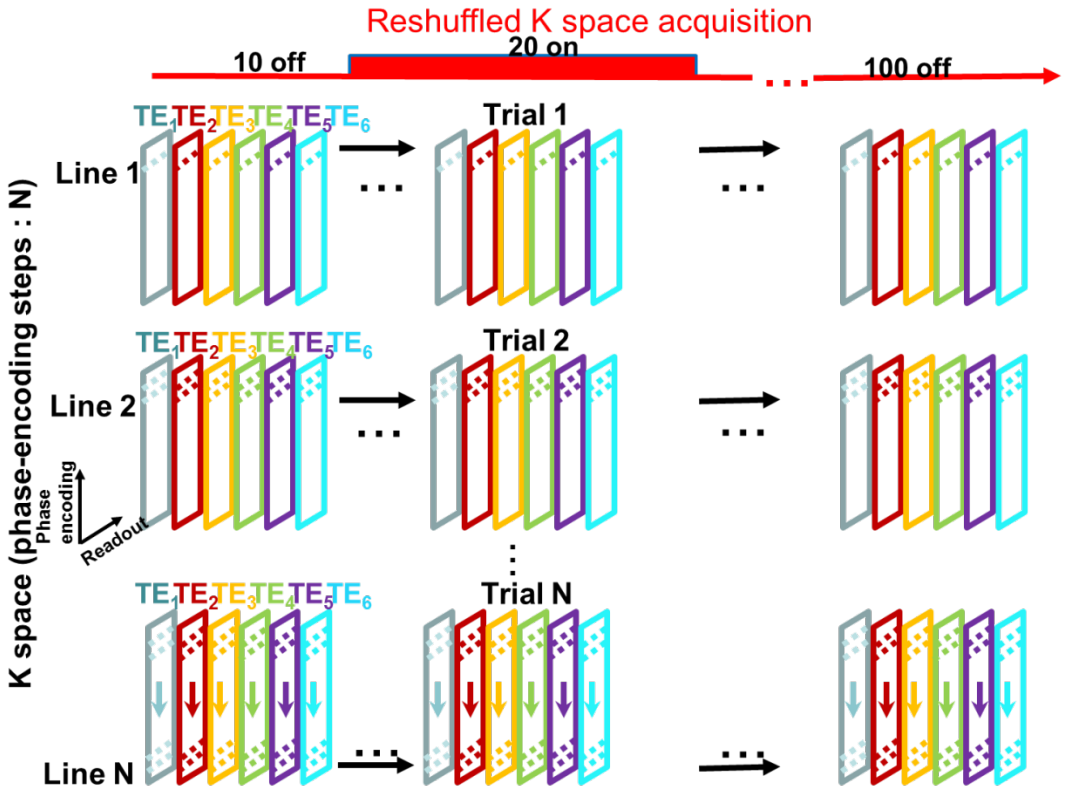

Supplementary Figure 1. K-space Trajectory of Multi-Echo Line-Scanning fMRI (MELS-fMRI). The k-space of MELS-fMRI is shown in a block-design paradigm with 10 scans off, 20 scans on and 100 scans off (the red line). Each box in different colors represents the k-space of the same slice acquired at different TEs. Within the box, each line indicated a k-space line. One line filled the k-space for each image at each trial consequentially. Then the trials were repeated for the number of phase-encoding steps.

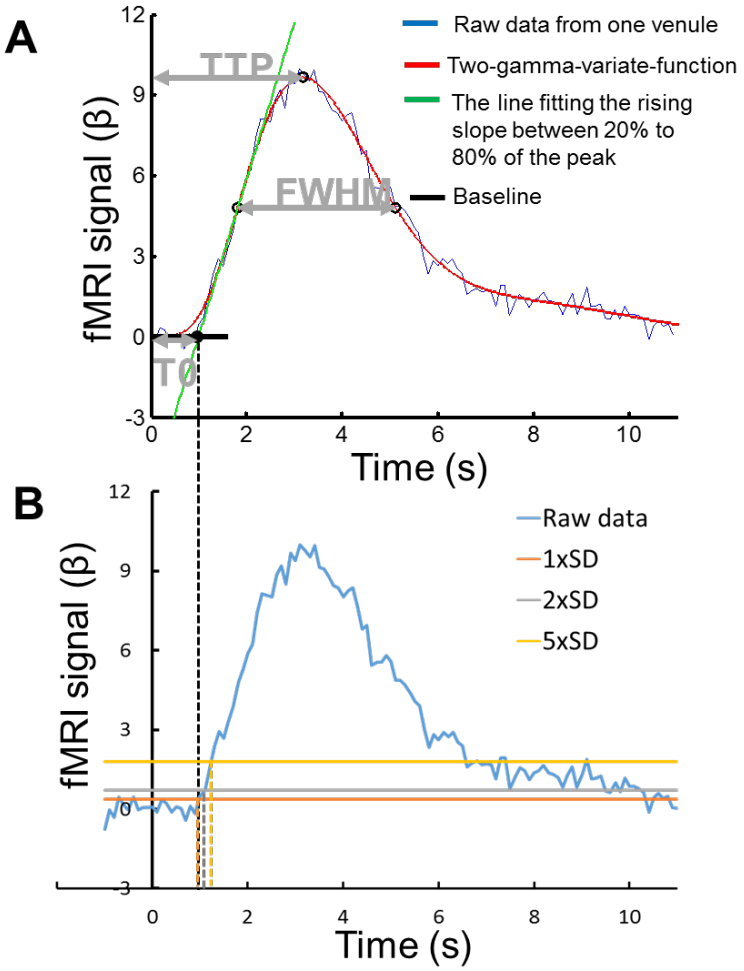

Supplementary Figure 2. The Definition of T0, TTP, FWHM. (A). The raw fMRI signal (blue line) was fitted with the two-gamma-variate function (red line). The green line was fit to the rising slope of fMRI signal between 20% and 80% to the peak amplitude of two-gamma-variate-function. The T0 was estimated as the intercept with the x-axis. The TTP was estimated by the time from the stimulus onset to the peak amplitude of the two-gamma-variate-function. The FWHM was estimated by the time between two points that are the half of the maximum amplitude of the two-gamma-variate-function. **(B).** the first (second, fifth) standard deviation (SD) from baseline show that the onset time defined here is between the first SD and the second SD from baseline.

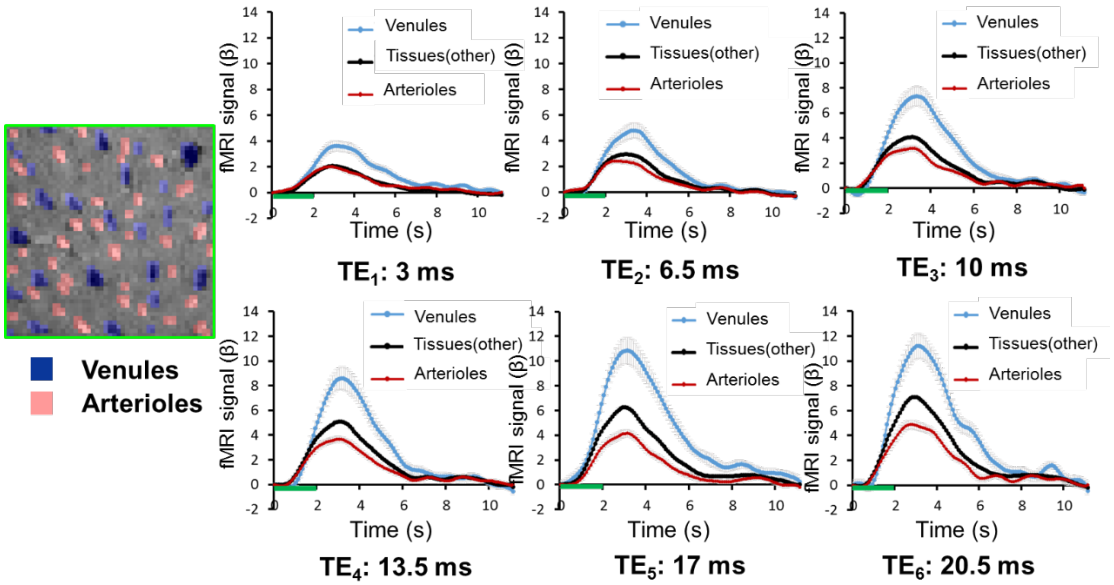

Supplementary Figure 3. The averaged time courses of fMRI signal from venule (blue), arteriole (red) and other non-vessel voxels (black) from one representative rat.

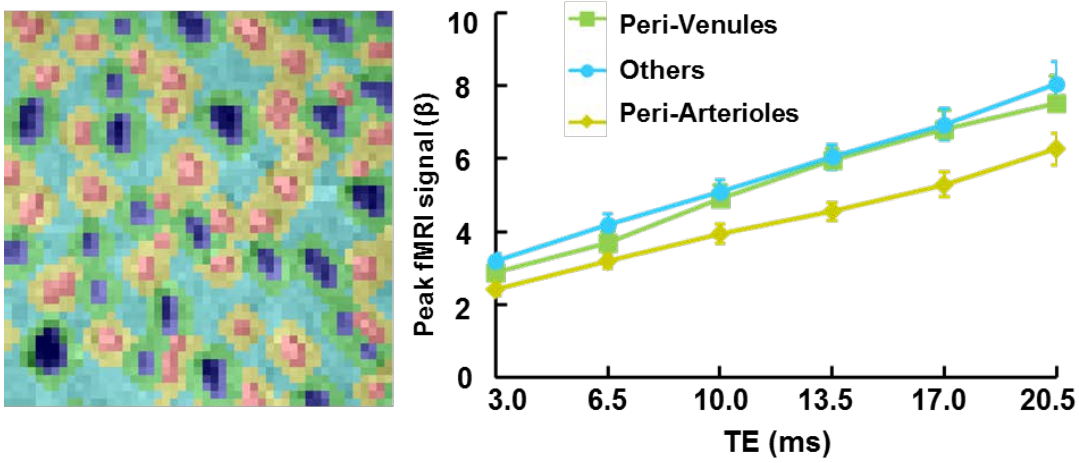

Supplementary Figure 4. The peak amplitudes of fMRI signal from peri-venule (green), peri-arteriole (yellow), and others (cyan) voxels are shown at different TEs (n = 5 rats, mean ± s.e.m). The left panel is an A-V map demo to show the definition of different ROIs.

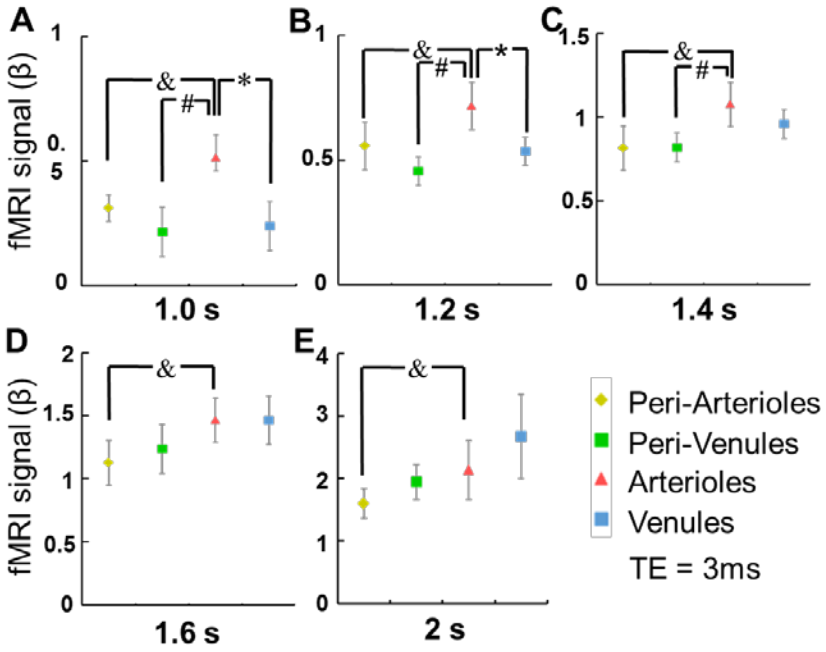

Supplementary Figure 5. Vessel-specific fMRI signal at different time (TE = 3 ms). The amplitudes (1.0s , 1.2s, 1.4s, 1.6s, 2s after the stimulation onset) of the fMRI signal from arteriole (red), venule (blue), peri-venule (green), and peri-arteriole (yellow) voxels were shown at 3 ms TE (n = 5 rats, mean ± s.e.m). **(A)** The fMRI signal of arteriole voxels was significantly higher than that of the venule, peri-venule, and peri-arteriole voxels at 1.0s after the stimulation onset. (Paired t-test, n = 5, *, p = 0.009, &, p = 0.04, #, p = 0.037). **(B)**. The fMRI signal of arteriole voxels was significantly higher than that of the venule, peri-venule, peri-arteriole voxels at 1.2 s after the stimulation onset. (Paired t-test, n = 5, *, p = 0.025, &, p = 0.047, #, p = 0.034) **(C)**. The fMRI signal of arteriole voxels was significantly higher than that of peri-venule and peri-arteriole voxels at 1.4 s after the stimulation onset. (Paired t-test, n = 5, &, p = 0.034, #, p = 0.049) **(D)**. The fMRI signal of arteriole voxels was significantly higher than that of peri-arteriole voxels at 1.6 s after the stimulation onset. (Paired t-test, n = 5, &, p = 0.049) **(E)**. The fMRI signal of venule voxels was significantly higher than that of arteriole voxels at 2.0 s after the stimulation onset. (Paired t-test, n = 5, &, p = 0.042)

Supplementary Movie Legends

Supplementary Movie 1. The three-dimensional plot of the mean signal intensity of multiple TEs from venule voxels as a function of time (block design: 1s off, 2s on, and 10s off).

Supplementary Movie 2. The spatial patterns of vessel-specific fMRI signal at different TEs. The voxel-wise BOLD fMRI signal was demonstrated from 7x7 voxel matrix covering one individual venule (middle panel: the dark voxel in the green square, in-plane resolution: 50 x 50 μm). The red curser in the center voxel (100 ms temporal resolution) indicated the fMRI signal changes at 6.5 ms TE (right panel).

Supplementary Movie 3. The T_2*-based fMRI maps from two representative rats. T_2*-based fMRI maps (middle panel) were overlapped with the A-V map (left panel). The most active voxels (red color, 100x100 μm) were primarily located at the underlying venule voxels (black dots, right panel).